Dynamical redistribution of column ozone in the Southern Hemisphere
Rogal, Marek J.
ProQuest Dissertations and Theses; 2009; Dissertations & Theses @ University of Wisconsin at Madison
pg. n/a

Dynamical Redistribution of Column Ozone in the Southern Hemisphere

by

MAREK J. ROGAL

A Dissertation submitted as a partial fulfillment of the requirements for the degree of

DOCTOR OF PHILOSPHY

(ATMOSPHERIC AND OCEANIC SCIENCES)

at the

UNIVERSITY OF WISCONSIN – MADISON

2009

Reproduced with permission of the copyright owner. Further reproduction prohibited without permission.

UMI Number: 3399940

All rights reserved

INFORMATION TO ALL USERS
The quality of this reproduction is dependent upon the quality of the copy submitted.

In the unlikely event that the author did not send a complete manuscript
and there are missing pages, these will be noted. Also, if material had to be removed,
a note will indicate the deletion.

UMI 3399940
Copyright 2010 by ProQuest LLC.
All rights reserved. This edition of the work is protected against
unauthorized copying under Title 17, United States Code.

ProQuest LLC
789 East Eisenhower Parkway
P.O. Box 1346
Ann Arbor, MI 48106-1346

Reproduced with permission of the copyright owner. Further reproduction prohibited without permission.

Committee's Page. This page is not to be hand-written except for the signatures

A dissertation entitled

Dynamical Redistribution of Column Ozone in the Southern Hemisphere

submitted to the Graduate School of the
University of Wisconsin-Madison
in partial fulfillment of the requirements for the
degree of Doctor of Philosophy

by

MAREK J. ROGAL

Date of Final Oral Examination: September 28, 2009

Month & Year Degree to be awarded: **December** 2009 **May** **August**

****

Approval Signatures of Dissertation Committee

Matthew H. Hitchman

Signature, Dean of Graduate School

Martin Cadwallader /AW

Committee's Page. This page is not to be hand-written except for the signatures

Reproduced with permission of the copyright owner. Further reproduction prohibited without permission.

Abstract

A detailed analysis of specific cases in 1998 and 2000 as well as a climatology spanning the period 1995-2004 are presented in this thesis in order to explain the influence that the dynamical regimes of the Upper Troposphere Lower Stratosphere region exert on the distribution of the Column Ozone in the Southern Hemisphere (SH). This study, reinforced with modeling experiments conducted using the University of Wisconsin Nonhydrostatic Modeling System (UW-NMS), has shown the extent to which the Tibetan Plateau and convection over Southeast Asia, which produces large anticyclones, namely the Tibetan High (TH) and Australian High (AH), shape the wave structure and the ozone distribution in the SH during the winter to spring transition period. It is found that a strong AH (southern part of the "*Gill* [1980] solution" to off-equatorial transient heating due to convection) leads to an "Ozone Croissant", while enhanced activity of the South African High (SAH) and Indian Ocean High (IOH) produces the column ozone structure reminiscent of the Ozone Collar. Isentropic trajectories underscore the importance of crossequatorial flow from the TH in modulating the AH and anticyclones over the Indian Ocean (IOH). This grand anticyclone (TH), resulting from heating of the Tibetan Plateau, is responsible for a large part of the meridional mass circulation during the boreal summer and fall in the vicinity of the Indian Ocean. The outflow associated with convectively-driven pair of anticyclones (TH and AH) was shown to be a major factor in the maintenance and modulation of the Australian Subtropical Westerly Jet located immediately poleward of the AH. It is also shown that the ozone distribution is strongly influence by the El Nino Southern Oscillation (ENSO). Results revealed that during La Niña column ozone is 5-10DU larger in 10-55°S. Additionally there is a 50° westward shift in the column ozone pattern during La Niña, with ~20 DU enhancement in the 50°W-100°E band. Significant column ozone increase occurs poleward of South Africa during September and lies in a deep barotropic warm anomaly, associated with northeastward displacement of the South Indian Ocean High (SIOH) from South Africa. El Niño conditions display an enhanced SAH (35°S) while the AH (20°S) displays enhancement during La Niña conditions.

Reproduced with permission of the copyright owner. Further reproduction prohibited without permission.

Acknowledgments

Special thanks to Prof. Matthew Hitchman, who supported me through the graduate school. I would not be where I am today without his friendship, patience and wisdom. I would like to give thanks to members of my Committee for their interest in subject, unlimited amount of encouragement and valuable scientific input. Thanks go to my family, who supported me during this long voyage, with love, encouragement and good words. Finally I am thankful for support and generosity of my friends, without whom, I would not have the strength to finish.

Reproduced with permission of the copyright owner. Further reproduction prohibited without permission.

Contents

Reproduced with permission of the copyright owner. Further reproduction prohibited without permission.

Reproduced with permission of the copyright owner. Further reproduction prohibited without permission.

Reproduced with permission of the copyright owner. Further reproduction prohibited without permission.

Reproduced with permission of the copyright owner. Further reproduction prohibited without permission.

List of Figures

Reproduced with permission of the copyright owner. Further reproduction prohibited without permission.

Reproduced with permission of the copyright owner. Further reproduction prohibited without permission.

Reproduced with permission of the copyright owner. Further reproduction prohibited without permission.

Reproduced with permission of the copyright owner. Further reproduction prohibited without permission.

Reproduced with permission of the copyright owner. Further reproduction prohibited without permission.

Reproduced with permission of the copyright owner. Further reproduction prohibited without permission.

Reproduced with permission of the copyright owner. Further reproduction prohibited without permission.

Reproduced with permission of the copyright owner. Further reproduction prohibited without permission.

List of Tables

Reproduced with permission of the copyright owner. Further reproduction prohibited without permission.

Chapter 1

1.1. Introduction

The goal of this study is to further the understanding of the role that convection over the Maritime Continent and Southeast Asia, the Tibetan Plateau and Southern Hemisphere (SH) general circulation features play in shaping of the column ozone distribution in the SH during the southern winter to spring transition. Even though several studies have furthered the understanding of the underlying mechanisms involved in the setup of specific dynamical conditions leading to the observed zonally asymmetric total ozone distribution (*MacDowall*, 1960; *Godson*, 1963; *van Loon and Jenne,* 1972; *Wirth,* 1991, 1993; *Randel*, 1987, 1993; *Hudson et al.*, 2003; *Olsen* et al., 2004; *Lahoz*, 2009) none of them fully explained the whole set of conditions that the SH atmosphere must meet to produce the peculiar wave 1 shape, named Ozone Croissant (OC). In particular, there is no existing reason given for the location of the OC maximum south of Australia. The reason why most of the observational, modeling and mechanistic studies fell short of reaching this goal is of a simple nature: all of them focus on one or more elements of this puzzle without analysis of the broad set of mechanisms that govern the whole general circulation in the atmosphere. Knowing the fractal-like nature of our branch of science, this thesis, not claiming to deliver the unified theory of ozone distribution in the SH, will try to improve our knowledge about all prerequisites needed to produce the OC. This complex problem is approached by employment of observational studies of specific winter to spring transition periods as well as modeling experiments and a climatological approach needed to establish long-term repeatability of mechanisms involving in the redistribution of ozone in the SH. The secondary goal of this study involves the

Reproduced with permission of the copyright owner. Further reproduction prohibited without permission.

analysis of the role which is played by El Nino Southern Oscillation (ENSO), and to smaller degree by the Quasibiennial Oscillation (QBO) in modulating these mechanisms, thus in reshaping the ozone distribution as well. The remainder of this chapter will provide an introductory view of the general circulation from the standpoint of view of the SH, the ENSO and QBO as well as preview of fundamental and most recent studies concerning the subject.

1.2. Review of the zonally averaged general circulation.

The global atmospheric circulation may be viewed as a redistribution of energy and entropy from equatorial regions to higher latitudes. This, in general, tends to account for the poleward flow of the high energy and entropy parcels and the corresponding return-flow of air parcels with lower energy and entropy content. Because of the very turbulent nature of the atmospheric motions this may be described only in an averaged sense. One of such systems of description is known as the Eulerian-mean circulation, obtained by averaging the flow at constant pressure or geopotential height. The Eulerian-mean circulation (Fig. 1.1) shows the classic three-cell structure with a thermally direct Hadley cell in the tropics, an indirect Ferrel cell in midlatitudes and a comparatively weak direct polar cell in high latitudes (*Hadley*, 1735; *Ferrel*, 1859; *Thomson*, 1892; *Defant*, 1921; *Jeffreys*, 1926; *Lorenz*, 1967; *van Loon* et al., 1971; *Swanson and Trenberth*, 1981; *Peixoto and Oort*, 1992; *James*, 1994 among others). The mean circulation in the Ferrel cell is toward the Equator in the upper troposphere and toward the pole near the surface, corresponding to a net energy transport toward the Equator. However, in midlatitudes the net energy transport is poleward due to the transport by eddies.

Reproduced with permission of the copyright owner. Further reproduction prohibited without permission.

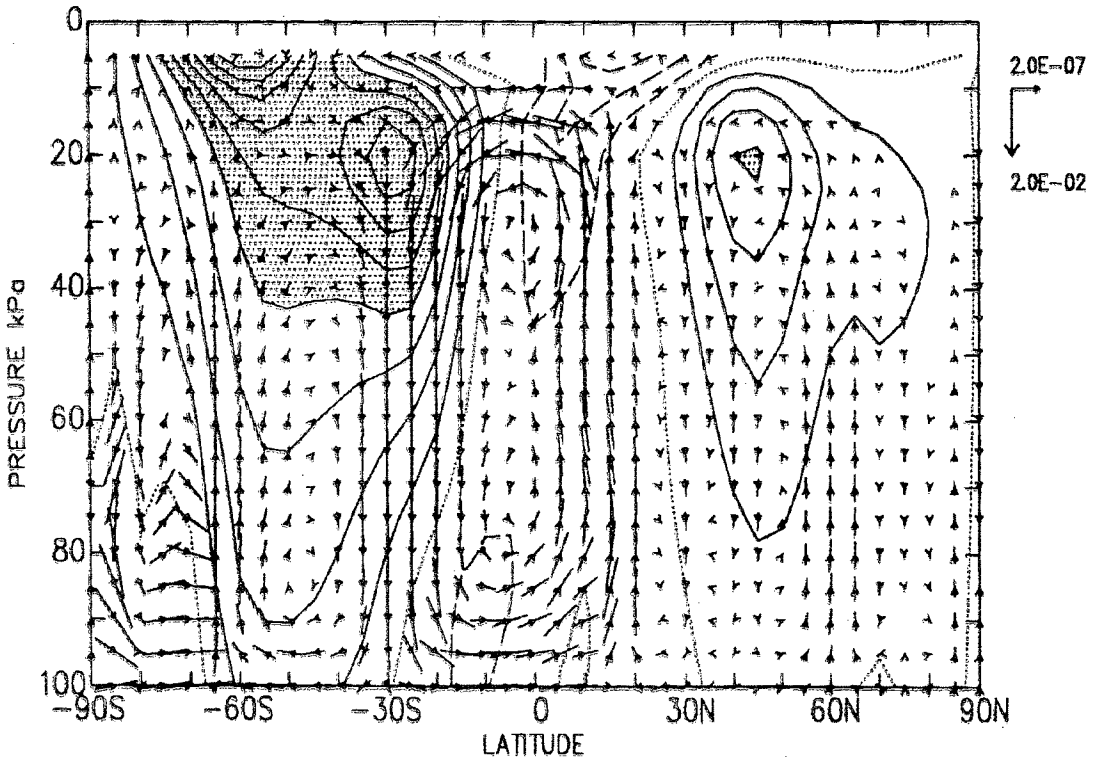

Figure 1.1. The zonal mean wind and vectors of the meridional circulation (m/s) for June-July-August. *After James* (1995)

To account for the influence of midlatitude eddies, different alternative to the Eulerian-mean circulation have been developed, including the transformed Eulerian-mean circulation (TEM, *Andrews and McIntyre*, 1976; *Dunkerton*, 1978; *Edmon et al.*, 1980). The TEM system, which will be fully disclosed in chapter two, includes the correction term to account for the mass transport by eddies, similar to the Stokes drift (*Stokes*, 1847) for shallow water as well as representing the nonacceleration theorem associated with wave momentum transports under the assumption of geostrophic balance and infinitesimal wave amplitudes. The TEM system introduced the residual circulation that differs remarkably from the Eulerian-mean by comprising a single cell with air rising in the equatorial regions and

Reproduced with permission of the copyright owner. Further reproduction prohibited without permission.

subsiding over the poles, with secondary ascent in the midlatitudes (*Edmon et al.,* 1980). Various authors (*Townsend and Johnson,* 1985; *Johnson,* 1985, 1989; *Held and Schneider*, 1999) have analyzed the circulation using either entropy or potential temperature as well as equivalent potential temperature (*Pauluis et al.*, 2008) as the vertical coordinates instead of pressure, which offers a more direct assessment of parcel trajectories (Fig. 1.2, contrast panel a with b).

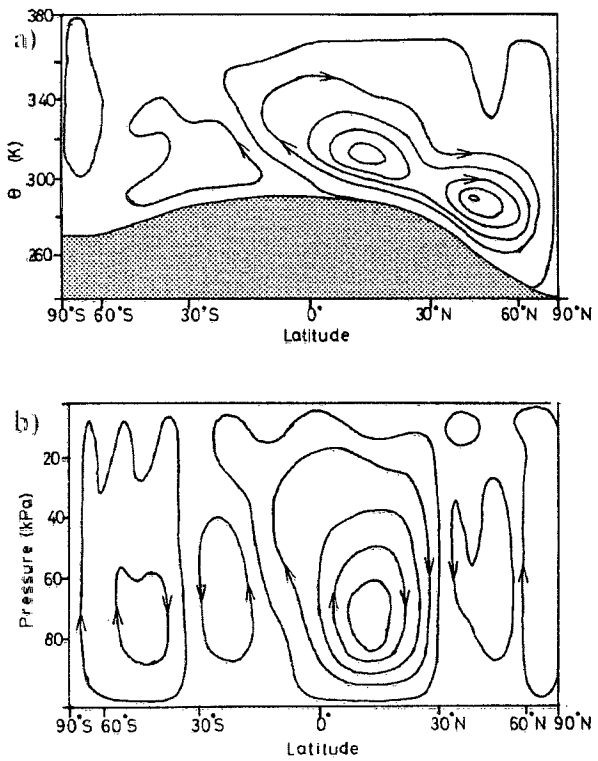

Figure 1.2. a) Meridional mass streamfunction on isentropes, b) Eulerian averaging of streamfunction in isobaric system. Both for January 1979, after *Townsend and Johnson*, 1985)

Atmospheric eddies are associated with large variations in the pressure and height of a parcel. However, the fluctuations in the parcels' entropy, potential temperature or potential

Reproduced with permission of the copyright owner. Further reproduction prohibited without permission.

density are much smaller, as long as eddies can be viewed as almost adiabatic. This allows for the fact that averaging the circulation along a surface of constant entropy provides a more direct description of the Lagrangian circulation. Nevertheless, as Bowman and Carrie (2002) noted, some differences persist between the circulations calculated using Lagrangian and isentropic approaches. The transformed Eulerian-mean circulation (Fig. 1.3), on isentropic surfaces shows a single global overturning cell from the equator to polar latitudes (*Johnson and Dutton*, 1976; *Gallimore and Johnson*, 1981; *Townsend and Johnson,* 1985; *Johnson*, 1989; *Held and Schneider*, 1999).

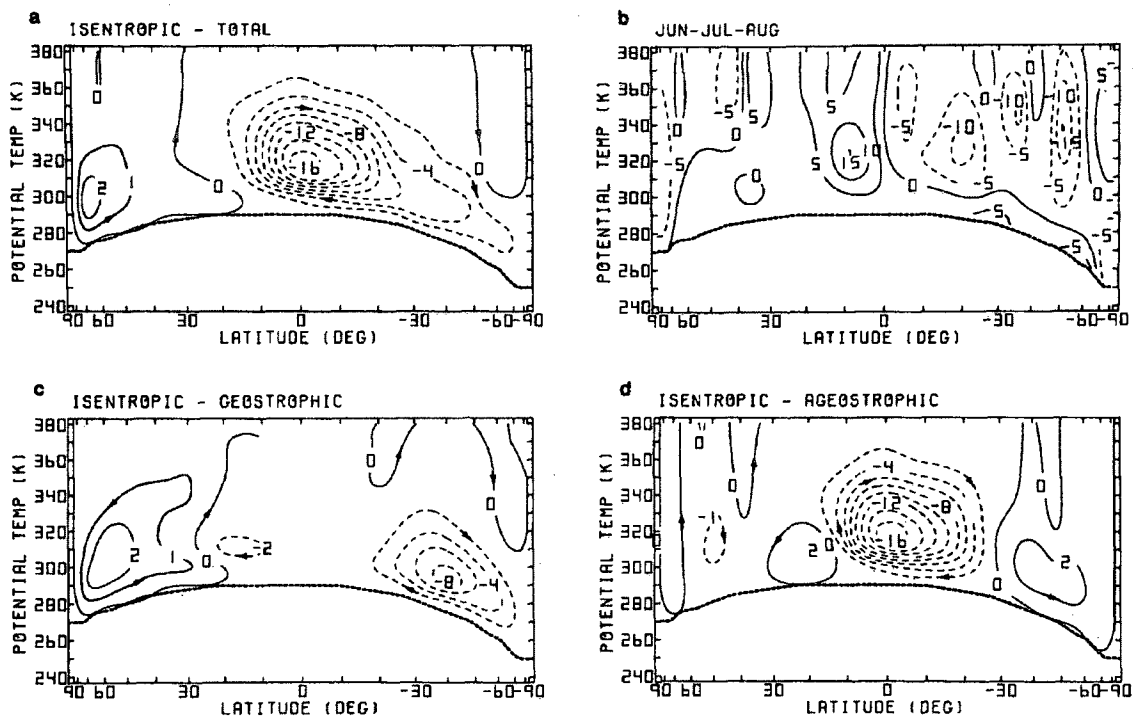

Figure 1.3. The June-August isentropic mass streamfunction for the a) isentropic mean, c) geostrophic and d) ageostrophic mean meridional circulations (10^{10} kg s^{-1}) and b) meridional cross-section of mass-weighted diabatic heating (10^{-1} K day^{-1}). Arrows indicate the direction of the circulation. After *Townsend and Johnson* (1985).

Reproduced with permission of the copyright owner. Further reproduction prohibited without permission.

Townsend and Johnson (1985) showed that during the March to May and September to November periods, the circulations resembling that of one cell global Hadley are almost symmetric about the equator and equipartitioned in terms of strength, while the one large Hadley circulation extend from 20°N to the Antarctic region during the SH winter almost without northern counterpart pointing to the overwhelming effect of the Asian monsoon in the time-averaged mass transport on the planetary scale (*Johnson*, 1985). Geostrophic mass circulation tends to dominate the midlatitudes (Fig. 1.3 c) while the ageostrophic mass circulation shows a direct Hadley cell component in low latitudes and an indirect Ferrel cell in midlatitudes, much weaker than the geostrophic counterpart at these latitudes. The meridional distribution of diabatic heating is characterized by tropical regions of diabatic heating, existing throughout the troposphere and resulting in the upward mass transport as well a,s to a smaller degree, heating zones within the extratropical lower troposphere. The diabatic cooling in the tropical SH is associated with the strong infrared signal and evaporation associated with clouds advected from the areas of deep convective systems.

The seasonal and zonal variations of the mass circulation result from the variation of planetary scale differential heating. Since a major part of this thesis is based upon the presumption of zonal differences in the atmospheric response to the thermal forcing, one must examine the intensity and location of the heat sources and sinks that determine the strength of the mass circulation. Most of the work presented in this thesis is based the isobaric perspective, but it is worthwhile to examine the sources of the most intense mass circulation resulting from strong diabatic heating well within the subtropical NH and the strong net diabatic cooling in the SH higher latitudes within the boreal summer and fall period as represented in the isentropic coordinates system.

Reproduced with permission of the copyright owner. Further reproduction prohibited without permission.

1.3 Horizontal distribution of the heat sources and moisture sinks

Several studies have contributed to our knowledge of the global distributions of atmospheric heat sources and sinks. Estimations of the seasonal global distributions of the mean tropospheric heating rates were made through the employment of vertical integration of the isentropic mass continuity equation using National Centers for Environmental Prediction (NCEP) and European Centre for Medium-Range Weather Forecast (ECMWF) analyses (*Wei et al.*,1983; *Johnson and Wei,* 1985; *Johnson et al.*, 1987 and *Schaack et al.*, 1990). The major heat sources were found to be located over the Intertropical Convergence Zone (ITCZ), Asian monsoon region, equatorial Africa and the South America (Fig. 1.4).

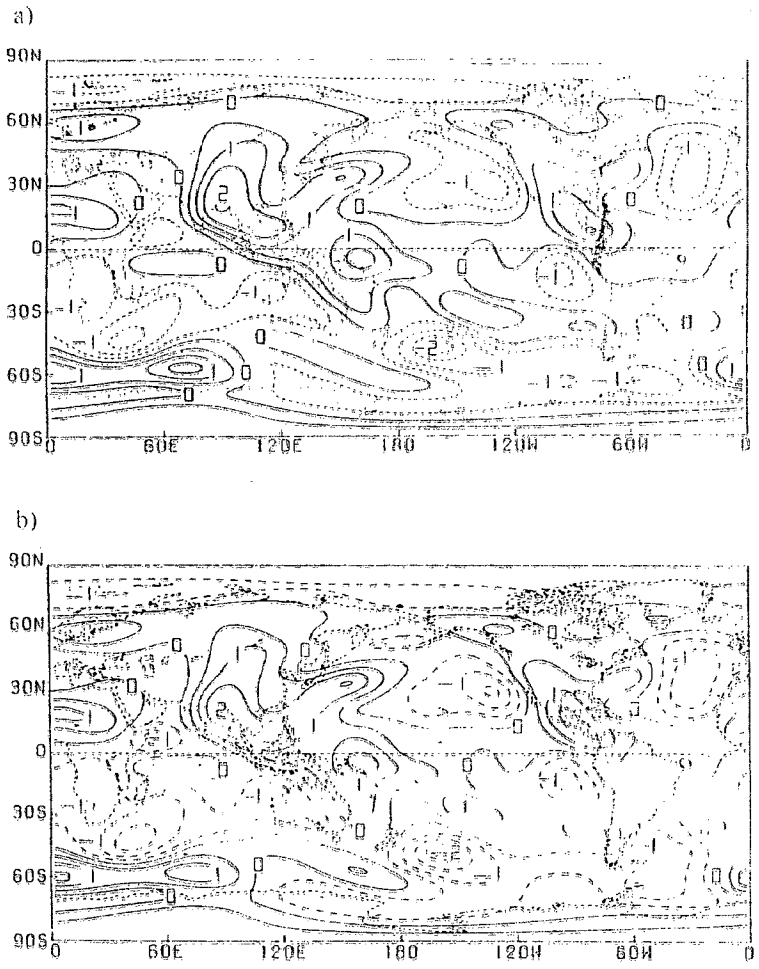

Figure 1.4. Vertically integrated global distribution of a) heating (10^2 W m^{-2}) and b) total divergence of the total flow energy transport (10^2 Wm^{-2}) during July 1979. After *Johnson*, 1989.

Reproduced with permission of the copyright owner. Further reproduction prohibited without permission.

The diabatic mass flux is pointing upward in the regions of heating and downward in the regions of cooling. The heat added by all components except those due to viscous processes (viscous dissipation of kinetic energy) constitutes the net of the vertically integrated horizontal divergence of the total flow energy in panel b) according to the energy equation by Johnson and Dutton (1976). These studies also showed that the primary centers of heating migrate meridionally and zonally with the annual variations of the incoming solar radiation and large-scale thermal contrast between land and sea. Hoskins et al. (1989) showed large seasonal and interannual variability of atmospheric heating in their estimation of sources and sinks based on the ECMWF-WMO data spanning from 1979 to 1989, while Shaack and Johnson (1994) showed large variations in the heating and distribution (both horizontal and vertical) of maxima and minima in the tropical regions during the 1986-1988 period in January and July in the ECMWF Tropical Oceans Global Atmosphere (TOGA) analyses. Li and Yanai (1996) also examined the global distributions of heat sources and sinks using the TOGA dataset (1985-1992) and found a high correlation between the strength of the Asian summer monsoons (*Webster and Yang*, 1992) and heating over the western Pacific, the Bay of Bengal and over the Arabian Sea, while heating over the equatorial Indian Ocean and central Pacific was found to be anticorrelated. Using the NCEP reanalysis, Yanai and Tomita (1998), calculated the global distribution of the apparent heat sources and the apparent moisture sinks (Fig. 1.5, *Yanai et al.*, 1973; *Yanai and Johnson*, 1993) for a period of 15 years (1980-1994). They found that dry regions like the Sahara are characterized by large sensible heating near the surface and intense radiative cooling in the upper troposphere, while the heat released by condensation with deep cumulus convection is a major contributor to

Reproduced with permission of the copyright owner. Further reproduction prohibited without permission.

heating over the tropical oceans. The atmosphere over the subtropical oceans undergoes radiative cooling and moistening due to evaporation in the areas with large subsidence.

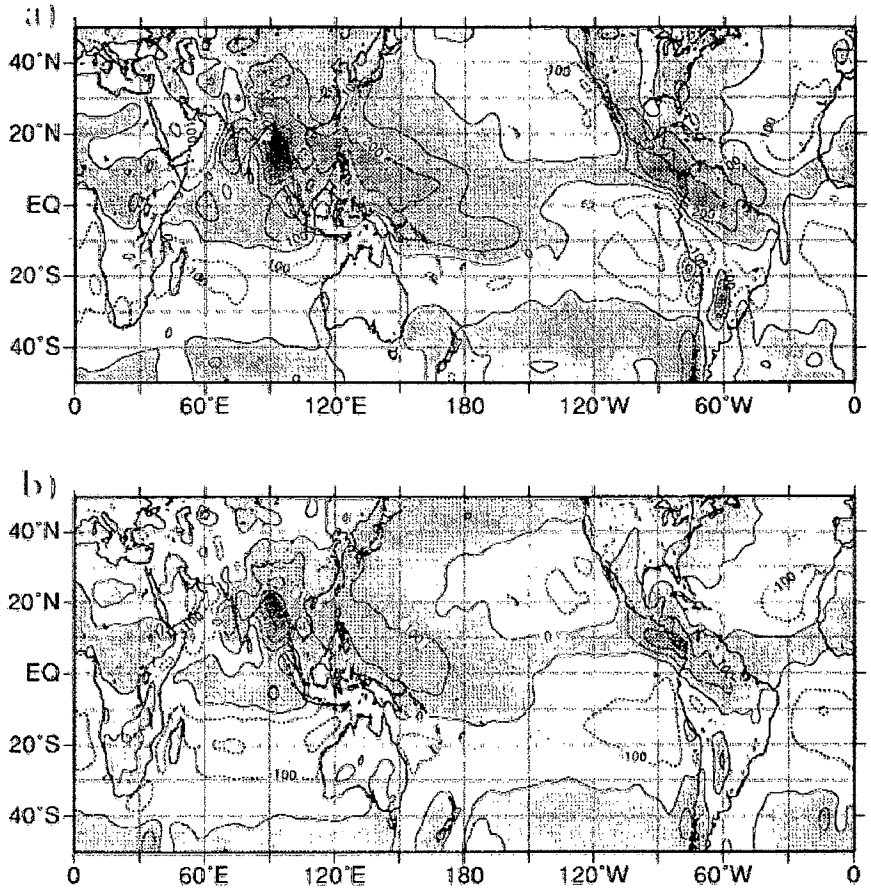

Figure 1.5. Global distribution of the 15-year (1980-1994) mean vertically integrated a) heat source and b) moisture sink for June-August. In W/m^2. After *Yanai and Tomita* (1998).

The major heat sources are located north of the equator during the boreal summer, both heating and convective activity is very robust in the centers mentioned above while cooling extends over the majority of the SH. Over the land areas including the Tibetan Plateau the apparent heat sources are larger than the moisture sinks which points to the relative importance of the sensible heating from the surface as being a significant contributor. During the SH spring period, major convective regions and heat sources in the Eastern Hemisphere

Reproduced with permission of the copyright owner. Further reproduction prohibited without permission.

shift southward toward the Equator and Southern Africa and South America start contributing to heating due to the release of latent heat in deep convection.

1.4 The Tibetan Plateau and Tibetan High.

The Tibetan Plateau is located in South Asia, covering more than one quarter of China; it has an average altitude above 4000 m. It is the highest plateau, with the most complex topography in the world, and it influences the atmospheric circulation over China, Asia, the NH and, as will be shown in this thesis, in the SH. The hypothesis that the Tibetan High may receive a large excess of the solar radiation in summer, leading to a setup of the thermal low immediately above the plateau and a corresponding high in the upper troposphere, is attributed to Flohn (1950, 1953) and revisited later by Rangarajan (1961) who performed the first analysis using available radiosonde observations from central and southern Asia. Its importance as an elevated heat source for the modulation of the Asian summer monsoon has been discussed by many authors afterward (*Flohn*, 1957, 1960, 1968; *Yeh*, 1957; *Koteswaram*, 1958; *Murakami*, 1958; *Hahn and Manabe*, 1975; *Luo and Yanai*, 1979; *Yeh and Gao*, 1979; *Yeh*, 1981; *Reiter and Gao*, 1982; *Zhang et al.*, 1988). The heat sources in the Tibetan Plateau are not accompanied moisture sinks of a similar magnitude, which underscores the relative dominance of sensible heating from the dry surface over net radiative cooling. Yeh and Gao (1979) estimated an average sensible heat flux of ~200 W/m^2 and net heating only at ~140 W/m^2 in the western part of the plateau in June. Luo and Yanai (1984) examined the 40-day mean distribution of apparent heat sources and moisture sinks over the plateau (Fig. 1.6) and found maximum heat sources and moisture sinks on the order of 4-5 K day^{-1}.

Reproduced with permission of the copyright owner. Further reproduction prohibited without permission.

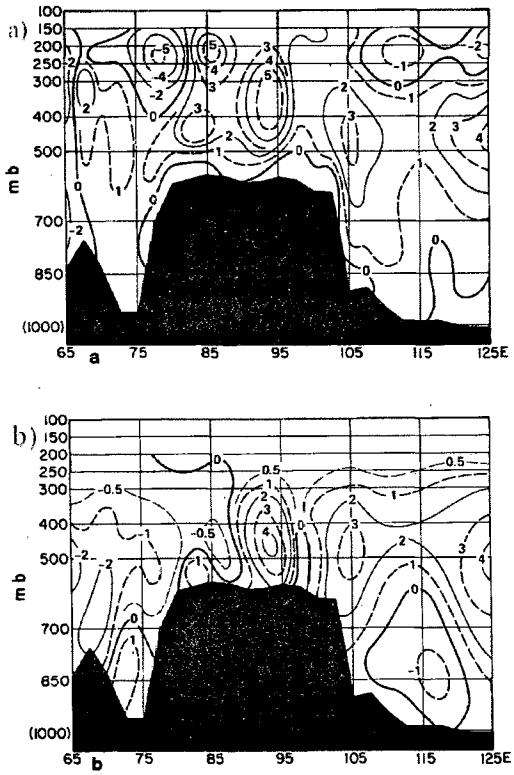

Figure 1.6. East-West cross-sections of the 40-day average in June-July period of a) heating (K day^{-1}) and b) drying (K day^{-1}). After *Luo and Yanai*, 1984.

Several studies of the influence of the Tibetan Plateau (TP) on the local and global circulation patterns revealed the multitude of scales this orographic feature exerts influence on, from more localized to truly global. The TP was found to play a major role in maintaining the South Asian low pressure system (*Hahn and Manabe*, 1975) with mountains allowing for much warmer temperatures in the middle and upper troposphere over the TP, while the Himalayan range was found to be a prerequisite for the moisture transport between the TP and the Indian subcontinent (*Lang and Barros*, 2002; *Barros,* 2004; *Magagi and Barros*, 2004). These recent studies further the case that the TP is a heat source in the warm season and the region of the highest near-surface potential temperature, a situation implying movement of air inward and upward along the flanks, which leads to cyclonic circulation tendency near the surface (*Hoskins*, 1991) and a deep and strong anticyclonic circulation

Reproduced with permission of the copyright owner. Further reproduction prohibited without permission.

above (*Yanai et al.*, 1992; *Li and Yanai*, 1996; *Duan and Wu*, 2005). This anticyclone which will be referred to as the Tibetan High (TH) is one of major components studied in this thesis. Throughout the period of July to October, the TH spans the most of central Asia, and, as will be shown, plays an important role in the modulation of the SH flow and wave structure. Southward meridional mass circulation associated with this system is a major contributor to the Hadley cell described in the previous chapters and it will be shown to be a strong contributor to the Australian Subtropical Westerly Jet by the means of unloading anomalous angular momentum air masses into the SH well toward 30°S.

1.5. The SH general circulation features

The mean state of the troposphere and stratosphere in the Southern Hemisphere (SH), as well as the dominant processes responsible for the maintenance of the general circulation throughout the annual cycle have been studied in depth in preceding years (*Newell et al.*, 1974; *Peixoto and Oort*, 1992; *Hoskins et al.*, 1983; *Hurrell et al.*, 1995; *Karoly et al.*, 1998; *Randel et al.*, 1990; *Randel and Held*, 1991; *Trenberth et al.*, 1992). As described in previous sections the net heating in the Tropics and net cooling in the middle and high latitudes create a differential that needs to be balanced by poleward transport of energy in the atmosphere and ocean. Most of general constraints on the circulation including distribution of land and ocean, the topography and other land and sea surface properties, as well as effective conservation of angular momentum, moisture, mass and total energy, are well-understood in both the climate and shorter time scale senses. Together with growing knowledge of these basic processes, understanding of stratospheric processes in the SH has greatly improved since the first dedicated monograph (*Labitzke and van Loon*, 1972). The

Reproduced with permission of the copyright owner. Further reproduction prohibited without permission.

Increased effectiveness of modern observational methods allowed for modern dynamics and constituent transport studies (*McIntyre et al.*, 1992; *Holton et al.*, 1995).

The difference in continentality of the two hemispheres makes their stratospheric circulations quite distinguishable. One rather conspicuous feature of the SH circulation is a singular poleward and downward movement of the polar night jet occurring in the midwinter (*Hartmann et al.*, 1984, 1998), as opposed to the Northern Hemisphere (NH), where this movement is recurrent throughout the winter.

Figure 1.7 illustrates the zonal mean temperatures for two periods in 2001. A similar situation is typically observed in the atmosphere during June-August (JJA) and September-November (SON) in any given year. The temperature in the stratosphere increases with height, which is partially due to the absorption of solar ultraviolet radiation by ozone. Carbon dioxide and its infrared emission is the main "coolant" in this part of atmosphere (*Andrews* et al., 1987).

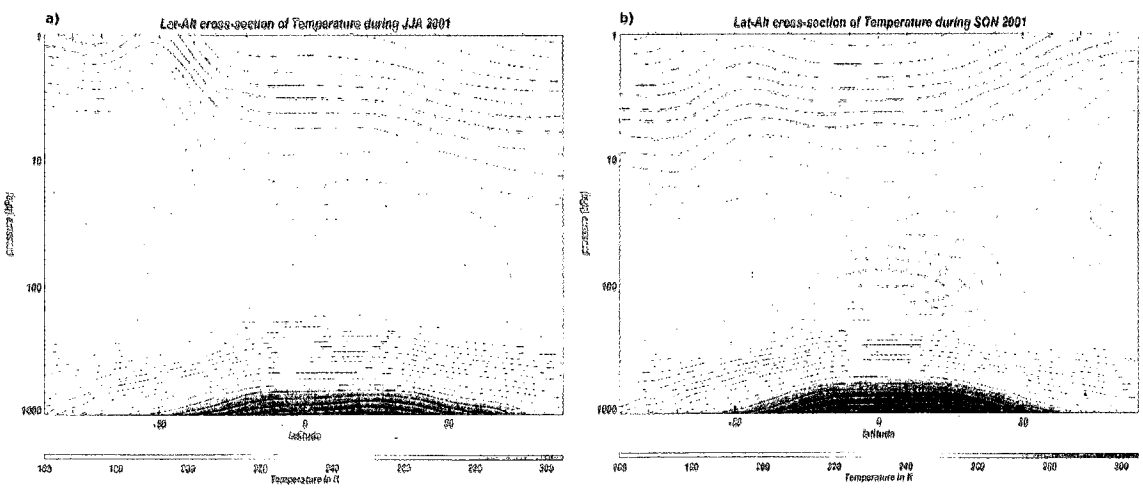

Figure 1.7. Latitude-Altitude cross-section of zonal mean temperatures (K), (a) in the atmosphere during June-August and (b) September-November periods

Reproduced with permission of the copyright owner. Further reproduction prohibited without permission.

Net heating due to radiative processes is strongly seasonal and dependent on latitude. As indicated on the Figure 1.7a and 1.7b, the polar stratosphere is relatively warmer than in low latitudes during the spring-summer months for both hemispheres, while it remains cooler throughout other seasons (*Hurrell et al.*, 1998, 1996; *Hirota et al.*, 1983).

The polar stratosphere is considerably colder in the southern hemisphere during the winter period than during the northern winter (*Hirota* et al., 1983). That is associated with much less planetary wave activity in the Southern Hemisphere and the complete lack of heating at high latitudes in the upper troposphere and lower stratosphere during the polar night (*Andrews at al.*, 1987). The colder southern stratosphere allows for stronger westerly winds throughout the most of the year, governed by the thermal wind balance. During the southern fall-winter period, the southern hemisphere stratosphere has a robust westerly jet structure (Fig. 1.8a and b), with wind speeds exceeding those in the northern hemisphere summer westerlies.

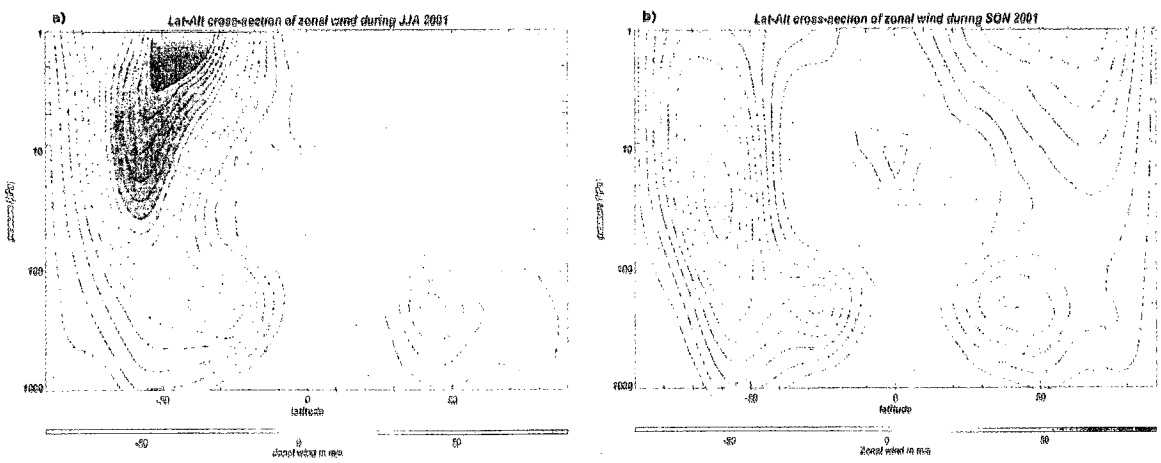

Figure 1.8. Latitude-Altitude cross-section of the zonal wind in the atmosphere during (a) June-August and (b) September-November.

Reproduced with permission of the copyright owner. Further reproduction prohibited without permission.

The strong wind maximum, known as the Polar Night Jet (PNJ), depicts the boundaries of the Polar Vortex (PV), which is by far more robust in the SH than in the NH, with much a colder core than its northern counterpart (*Hurrell et al.*, 1998; *Hirota et al.*, 1983).

The seasonal cycle works from top to bottom, mainly due to wave-mean flow interaction (*Hartmann et al.*, 1984, 1983; *Hitchman et al.*, 1987; *Garcia and Booille*, 1994) but also because the radiative relaxation time scales are ~5 days at the top of the stratosphere as opposed to the ~30-50 days in the lower parts, so wintertime conditions appear there first in the early fall (April), and westerly circulation strengthens and descends (comparison between the figures 1.8a and b) with time through the midwinter period.

The SH polar vortex, being much stronger than in the NH, stays as a cohesive feature until around the final warming in late spring. Minor warmings might be caused occasionally by planetary waves, originating in the troposphere but mostly instigated by *in situ* mechanisms. Interaction with the mean flow occasionally leads to stratospheric warming events. However, major ones are less frequent in the SH and are usually present during the final transition from winter to summer circulation patterns, the final warming. The final warming is usually driven by a combination of gravity wave drag and net radiative heating. September 2002 was a notable exception, with the major warming occurring in late October.

1.6. Planetary-Scale Waves in the SH during winter-spring

Due to the late abundance of satellite observational techniques, several studies of planetary waves in the SH emerged (*Harwood,* 1974; *Hartmann*, 1976, 1978, 1979; *Leovy and Webster*, 1976; *Mechoso and Hartmann*, 1982; *Hartmann et al.*, 1984; *Venne and Stanford*, 1982 and *Randel*, 1987, 1988, 1990, 1992) to widen understanding of the

Reproduced with permission of the copyright owner. Further reproduction prohibited without permission.

climatological characteristics of planetary-wave signatures. Time means clearly show a double-peak of a weak maximum during austral fall followed by a minimum in midwinter and then a large maximum in early spring (September-October). This is true for both the stationary and transient components as well as throughout the SH whole stratosphere (*Geller and Wu*, 1987; *Geller*, 1988; *Randel*, 1988; *Plumb*, 1989). While both k=1 and 2 stationary waves are almost equally important in the Northern Hemisphere (NH) the SH power spectra emphasizes the importance of stationary wave 1 (*Matsuno*, 1970, *Karoly and Hoskins*, 1982). Its genesis and phase is not understood enough even though there were several modeling and conceptual studies dealing with this problem (*Karoly*, 1989, *Shiotani and Hirota*, 1988, Wirth, 1990).

In this study we examined the influence of the Southeast Asian Convective regions as energy sources for disturbances over the Indian Ocean which, in turn, strongly influence the behavior of wave 1 in the SH. The eastward travelling wave 2, with period of 9-25 days, is the most prominent feature of power spectra in the SH (*Harwood*, 1975; *Hartmann*, 1976; *Randel*, 1987; *Shiotani and Hirota*, 1985; *Shiotani et al.*, 1990; *Manney et al.*, 1991), drawing its power from instability mechanisms in the stratosphere and nonlinear vortex interactions (*Lahoz et al.*, 1996; *Mechoso and Hartmann*, 1982; *Manney*, 1991). The SH zonal asymmetries are of less magnitude as the topography and land-ocean thermal contrasts in mid-latitudes are much smaller in the SH than in the NH. The SH stratosphere is characterized by significantly less synoptic variability then the NH. The mid-latitude storm track is more zonally uniform in the SH, leading to a wide geographical region of interaction of the weather systems with hemisphere's strong westerlies in the Upper Troposphere - Lower Stratospheres (UTLS).

Reproduced with permission of the copyright owner. Further reproduction prohibited without permission.

The differences in wave activity that exist between the two hemispheres are well established and shown here using the concept of E-P flux (Fig. 1.9).

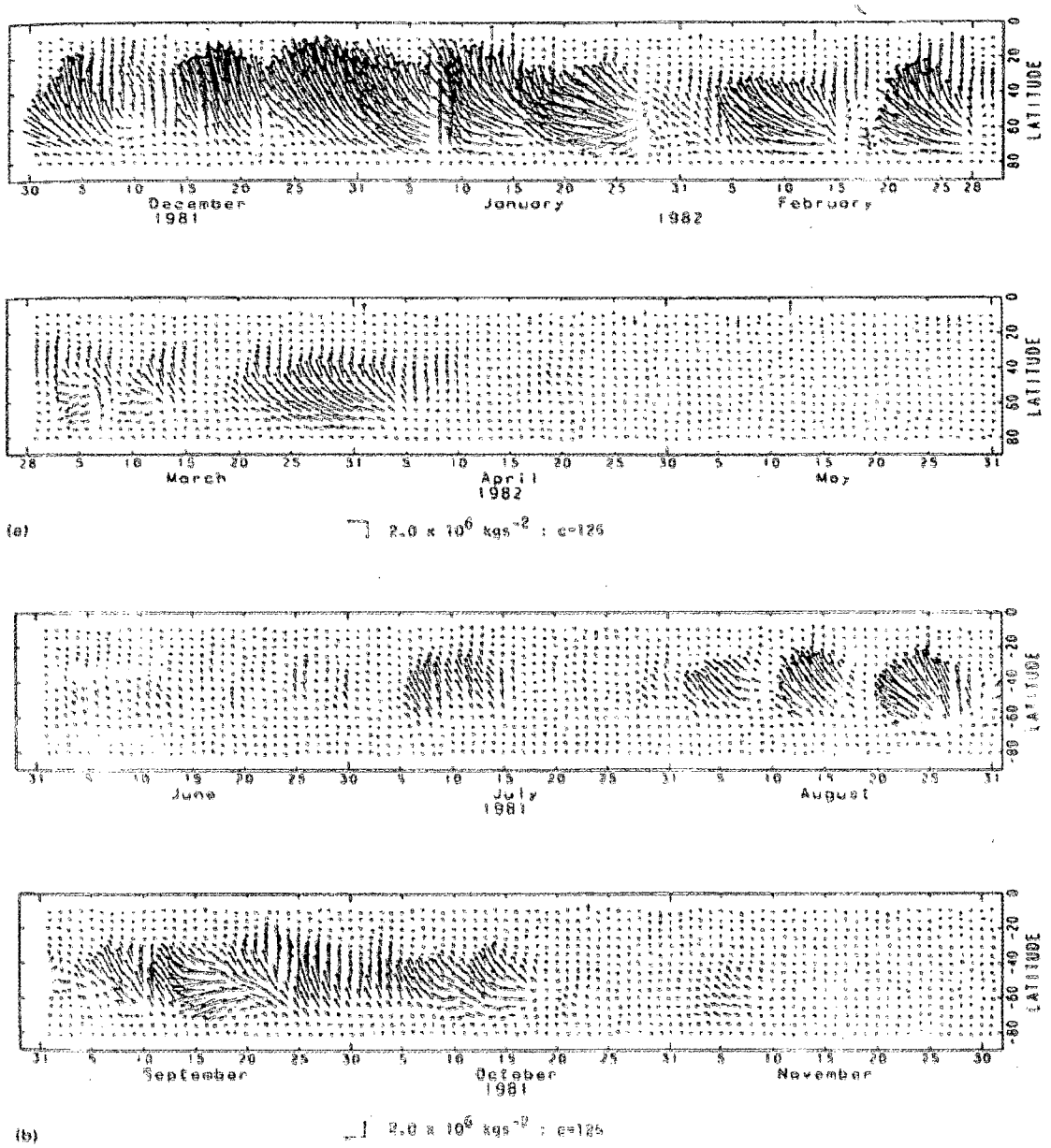

Figure 1.9. Latitude-time section of total E-P flux at the 5 hPa level from winter to summer for a) the NH and b) the SH. The scale arrow and scaling factor are in the figure. After *Shiotani and Hirota*, 1985

The relative weakness of the wave activity in the SH is pronounced when comparing winter months in both hemispheres. A strong westerly jet exists in the SH from the beginning

Reproduced with permission of the copyright owner. Further reproduction prohibited without permission.

of June through the beginning of August. Pulses of wave activity are observed in August but never reach the levels indicated in Figure 1.9a that are observed in the NH. There is 7-10 day variability in the activity pattern (E-P flux) until September, when it becomes continuous. The transition to summer circulation is abrupt. One of the major differences between the hemispheres is the absence of major warming events associated with sharp reversals of westerlies to easterly flow regime that occur in the NH (*Shiotani and Hirota*, 1985) but seldom occur in the SH.

In the SH winter traveling planetary waves play a more pronounced role in the wave pattern than in the Northern Hemisphere winter, where the spectrum is dominated by stationary wave components (*Leovy and Webster*, 1976; *Hartmann,* 1976; *Mechoso and Hartmann*, 1982). The life cycle of stationary planetary-scale waves in the stratosphere has been documented to exhibit seasonal behavior. In general, wave activity is almost absent in the summer hemisphere and concentrated in the winter hemisphere. The dynamical behavior of waves in the stratosphere was described first by the one-dimensional beta-plane model of Charney and Drazin (1961), which explained stratospheric wave dynamics in terms of the wave transmission properties of the underlying atmosphere, and the mean circulation. From the linear dispersion relation,

$$c = \bar{U} - \frac{\beta}{k^2 + l^2 + \varepsilon^2 m^2}, \qquad (1.1)$$

where c is the zonal trace speed (sometimes called "phase velocity") of the Rossby wave, $\bar{U}$ is mean zonal flow, $\beta = \partial f / \partial y$, k, l and m are respectively the zonal, meridional and vertical wavenumbers and $\varepsilon=(f_0/N)^2$.

Reproduced with permission of the copyright owner. Further reproduction prohibited without permission.

From the dispersion relation given above we may deduce that for any given c and k, as the Rossby wave energy ascends, through changing $\overline{U}$, l^2 and m^2 must vary to compensate. When we carefully consider Equation 1.1, two inequalities arise:

1.2) $$0 < \bar{U} - c < \bar{U}_{cr},$$

constituting the Charney-Drazin criterion. $\bar{U}_{cr}$ in Equation 1.2 is the critical zonal velocity. For a stationary wave with c~0, the wave activity cannot ascend into summer easterlies, because m and l go to infinity, indicating absorption at a critical level. Similarly, stationary waves cannot propagate into the SH winter westerlies with high zonal wind velocities, because m and l would have to approach 0 (a turning surface). This is the main reason for the mid-winter low wave activity in the SH (Figure 1.10). In NH winter the wave activity is strong enough to maintain $\bar{U}$ at moderate speeds, so that wavenumbers 1, 2 and 3 propagate upwards quite often.

There are noticeable differences between the wave structures, life cycles and wave amplitudes of the NH and the SH (*Hirota and Shiotani*, 1983). Wave amplitudes in the SH stratosphere are climatologically roughly half of those in the NH stratosphere, as is apparent in the wavenumber 1 example in Figure 1.10. The wave activity maxima in the SH are visible in Figure 1.10 as well, starting from the beginning of May to late July and then again at the end of the winter period, around October-November. The SH westerlies reach their maximum between these periods. The mid-winter (MJJ) minimum is also much more pronounced in the SH than during the corresponding season in the NH. Many previous studies suggested that these major differences might be explained through contrasting wave propagation modes according to Charney-Drazin theory.

Reproduced with permission of the copyright owner. Further reproduction prohibited without permission.

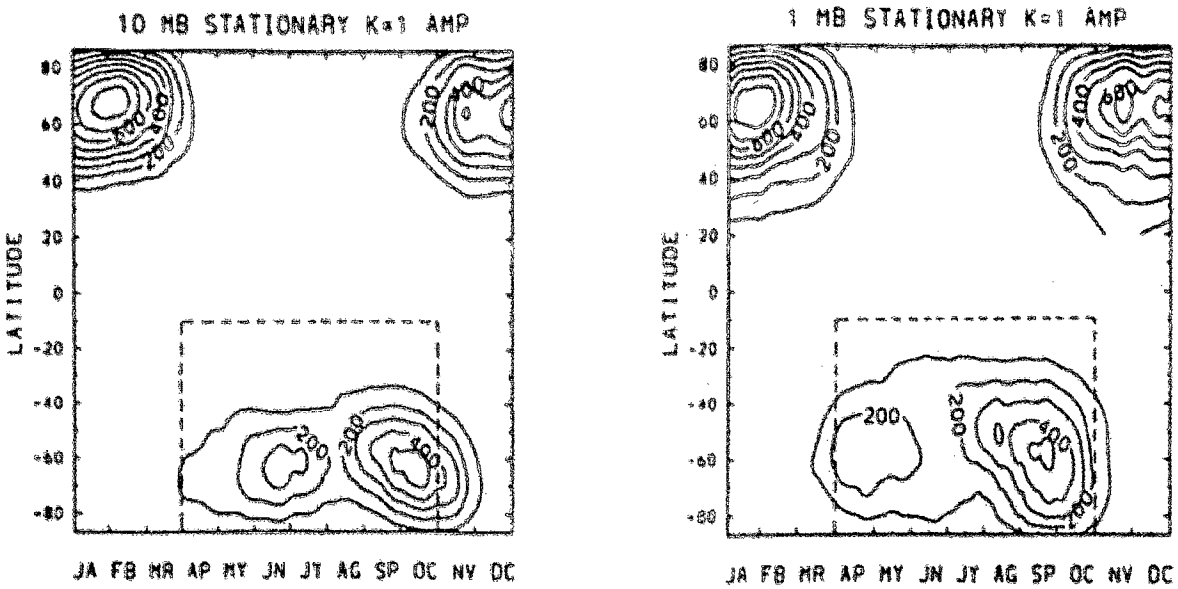

Figure 1.10. Latitude-time section showing seasonal cycle of stationary wave amplitude (in m) for a wavenumber 1 at 10 hPa (left panel) and 1 hPa (right panel), contour interval 100 m (after *Wirth,* 1991).

Several models (*Karoly and Plumb*, 1989; *Wirth*, 1991) showed that in the NH, wave-mean flow interaction is more substantial, reducing the strength of westerlies, thus allowing waves to propagate higher into the stratosphere (*Matsuno*, 1970). The seasonal and hemispheric asymmetry in tropospheric forcing is a main cause of these different flow regimes. Neither of them may be sufficient to explain the substantial amplitude variations throughout the seasons in the SH (strengthening from April to October) alone, certainly not the tropospheric forcing, since variability of wave activity in the troposphere is moderate during this period. In the case of the NH, the midlatitude continentality forces wavenumbers 1, 2, and 3, which is not the case for the SH.

During the SH winter, eastward-traveling wave components are more prominent than the westward moving waves. Eastward-moving disturbances are observed at high southerly

Reproduced with permission of the copyright owner. Further reproduction prohibited without permission.

latitudes during August until October, and according to the Charney-Drazin criterion are the only ones that can exist in such strong westerlies. The zonal wavenumber 2 component propagates eastward. Its period ranges from 8 to 20 days, while amplitudes are usually between 600 to 1000 geopotential meters (gpm) in the middle to upper stratosphere. Our knowledge of the mechanisms exciting eastward traveling modes which may propagate well into the stratosphere is not complete. One of the possibilities might be baroclinic instability of the zonally averaged wind and temperature fields translated into the planetary-scale disturbances in the troposphere (*Simmons and Hoskins*, 1977; *Hartmann*, 1979; *Straus*, 1981). Without assessing whether linear or nonlinear dynamics are prevalent in the life cycle of eastward moving waves, we still favor the baroclinic instability of the zonally averaged state in the troposphere as one of fundamental mechanisms governing their evolution.

It has been shown that some instances of wavenumber 2 growth originate within the upper troposphere, while in many cases the growth had been confined to the stratosphere (*Shiotani and Hirota*, 1985; *Manney et al.,* 1994, 1995). The winter and spring is also a time when eastward propagating wave 3 components with periods of up to a week are observed (*Hartmann*, 1976). Maximum amplitudes of this component of the flow are usually between 200 to 400 gpm and usually occur between 50-60°S. In contrast to wavenumbers 2 and 3, wavenumber 1 is a quasi-stationary feature in the Southern Hemisphere, with amplitudes reaching 1800 gpm in the middle stratosphere during the early spring. This component generally resembles wavenumber 2 and 3 in meridional structure, but peaks at somewhat higher latitudes.

Studies by Mechoso (1988) and Randel (1987, 1988) associated the quasi-stationary nature of wavenumber 1 in the SH stratosphere with zonal asymmetries in the atmosphere.

Reproduced with permission of the copyright owner. Further reproduction prohibited without permission.

This is particularly true for the troposphere, where latent heat release and the mixing of momentum and heat by large-scale transients are both dependent on the boundary conditions and the forced wave structure, one still poorly understood and one this thesis tries to partially explain.

It is still not fully explained what is responsible for the life cycles of the eastward-moving wavenumber 2 and 3 modes. It might be deduced from some cases, when the growth of wavenumber 2 was confined to the stratosphere, that there are significant *in situ* dynamical contributions. This, as well as the eastward propagation, points to instability as one possible explanation (*Manney et al.*, 1991). In most cases, when growth is confined to the stratosphere, wave 2 has very little vertical phase tilt and can be associated with equatorward momentum flux. This also points to barotropic instability. Equatorward momentum fluxes and significantly small heat fluxes are indicative of kinetic energy transfer from the mean flow into wavelike disturbances. Both baroclinic and barotropic modes exhibit waves growing from the available potential energy (APE) and are usually associated with poleward momentum flux and pronounced poleward heat fluxes. Analyses of modeled idealized flows and observations of the SH polar night jet (PNJ, *Hartman,* 1983; *Manney et al.*, 1991) showed the ability of unstable modes to arise on the equatorward side of the polar night jet (PNJ). The modeled modes closely resembled observed components with wavenumber 2 and 3, displaying very similar periods and horizontal structure.

On the other hand, upper tropospheric baroclinically unstable disturbances work quite efficiently to maintain quasi-stationary flow components (*Yasuko and Hirota*, 2002). The variation in amplitude and phase of wavenumber 4 and 5 is correlated well with the upper tropospheric circulation. Dynamical connections include the feedbacks between tropospheric

Reproduced with permission of the copyright owner. Further reproduction prohibited without permission.

zonal wind and the direction of wave propagation, eddy heat flux and the amplitude of those disturbances.

Study and experiments performed by Mechoso and Hartmann (1982) have also shown that eastward traveling waves 1 and 2 in the stratosphere exhibit rather little correlation with their counterparts in the troposphere. The opposite is true for wavenumber 3 and 4 disturbances. There are several possible explanations for this. One of the possibilities might be nonlinearities between waves having large amplitudes in the stratosphere, coupled with a finite propagation time from the source region in the troposphere to the stratosphere. In this dynamical scenario, during the finite propagation time from the troposphere to the stratosphere, the wave structure is altered in the latter (*Young and Houben*, 1989). As previously discussed, *in situ* instabilities in the stratosphere may play a key role as well, since the finite traveling time alone cannot account for the lack of coherence. Strong wave-wave and wave-mean flow interactions do occur above the regions of wave generation. In turn, those interactions change wave structures on time scales smaller or similar to the troposphere to stratosphere traveling time. It is also possible that two independent baroclinic planetary modes at the same wavenumber but with different structures may exist at the same time in both the troposphere and stratosphere (*Hartmann,* 1982).

1.7. Convection over Southeast Asia and the Maritime Continent

A large part of the thesis leans on the one of the most potent dynamical forces on Earth, the South East Asian Monsoon. The location of the two most interesting sources of heat in the Earth's tropics are Southeast Asia and the India-Australia-Indonesia-Papua New

Reproduced with permission of the copyright owner. Further reproduction prohibited without permission.

Guinea (sometimes being separately considered as the region of the Southern Hemisphere Monsoon). The latter is sometimes referred to as the Maritime Continent (MC, *Braak*, 1929; *Murakami*, 1982; *McBride*, 1983, 1987; *Troup*, 1961; *Ramage*, 1968). The monsoonal character of this regions has been well documented for many decades (*Berson*, 1961; *Troup*, 1961; *McBride*, 1987; *Malton and McBride*, 1992). One of the key synoptic features of this area is the monsoon trough, the separation between tropical and extra-tropical low-level westerlies and higher latitude trade-wind easterlies (*McBride et al.*, 1983; *McBride*, 1995). The El Nino Southern Oscillation (ENSO) was found as the strong modulator of monsoon in the Northern Australia-Indonesian region, especially during the late winter to spring transition (*Nicholls*, 1981; *McBride and Nicholls*, 1982, 1983; *Collimore et al.*, 2003). The 30-60 day Madden-Julian oscillation (MJO) is strongly related with the eastward moving Outgoing Long-wave Radiation pattern (OLR) that will be linked with corresponding dynamic and ozone pattern in our study. The onset of the Australian Monsoon has been linked to the MJO (*Hendon and Liebmann*, 1990; *Drosdovsky*, 1996; *Wheeler et al.*, 2004, 2005) as the eastward moving 40-50 day wave expands the convection region southward over the Australia before contracting it back northward as the wave continues its eastward shift. The latent heat release in the deep cumulonimbus convection over the MC has been well studied (*Lorenz*, 1970; *Matsuno*, 1966; *Webster*, 1966; *Gill*, 1980 among other mentioned in chapters before) and found crucial to the maintenance of large scale tropical circulation.

Reproduced with permission of the copyright owner. Further reproduction prohibited without permission.

1.8. The Southern Hemisphere's anticyclones.

The subtropical quasistationary anticyclones of the austral late winter to spring transition period occur predominantly over Australia, South Africa and South America. Their day to day position does not veer off their continental anchor points more than 30° in longitude. Moving anticyclonic systems of the SH extratropics tend to travel predominantly eastward, with more regular motion and periodicity than their conterparts in the boreal hemisphere and the length of their active phase tends to be longer as well. As these migrating anticyclones move eastward in the UTLS region and higher, around the PV, the axis of the PV rotation tends to move in the same direction hence the term eastward travelling wave 2 noted in previous studies (*Mechoso and Hartmann,* 1982, *Shiotani et al.,* 1990).

The Australian High, in all its vertical extent plays a major role in the SH ozone budget, similiarily to more elusive SAH. Similarly, the South American High (SamH) which appears in our analysis below is known to be the beginning pathway for migrating anticyclones (*Harvey*, 2001). The anticyclogenesis occurs off the coast of South America with high frequency and some of resultant anticyclones move eastward around the PV well into the southern Indian Ocean.

1.9. Overview of Ozone

In 1930 the British geophysicist Sidney Chapman proposed the idealized set of equations governing the chemical production and destruction of ozone. According to this simplified view, the stratospheric ozone life cycle is prominently controlled by the following reactions, referred to as the Chapman mechanism:

Reproduced with permission of the copyright owner. Further reproduction prohibited without permission.

1.3) $O_2+h\nu \rightarrow O+O$, photolysis with $\lambda<242$ nm

1.4) $O+O \rightarrow O_2$

1.5) $O+O_2+M \rightarrow O_3+M$

1.6) $O+O_3 \rightarrow 2O_2$

1.7) $O_3+h\nu \rightarrow O_2+O$, with $\lambda<310$ nm

where M denotes an arbitrary molecule. The first three reactions are responsible for production of ozone. Mechanism in 1.5 is the primary chemical destruction of ozone. Reaction 1.6 leads to recombination of ozone rather than loss, mainly because of the timescales involved and the reaction efficiency. From the Chapman mechanism alone, one cannot deduce the real cycle of ozone in our atmosphere, since the production rate in the Chapman cycle is 5 times faster than the destruction rate. The catalytic cycles involving species of the hydrogen, nitrogen and chlorine, namely HOx, NOx and Clx, with ozone destruction efficiency by far greater than that of reaction 1.6, have to be introduced to close this chemical system. The general distribution of ozone, involving the ozone hole in the SH will be examined in subsequent chapters.

The vertical distribution of ozone differs latitudinally because of the complex system of transport and radiative processes. The maximum ozone mixing ratio, in parts per million by volume (ppmv) is at a height of approximately 35 km (roughly 5 hPa) for midlatitudes. The maximum ozone concentration is lower in the stratosphere, around 20-25 km. The ozone concentration for a number of southerly latitudes is depicted in Figure 1.11. The horizontal distribution of ozone is also a result of the combined influences of dynamics and chemistry. A snapshot of the global distribution is shown in Figure 1.12.

Reproduced with permission of the copyright owner. Further reproduction prohibited without permission.

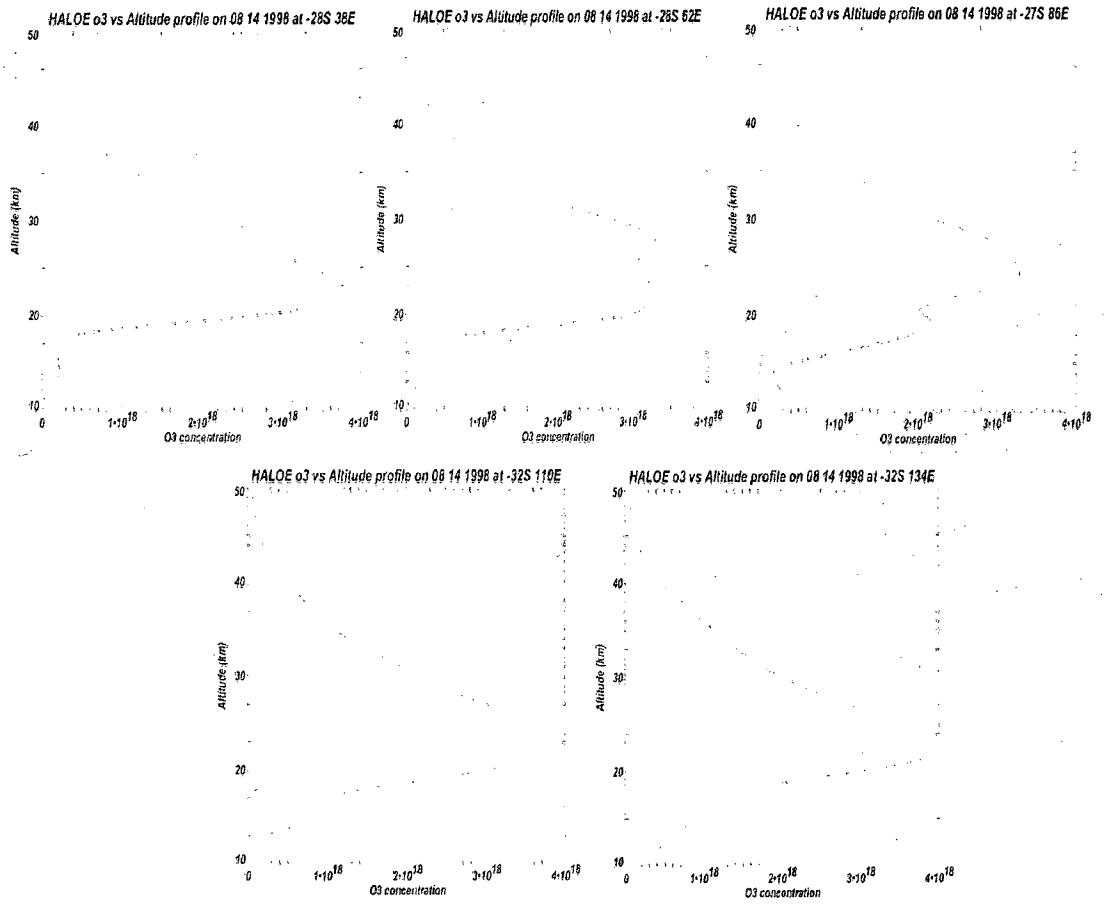

Figure 1.11. Vertical profiles of ozone for five different locations between latitudes 27° and 32°S. Ozone concentration is in molecules per m^3.

The effects of transport are apparent in the fact that there is more column ozone in regions neutral to its production, than in those being a net source of the ozone due to the abundance of sunlight. The mean distribution of ozone as well as interseasonal and intraseasonal variability depend largely on latitude but there are pronounced seasonal variations, as shown in Figure 1.13. Vigorous NH wave driving by wavenumbers 1-3 spreads ozone throughout the NH winter and spring, while in the SH synoptic scale waves transport ozone at a lesser distance, to around 60°S (Figures 1.12 and 1.13, *Andrews et al.,* 1987). This

Reproduced with permission of the copyright owner. Further reproduction prohibited without permission.

transport by waves also gives rise to longitudinal variations of ozone distribution, a focal aspect of this thesis.

The annual cycle for pre-1980 total ozone (Figure 1.13) is prominent in both hemispheres, but quantitatively larger in amplitude for the NH. Because of differences in the polar thermal fields, and most importantly in the wave activity, the ozone maximum is very close to the North Pole, while similar latitudes in the SH are deeply submerged in the Antarctic Ozone Hole.

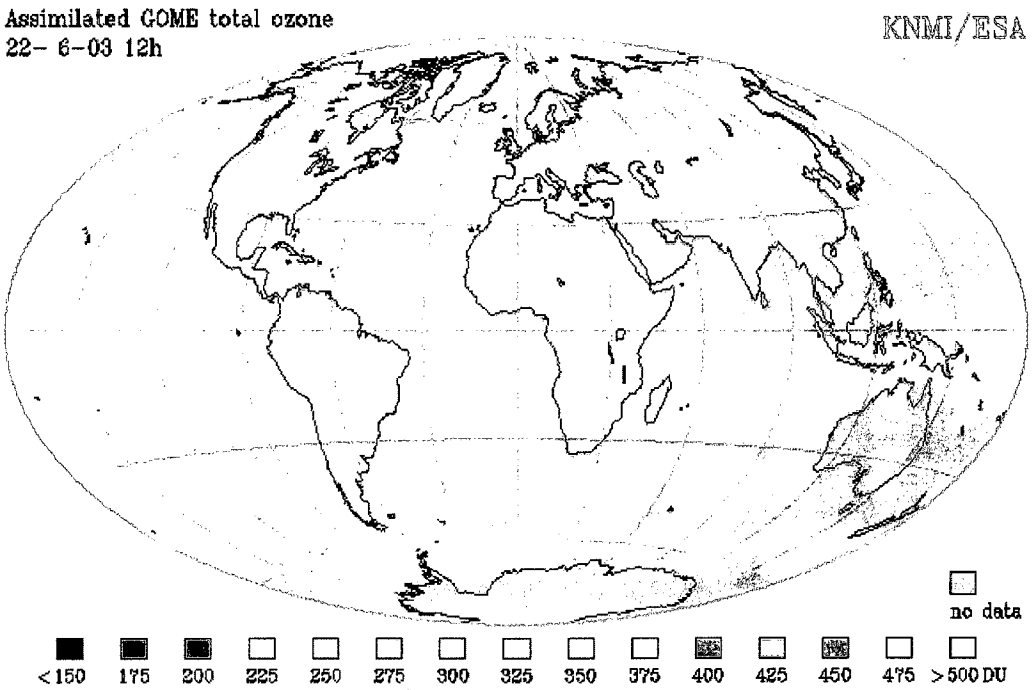

Figure 1.12. Snapshot of the total ozone distribution on June 22nd, from the Global Ozone Monitoring Experiment (GOME). In DU.

Reproduced with permission of the copyright owner. Further reproduction prohibited without permission.

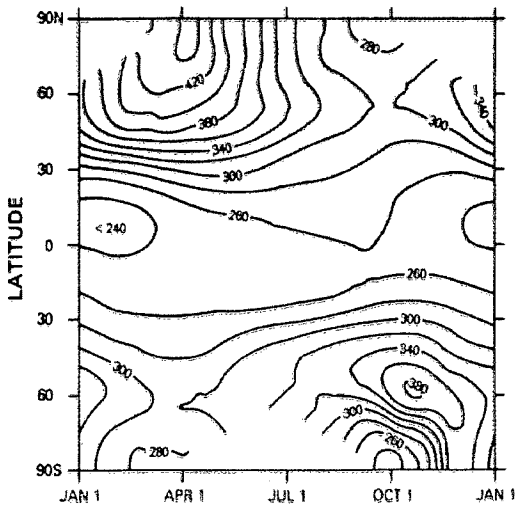

Figure 1.13. Time-latitude section showing the seasonal variation of total ozone (in DU) derived from TOMS. Note the spring maxima near 90°N and 60°S and the minimum near 90°S, referred to as the natural ozone hole. After *Andrews et al.*, 1987

Since 1980, the anthropogenic ozone hole has emerged because of the entrapment of air masses in the strong southern polar vortex for a prolonged time, during which catalytic processes taking place on the surface of Polar Stratospheric Clouds at very low temperatures and absence of light, produce chemical compounds that deplete ozone when the sunlight is finally present later during the SH spring.

1.10. The hypothesis

This study analyzes the 10 year period (1995-2004) of interactions between the convection over the Southeast Asia, the MC, dynamical features over the Indian Ocean and the total ozone distribution over the SH. It focuses on the late winter-spring transition (August through October) which encompasses a period of striking variability in wave and

Reproduced with permission of the copyright owner. Further reproduction prohibited without permission.

ozone structure in the austral hemisphere. The most important feature that this study has tried to explain is the influence that the large anticyclonic system placed during the boreal summer and fall over the Tibetan Plateau exerts on the SH UTLS region in terms of modulation of the AH, maintenance of the ASWJ and the driving of Indian Ocean Highs (IOH) by the Indonesian – North Australian convection. These three systems, the TH, IOH and AH impose implications for the redistribution of column ozone into observed zonally asymmetric feature, namely the Ozone Croissant.

The hypothetical multi-stage dynamical coupling between the NH and SH during the austral winter to spring transition is as follows:

1. The excess heating of the Tibetan Plateau during the boreal summer produces a large anticyclone in upper troposphere, namely the TH. This grand system is joined during summer and fall by the smaller anticyclones over Southeast Asia to produce the biggest anticyclonic feature of the planet.
2. Simultaneously the Southeast Asian and MC convections produce the AH (*Gill*, 1980)
3. The outflow from the TH, wraps around the AH circulatory system bringing to the SH air masses with larger PV, anomalous momentum, as far as 35°S, strengthening the AH and allowing for the ASWJ to setup just south of the AH.
4. Increased downward motion and loading of the ozone-rich air masses at the edges of the strengthened AH and transport by synoptic scale Rossby waves produce the sharp maximum in the column ozone immediately south to the ASWJ. This is also consistent with distribution of heat sources and sinks described in previous chapters.

Reproduced with permission of the copyright owner. Further reproduction prohibited without permission.

5. As time progresses from August to October and the sun "travels" southward, other convective systems over the Equatorial Africa and the South America increase the strength and extent of the anticyclones over these continents, the SAH and SAmH respectively which tends to elongate the ozone distribution of 300 DU and more, stretching from the South Atlantic to the southwestern Pacific. The SAmH system is responsible for the breaking of 300 DU isoline south of Patagonia.

The latter part of this thesis deals with the problem of the modulation of the SH wave and ozone patterns by El Nino Southern Oscillation (ENSO) and to lesser extent by the Quasi-biennial Oscillation (QBO).

1.11. The layout of the thesis

Chapter two describes the datasets and methodology of analyses and modeling studies presented in this thesis. The following chapter presents a paper providing a two-step study of the TH-AH-IOH coupling and the influence of these systems on the distribution of column ozone during 1998. It consists of observational part as well as modeling part that uses the University of Wisconsin Nonhydrostatic Modeling System (UW-NMS). It has been submitted as "Modeling the effects of Southeast Asian monsoon outflow on subtropical anticyclones and midlatitude ozone over the Southern Indian Ocean" (*Rogal M., Hitchman M., Buker M., Tripoli G., Stajner I. and Hayashi H.*, 2009) to JGR. Chapter four presents a paper dealing with the maintenance of the ASWJ and AH as well as the episodes of stalling of the traveling wave 2 in the SH using observational study of the winter-spring period of 2000 (*Hitchman M, Rogal M.*, Seasonal evolution of the Ozone Croissant: Zonal contraction

Reproduced with permission of the copyright owner. Further reproduction prohibited without permission.

of monsoon outflow and stalled planetary wave ridges, 2009, submitted to JGR). It also provides detailed momentum budget for the SH for the period of 10 years in order to establish the mechanisms governing the setup and modulation of the ASWJ jet and additional observations of the dynamical ozone redistribution in the SH. Chapters five and six contain a climatology of the SH troposphere and lower stratosphere regions for the 10 year period 1995-2004. The latter introduces the E-P flux as well as expanded momentum budget analyses. Chapter seven contains a paper examining the influence of the ENSO and partially QBO on the SH upper troposphere and stratosphere and ozone distribution (*Hitchman M., Rogal M.*, ENSO influences on monthly mean column ozone and stratospheric geopotential height and temperature anomalies during the Southern Hemisphere winter to spring transition, 2009, submitted to JGR). Chapter eight provides general conclusions that arise from studies performed in the various parts of the thesis.

Because of the broad spectrum of dynamical problems studied in this thesis as well as tools and methods of analysis, some chapters retain the original introduction as well as the tools and methods and conclusion parts (the three submitted papers presented in chapters three, four and seven). Only a brief overview of methods used in these chapters is presented in chapter two, alongside with a full description of methods used in the climatological study contained in chapter five and six.

Reproduced with permission of the copyright owner. Further reproduction prohibited without permission.

Chapter 2

Chapters three, four and seven being self-contained papers, retained the data and methodology sections which would be hard to disentangle otherwise. Chapters five and six use the following datasets and methods of analysis. The analyzed data was limited to the August-September-October (ASO) periods to focus on SH late winter and early spring.

2.1. Ozone datasets

A wide variety of ozone data were used to fulfill different research requirements. These included data containing information about the 3 dimensional structure of ozone from the Global Modeling and Assimilation Office at the NASA Goddard Space Flight Center, in Greenbelt, MD (GMAO), individual vertical ozone profiles from the Halogen Occultation Experiment (HALOE), as well as the data providing the daily global structure of total ozone, from the Total Ozone Mapping Spectrometer (TOMS) team.

The GMAO datasets are gridded assimilated ozone fields with a horizontal resolution of 2° in latitude and 2.5° in longitude on 36 pressure levels from 1000 hPa up to 0.2 hPa. The ozone fields are provided 4 times daily at 0000Z, 0600Z, 1200Z, 1800Z. The assimilation system combines the Solar Backscatter Ultra-Violet Instrument (SBUV) data and the National Oceanic and Atmospheric Agency's (NOAA) Geostationary Earth Observing Satellite (GEOS) ozone data. Further details are provided by Stajner et al. (2001, 2003, 2004), and Riishojgaard at al. (2000). Because of their availability and comprehensive 3-dimensional structure, the assimilated ozone datasets from GMAO

Reproduced with permission of the copyright owner. Further reproduction prohibited without permission.

proved invaluable for UW NMS initialization, and combined with the HALOE and TOMS data sets, were thoroughly used in the observational analysis part of the research.

The Halogen Occultation Experiment (HALOE) datasets are from an instrument located onboard the Upper Atmosphere Research Satellite (UARS), orbiting the Earth since September 12, 1991. HALOE uses solar occultation measurements to extract vertical profiles of O_3, HCl, HF, CH_4, H_2O, NO, NO_2, aerosol extinction, and temperature. Ozone profiles span the altitudinal range of 15 to 60 km, with observations in individual locations 'marching' from 80°S to 80°N several times during the year. These data provide a valuable tool for analysis of the global distribution and temporal behavior of the vertical ozone structure. Further details are given by Russell et al. (1993).

While the HALOE data give an excellent insight into ozone structure, spatially limited to individual profiles, the TOMS experiment provides invaluable information about the global distribution of column ozone. The TOMS column ozone dataset used in our study encompasses the period 1995-2004, ending with the demise of the Earth Probe satellite data. The TOMS dataset includes data from the Earth Probe spacecraft (7/22/1996 – 12/14/2005). There is a gap in 1996 due to calibration problems. TOMS measures total ozone using the combination of observations of the incoming solar energy and the UV radiation backscattered through the stratosphere at six wavelengths. Comparison of the backscattered radiation to the incoming solar radiation at a given wavelength reveals the specific albedo of the planet, while changes in the albedo at selected wavelengths allow for calculation of the amount of ozone in the Earth's atmosphere up to the Top of the Atmosphere (TOA). A total of 35 measurements are produced every 8 seconds. The measurements span a rectangle of 50 km in latitude and 200 km in longitude. Except for the

Reproduced with permission of the copyright owner. Further reproduction prohibited without permission.

Polar Regions, where the sun stays close to or below the horizon, the daily measurements cover almost the entire planet. Further information on the TOMS project is given at Goddard Space Flight Center website at http://jwocky.gsfc.nasa.gov/ and http://sedac.ciesin.org/ozone/rtm/nasadata.html.

2.2. **Meteorological datasets used for modeling and observational analysis**

The meteorological data fields were derived from 2.5° gridded European Centre for Medium Range Weather Forecasts (ECMWF) global surface and upper air analyses (*Trenberth,* 1988, 1992; *Hollingsworth* et al., 1986). The ECMWF (Reading, UK) provides data sets containing gridded analyses of 14 meteorological variables including geopotential height, temperature, meridional, zonal, as well as the vertical wind components, twice daily at 0000Z and 1200Z. The ECMWF global surface and upper air analyses have 2.5° resolution in the horizontal on 22 levels reaching up to the 1 hPa level. The sophisticated intermittent-insertion assimilation system consists of three major steps: analysis, initialization, and forecast to provide the next first guess field.

The Outgoing Longwave Radiation (OLR) data from NOAA archives was used as a proxy for the Southeast Asian and MC region convection. Any gaps in this dataset were filled with temporal and spatial interpolation (*Liebmann and Smith,* 1996). This dataset contains daily mean (averaged nighttime and daytime crossings) TOA estimations of the OLR spanning the 1974/06 - 2009/02/28 period and were derived from instruments onboard the National Oceanic and Atmospheric Administration (NOAA) polar orbiting satellites (*Gruber and Winston*, 1978; *Gruber and Krueger,* 1984). These 2.5° x 2.5°

Reproduced with permission of the copyright owner. Further reproduction prohibited without permission.

gridded datasets are frequently used to estimate the earth's radiation budget and destinguish the areas of deep tropical convection.

2.3. Elliassen-Palm Flux.

One of the most important instruments in the analysis of the general circulation is the separation of the meteorological variables into zonal averages and deviations from them. The Eliassen-Palm (EP) theory (*Eliassen and Palm*, 1960) provides an additional framework with which to understand the eddy-mean flow interaction and makes possible the use of the divergence of E-P flux, which requires the usage of the Transformed Eulerian Mean (TEM) in lieu of the Eulerian Mean set of equations. Since the original Eliassen and Palm work, several studies have extended the use of this theory including introduction of the isentropic coordinates (*Andrews et al.*, 1987) and studies of the middle and upper troposphere (*Trenberth*, 1986).

The separation of each of variables in the set of primitive equations in the spherical coordinates into a zonal mean and departure wherefrom (*Andrews*, 1987) enables us to formulate Eulerian-Mean set of primitive equations for a flow in the spherical coordinates:

$$\frac{\partial \overline{u}}{\partial t} + \overline{v}\left[(r\cos\varphi)^{-1}\left(\frac{\partial(\overline{u}\cos\varphi)}{\partial\varphi}\right) - f\right] + \overline{w}\frac{\partial \overline{u}}{\partial z} + (a\cos^2\varphi)^{-1}\frac{\partial\left(\overline{u'v'}\cos^2\gamma\right)}{\partial\varphi} + \frac{1}{\rho_0}\frac{\partial\left(\rho_0\,\overline{u'w'}\right)}{\partial z} = \overline{X}$$

(2.1)

Reproduced with permission of the copyright owner. Further reproduction prohibited without permission.

$$\frac{\partial \overline{v}}{\partial t}+\frac{\overline{v}}{r}\frac{\partial \overline{v}}{\partial \varphi}+\overline{w}\frac{\partial \overline{v}}{\partial z}+\overline{u}\left(f+\frac{\overline{u}}{r}\tan\varphi\right)+\frac{1}{r}\frac{\partial \overline{\phi}}{\partial \varphi}+(r\cos\varphi)^{-1}\frac{\partial\left(\overline{v'^2}\cos\varphi\right)}{\partial \varphi}$$

$$+\frac{1}{\rho_0}\frac{\partial\left(\rho_0\overline{v'w'}\right)}{\partial z}+\frac{\overline{u'^2}}{r}\tan\varphi=\overline{Y} \quad (2.2)$$

$$\frac{\partial \overline{\phi}}{\partial z}-\frac{R\overline{\theta}e^{-\kappa z/H}}{H}=0 \quad (2.3)$$

$$(r\cos\varphi)^{-1}\left(\frac{\partial(\overline{v}\cos\varphi)}{\partial \varphi}\right)+\frac{1}{\rho_0}\frac{\partial(\rho_0\overline{w})}{\partial z}=0 \quad (2.4)$$

$$\frac{\partial \overline{\theta}}{\partial t}+(r\cos\varphi)^{-1}\left(\frac{\partial\left(\overline{v'\theta'}\cos\varphi\right)}{\partial \varphi}\right)+\frac{\overline{v}}{r}\frac{\partial \overline{\theta}}{\partial \varphi}+\overline{w}\frac{\partial \overline{\theta}}{\partial z}+\frac{1}{\rho_0}\frac{\partial\left(\rho_0\overline{w'\theta'}\right)}{\partial z}=\overline{Q} \quad (2.5)$$

The terms X, Y and Q represent body forces in the new momentum balance equations and the heating in the thermodynamic equation respectively. The overbars denote the usual zonal mean and prime the departure therefrom. The symbols Φ and θ denote geopotential and potential temperature respectively, r is an Earth's radius and ρ is air density, while H is a scale height and R is a gas constant multiplied by $(p_o/p)^{1/(cp/cv)}p_o^{-1}$.

To quantify the influence of momentum and heat fluxes on the mean-flow and further establish the physical interplay between zonal mean-flow and waves in the atmosphere, it is convenient to establish a Residual Mean Meridional Circulation by noting that:

$$\overline{v}^{*}\equiv\overline{v}-\frac{1}{\rho_0}\left(\frac{\partial}{\partial z}\left(\frac{\rho_0\overline{v'\theta'}}{\frac{\partial\overline{\theta}}{\partial z}}\right)\right) \quad (2.6)$$

Reproduced with permission of the copyright owner. Further reproduction prohibited without permission.

$$\overline{w}^* \equiv \overline{w} + \frac{1}{r\cos\varphi}\frac{\partial\left(\frac{\cos\varphi\,\overline{v'\theta'}}{\frac{\partial\overline{\theta}}{\partial z}}\right)}{\partial\varphi} \qquad (2.7)$$

When 2.7 and 2.6 are substituted for the zonal mean v and w in equations 2.1 and 2.2 we can obtain the Transformed Eulerian Mean (TEM) set of equation:

$$\frac{\partial\overline{u}}{\partial t} + \overline{v}^*\left[(r\cos\varphi)^{-1}\left(\frac{\partial(\overline{u}\cos\varphi)}{\partial\varphi}\right) - f\right] + \overline{w}^*\frac{\partial\overline{u}}{\partial z} - \overline{X} = (\rho_0 a\cos\varphi)^{-1}\nabla\bullet F \quad (2.8)$$

$$\overline{u}\left(f + \frac{\overline{u}}{r}\tan\varphi\right) + \frac{1}{r}\frac{\partial\overline{\phi}}{\partial\varphi} = G \qquad (2.9)$$

$$\frac{\partial\overline{\phi}}{\partial z} - \frac{R\overline{\theta}e^{-\kappa z/H}}{H} = 0 \quad (2.10)$$

$$(r\cos\varphi)^{-1}\left(\frac{\partial(\overline{v}^*\cos\varphi)}{\partial\varphi}\right) + \frac{1}{\rho_0}\frac{\partial(\rho_0\overline{w}^*)}{\partial z} = 0 \quad (2.11)$$

$$\frac{\partial\overline{\theta}}{\partial t} + \frac{\overline{v}^*}{r}\frac{\partial\overline{\theta}}{\partial\varphi} + \overline{w}^*\frac{\partial\overline{\theta}}{\partial z} + \frac{1}{\rho_0}\frac{\partial\left(\frac{\rho_0}{r}\overline{v'\theta'}\frac{\frac{\partial\overline{\theta}}{\partial\varphi}}{\frac{\partial\overline{\theta}}{\partial z}} + \overline{w'\theta'}\right)}{\partial z} = \overline{Q} \qquad (2.12)$$

Reproduced with permission of the copyright owner. Further reproduction prohibited without permission.

The Q and X terms correspond to Eulerian heating and friction. The TEM comprises a complete set of equations describing the mean state in term of $\{\overline{u},\overline{v}^*,\overline{w}^*,\overline{\theta}^*\}$. The F vector is the Eliassen-Palm vector $F \equiv (0, F^{\varphi}, F^{z})$ with components as follows:

$$F^{\varphi} \equiv \rho_0 r \cos\varphi \left(\overline{v'\theta'} \frac{\dfrac{\partial \overline{u}}{\partial z}}{\dfrac{\partial \overline{\theta}}{\partial z}} - \overline{v'u'} \right) \qquad (2.13)$$

$$F^{z} \equiv \rho_0 r \cos\varphi \left[\left(f - (r\cos\varphi)^{-1} \left(\frac{\partial(\overline{u}\cos\varphi)}{\partial\varphi} \right) \right) \frac{\overline{v'\theta'}}{\dfrac{\partial \overline{\theta}}{\partial z}} - \overline{u'w'} \right] \qquad (2.14)$$

The divergence of the F vector in the spherical, log-pressure coordinates is further denoted as:

$$\nabla \cdot F \equiv \frac{1}{\rho_0 r \cos\varphi} \frac{\partial F^{\varphi} \cos\varphi}{\partial\varphi} + \frac{\partial F^{z}}{\partial z} \qquad (2.15)$$

The divergence physically represents the zonal force on the mean state comprising the total effect of eddies. The TEM transformation takes into account the fact that within the set of equations 2.1 - 2.5 there tends to be a strong cancellation between the eddy heat flux convergence and adiabatic cooling (the thermodynamic equation). Similarly, the adiabatic heating term is a small residual and an air parcel should rise to a higher equilibrium altitude only if its potential temperature is increased by adiabatic heating. Hence, it is the residual

Reproduced with permission of the copyright owner. Further reproduction prohibited without permission.

meridional circulation associated with adiabatic processes that is directly related to the mean meridional flow. Under the quasi-geostrophic framework, we can interpret the E-P flux divergence (eq. 2.15) as the internal forcing of the mean state of the disturbances. One of the most important cases arises when $\overline{X}, \overline{Q}$ and $\nabla \cdot F$ vanish to zero, then $\frac{\partial \overline{u}}{\partial t}, \frac{\partial \overline{\theta}}{\partial t}, \overline{v}^*$ and $\overline{w}^*$ are also zero. This case constitutes the main reasoning behind the Charney and Drazin **nonacceleration theorem** (Charney and Drazin, 1961).

Approaching the E-P flux from a different perspective, we may deduce further advantages of it. From linear quasi-geostrophic theory the poleward momentum flux can be associated with the poleward group velocity

$$c_{gy} = -\frac{4[q]_y e^{-z'/H}}{K_T^4 |\psi_0|^2}(u'v'), \tag{2.16}$$

while the poleward potential temperature flux may be connected with the vertical component of the group velocity by

$$c_{gz} = \frac{f}{\theta_{Rz'}} \frac{4[q]_y e^{-z'/H}}{K_T^4 |\psi_0|^2}(v'\theta'), \tag{2.17}$$

where $[q]_y$ is the meridional gradient of quasi-geostrophic PV, f is the Coriolis parameter, ψ_0 is the base streamfunction wave amplitude, θ_R is the reference θ, and K is the total wave number.

Reproduced with permission of the copyright owner. Further reproduction prohibited without permission.

2.4. Methodology

For the purpose of analysis of the SH general circulation, wavestructure and ozone distribution the 1995-2004 period was divided into temporal composites according to the relative strength of the Australian High (AH), the South African High (SAH) and Indian Ocean Highs (IOH) at 20°S to differentiate the convective forcing and dynamical regimes. This differentiation scheme was subjective and depends on the relative strength of these three system determined by inspection of hovmoller plots of geopotential height anomalies for each of the years included in our dataset, however the positive height anomalies associated with strong AH were always on the order of 100 m or more. Further details are included in chapter five.

Reproduced with permission of the copyright owner. Further reproduction prohibited without permission.

Chapter 3

Modeling the effects of Southeast Asian monsoon outflow on subtropical anticyclones and midlatitude ozone over the Southern Indian Ocean

Marek Rogal, Matthew H. Hitchman, Marcus L. Buker, Gregory J. Tripoli, Ivanka Stajner and Hiroo Hayashi (2009), submitted to *J. Geophys. Res.*

3.1 Introduction

The distribution of ozone is determined through a combination of dynamical and photochemical processes. It has been observed that transient wave activity in the upper troposphere / lower stratosphere (UTLS) strongly modulates total column ozone through horizontal and vertical advection [*Andrews et al.,* 1987; *Trenberth,* 1992; *Orsolini et al.,* 1995, 1998; *Randel and Park*, 2006]. There is a high correlation between total ozone and tropopause pressure in middle latitudes on synoptic time scales [*Schubert et al.,* 1988; *Hudson et al.,* 2002; *Wirth*, 1990, 1993]. Long-term observations of column ozone in the SH show the anthropogenic ozone minimum or "Ozone Hole" [*London et al*, 1976; *Solomon et al*, 1986; *Newman and Randel*, 1988; *Randel et al.*, 2002], situated over Antarctica and surrounded by an asymmetric total ozone maximum in latitudes 40-60°S. This maximum, recurrent during the southern winter and spring, is centered south of Australia and spans a longitudinal band of about 200° (Fig. 3.1). Interannual and monthly variability is explored in separate manuscripts [*Hitchman and Rogal*, 2009; *Hitchman et*

Reproduced with permission of the copyright owner. Further reproduction prohibited without permission.

al., 2009]. Classical theory of SH wave-mean flow dynamics does not fully explain the mechanisms governing such a pronounced zonal asymmetry in the ozone distribution, with such a specific seasonal and longitudinal signal. Previous studies by *Wirth* [1990, 1993] showed high correlation with the climatological structure of lower stratospheric temperature, which exhibits similar behavior to column ozone. The position of the time-mean maximum in total ozone is highly correlated with the region of the maximum mean baroclinicity and SH storm track, which are zonally-oriented features residing at latitudes 50-60°S [*Berbery and Vera*, 1996].

Part of the hypothesis under consideration is that this ozone maximum is partially attributable to the dynamical coupling between the Northern Hemisphere's (NH) Tibetan High (TH) and the SH synoptic wave regime. Outflow from the Tibetan High in the UTLS extends southwestward across the Indian Ocean during most of the boreal summer and fall. This phenomenon occurs at the top of the summer monsoon in Southeast Asia during the mature state and is linked to oscillations in circulation and deep convection with timescales of roughly 10-20 days [*Krishnamurti and Bhalme*, 1976; *Krishnamurti and Ardanuy*, 1980; *Park and Randel*, 2006] during the active/break cycles. Manifestations of the TH outflow may be seen in Fig. 3.2, as predominantly southward pulses of the meridional wind component at the position of the Singapore/Changi WMO weather station (1°22'N, 103°59'E), as seen in winds interpolated from analyses from the European Centre for Medium-Range Weather Forecasts (ECMWF).

The hypothesis is that upon arrival in the SH, air masses from the outflow, which have higher potential vorticity (PV), spin up anticyclonically, interfere with the anticyclonic features projecting onto the local wave pattern, disturb the base of the

Reproduced with permission of the copyright owner. Further reproduction prohibited without permission.

Southern Polar Vortex (SPV), and create a preferential longitudinal band of higher column ozone values. This outflow is driven in pulses on quasi-weekly time scales. Outflow pulses from the Southeast Asian monsoon occur at different longitude bands from Africa to Australia.

An example of the effects of one such outflow event on the distribution of ozone mixing ratio at 100 hPa from August 4, 1998 is shown in Fig. 3.3. There is a pronounced ozone mixing ratio maximum in a trough southwest of Australia. This is immediately adjacent to the low-ozone anticyclones south of Madagascar and over northwestern Australia. Outflow surges occur in association with a stronger Australian High (AH), a quasi-stationary system which resides climatologically over northwestern Australia during late winter and early spring. It may be seen in Fig. 3.4a as a quasi-constant patch of high positive Montgomery streamfunction anomaly near 13°S and 80-160°E.

Figure 3.4b shows that the AH and TH near 23°N, 10-140°E tend to amplify at the same time, coinciding with strengthened southwestward flow toward the SIO. Both highs are amplified on August 3, 9, 18 and 23, notably when amplification occurs in the eastern part of the TH. The correlation coefficient between Montgomery streamfunction anomalies at 13°S, 120°E and 23°N, 100°E at lags ranging from 1-6 days is in the range of 0.5-0.7. An explanation of the TH and AH was first proposed by *Gill* [1980], with precursory work by *Webster* [1972] and was explored further by *Hoskins and Rodwell* [1995]. Their coupling is consistent with the dynamical structure forced by transient off-equatorial heating associated with monsoon convection. Conditions similar to those shown in Figs. 3.2 and 3.3 occur during August-October in all years examined. In order to investigate the specific conditions leading to the climatological structure of the distribution of ozone, we have analyzed the

Reproduced with permission of the copyright owner. Further reproduction prohibited without permission.

synoptic situation observed during August 1998 (section 3.3) and compared 3D ozone convergence patterns at 150 hPa with the evolution of synoptic-scale column ozone anomalies. The observational analysis is followed by two modeling studies described below.

In the first study, to qualitatively characterize the coupling between TH and AH we have employed the NASA Langley Research Center (LaRC) 3-D trajectory model. A back-trajectory study performed with this model showed the origins of several "patches" of airmasses being well within the NH at the shedding edges of an active TH. These airmasses are discussed in further detail in section 3.5.

In the second study, we have modeled the theoretical TH-AH coupling through use of the University of Wisconsin - Madison Nonhydrostatic Modeling System (UWNMS), initialized with ozone from the NASA Goddard Global Modeling and Assimilation Office (GMAO). A control run for the inflow surge in early August 1998 captured the essence of the dynamical regime associated with ozone transport, which, over time, leads to the climatological Ozone Croissant. Section 6 contains a comparison between the control run and a perturbed run (with the inflow surge amplified) to highlight the dynamical mechanism, and includes a full discussion of the results.

3.2. Model, Data and Methods

The analysis presented in this paper was performed using 2.5° gridded global surface and upper air analyses from ECMWF [*Trenberth*, 1992; *Hollingsworth et al.*, 1986] for meteorological fields. The month of August from 1998 was split into 5 phases: August 1-7, 8-11, 12-17, 18-23, and 24-31 by inspection of the location and strength of anticyclones

Reproduced with permission of the copyright owner. Further reproduction prohibited without permission.

over the SIO. Subsets were created to enable us to evaluate the synoptic situation characterizing different regimes. These regimes consist of the presence of the AH alone, the South African High (SAH) alone, and the AH together with the IOH.

The column ozone data set used in conjunction with ECMWF data is a product of the Total Ozone Mapping Spectrometer (TOMS) series. The particulars of this widely-used dataset may be found at http://toms.gsfc.nasa.gov. We have used 3-D ozone assimilation data from the NASA GMAO in order to initialize the UWNMS model with ozone acting as a tracer and to construct an ozone budget [*Stajner at al.*, 2001, 2004, 2006].

The ozone budget at a given altitude is given by the chemical constituent transport equation:

$$\frac{\partial n}{\partial t} + \vec{\nabla} \cdot \left(\vec{V} n\right) = \left(P - L\right) \quad (3.1)$$

where n is ozone mixing ratio in ppmv and the right side (Production – Loss) represents photochemical sources and sinks. Daily ozone fluxes were calculated using fourth-order differencing at standard pressure levels in the layer 500-50 hPa for August 1998. The time rate of change and photochemical terms were not computed; here the convergence patterns are emphasized. The sum of horizontal and vertical flux convergences at 150 hPa is compared with the ozone distribution for each sub-period defined above.

The LARC trajectory model [*Pierce and Fairlie*, 1993] was used to perform back-trajectory experiments. Three dimensional trajectory paths were computed using the fourth-order Runge-Kutta timestep scheme [*Butcher*, 1987], with the timestep kept at 20 minutes to ensure computational stability. Horizontal winds were linearly interpolated in time and space to trajectory positions.

Reproduced with permission of the copyright owner. Further reproduction prohibited without permission.

The core of the modeling study presented in section 3.5 is the UWNMS. The original purpose of this model [*Tripoli*, 1992; *Pokrandt et al.*, 1996] was to study mesoscale and synoptic scale tropospheric phenomena such as tropical cloud clusters, lake effect snow storms, gravity waves, cyclogenesis and mesoscale convective complexes. Its variable vertical resolution makes it useful to study a variety of problems in the UTLS [*Hitchman et al.*, 2001, 2004], and its limited domain allows for the use of forcing by inflow from the side.

The model was employed in a "hemispheric" mode, with its domain stretching over most of the SH. We initialized the model using ECMWF data interpolated to the 85 x 85 x 30 grid (~ 200 km horizontal and ~1 km vertical resolution), with the domain centered over the South Pole. To study the ozone transport problem, we initialized the model with 3-D ozone assimilation data from the GMAO, described before in association with the ozone budget. GMAO ozone was interpolated to the ECMWF grid and then used to initialize the UWNMS and update ozone values along its boundaries.

The time step of integration was 90 s. The domain side walls were updated every hour with temporally-interpolated ECMWF and GMAO data, while flow structures were allowed to evolve in the interior of the model. Although GMAO ozone provides realistic distributions of this constituent, it was treated as a passive tracer in the UWNMS. The problem of possible reflections from the upper rigid-lid boundary at 30 km was eliminated with a Rayleigh friction "sponge layer" in the five uppermost levels. The simulation dates chosen span August 1-8, 1998, which corresponded to an amplification and decay cycle of the coupled TH-AH duet.

To model the cross-equatorial influence of the TH on the SH dynamical structure,

Reproduced with permission of the copyright owner. Further reproduction prohibited without permission.

several experiments with different parameterizations were performed. Perturbation of the wind field was assessed as the most promising and direct parameterization for modeling outflow from the TH. The wind field was relaxed to a northeasterly wind, $\vec{U}'$ = (-10 m/s, -20 m/s) in the area of maximum perturbation at 5°S, 90°E over the SIO (right lower corner, Fig. 10a) by adding term (2) to the model's horizontal equations of motion:

$$-\frac{\left[\vec{U}-\vec{U}'\cdot S\right]}{\tau} \quad (3.2)$$

where τ is a relaxation time scale of 0.5 days and S describes the shape of the perturbation:

$$S(x,y,z) = \exp\left[-\left(\frac{(x-85)}{20}\right)^2 - \left(\frac{(y-1)}{10}\right)^2 - \left(\frac{(z-15)}{3}\right)^2\right] \quad (3.3)$$

The point (x,y) =(1,1) is at the lower left corner. Note the Gaussian half-widths of 20 grid points in the x-direction, 10 in the y-direction and 3 in the vertical. The altitude of maximum perturbation is taken to be 15 km, diminishing to zero at 9 km and 21 km. The spatial profile of the perturbation allowed for the reconstruction of very broad cross-equatorial inflow, with a width of around 4000 km in the middle of the SIO.

The UWNMS was run unforced for 24 hours to provide stable dynamical conditions. Subsequently, the wind perturbation was spun up in a Gaussian fashion to its maximum value at the end of day two and was kept constant between days 3-5, then linearly diminished to zero between the end of days 5 and 7. The 6 day period of wind perturbation influence was chosen to resemble the observed characteristic duration of a strong direct outflow pulse from a UTLS monsoon. By directly injecting air into the SH, we simulated an event of strong and longitudinally-limited flow in the SIO. A control run was performed

Reproduced with permission of the copyright owner. Further reproduction prohibited without permission.

with no inflow parameterization, and compared to the perturbed run in order to highlight the effects of inflow.

3.3. Time evolution and case analysis of geopotential height and ozone anomalies and during August 1998

August 1998 geopotential height anomalies at 20°S display five coherent phases (Fig. 3.5a) at the 150 hPa level. In Phase I, August 1-7, only one anticyclonic center (the AH) exists over the Indian Ocean and Australia region (60-140°E). During Phase II, August 8-11, an IOH is seen to retrogress to ~30°E and the AH near 110°E is visibly weaker than in previous days, yielding a two-cell system. In Phase III (August 12-17) these features are no longer present, but the South African High (SAH) is well established in the band 10°W-50°E. The demise of the SAH at the beginning of Phase IV on August 18 marks the return of the IOH as the strongest anticyclonic feature at this latitude. Finally, the fifth phase of the month analyzed starts on the August 24 with the reestablishment of the AH and IOH as the dominant pair of anticyclones.

At 35°S (Fig. 3.5b) the flow is predominantly westerly, with cyclones and anticyclones traveling eastward at ~15 m/s. The Eastern Pacific contains more stationary anticyclones, notably near 110°W, the Eastern Pacific High. As the AH migrates westward toward a SAH during the first half of the month at 20°S, stalled amplifying anticyclonic structures are seen near South Africa at 35°S, peaking on August 5 and 13 (Fig. 3.5b). In general, in the eastern hemisphere there is a moderate correspondence between amplifying anticyclones near 20°S and the stalling and amplification of anticyclones just to the

Reproduced with permission of the copyright owner. Further reproduction prohibited without permission.

southeast, near 35°S (Figs. 3.5a, b). Poleward flow to the west of subtropical anticyclones will advect low PV into the midlatitude westerlies, tending to amplify and stall the eastward progression of traveling anticyclones in the westerlies. During August 1-15 ozone-rich traveling troughs near 50°S and 60°S (Figs. 3.5c, d) tend to stall and amplify, immediately poleward and downstream of the SAH (Figs. 3.5a, b). A weaker version of this combination is seen in late August.

The division of August 1998 into 5 distinctive phases enables us to distinguish between the different synoptic regimes in the SH, which are visible in Fig. 3.6. The monthly mean Mercator projection of ECMWF geopotential height anomalies at 150 hPa (Fig. 3.6a) makes it possible to define the AH, centered at 25°S, 120°E, as well as the SAH – IOH system, stretching across most of the SIO. The northeast-southwest tilting trough over the higher latitude SIO and the ridge southeast of Australia play important roles in our analysis, although their area is amplified significantly by the projection. This structure is compatible with radiation of Rossby wave energy from the subtropics [*Sardeshmukh and Hoskins*, 1988]. When comparing eddy heights with TOMS time mean column ozone from August 1998 (Fig. 3.7a), the monthly mean residence of the ozone maximum coincides with the trough, and the 300 DU isoline (thicker contour) is roughly collocated with the southern and southeastern boundaries of the positive anomaly.

However, using the five phase division described earlier reveals changes in the strength, position and relative importance of both geopotential height disturbances and column ozone extremes. During Phase I (Fig. 3.6b) there is an amplified SAH and broad positive anomaly stretching over the Indian Ocean northeastward to the AH. Maxima over the Weddell Sea, Victoria Land, and the Eastern South Pacific High are relatively strong.

Reproduced with permission of the copyright owner. Further reproduction prohibited without permission.

Column ozone tends to reach its maximum concentration in the center of the trough between the SAH and the anticyclone to the south of Australia (Fig. 3.7b). A 300 DU contour traces the SAH, displaying a filament of higher ozone masses wrapped around this time-mean anticyclone, with a signal similar to the PV filaments associated with wave-breaking at these latitudes [*Huesmann and Hitchman*, 2007]. The 300 DU isoline also surrounds the Eastern Pacific High, with a similar wave-breaking meridional gradient reversal.

Phase II is characterized by a westward extension of the SAH toward the Atlantic, a southward migration of the AH, and a general weakening of the connection across the SIO (Fig. 3.6c). The high centered over Weddell Sea is much stronger, and its diminished downstream counterpart moved from south of Australia to within the vicinity of the dateline. In addition to changes in the synoptic structure, altered column ozone distribution is also visible (Fig. 3.7c). The 300 DU isoline has moved northward over the Indian Ocean, tracing the edges of the stronger SAH and AH. The eastward displacement of the Eastern Pacific High left lower ozone (< 300 DU) airmasses intruding toward 45°S, 90-140°W. The column ozone maximum now resides just south of the strengthened AH at 50°S, 110-170°E. A secondary maximum, resulting from horizontal advection along the eastern edges of the high system displaced from Victoria Land is located at 40°S, between 130°W and 160°W.

The Phase III (Fig. 3.6d) geopotential height anomaly field shows a lack of definition of the AH, with the Victoria Land High stronger than in the previous phase. The SAH remains distinguishable, and a trough resides over the Weddell Sea, with ridges over the Southern Atlantic and upstream of the Southeastern Pacific High. A diminishing ozone

Reproduced with permission of the copyright owner. Further reproduction prohibited without permission.

maximum is seen to the southeast of the weakening high migrating south of Australia (Figs. 3.6d, 3.7d). A diffuse ozone maximum is located over the high latitude SIO in the weakening trough over the coast of Antarctica near 0°E. The 300 DU contour closely traces the longitudinal elongation of the SAH as well as the Southeastern Pacific High.

Panel 3.6e shows a regenerating AH and a diminished SAH during Phase IV. The anticyclone to the southeast of Australia has weakened and the ozone maximum to its east is becoming more diffuse (Figs. 6e, 7e). The eastward-traveling baroclinic systems are diffusing ozone eastward, contributing to the monthly mean Ozone Croissant shape (Fig. 3.1).

In Phase V a weak SIOH has formed, and a focused column ozone maximum is found in the trough immediately to its southeast near 47°S, 80-110°E (Figs. 3.6f, 3.7f). Again, the 300 DU isoline closely traces the edges of all three anticyclones: the SAH, IOH and AH.

3.4. Simple ozone budget

Evaluation of the chemical constituent transport equation for the duration of the month of August of 1998 allowed us to identify areas of positive flux convergence of ozone associated with horizontal and vertical transport. The monthly mean ozone flux convergence (Fig. 3.8a) has negative values on the axis drawn between the SAH and the high located around the Weddell Sea (Fig. 3.6a), indicating an area of mean flux divergence. This corresponds to the minimum in TOMS ozone south of Africa, with its axis tilting westward with increasing latitude (Fig. 3.7a). Immediately to the east there is a region of positive flux convergence, indicating a monthly mean influx of ozone which leads

Reproduced with permission of the copyright owner. Further reproduction prohibited without permission.

to the creation of climatological maxima over the Southern Indian Ocean. This feature includes contributions by the mean AH (a positive patch south of Australia), the SAH (on its western time-mean edges), and transport of ozone from the IOH-SAH couplet (60-90°E). Note the positive flux convergence near the tip of South America, immediately southeast of the Southeast Pacific High.

Since ozone transport depends on synoptic conditions, which differ for the 5 cases identified, analysis of only the monthly mean would be misleading. Phase I (Fig. 3.8b) reveals strong flux convergence associated with enlarged IOH-AH systems, spanning the southern coast of Australia and trending westward with latitude. This pattern contributes strongly to the monthly mean. There is also a strong positive patch at the southwestern edge of the SAH. Fluxes in the Eastern Pacific area are more complicated due to the combined circulatory effects of the Southern Pacific High, Eastern Pacific High and the anticyclone over the Weddell Sea, all of which produce positive flux convergences on their southwestern edges.

Phase II flux convergence clearly shows a dependence on the distribution of anticyclones (Fig. 3.8c). Strong positive flux convergence west and southeast of Australia results in a well defined AH (Fig. 3.7c) during this time. Strong meridional transport is a dominant feature over the SIO, with positive fluxes wrapping around the SAH system. The Eastern Pacific High produces large positive anomalies immediately west of South America and the Weddell Sea High causes advective redistribution of ozone in the high latitudes.

The weakened AH (Fig. 3.6d) diminishes the positive flux convergence south of Australia during August 11-17 (Fig. 3.8d). This leads to a diminished maximum in column ozone, as noted earlier (Fig. 3.7d). The troughs in the Southern Pacific and Atlantic, which

Reproduced with permission of the copyright owner. Further reproduction prohibited without permission.

were displaced eastward during Phase III, produce the usual pattern of positive flux divergence associated with their circulation.

The simultaneous resurgence of the AH and demise of the SAH (Fig. 3.6e) immediately change the distribution of ozone flux convergence in the SH (Fig. 3.8e). The strength of the AH leads to positive patches in the central part of the Indian Ocean and south of Australia. This ozone is then meridionally redistributed by high latitude systems residing around 55°S (indicated by flux divergence in the Victoria Land High and convergence to the east of this system). By comparing wind vectors (not shown) with TOMS ozone data for this time period (Fig. 3.7e), it becomes apparent that meridional advection by high latitude flow is the main contributor to the elongated maximum observed in the region between Australia and Antarctica.

The return of the SAH and IOH (Fig. 3.6f) is marked by a subsequently stronger positive flux convergence at the Perth–Amery Ice Shelf axis (Fig. 3.8f) along the trough associated with the IOH and a strong influx of ozone south and southwest of Africa (along the southwestern edge of the SAH). The positive flux convergence zones south of the IOH and southwest of the AH are the main contributors to the collocated column ozone maximum (panel 3.7f). The good agreement of flux convergence pattern accentuates the relative importance of dynamical features in producing column ozone distributions on the synoptic scale. Differences arise from the fact that flux convergence is shown near 150 hPa, near the level of maximum ozone concentration, but convergences at other levels contribute to column ozone patterns.

Reproduced with permission of the copyright owner. Further reproduction prohibited without permission.

3.5. Trajectory analysis

Analysis of isentropic back-trajectories identified the latitudinal extent of areas influenced directly by the inflow from the TH. Four main sets of parcels were initialized in areas associated with IOH anticyclones at 12°S, 80-87°E (Fig. 3.9a) 22°S, 80-87°E (Fig. 3.9 b) and the AH system at 12°S, 107-114°E (Fig 3.9c) and 22°S, 107-114°E (Fig. 3.9d) on the 360 K isentropic surface. These air parcels were then advected back in time for 12 days, starting from August 5, 1998, during the first phase of our analysis, and the buildup period of the modeling study performed in the subsequent chapter.

Air parcels, such as the those in the Tibetan High and highs over the Arabian Peninsula, that were initialized in an area influenced by the IOH (12°S latitude) originated within NH circulatory systems (Fig 3.9a). However, parcels initialized at 22°S had more diverse origins, some making their way to the IOH from the convective zones over Africa and Amazonia, and a few advected from SE Asia (Fig. 3.9b).

Unlike their counterparts, parcels arriving from the western boundary of the AH (Fig. 3.9c and d) originated well within the NH TH system's circulation. This supports the idea that the TH-AH couplet plays a major role in the crossequatorial transport of air. Notable is a parcel trajectory collocation (Fig. 3.9a and c) with the higher ozone mixing ratio patch crossing the Philippines and then southwestward across the equator over Sumatra in the 100 hPa Mercator projection of GMAO ozone (Fig. 3.3).

3.6. UW-NMS results

During the years studied (1992-2004), a zonal wavenumber 5 pattern emerged as a dominant feature of the extratropical winter UTLS in the band 40°-60°S. The basis of our

Reproduced with permission of the copyright owner. Further reproduction prohibited without permission.

dynamical forcing study is the pressure pattern from August 4, 1998 (Fig. 3.10a), which prevails during most of July – October and exhibits a wave 5 aspect. We chose to focus specifically on Phase I as an example of forcing the SH flow by outflow from the SIOH system. The cross-equatorial meridional wind component over Singapore indicated a buildup in part of the TH inflow (Fig. 3.2), which we have magnified and used as a basic component of our modeling study, without introducing other unintended flow perturbations.

During the perturbation spin-up period we observed the formation of poleward flow into the extratropical westerly jet and subsequent counterclockwise anticyclonic circulation, consistent with quasi-conservation of high potential vorticity from the north. Thus, an anomalous high pressure system was established to the southwest of Australia (seen here in Fig. 3.10b as a contoured pressure difference between forced and control model runs).

This development was already a robust feature 48 hours into the simulation. As with the North Atlantic High studied by *O'Neill and Pope* [1988], the anomalous high became vertically prominent, 'growing' into the lower stratosphere. The elongated and deepened trough on the southeast periphery of the anomalous high allowed for more high ozone content air to enter it (Figs. 3.10a, b). Figure 3.11a shows the 0.2 ppmv ozone anomaly isosurface (forced run – control run) colored by pressure, which highlights the vertical extent of the anomaly. The pressure perturbation (the pressure difference between forced and control runs) is visible at an altitude of 15 km. The convergence and downward advection of air with a high ozone mixing ratio into traveling troughs over the higher latitude SIO leads to increased ozone concentration, and hence, greater column values in

Reproduced with permission of the copyright owner. Further reproduction prohibited without permission.

the center of the ozone croissant (Fig. 3.1).

After the establishment of the transient anticyclone, the wave train started to travel east and modulated the hemispheric wave pattern, creating a wavenumber 4 mode. This setup of anticyclonic anomalies projected into wave-space as a change from wavenumber 5 to 4 has been noted in previous observational studies as a recurrent feature of SH dynamics [*Wirth,* 1991; *Trenberth,* 1991; *Shiotani et al.*, 1985, 1993]. The breadth of the perturbation, being wider than $L_X = 2\pi \cos 50° \cdot 6357 km/5$ at this latitude, acted to elongate the trough south of Australia. Inspection of the ECMWF data shows that strong inflow events are often precursors to this shift. This situation continued throughout the run. The wave pattern appears to be smoothed by the elongation of the trough (Fig. 3.10b, 3.11a), with stronger height gradients indicating a more intense westerly jet to the south of the anticyclone. This is consistent with understanding of the secondary circulation around jets poleward and downward into the trough in the UTLS [e.g., *Shapiro,* 1978]. This is further consistent with the Stokes drift for Rossby waves [*Wallace,* 1978] and the downward control principle for synoptic waves absorbed in the lower stratosphere [*Haynes et al.,* 1990].

By 72 hr there is downstream development of alternating high and low pressure perturbations around Antarctica. The zonal phase speed of the resulting wave was close to 30 m/s, which is consistent with the Rossby wave dispersion relation. Consequently, we observed higher ozone concentrations anchored around these perturbations (Fig. 3.4a), especially at their southeastern edges. A vertical section through the center of anticyclonic perturbation shows a 'medusa'-like pattern of ozone descent (Fig. 3.11b). The 1.5 ppmv O_3 contour (marked green) extends deep into the troposphere on the southern side of the anomalous anticyclone, while the northern edge is more vertically localized. We can also

Reproduced with permission of the copyright owner. Further reproduction prohibited without permission.

observe cut-off high ozone content masses that have originated from deep tropospheric intrusions (Fig. 3.11a between Australia and Antarctica).

Such deep incursions occur many times during one June-November season in the South Indian Ocean / Australian sector. Some of the high ozone content masses are advected eastward, contributing to the elongation of the croissant. Monthly means of synoptic snapshots yield the croissant-shaped maximum in column ozone, due to stratospheric intrusions being more common upstream of and in the maximum.

This general dynamical situation is maintained until the inflow from the NH ceases, then the whole downstream wave train slowly decays and wavenumber 5 is reestablished as the dominant pattern in the SH. In the absence of broad forcing introduced earlier in the run, the circulation adjusts back to the initial wave five pattern.

3.7. Conclusions

The observational part of the study, which consisted of careful analyses of 5 periods in August, led to the marking of distinctive modes in the lifecycle of SH anticyclones. Via analysis of geopotential height anomalies and ozone flux convergence associated with phases 1-5, we showed the relative importance of the SAH, IOH and AH in the cumulative transport of ozone in the Indian Ocean region, leading to the studied zonal asymmetry in column ozone distribution. Analysis revealed that the ozone maximum tends to be zonally elongated in the presence of the IOH and SAH systems. In contrast, the presence of a relatively stronger AH introduces a more zonally limited column ozone maximum (Fig. 3.6d and 3.7d versus 3.6f and 3.7f). We also noted that anticyclones located in the surf zone tend to induce meridional transport of ozone, while their high latitude counterparts tend to

Reproduced with permission of the copyright owner. Further reproduction prohibited without permission.

cause a more zonal redistribution through horizontal advection. The importance of the northern "*Gill* [1980] solution" to off-equatorial transient heating due to convection (namely the Tibetan High) was highlighted through use of trajectory analysis. This part of the study showed that a significant amount of air reaching the SH subtropical westerlies over the SIO originated well within the NH, sometimes inside the TH circulation zone. The meridional transport of air masses, linked in this study with the outflow from the TH, is well known from the classic concept of monsoonal circulations (*Shaw*, 1930), where mass circulation occur by upward vertical mass transport in the region of net heating and downward mass transport in the cooling regions. The mass continuity requires the quasi-horizontal mass transport from the heat source to heat sink in the upper branches with corresponding reversed transport below. The net horizontal transports of momentum, entropy and energy are necessary for the equilibration of the atmospheric time-averaged thermal structure in relation to the observed heat sources and sinks (*Townsend*, 1981, *Johnson*, 1989, *Johnson et al.*, 1980) and result in the development of the isentropic mass circulation (*Johnson, et al.*, 1982, *Schaack,* 1982, *Hoerling and Johnson,* 1986).

The second part of this study focused on modeling the southern part of the major cross-equatorial dynamical connection between two of the most prominent quasistationary anticyclones in the Indian Ocean region: the Tibetan High and Australian High. We have tested the model's response to lateral inflow in the UTLS, the mechanism hypothesized to be responsible for the dynamical redistribution of ozone in the SH. The direct wind forcing used in these simulations provided a novel and robust way to model the impact of the boreal summer monsoon outflow on the SH.

In the southern subtropics (~13°S, Fig. 3.4a), quasistationary anticyclones occur near

Reproduced with permission of the copyright owner. Further reproduction prohibited without permission.

Africa (20°E) and South America (50°W), and especially near Australia (110°E). In the NH, differences in the continentality alter the distribution of quasistationary anticyclones somewhat. During late summer and fall the TH is the most prominent anticyclonic feature in our atmosphere (Fig. 3.4b, around 40-120°E). The existence of the AH near 110°E in the SH and the TH over the Tibetan Plateau was partially explained by *Gill* [1980]. Established as a direct outcome of convective forcing, the AH is later maintained and heavily modulated by direct connection with its stationary counterpart in the NH, the Tibetan High. The geographical location of these mutually-connected anticyclones introduces a peculiar shape in the total ozone distribution climatology (as seen from analysis and through modeling study), since downward transport of high ozone-content air is especially strong in the deep troughs on the periphery of the anticyclones forced in the model. This two-step study provided insight into the mechanisms governing synoptic ozone distributions in the SH. It may supplement the abundance of documented, well established teleconnection patterns [e.g., *Wallace et al.,* 1981; *Hines and Bromwich,* 2002] in an effort to explain some of our planet's dynamic variability and distribution of constituents.

Reproduced with permission of the copyright owner. Further reproduction prohibited without permission.

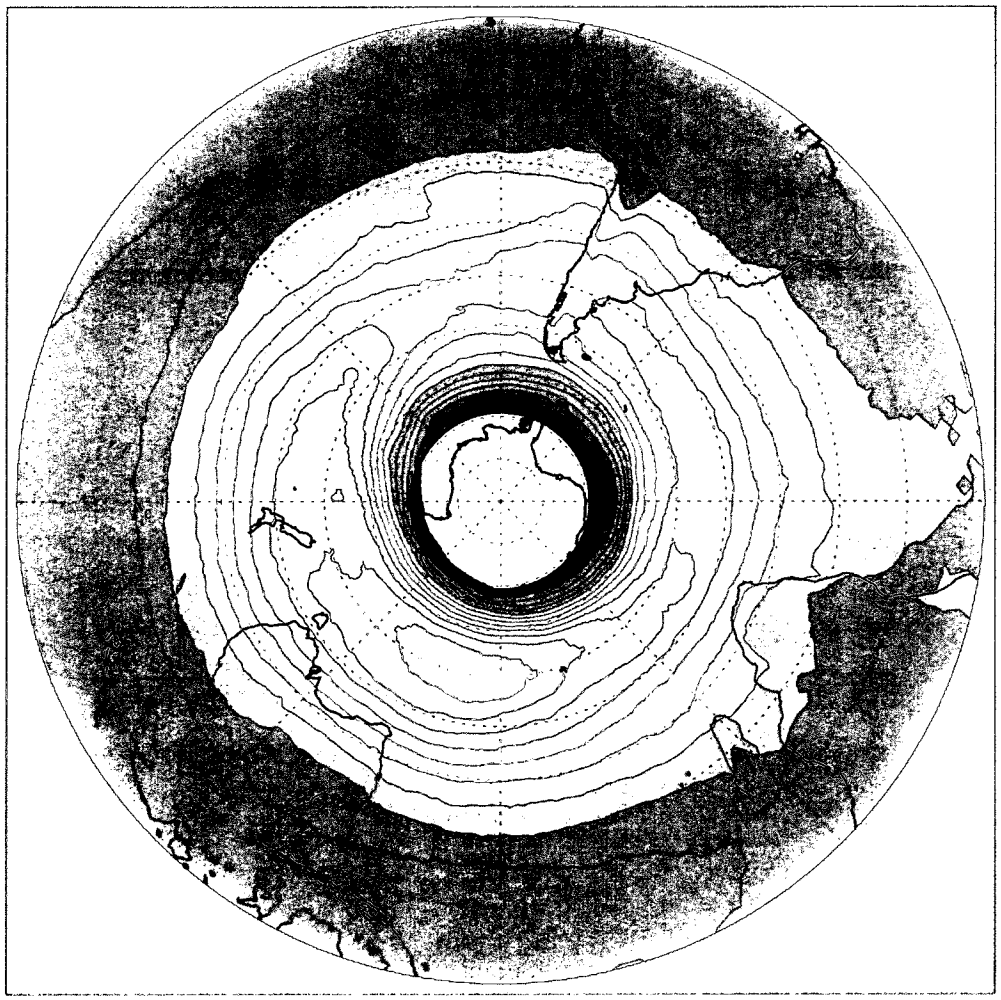

Figure 3.1. Monthly mean of TOMS column ozone in August 1998, contour interval 15 Dobson Units (DU). The maximum value south of Australia is 379 DU and the minimum value over Indonesia is 238 DU. Latitudes are shown every 10° and 0°E is at the right.

Reproduced with permission of the copyright owner. Further reproduction prohibited without permission.

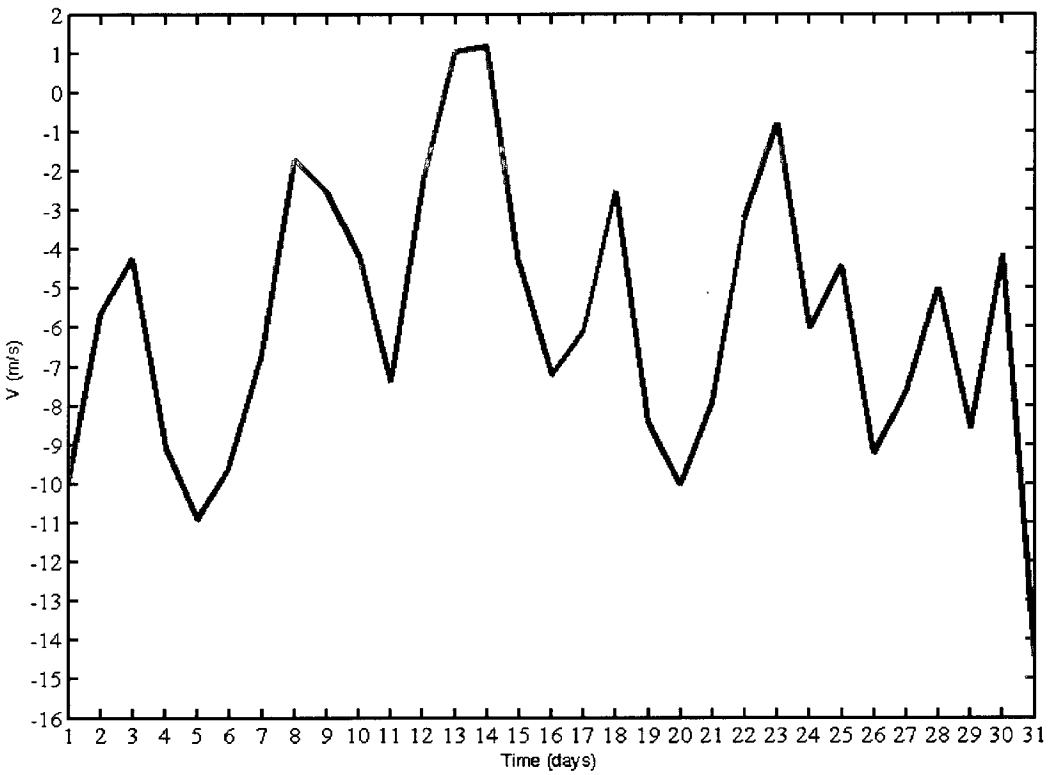

Figure 3.2. Meridional wind component (m/s) at Singapore (1°22' N, 103°59' E) extracted from daily ECMWF data at 1200 UT for August 1998 at 150 hPa.

Reproduced with permission of the copyright owner. Further reproduction prohibited without permission.

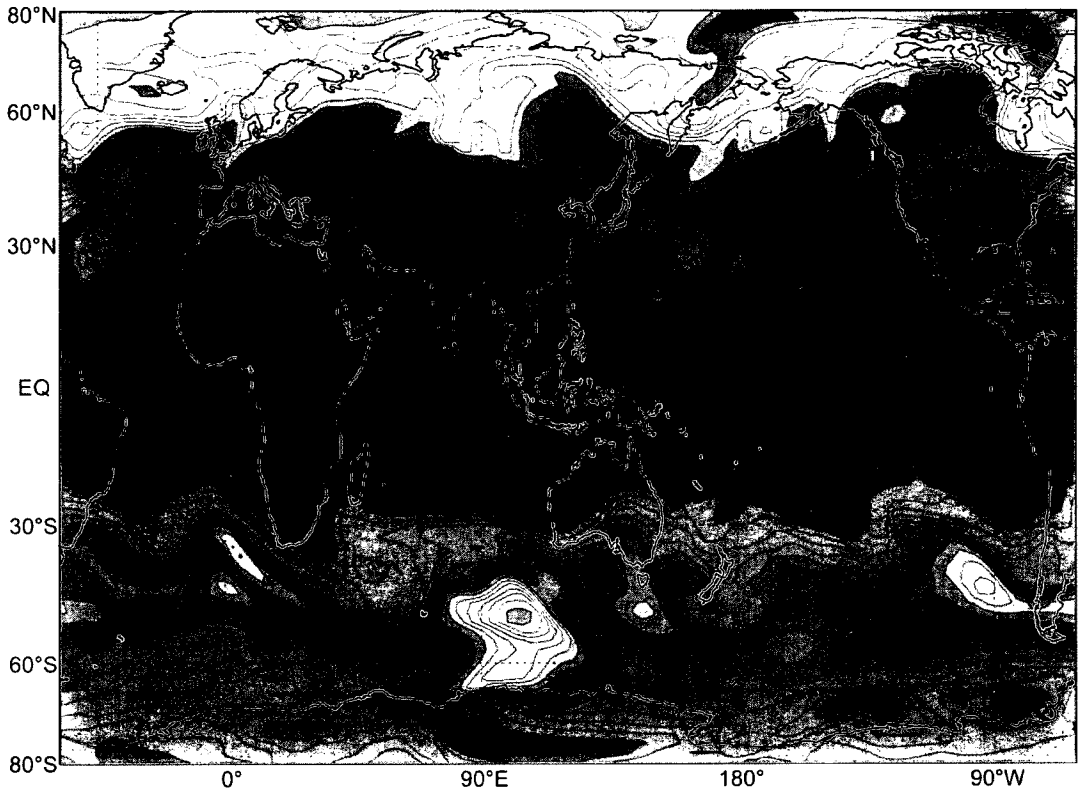

Figure 3.3. GMAO ozone mixing ratio at 100 hPa on 4 August 1998, contour interval 0.08 ppmv, with values ranging from 0.055 to 1.8 ppmv. The maximum value in the trough southwest of Australia is 1.63 ppmv.

Reproduced with permission of the copyright owner. Further reproduction prohibited without permission.

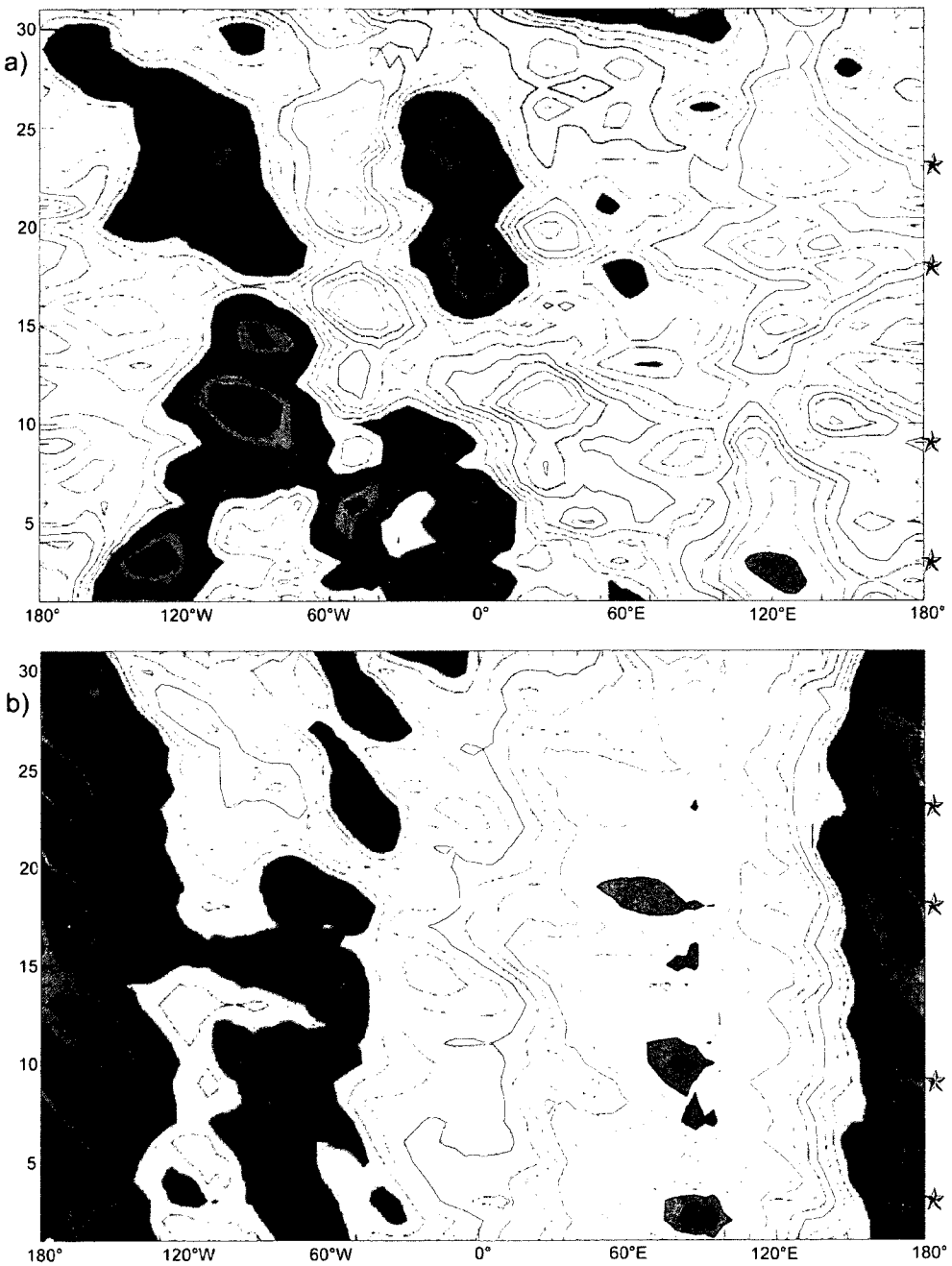

Figure 3.4. Hovmöller (longitude-time) plot of ECMWF Montgomery streamfunction at 360 K at a) 13°S and b) 23°N during August 1998. The contour interval is 100 m^2/s in a) and 200 m^2/s in b). The stars indicate contemporaneous amplification of the TH and AH.

Reproduced with permission of the copyright owner. Further reproduction prohibited without permission.

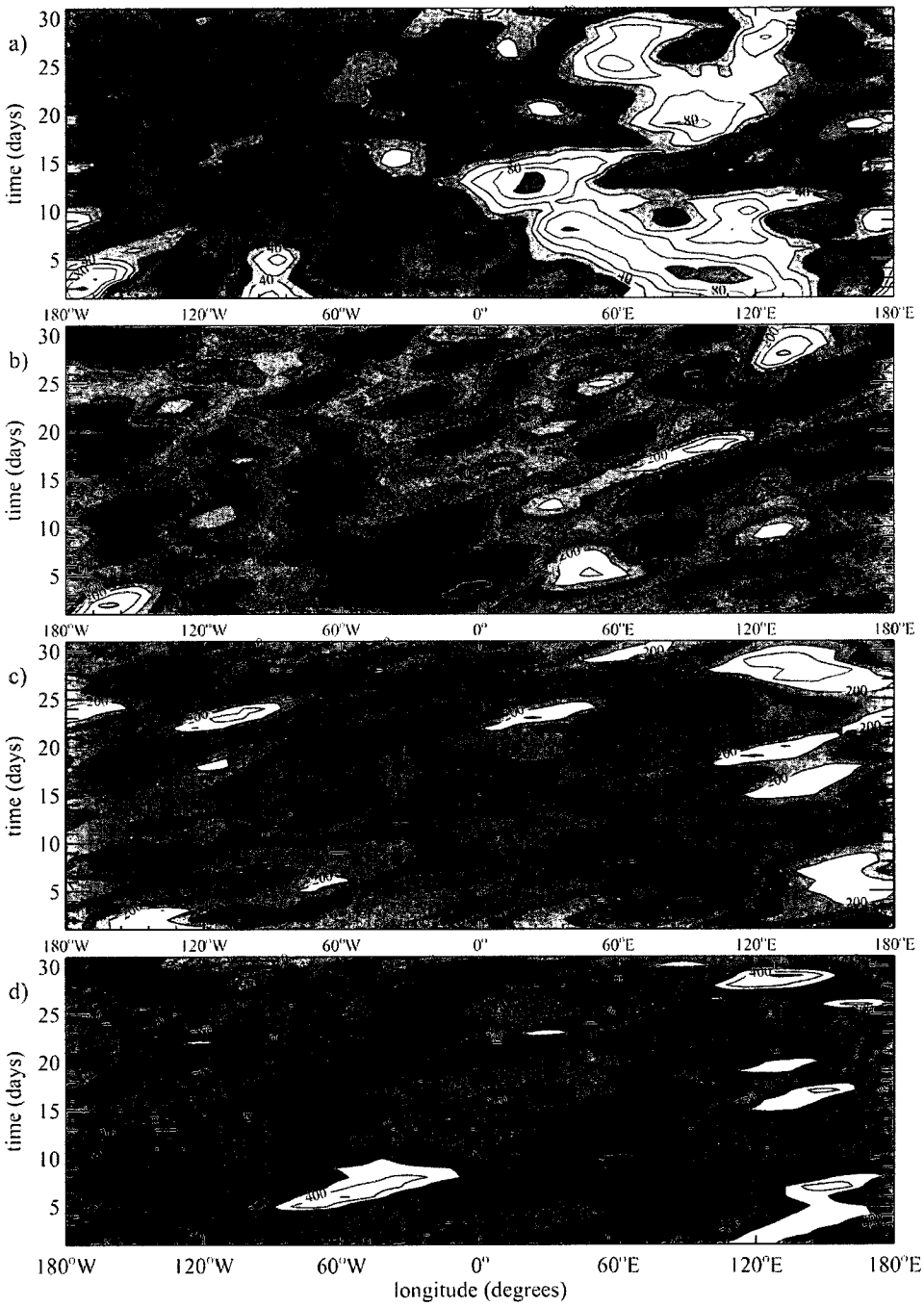

Figure 3.5. Hovmöller (longitude-time) plot of ECMWF geopotential height anomalies at 150 hPa at a) 20°S, b) 35°S, c) 50°S, d) 60°S during August 1998. The contour interval is 20 m in a), 50 m in b), 100 m in c) and d).

Reproduced with permission of the copyright owner. Further reproduction prohibited without permission.

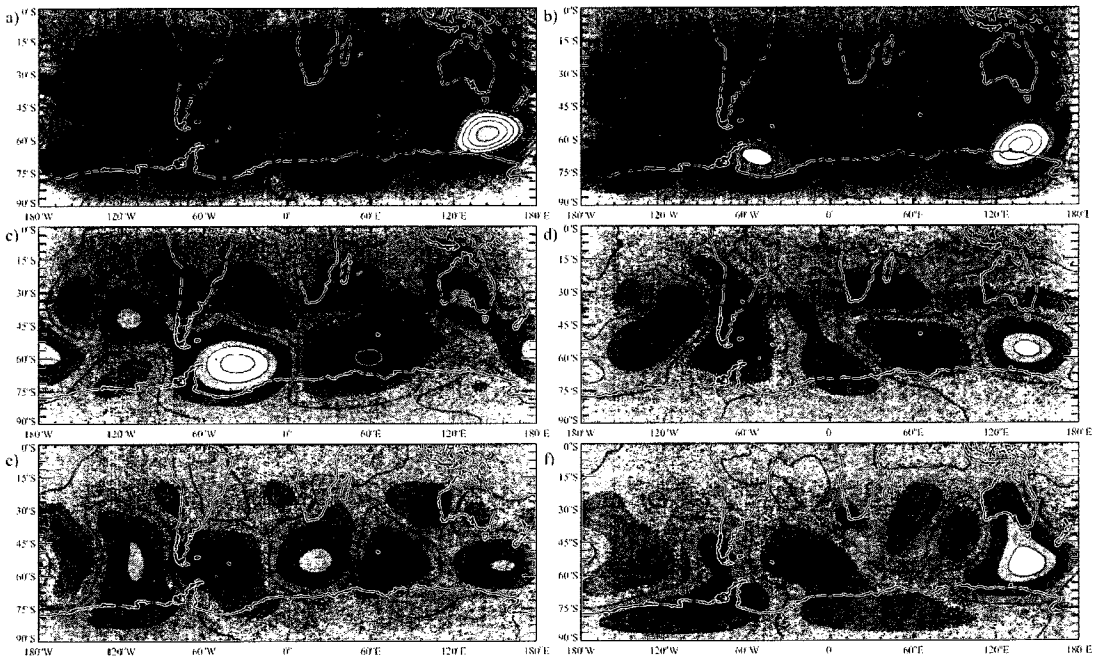

Figure 3.6. Time-composite of ECMWF geopotential height anomalies in the Southern Hemisphere for a) August 1998 monthly mean, b) August 1-7 (Phase I), c), August 8-11 (Phase II), d) August 12-17 (Phase III), e) August 18-23 (Phase IV), and f) August 24-31 (Phase V). The contour interval is 20m in a), 50 m in b) - f).

Reproduced with permission of the copyright owner. Further reproduction prohibited without permission.

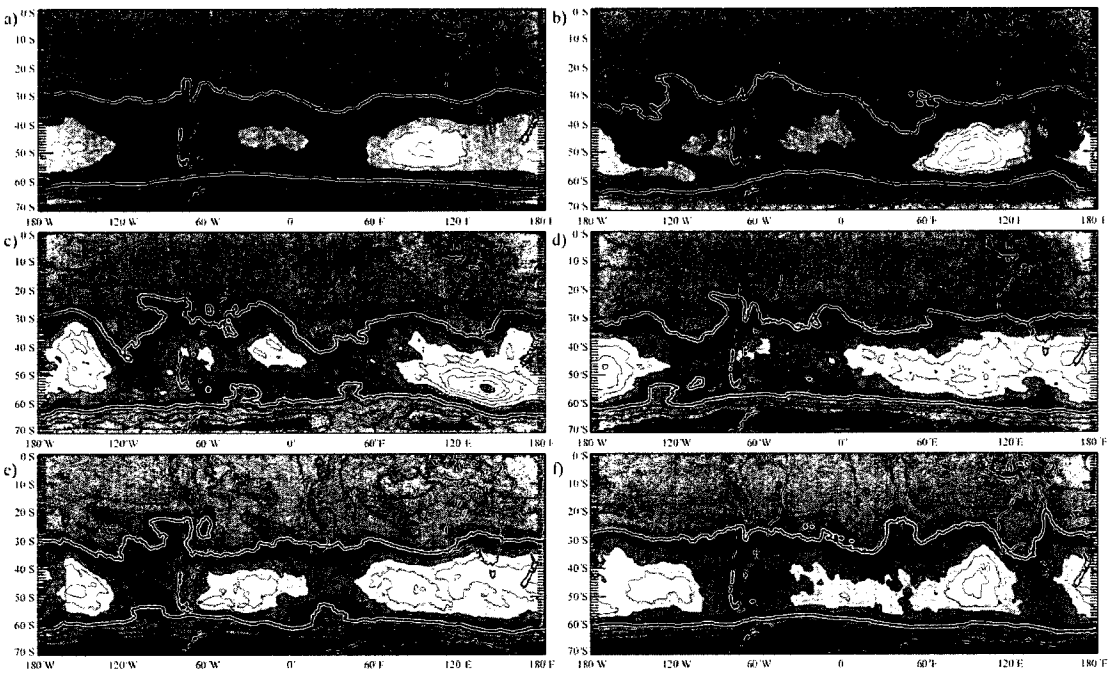

Figure 3.7. Time-composite of TOMS column ozone in the Southern Hemisphere for a) August 1998 monthly mean, b) August 1-7 (Phase I), c), August 8-11 (Phase II), d) August 12-17 (Phase III), e) August 18-23 (Phase IV), and f) August 24-31 (Phase V). The contour interval is 15 DU in a) through f).

Reproduced with permission of the copyright owner. Further reproduction prohibited without permission.

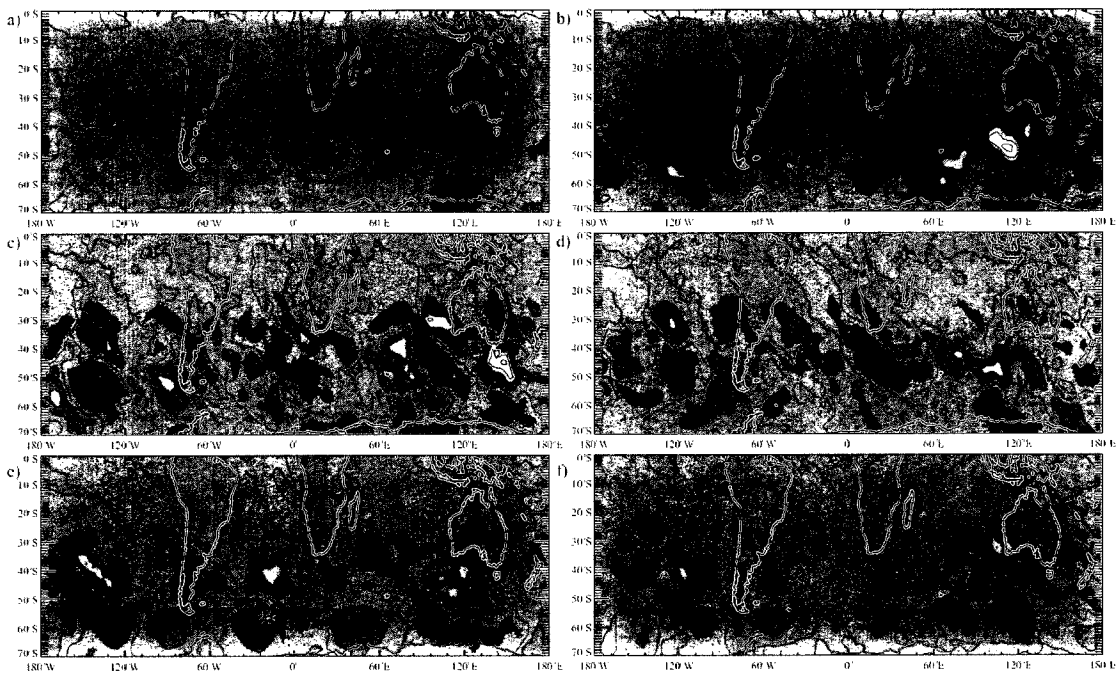

Figure 3.8. Time-composite of ozone flux convergence in the Southern Hemisphere for a) August 1998 monthly mean, b) August 1-7 (Phase I), c), August 8-11 (Phase II), d) August 12-17 (Phase III), e) August 18-23 (Phase IV), and f) August 24-31 (Phase V). The contour interval is 10 ppbv/day in a) through f).

Reproduced with permission of the copyright owner. Further reproduction prohibited without permission.

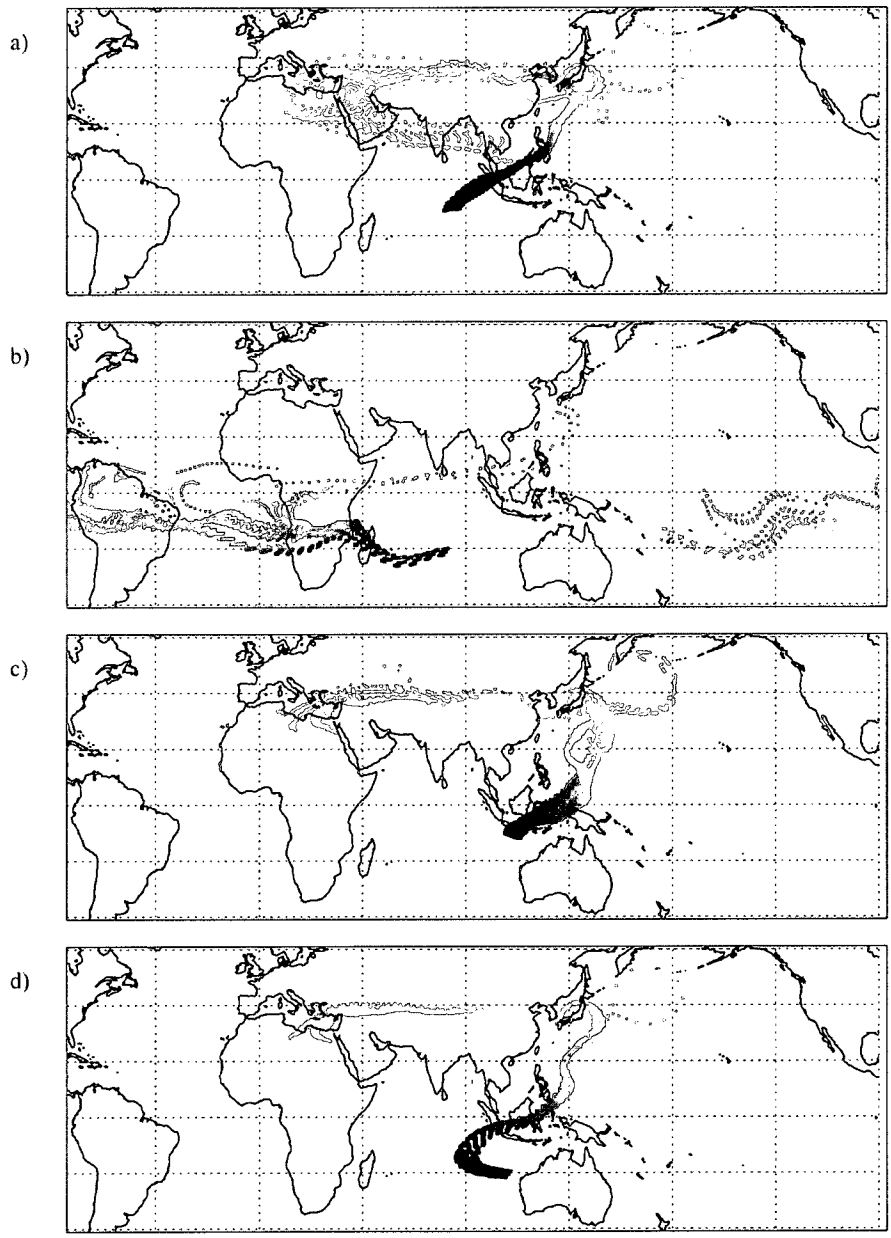

Figure 3.9. Twelve-day back-trajectories for air parcels arriving on August 5, 1998 at a) 12°S, 80-87°E, b) 22°S, 80-87°E, c) 12°S, 107-114°E and d) 22°S, 107-114°E. Color coded ages: black (1-2 days), purple (3-4 days), blue (5-6 days), green (7-8 days), yellow (9-10 days) and orange (more than 11 days).

Reproduced with permission of the copyright owner. Further reproduction prohibited without permission.

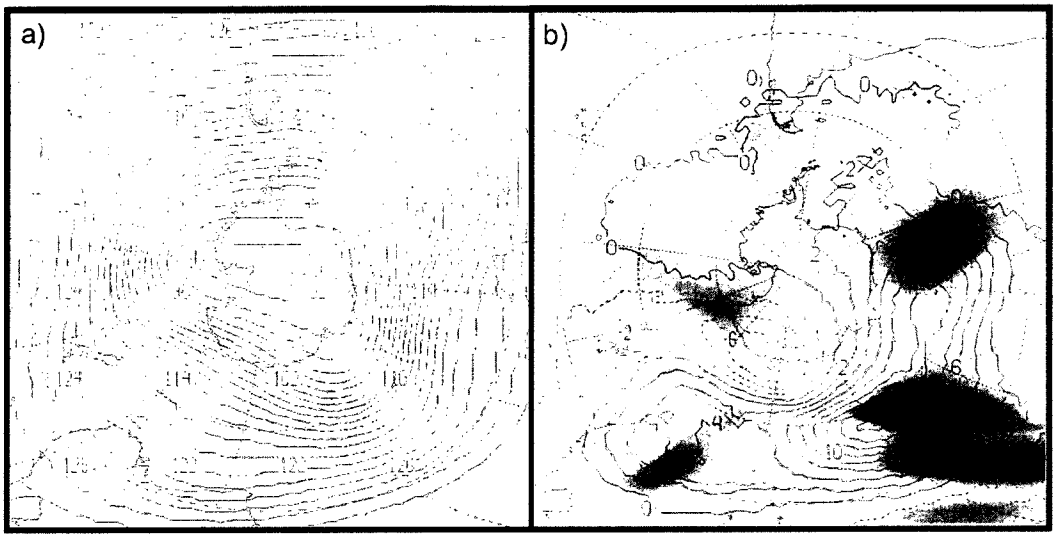

Figure 3.10. Pressure distribution at 15 km (contour interval 2 hPa), in the UWNMS for a) the control run at hour 48 of the model run (2 August 1998), b) perturbed minus control runs at the same model time, after the perturbation achieved its maximum. In a) the red shading indicates the extent of wind perturbation. In b) dashed lines indicate negative pressure differences, while color indicates meridional velocity difference, with blue (red) indicating more southward (northward) flow in the perturbation. The velocity difference ranges from -39 m/s to +36 m/s.

Reproduced with permission of the copyright owner. Further reproduction prohibited without permission.

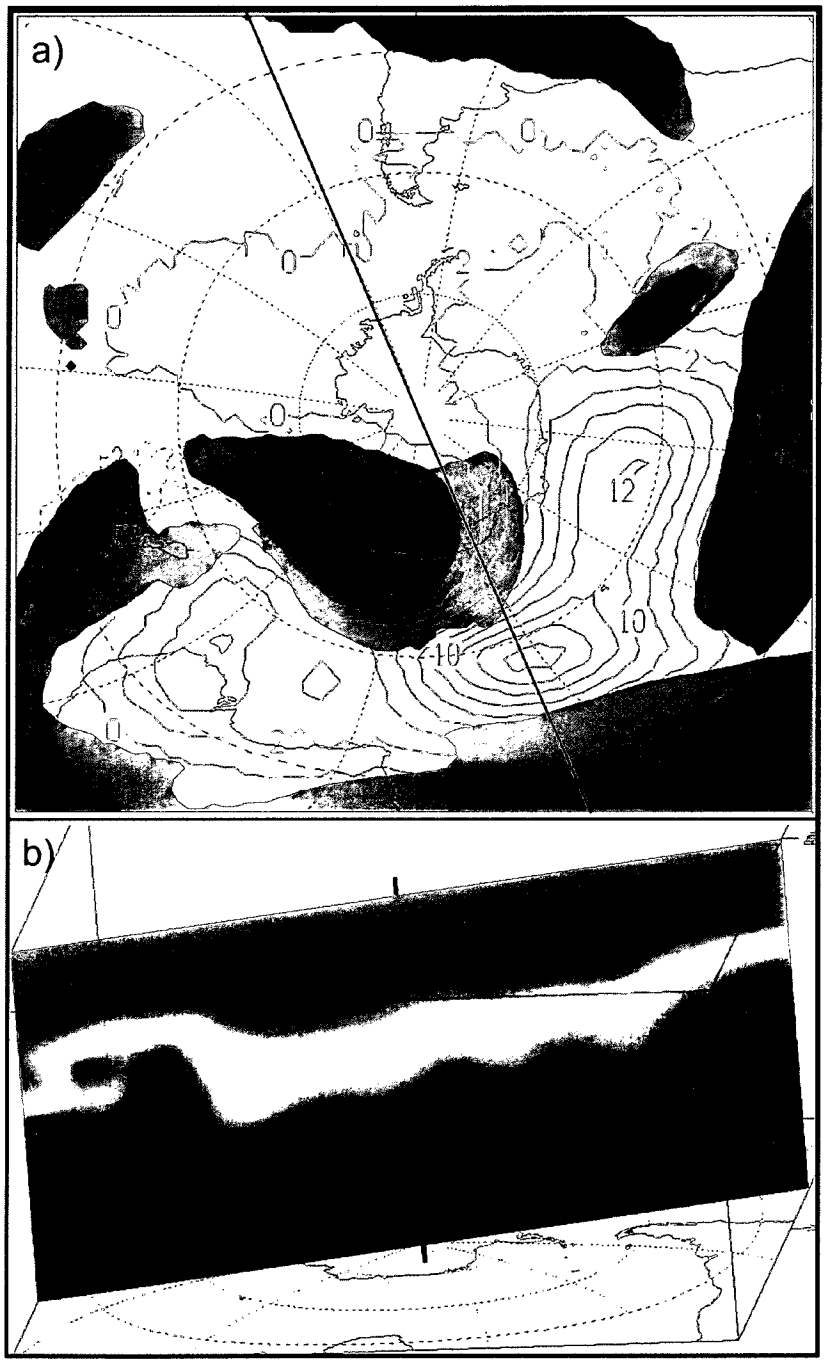

Figure 3.11. a) UWNMS perturbation pressure at 15 km (contour interval 2.0 hPa) and +0.2 ppmv ozone anomaly isosurface, colored by pressure, at 1200 UT 4 August 1998 in the perturbed run. Pressure levels of anomaly isosurfaces range from 448 hPa at

Reproduced with permission of the copyright owner. Further reproduction prohibited without permission.

5.8 km (red) to 12.3 hPa at 25.5 km (blue). The black line shows the position of the vertical section shown in b), with the SIO at left. b) Latitude-height section of UWNMS ozone volume mixing ratio and 15 km pressure (contour interval 2 hPa) at 12 UT 4 August. The transition zone between blue and red colors denotes values close to 1.5 ppmv. Note the elevated tropopause over the forced anticyclone and ozone streamer into the troposphere on its poleward periphery.

Reproduced with permission of the copyright owner. Further reproduction prohibited without permission.

Chapter 4

Seasonal evolution of the Ozone Croissant: Zonal contraction of monsoon outflow and stalled planetary wave ridges

Matthew H. Hitchman, Marek Rogal (2009), submitted to *J. Geophys. Res.*

4.1. Motivation

Monthly mean column ozone in the Southern Hemisphere (SH) winter and spring usually exhibits an elongated maximum near Australia centered in the band 40-60°S, extending from the Southern Indian Ocean (SIO) to the Eastern Pacific (Fig. 4.1). This zonal asymmetry gradually amplifies during winter, reaches its maximum in October, and wanes during November (Fig. 4.1c). This asymmetry is modulated by eastward-travelling planetary waves, which increase in amplitude during the winter to spring transition. This fundamental shape has been known for many years [*MacDowall*, 1960; *Godson*, 1963; *London et al.*, 1976], and has come to be called the "ozone croissant" (OC), due to its appearance in polar stereographic projection. *Wirth* [1991, 1993] studied this fundamental ozone asymmetry by assuming, *a priori*, a planetary wave one thermodynamic structure in the linearized stationary ozone continuity equation. He found that both vertical and horizontal advection substantially contribute to the total ozone perturbation. High column ozone amounts coincided with warm lower stratospheric temperatures. Other studies of the standingwave, jet, and ozone structures in the SH extratropical stratosphere include *Van Loon and Jenne* [1972], *Hartmann* [1977], *Mechoso and Hartmann* [1982], *Shiotani and Hirota* [1992], *Randel* [1987], *Randel et al.* [1987], *Newman and Randel* [1988], *Shiotani et al.* [1993], *Aoki et al.* [1996], and *Hio and*

Reproduced with permission of the copyright owner. Further reproduction prohibited without permission.

Yoden [2005; 2007]. This body of work, however, does not address the underlying cause of the geographical position of the OC, nor does it address the cause of the seasonal intensification from August through October, the primary foci of this paper.

Here a more thorough exploration of the dynamical processes which create the OC and wave one structure in the lower stratosphere is undertaken, including the roles of convective out-flow in the upper troposphere / lower stratosphere (UTLS), the Australian Subtropical Westerly Jet (ASWJ), synoptic waves breaking on the ASWJ, stalling planetary wave ridges, and their connection with Southern Indian Ocean (SIO) UTLS anticyclones.

This fundamental ozone asymmetry in the SH winter and spring has important implications for the distribution of radiative heating [*Crook et al.*, 2008] and planetary wave propagation [*Nathan and Cordero*, 2007]. Moreover, the anthropogenic ozone hole in October is usually displaced toward the South America/ Atlantic sector, away from the OC in the Australian sector (Fig. 4.1b). Since the OC and ozone hole are intimately linked as parts of a planetary wave pattern, a better understanding of the dynamics underlying the OC would aid understanding of the variability of the ozone hole [e.g., *Solomon et al.*, 2005; *Grytsai et al.*, 2007]. It is also of interest to better understand the relationship between anthropogenic changes in ozone and greenhouse gases and dynamical feedbacks [*Butchart et al.*, 2006; *Eyring et al.*, 2006; *Garcia and Randel*, 2008]. This is becoming increasingly important in light of the apparent relationship between increasing SH westerlies and delayed warming of Antarctica [e.g., *Randel andWu*, 1999; *Polvani and Kushner*, 2003; *Gillet and Thompson*, 2003; *Thompson et al.*, 2005].

Reproduced with permission of the copyright owner. Further reproduction prohibited without permission.

4.2. Fundamental mechanism

In this paper the fundamental cause of the OC and its intensification during the austral winter to spring transition is explored. The explanation is found by connecting processes which are usually treated separately in the literature: the relationship between tropical convection and subtropical westerly jets, ozone transport by synoptic waves breaking on the jets, and ozone transport by stratospheric planetary waves. A key dynamical principle is that Southeast Asian monsoon tropical convective outflow exerts an order-one control over the distribution of extratropical column ozone by determining the location of subtropical westerly jets (Fig. 4.2). The distribution of convection and of 5-10 day outflow pulses modulate the location of subtropical high pressure systems in the upper troposphere – lower stratosphere (UTLS) over the Southern Indian Ocean (SIO). *Rogal et al.* [2009] focuses on the relationship between SIO highs and synoptic ozone maxima, which occur in the troughs immediately poleward and eastward of SIO anticyclones, with subsequent eastward dispersion of ozone in the westerly jet. Here we focus on the zonal extent of the Australian Subtropical Westerly Jet (ASWJ, Fig. 4.2) and its seasonal sharpening. It will be shown that the OC lies immediately poleward of the ASWJ, coinciding with warm temperatures and a poleward Rossby wave breaking (RWB) surf zone.

Nogues-Paegle and Zhen [1987] showed that Southeast Asian monsoon outflow during boreal summer supplies westerly zonal momentum to the ASWJ. Strengthening of the ASWJ occurs with bursts of deep convection over Southeast Asia and Indonesia. The coupling between the forcing region and the rotational wind response extends through the tropics into the winter hemisphere. When projected onto normal modes, convective bursts create westward flow in the UTLS as part of a Kelvin wave, then southward flow as part of a

Reproduced with permission of the copyright owner. Further reproduction prohibited without permission.

large inertia-gravity wave, then as short Rossby waves modulating the ASWJ, then as tall Rossby waves modulating the polar night jet (PNJ). This is consistent with the idea that tropical convection can modulate stratospheric jets via outflow in the UTLS and radiation of planetary waves [*Dickinson*, 1971].

Nogues-Paegle and Mo [1988] found that tropical convective divergence maximum for these events lies ~50° east of jet accelerations. The effects of latent heating maxima are noticed within 2-4 days in the SH subtropics, and are fully established by 6 days. Week to week variations in divergent outflow are intimately related to variations in convection [*Kiladis and Mo*, 1998; *Renwick and Revell*, 1999]. *Randel and Park* [2006] found a lag of about 5 days between monsoon convective maxima and maxima in the area of the Tibetan High. *Berberry et al.* [1992] concluded that the ASWJ and PNJ act as waveguides for disturbances emanating from the SIO.

The energetic tropical circulation is intrinsically zonally asymmetric, being composed of local monsoon circulations linked to the distribution of continents [*Bjerknes et al.*, 1933; *Krishnamurti et al.*, 1973; *Johnson*, 1989]. The contrast between the hot Asian land mass and cool Southern Indian Ocean (SIO) creates a unique configuration in the general circulation of the planet. During boreal summer most of the zonal mean meridional mass flow across the equator in the upper UTLS occurs over the Indian Ocean [*Newell et al.*, 1972]. This basic structure can be understood in terms of steady-state solutions to tropical tropospheric heating anomalies associated with convective centers over Southeast Asia and Indonesia [e.g., *Gill*, 1980; *Hendon and Hartmann*, 1982; *Rodwell and Hoskins*, 2001]. Near the equinoxes convection tends to be centered over Indonesia. During boreal summer the center of

Reproduced with permission of the copyright owner. Further reproduction prohibited without permission.

convection migrates northwestward toward the Himalayas, then back toward Indonesia during austral spring [*Liebmann and Hartmann*, 1982].

This shift from August to October 2000 is shown in Fig. 4.3. During August outgoing long wave radiation (OLR) is low throughout Southeast Asia and western tropical Pacific (Fig. 4.3a). This blue region indicates cold high clouds associated with deep convection. Its zonal extent during August is ~100° of longitude. Note also the regions of tropical convection over northern subtropical Africa and the Gulf of Panama in August. Convection migrates southward to Amazonia, Central Africa, and Indonesia in October (Fig. 4.3b). The zonal extent of the Indonesian convection in October is ~60° of longitude, a significant zonal contraction. It will be shown that the change in the shape of convection over Southeast Asia and Africa are directly related to changes in the position of two anticyclone centers that statistically compose the South Indian Ocean High (SIOH) system and to changes in the zonal extent of the ASWJ and the sharpness of the OC.

A case study during August 2000 serves to illustrate synoptic structures associated with the OC, including the distribution of Rossby wave breaking (RWB) for synoptic and planetary waves in the midlatitude lower stratosphere, and the interaction between the SIO high and stalled planetary wave ridge (section 4.4). An interhemispheric chemical transport pathway from the boreal summer lower stratosphere to the austral winter lower stratosphere is highlighted, which travels around the Tibetan High, across the equator, and around the SIOH system. During its journey through thousands of km of cumulonimbus tops, this air is overwhelmingly diluted by detrained tropical tropospheric air. A ten-year momentum budget at 150 hPa documents the causal relationship between convective outflow in the UTLS, the SIO highs and the ASWJ (section 4.5). The relationship between SIO highs and the stalling

Reproduced with permission of the copyright owner. Further reproduction prohibited without permission.

and amplification of ozone-rich planetary wave ridges is explored in section 6. Modulation of tropical / extratropical planetary wave relationships by the El Nino Southern Oscillation is described in *Hitchman and Rogal* [2009].

4.3. Data and analysis

Daily data from the European Centre for Medium Range Weather Forecasting (ECMWF) [*Hollingsworth et al.*, 1986; *Kallberg et al.*, 2005], National Center for Environmental Prediction (NCEP) [*Kalnay et al.*, 1996], and the United Kingdom Meteorological Office (UKMO) [*Swinbank and O'Neill*, 1994] were used to depict general circulation structures and statistics. Total Ozone Mapping Spectrometer (TOMS) column ozone, and3Dglobal ozone from the NASA Global Modeling and Analysis Office (GMAO) Goddard Earth Observing System-4 (GEOS-4) data [*Stajner et al.*, 2001; 2004; 2006] were used to describe ozone variability. The GEOS-4 data set was specially produced for the years 1998, 2000, and 2004 by assimilating meteorological

data and ozone from the Solar Backscatter Ultraviolet Instrument on a 2°x 2.5° grid. We have examined the behavior of the OC and the SH general circulation for each year during 1982-2004. The year 2000 is chosen for study since GEOS-4 data are available. The structures and their seasonal evolution for the year 2000 are quite representative. Monthly mean outgoing longwave radiation (OLR) plots were obtained from theNOAA ESRL Physical Sciences Division to show the distribution of convection. The Langley Research Center isentropic trajectory code [*Pierce and Fairlie*, 1993] was used to illustrate the cross-equatorial transport pathway.

Reproduced with permission of the copyright owner. Further reproduction prohibited without permission.

The statistics of Rossby wave breaking (RWB) are useful as an indicator of irreversible transport. Montgomery streamfunction (M) and potential vorticity (PV) were calculated and interpolated to isentropic levels spaced 10-50 K apart on a 2.5°x 5° grid [*Andrews et al.*, 1987; 1 PVU =10^{-6} $Km^2kg^{-1}s^{-1}$]. On potential temperature surfaces the geostrophic wind flows parallel to $M = C_pT + \phi$, where T is temperature and Φ is geopotential. An RWB event occurs when the meridional gradient of PV, P_y, is negative. *Hitchman and Huesmann* [2007] presented seasonal climatological distributions of P_y, RWB frequency υ in reversals per 100 days, the strength, S, of PV gradient reversal, and other metrics. *Hitchman and Huesmann* [2009] discuss the effects of the stratospheric QBO on the structure of jets and RWB. Here seasonal RWB statistics using NCEP data for the period 1979 - 2005 are shown for June-July-August (JJA).

In order to emphasize the continuity of wave activity from a UTLS SIO high to a stratospheric ridge it is useful to multiply eddy geopotential height, Z, by $p^{-1/2}$, where p is the pressure level (cf. Fig. 4.15). This makes it easier to compare the magnitude of wave activity at different altitudes and emphasizes the upward influence of a UTLS SIOH. This scaling emerges from linear Rossby wave theory and conservation of wave activity, $A \propto pq'^2 \propto \rho Z'^2$, where ρ is atmospheric density, and q' is quasi-geostrophic potential vorticity. Since $p \propto q \propto \exp(-z/H)$, $Z' \propto \exp(z/2H)$, and for a constant distribution of A, Z'/p'^2 would be constant with altitude.

Reproduced with permission of the copyright owner. Further reproduction prohibited without permission.

4.4. Case Study of August 2000

Figures 4.4 and 4.5 show ECMWF 150 hPa wind and geopotential height, 150 hPa eddy geopotential height, 150 hPa zonal wind, 100 hPa temperature, and TOMS column ozone averaged during JAS 2000. Anticyclonic flow around the TH crosses Indonesia, and curves clockwise around the SIOH into the entrance of the ASWJ (Figs. 4.4a, b). This seasonal flowstructure may be seen in *Krishnamurti et al.* [1973], *Vincent and Silva Dias* [1998] and *Annamalai et al.* [1999]. The eddy height field in Fig. 4b emphasizes the power of tropical heating and its influence on the extratropical planetary wave pattern in the UTLS, starting with the SIOH [*Dickinson*, 1971; *Sardeshmukh and Hoskins*, 1979], the focal topic of section 4.7.

The strong southwestward current across Southeast Asian into the SIO at 150 hPa (Fig. 4.4a) flows amidst the tops of convective complexes for a distance of 5,000-10,000 km (Fig. 4.3). This flow pattern exerts a strong effect on the momentum distribution in the SH, notably the ASWJ (section 4.5).

Immediately poleward of the ASWJ (Fig. 4.5a) lies a region of warm air at 100 hPa (Fig. 4.5b), also shown by *Hurrell et al.* [1998], which is coincident with high column ozone in the OC (Fig. 4.5c). *Newman and Randel* [1988] document this climatological high spatial correlation between lower stratospheric temperature and column ozone for October 1979-1986. This strong correlation is the result of chronic poleward and downward Lagrangian circulation within synoptic waves modulating the jet [*Kida*, 1977; *Wallace*, 1978]. This Stokes drift results from the eddy amplitude maximum near the jet axis. Absorption of synoptic Rossby waves and inertia-gravity waves radiating into the lowest stratosphere from evolving tropospheric disturbances [*O'Sullivan and Dunkerton*, 1995] constitutes an easterly

Reproduced with permission of the copyright owner. Further reproduction prohibited without permission.

body force, which implies a poleward and downward flow [*Haynes et al.*, 1990]. High resolution observational studies with dropwinsondes [*Shapiro*, 1980] highlight upper level frontogenesis and a Sawyer-Eliassen circulation transporting stratospheric air poleward and downward around the jet and into the troposphere [*Keyser and Shapiro*, 1986]. *Hudson et al.* [2003] emphasize the subtropical westerly jets as separating a tropical regime with low column ozone from a midlatitude regime with high column ozone.

A comparison of Figs. 4.1 and 4.5 shows the striking spatial relationship between the OC and the ASWJ on its poleward flank, where the tropopause altitude is significantly lower. A schematic of this relationship is shown in Fig. 4.2, with transparent curved arrows indicating the poleward and downward transport by synoptic waves breaking on the ASWJ. It should be emphasized that the pathway of ozone from its production region in the subtropical stratosphere to the lowest stratosphere poleward of the ASWJ is long and complex, involving protracted poleward and downward spirals in the predominating westerlies [e.g., *Sato et al.*, 2009]. We now examine the RWB regime poleward of the ASWJ which includes upwardly-evanescent synoptic waves and upwardly-amplifying planetary waves equatorward of the polar night jet.

A 27 year seasonal climatological distribution of RWB statistics for JJA at 360 K (~150hPa) is shown in Fig. 4.6. PV gradient maxima highlight the ASWJ near 30°S and the base of the PNJ near 55°S. In conjunction with the planetary wave pattern seen in Fig. 4.4a, the PNJ is not purely zonally symmetric, but trends poleward and diminishes south of Australia. The ASWJ near 30°S begins over the SIO west of Australia and extends eastward toward Chile. Immediately poleward of the ASWJ is a synoptic wave surf zone. RWB is common (large circles) and moderately strong (green). The synoptic RWB regime near 45°S

Reproduced with permission of the copyright owner. Further reproduction prohibited without permission.

at 360 K coincides geographically with the distribution of column ozone (Figs. 4.1, 4.5c). This pattern is also strikingly similar to the pattern of stratosphere to troposphere flux in model diabatic heating calculations [*Olsen et al.*, 2004].

The vertical distribution of RWB during JJA is shown in Fig. 4.7, with v and S superimposed on zonal winds (Fig. 4.7a) and on P_y (Fig. 4.7b). The synoptic RWB surf zone poleward of the ASWJ blends seamlessly with the planetary RWB surf zone equatorward of the PNJ [*Hitchman and Huesmann*, 2007]. It occurs in the broad minimum in P_y from the PNJ near 60°S to the equator (Fig. 4.7b). Vertical propagation of EP fluxes in this waveguide was originally studied by *Randel et al.* [1987]. The vertical coherence of planetary wave phase in this regime is shown by *Hurrell et al.* [1998]. This surf zone has the potential for significant ozone transport, involving interaction between upwardly evanescent synoptic waves and travelling planetary waves.

An example of the synoptic structures associated with ozone patterns is shown for August 24, 2000 in Figs. 4.8-4.9. At 150 hPa the subtropical westerly jet separates low column ozone in the tropics from higher amounts in the extratropics (Figs. 4.8a, b). Ozone is concentrated in synoptic troughs, with the most prominent concentration in the trough just poleward of the outflow pulse, near 50°S, 90°E (Fig. 4.8b). This relationship is explored more fully in *Rogal et al.* [2009].

A meridional section (Fig. 4.9a) shows a striking and characteristic pattern of subsidence into the subtropical troposphere. This deep region of concentrated ozone near 50°S lies in the stratospheric winter surf zone poleward of the ASWJ and equatorward of the PNJ (Fig. 4.7). A zonal section at 46°S (Fig. 4.9b) shows the transition in zonal scale of ozone variation across the UTLS, with ozone maximizing in the planetary wave ridges and in

Reproduced with permission of the copyright owner. Further reproduction prohibited without permission.

the synoptic scale troughs. The two "feeder highs" make ozone available for subsidence into the troughs in the UTLS, especially near 95°E. This relationship can also be observed near 160°W, 90°W, and 20°W (compare Figs. 4.8b and 4.9b).

The extratropical stratospheric wave structure will be explored more completely in section 4.7. It is important to distinguish between ozone transport pathways into the OC and the subtropical outflow pathways which cause the ASWJ by showing isentropic parcel trajectories which arrive in the ASWJ. A sample of trajectories at 350 K is shown for the case study of August 24, 2000 in Fig. 4.10. The ending locations are positioned from the ASWJ entrance successively eastward to eastern Australia. Each of the eight days is colored separately, with orange the oldest and black the youngest portions of the trajectories. Parcels arriving near the jet entrance at this time (Fig. 4.10a) come from the RWB mixing zone near Japan discovered by *Postel and Hitchman* [1999] and cross the equator southwestward. A 40 year climatology of radiosonde data at Singapore and Diego Garcia [*Yao*, 1994; not shown] document southwestward flow in the layer 10-17 km, 300 – 100 hPa, with the southward component exceeding 5 m/s near 14 km, 150 hPa during May-October. Parcels arriving farther east in the ASWJ are a mixture of air in the cross-equatorial pathway and air coming from the west in the southern subtropics (Figs. 4.10b, c). Parcels appearing in the middle of the ASWJ at this time originated in the subtropical westerlies, making nearly two trips around the globe in 8 days (Fig. 4.10d). The trajectories in Figs. 4.10a-c pass through thousands of kilometers of cumulonimbus turrets and anvils (Fig. 4.3), which inject detrained tropical tropospheric air into this pathway. This explains why this pathway is not apparent in maps of ozone (Fig. 4.8b). It also accounts for how westerly angular momentum is supplied to the ASWJ by "cumulus friction" along this pathway [*Schneider and Lindzen* 1980].

Reproduced with permission of the copyright owner. Further reproduction prohibited without permission.

4.5. Momentum budget of the Australian Subtropical Westerly Jet

The zonal momentum equation in log-pressure coordinates on a sphere is

$$\frac{\partial u}{\partial t}+u\frac{\partial u}{\partial x}+v\frac{\partial u}{\partial y}+w\frac{\partial u}{\partial z}-fv+g\frac{\partial Z}{\partial x}=X \qquad (4.1),$$

where X is the body force due to surface work by nonconservative subgrid-scale processes, including turbulence and wave drag [*Andrews et al.* 1987]. For monthly averages, [ ], (1) may be written:

$$\frac{\delta[u]}{\delta t}+[u\frac{\partial u}{\partial x}]+[v\frac{\partial u}{\partial y}]+[w\frac{\partial u}{\partial z}]-f[v]+g[\frac{\partial Z}{\partial x}]=[X] \qquad (4.2)$$

An estimate of $[X]$ may be calculated as a residual of the terms on the left hand side of (2). The term $[u\frac{\partial u}{\partial x}]$ represents the spatial acceleration (jet entrance) and deceleration (jet exit) of the monthly mean jet. Neglecting transience and vertical advection, a dynamical explanation can be sought for jet acceleration by gathering other terms on the right hand side, and comparing the magnitudes of advection of absolute vorticity, height gradient, and subgrid scale processes:

$$[u\frac{\partial u}{\partial x}]\approx[(f-\frac{\partial u}{\partial y})v]-g[\frac{\partial Z}{\partial x}]+[X] \qquad (4.3)$$

Replacing the height gradient term with the geostrophic wind v_g, *Lau and Wallace* [1979] and *White* [1982] have shown that subtropical westerly jet entrances are the result of ageostrophic outflow from tropical convection in the approximate balance:

$$[u\frac{\partial u}{\partial x}]\approx f[(v-v_g)=f[v_a] \qquad (4.4)$$

Reproduced with permission of the copyright owner. Further reproduction prohibited without permission.

In this analysis we retain meridional advection of relative vorticity and calculate advection of absolute vorticity as in (4.3).

The ASWJ near 150 hPa is featured in 10-year averages of ECMWF data for August and October in Figs. 11a, b. During August the ASWJ entrance is located near 30°S, 70°E and the jet exit region is located near 140°W. The broad tropical easterly flow equatorward of the TH transitions to westerly flow near 30°S, with $\frac{\partial u}{\partial y} \sim$ -70 m/s from 30°S to the equator, implying fairly neutral inertial stability. In October the ASWJ maximum is more concentrated zonally over Western Australia (Fig. 4.11b).

The corresponding UTLS meridional outflow into the SIO is shown in Figs. 4.11c,d. Southward flow near 14km reaches -9 m/s near Diego Garcia in August (not shown), with the zero meridional wind line near 30°S in the western and central SIO (Fig. 4.11c). This southward meridional jet ends near the entrance to the ASWJ to the southeast of Madagascar (Figs. 4.11a, c). The zonal extent of southward flow is more confined in October (Fig. 4.11d) and the ASWJ is noticeably shorter in longitude (Fig. 4.11a, b). This is related to the seasonal contraction of convection as shown in OLR in Fig. 4.3.

The ten year mean ECWMF distribution of 150 hPa Z is shown for August and October in Figs. 4.11e,f. In daily synoptic maps UTLS anticyclones over the SIO can occur near South Africa, over the SIO, or over Australia. In August the statistical mean produces a broad SIOH (Fig. 4.11e). In October the statistical mean shows a more distinct separation of a South African High (SAH) and an Australian High (AH), which is related to strengthening convection over Africa and zonal contraction over Indonesia (Fig. 4.3b). These anticyclonic systems are collectively referred to here as the SIOH system. The SIOH system resides at the

Reproduced with permission of the copyright owner. Further reproduction prohibited without permission.

poleward edge of the monsoon outflow and represents the boundary between subtropical, nearly inertially neutral flow, and midlatitude quasi-geostrophic flow. The AH component lies just to the northwest of the ASWJ entrance in both August and October.

Terms in the 10-year zonal momentum budgets for August and October at 150 hPa are shown in Fig. 4.12. From top to bottom, panels show meridional advection of angular momentum $[(f-\frac{\partial u}{\partial y})v]$ (the first term on the rhs of (4.3)), ageostrophic meridional advection of angular momentum (the first two terms rhs of (4.3)), zonal acceleration $[u\frac{\partial u}{\partial x}]$ (lhs of (3)), and the residual term $[X]$(last term in (3)).

Outflow from Indonesian convection in the UTLS exports a large amount of westerly angular momentum and creates a large region of westerly acceleration in the SIO north of 30°S (Figs. 4.12a, b). By including the height gradient term (Figs. 4.12c, d), a better agreement is found with the pattern of zonal acceleration (Figs. 4.12e, f) between Madagascar and Australia near the ASWJ entrance. This tends to confirm diagnostic relationship (4.4) and underscores the fundamental role of tropical convective outflow in supplying angular momentum to the ASWJ. There is also general agreement in the jet exit region in the Eastern Pacific, although not as good.

The residual term (Figs. 4.12g, h) exhibits interesting structure, including notable westerly accelerations over Indonesia, the higher latitude SIO and near South America, with easterly accelerations over South Africa and near the Date Line. Some of this is due to the monthly shift in wind patterns and some is due to subgrid-scale wave drag, including gravity waves and convection.

Reproduced with permission of the copyright owner. Further reproduction prohibited without permission.

4.6. Connection between SIO highs and extratropical stratosphere

Quintanar and Mechoso [1995a] found that the quasi-stationary wave one in dynamical fields in the UTLS is linked to EP fluxes from the tropical Indian Ocean. *Quintanar and Mechoso* [1995b] carried out general circulation experiments with Antarctic topography and concluded that the subtropical wave one pattern is not related to Antarctica. *Renwick and Revell* [1999] showed that blocking events in the Southeast Pacific are associated with synoptic Rossby wave trains emanating from the Australian sector and linked them to anomalous convection events in the tropics. *Newman and Nash* [2005] identified subtropical forcing as a key ingredient in the unusual sudden warming that occurred during September 2002.

Mechoso et al. [1988] and *Charlton et al.* [2005] summarized the seasonal transition from southern winter to spring as follows. During September the polar vortex is often elongated, with a pair of anticyclones 180° apart, each at a different stage in their life cycle. They tend to form over the SIO, with a life cycle of growth and decay over about 10 days as they migrate eastward. In October the flow regime often changes to a quasi-stationary wave one anticyclone over the Pacific.

An example of the temporal coindicence between amplification of subtropical highs in the SIO UTLS and stalling and amplification of travelling planetary wave ridges in the extratropical lower stratosphere is shown for our case month of August 2000 in Fig. 4.13. Near 360 K (~15 km) at 17°S, quasi-weekly variability of the AH may be seen (Fig. 13a). Near 700 K (~26 km) at 46°S planetary scale ridges and troughs may be seen travelling eastward at 14 ms^{-1} (Fig. 4.13b). The wave two component has zonal wavelength ~14,000 km and period ~10 days, characteristic behavior of the southern winter [*Leovy and Webster*,

Reproduced with permission of the copyright owner. Further reproduction prohibited without permission.

1976; *Mechoso and Hartmann*, 1982; *Randel*, 1987]. These finite amplitude regional ridges and troughs project onto zonal wavenumbers 1-2, with wave two dominating during August 2000.

During August 8-11 a subtropical monsoon high near 150°E (Fig. 4.13a) amplified while the planetary ridge in the extratropical stratosphere (Fig. 4.13b) stalled near 100°W. During August 12-19 a monsoon high near 110°E amplified (Fig. 4.13a) while the ridge near 0°E stalled. During August 20-28 the AH amplified repeatedly as the ridge near 80°E stalled and amplified, with M' exceeding 6000 m^2s^{-2} at 700 K on August 24 (Fig. 4.13b). This planetary wave two remained stalled for over a week. Many similar sequences exist in the years examined (1990-2004), consistent with the high correlation between the AH and OC maximum. During 2002 travelling wave two stalled in early and in mid-September [*Harnik et al.*, 2005, their Fig. 8]. *Lahoz et al.* [2006] discussed flow evolution during southern spring 2003, with a notable feature being stalling of a planetary wave ridge near Australia. They also described a "wineglass" shape to the amplitude of wave structures, with a minimum in the lower stratosphere.

The horizontal and vertical structure of the SIOH and wave two ridge on August 24 2000 is shown in Fig. 4.14. The AH just west of Australia at 360 K (Fig. 4.14c) tilts westward and poleward with height to 525 K (Fig. 4.14b), consistent with linear Rossby wave theory. The travelling wave two ridge at 525 and 800 K is greatly amplified in this quadrant (Figs. 4.14b, a). The ridge in Fig. 4.14b is accompanied by poleward flow over the South Atlantic, then eastward flow along its poleward side near 47°S (cf. Fig. 4.13b). Since ozone concentration maximizes in the lower stratosphere this pattern makes ozone available

Reproduced with permission of the copyright owner. Further reproduction prohibited without permission.

to synoptic troughs on the poleward and downstream end of the ridge just southwest of Australia (Fig. 4.14c).

This suggests an ozone transport pathway out of the tropical Atlantic, around a stalled wave 2 ridge near Australia, and into synoptic troughs preferentially in this longitude band. Previous studies have found a preferred pathway for ozone and volcanic aerosol out of the tropical stratosphere into the SH in the Atlantic sector [*Leovy et al.*, 1985; *Trepte et al.*, 1993; *Randel et al.*, 1993; *Hitchman et al.*, 1994; *Knox and Harvey*, 2005]. The spatial relationship between ozone and the Aleutian High during the northern winter is very similar, with maximum values on the poleward side of the ridge [*Harvey and Hitchman*, 1996]. Moreover, the source of air for the Aleutian High is also commonly over the tropical Atlantic [*Leovy et al.*, 1985; *Lahoz et al.*, 1994; *Harvey et al.*, 1999]. Extratropical anticyclones have tropical air mass characteristics, with enhanced ozone and small absolute vorticity. The strong correlation between high ozone and anticyclones in the stratosphere is documented in *Harvey et al.* [2004]. The description of the year 2003 by *Lahoz et al.* [2006] also supports this preference for high ozone on the poleward side of anticyclones.

A longitude-altitude section of Z' at 22°S on August 24, 2000 is shown in Fig. 4.15. At this latitude the SIOH and wave two ridge appear to be continuous with each other. The amplitude of the upper stratospheric ridge near 45°E is much larger than the one near 140°W (Fig. 4.15a). In panel b height anomalies were scaled by $p^{-1/2}$ to compare Rossby wave activity magnitudes across altitude. This indicates a continuous anticyclone with wave activity diminishing upward and westward from the SIOH. Progressing from the subtropics to the extratropics, the AH gradually fades as the wave two ridge gradually grows in

Reproduced with permission of the copyright owner. Further reproduction prohibited without permission.

amplitude (Fig. 4.14). Relative to 22°S (Fig. 4.15a), at 47°S (Figs. 4.13b, 4.14a) the ridge near 100°W is more substantial but the ridge near 60°E dominates at all latitudes.

The mean geopotential height anomalies for JAS 2000 exhibit a connection between the SIOH in the tropical UTLS (Fig. 4.4b) and a barotropic anticyclone south of Australia in the winter stratosphere(Fig. 4.16). At 100 hPa a pair of anticyclones is seen westward and poleward of Indonesian convection, the Tibetan High and the SIOH. The SIOH extends diagonally south westward from New Guinea to South Africa (Fig. 4.16c). The southward flow field in Fig. 4.4a exhibits counter-clockwise curvature centered near the axis of maximum heights. The maximum in column ozone (45°S, 110°E; Fig. 4.5c) lies immediately poleward and downstream of this anticyclonic anomaly. Poleward and downstream of the SIOH lies a trough, then a long ridge near 60°S (Fig. 4.4b). This pattern is consistent with Rossby wave energy radiating from the tropics [*Sardeshmukh and Hoskins*, 1988].

Fig. 4.7a shows that from 10°S westerly winds increase poleward into the winter stratosphere, but easterlies occupy the middle and upper summer stratosphere. Therefore, according to the Charney-Drazin criterion, Rossby wave energy associated with quasi-stationary monsoon anticyclones in the subtropical UTLS may propagate readily from the tropics into winter stratospheric westerlies, but critical surfaces would prevent wave activity from propagating into summer stratospheric easterlies. This hemispheric differential filtering begins to be seen at 50 hPa (Fig. 4.16b). The TH does not penetrate very far into the easterlies, but the SIOH and extratropical ridge in the winter westerlies are prominent and have merged into one elongated ridge. Note the upward amplification of the ridge south of Australia, while that near South America shrinks with altitude. At 10 hPa (Fig. 4.16a) the merged anticyclone extends from the South Pole to Australia and 30°E to 150°W. This

Reproduced with permission of the copyright owner. Further reproduction prohibited without permission.

position is similar to the stalled ridges observed by *Mechoso et al.* [1988]. The Charney-Drazin criterion also holds that strong westerly winds select for longer zonal scales. An upward transition to a wave one pattern in the strong PNJ (Fig. 4.7a) is seen in Fig. 4.16. Considering eddy geostrophic flow around the anticyclonic anomalies in Fig. 4.16, at 50 hPa and 10 hPa flow from the subtropical South Atlantic makes its way around the poleward side of the high. This structure can contribute to the seasonal transport of ozone out of the sunlit tropics into the poleward side of the ridge (cf. Figs. 4.9b, 4.14b), ultimately becoming available for convergence into a synoptic wave trough (Figs. 4.9b, 4.14c).

4.7. Conclusions

During austral winter and spring monthly mean column ozone near 40-60°S exhibits a zonally asymmetric maximum centered near Australia, the Ozone Croissant, which extends from the Southern Indian Ocean to the Eastern Pacific and amplifies from August to October. Deep convection over Southeast Asia and Indonesia during boreal summer drives a broad southwestward current in the upper troposphere and lower stratosphere across the equator deep into the SIO. Lagrangian trajectories and a detailed momentum budget confirm that this outflow leads to the entrance of the Australian subtropical westerly jet (ASWJ). The OC lies immediately poleward of the ASWJ and is spatially coincident with warm temperatures and the poleward Rossby wave breaking surf zone. This is consistent with vigorous poleward-downward ozone transport by Rossby and gravity waves in the jet.

An interhemispheric transport pathway from the northern lower stratosphere to the southern lower stratosphere is identified, which travels around the Tibetan High, across the equator, and around the SIO High. It crosses thousands of km of chronic deep convection,

Reproduced with permission of the copyright owner. Further reproduction prohibited without permission.

where detrainment overwhelmingly dilutes the air in this current with tropical tropospheric air. The nearly-inertially neutral southward flow into the SIO helps to create an adverse height gradient, the southwest-northeast tilting SIO High.

Sharpening of the zonal ozone asymmetry occurs from austral winter to spring, as tropical convection shifts from a broad region across Southeast Asia to a smaller region over Indonesia. In addition, from August to October increased travelling planetary wave activity transports more ozone poleward and downward into the lower stratosphere. A significant enhancement of ozone in the Australian sector occurs through frequent stalling of travelling planetary wave ridges, with co-amplification and merging with the SIO High. This structure is seen in the late winter mean height field. A case study from August 2000 illustrates how planetary wave ridges provide a rich source of ozone for descent into synoptic troughs in the OC. This study supports the idea that Rossby wave activity associated with subtropical monsoon anticyclones can propagate through weak westerlies and influence the extratropical stratosphere.

In summary, it has been shown that: 1) The longitudinal configuration of monsoon outflow determines the positions of anticyclones in the SIO (the SIOH system) and the longitudinal distribution of the Australian Subtropical Westerly Jet (ASWJ). 2) The OC lies immediately poleward of the ASWJ. 3) Poleward and downward ozone transport by synoptic Rossby waves is most vigorous in the longitude band of the ASWJ / OC. 4) Ozone-rich travelling planetary wave ridges often stall in the Australian sector, making more ozone available to the OC. 5) Co-amplification of the SIOH and stalled planetary wave ridge provides an important dynamical conduit for the effect of tropical convection on the winter SH stratospheric circulation.

Reproduced with permission of the copyright owner. Further reproduction prohibited without permission.

This connection between the geographical distribution of ozone and Asian monsoon outflow illustrates that Asian summer monsoon variability can directly affect the major features of the ozone distribution in the southern hemisphere.

Reproduced with permission of the copyright owner. Further reproduction prohibited without permission.

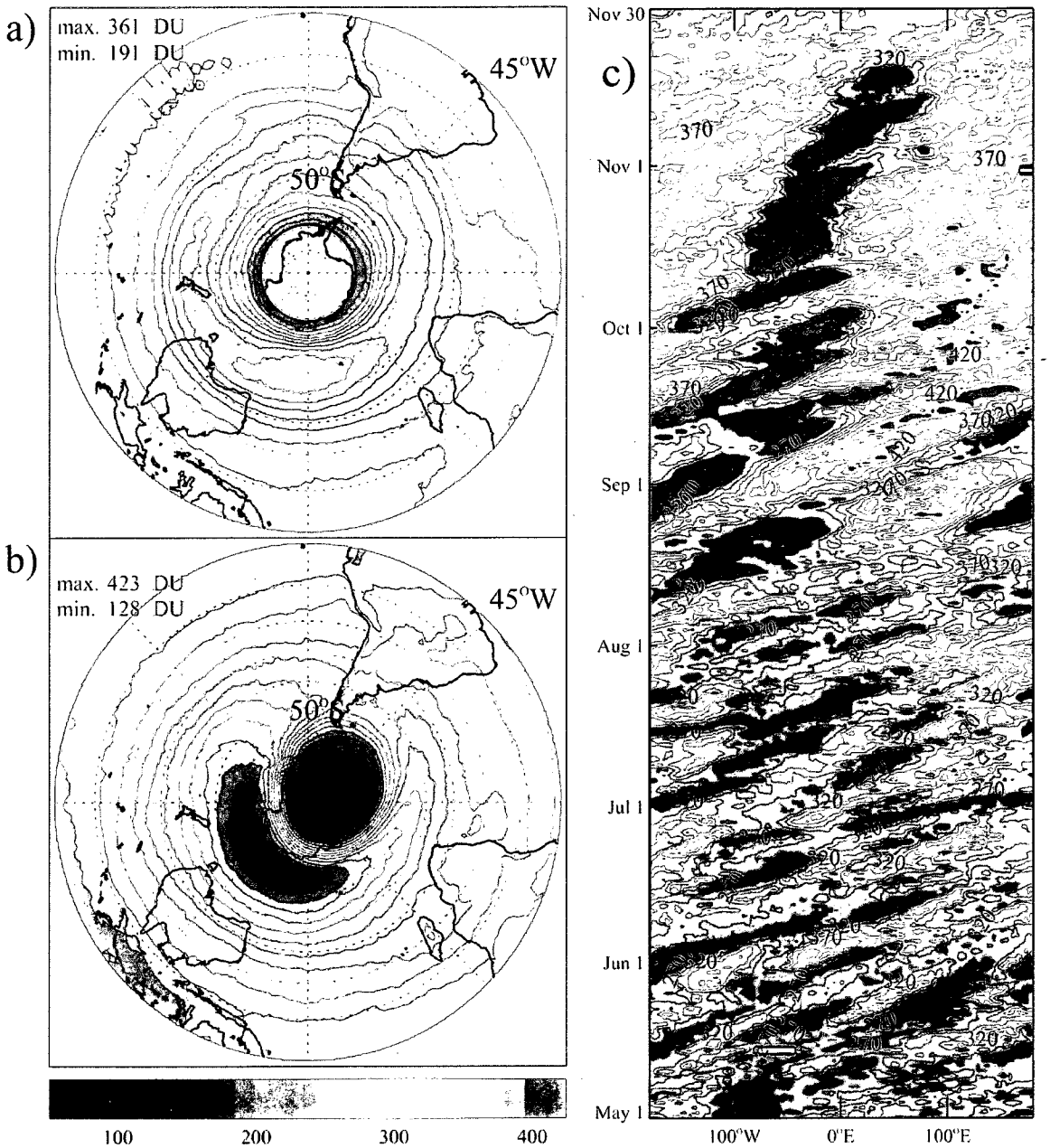

Figure 4.1. Monthly mean column ozone from the Total Ozone Mapping Spectrometer (TOMS) for a) August and b) October 2000, contour interval 15 DU, and c) longitude-time section of column ozone at 55°S during May 1 – November 30, 2000, contour interval 25 DU.

Reproduced with permission of the copyright owner. Further reproduction prohibited without permission.

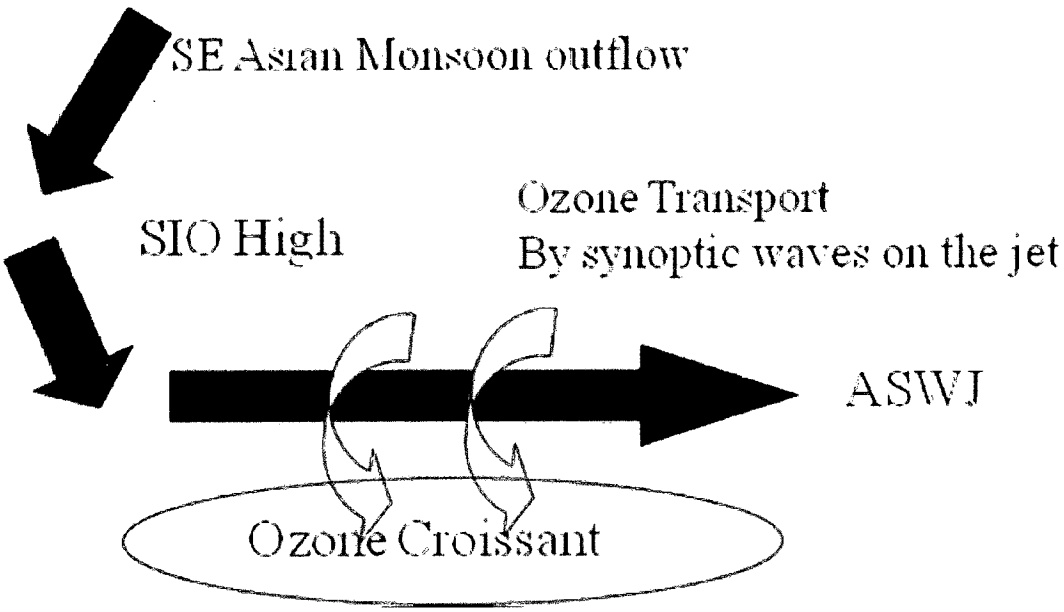

Figure 4.2. Idealized sketch of the relationship between outflow from Asian tropical convection in the UTLS, the SIO anticyclone system, the Australian Subtropical Westerly Jet, and the column ozone maximum poleward of the jet.

Reproduced with permission of the copyright owner. Further reproduction prohibited without permission.

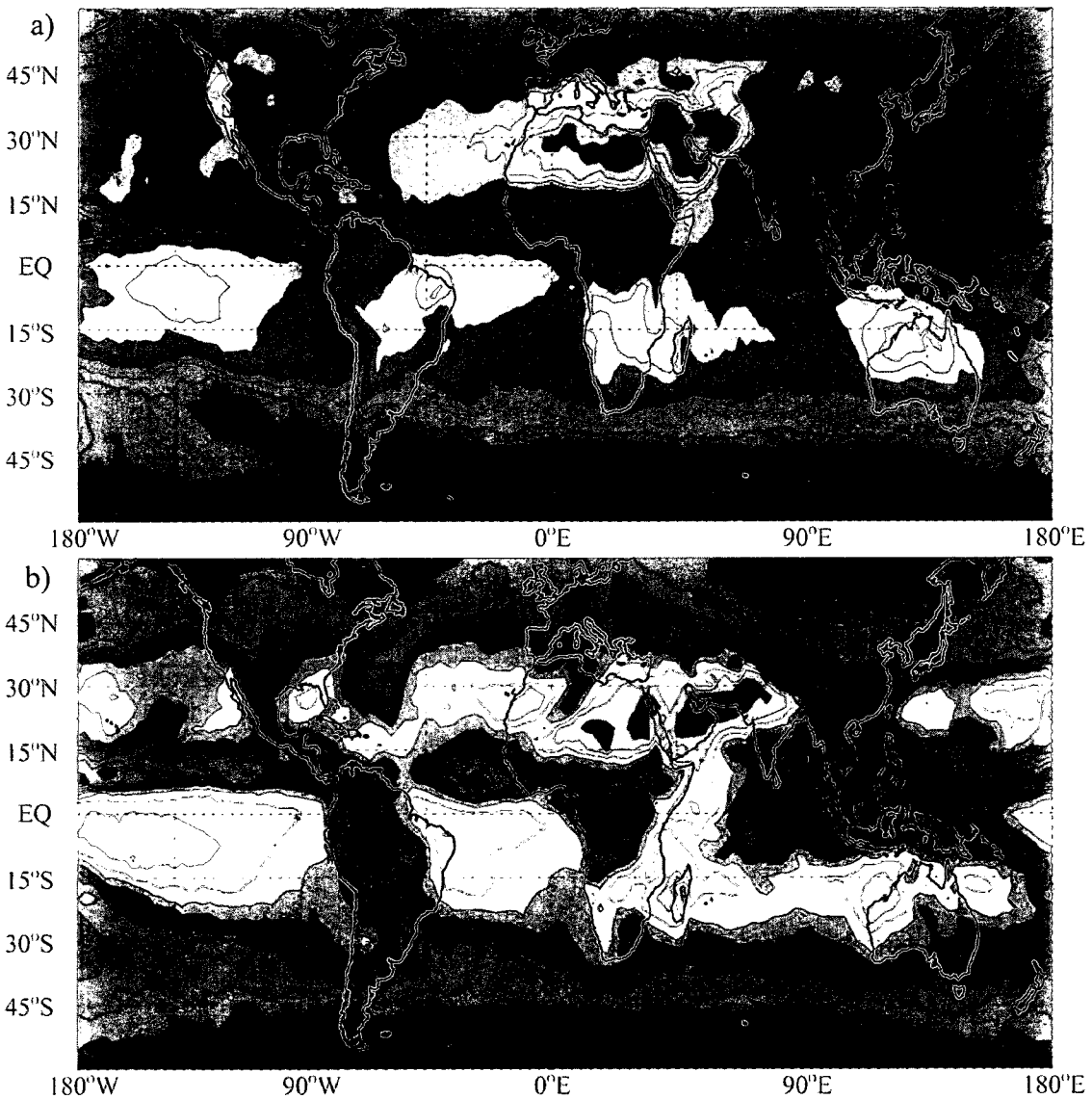

Figure 4.3. Monthly mean outgoing longwave radiation, contour interval 10 W m^{-2}, during a) August, range 0-160 W m^{-2}, and b) October 2000, range 20-170 W m^{-2}. Values were obtained from the NOAA Earth System Research Laboratory. Arrows denote breadth of deep convection near Southeast Asia.

Reproduced with permission of the copyright owner. Further reproduction prohibited without permission.

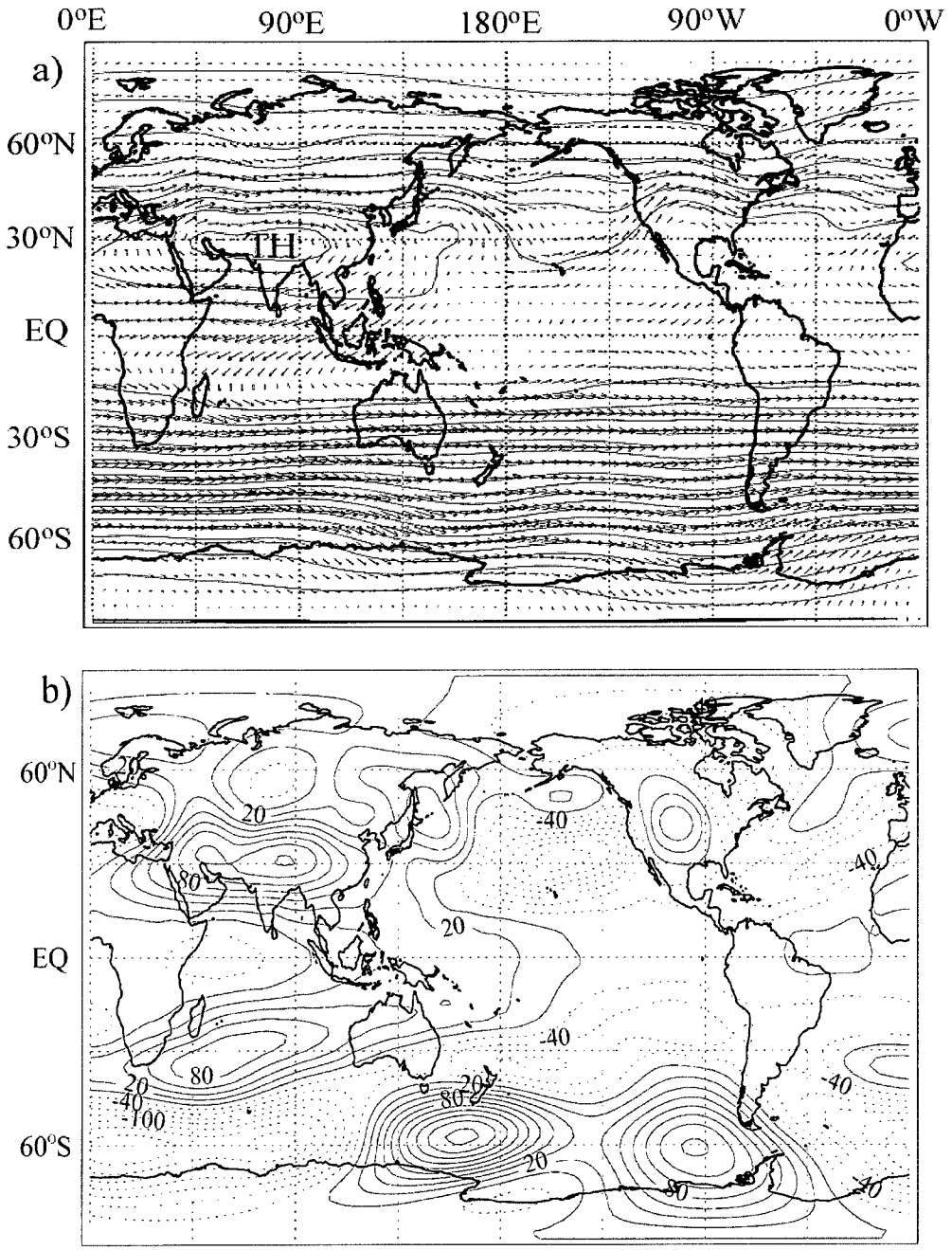

Figure 4.4. ECMWF JAS 2000 average 150 hPa a) geopotential height, contour interval 100 m, and wind vectors, maximum length 50 m/s, and b) eddy geopotential height, contour interval 20 m.

Reproduced with permission of the copyright owner. Further reproduction prohibited without permission.

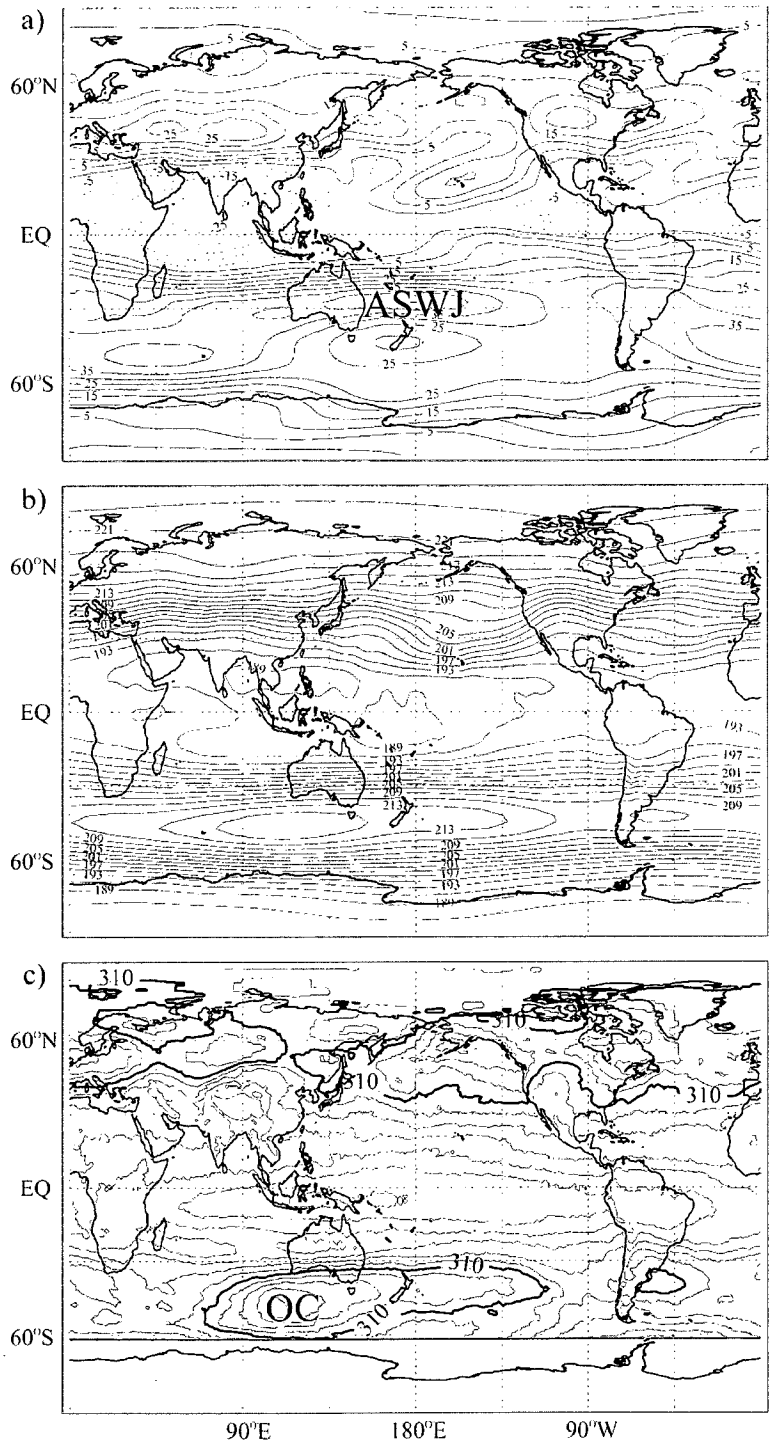

Figure 4.5. ECMWF JAS 2000 average a) 150 hPa zonal wind speed, contour interval 5 m/s, and b) 100 hPa temperature, contour interval 2 K, with c) TOMS column ozone, contour interval 10 DU, with the 310 DU contour emphasized to show the SH ozone croissant.

Reproduced with permission of the copyright owner. Further reproduction prohibited without permission.

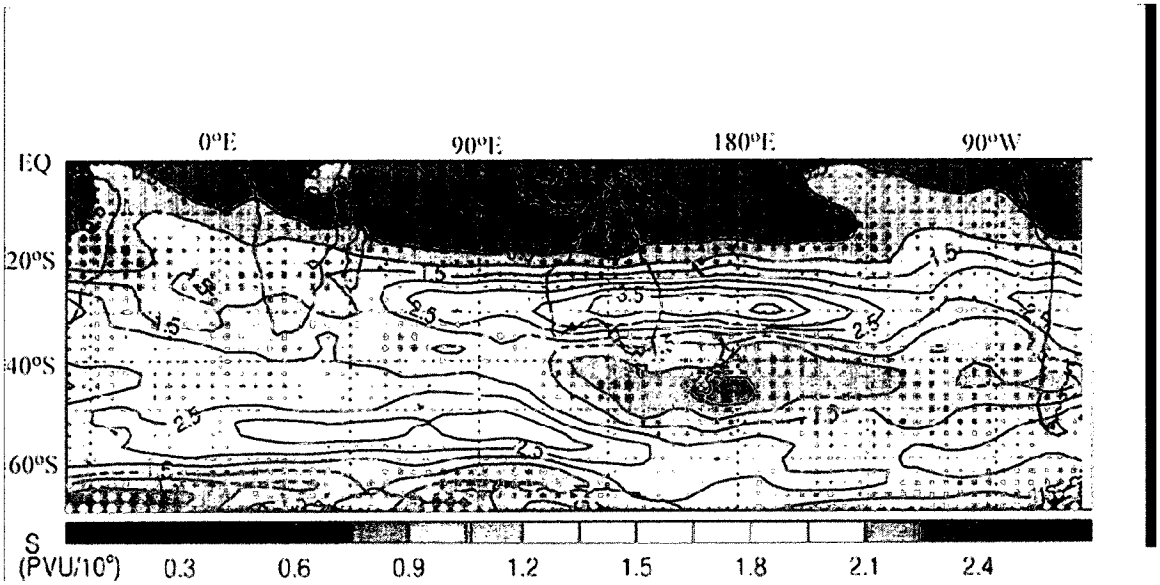

Figure 4.6. NCEP 360 K JJA average PV gradient (contour interval 0.5 PVU per 10° latitude), reversal frequency (circle size, maximum 35 reversals per 100 days), and reversal strength (colorbar).

Reproduced with permission of the copyright owner. Further reproduction prohibited without permission.

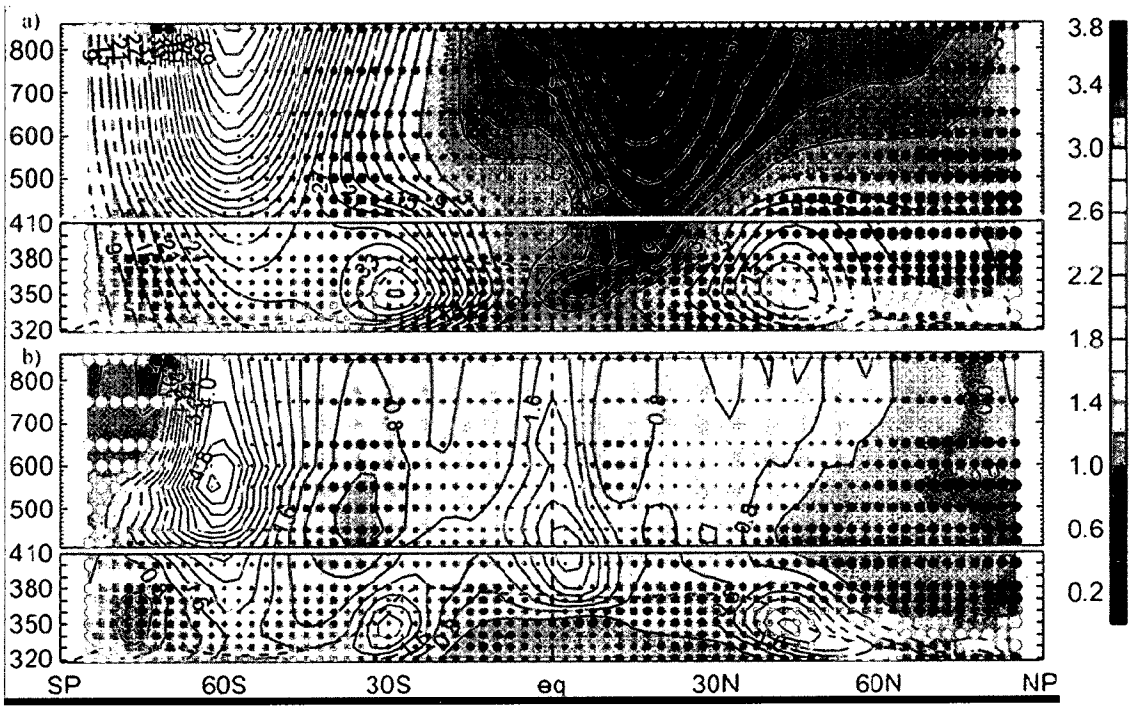

Figure 4.7. NCEP JJA zonal mean a) zonal wind, contour interval 3 m s^{-1}, and b) PV gradient normalized by the global mean at each level, contour interval 0.3, with PV gradient reversal frequency (circle size, maximum 35 per 100 days) and reversal strength (color bar).

Reproduced with permission of the copyright owner. Further reproduction prohibited without permission.

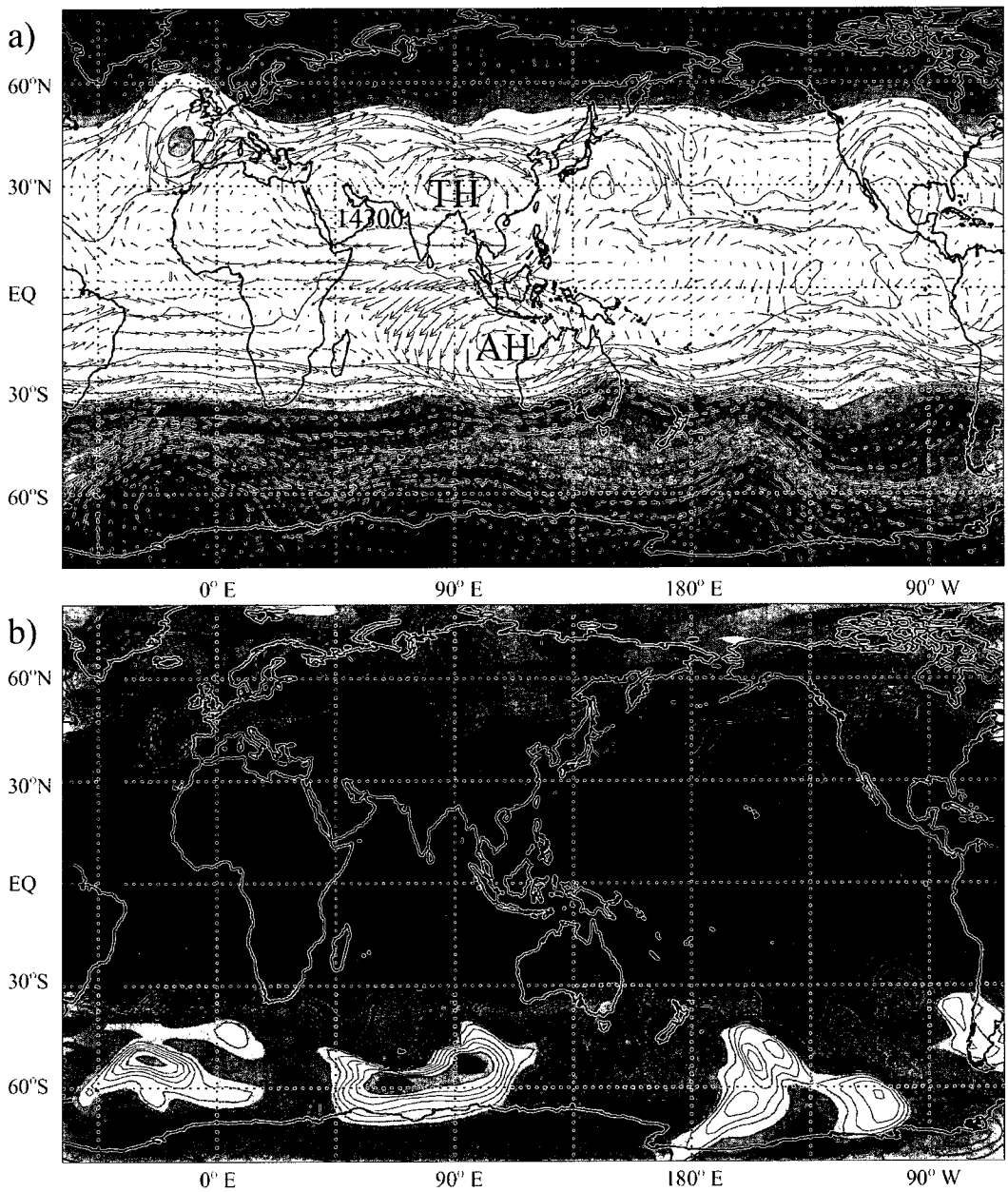

Figure 4.8. Sections through the ozone transport case study at 1200 UT on 24 August 2000 of a) ECMWF 150 hPa geopotential height, contour interval 100 m, and wind vectors (reaching 40m/s just northwest of the Australian High) and b) 150 hPa GMAO ozone mixing ratio, contour interval 50 ppbv.

Reproduced with permission of the copyright owner. Further reproduction prohibited without permission.

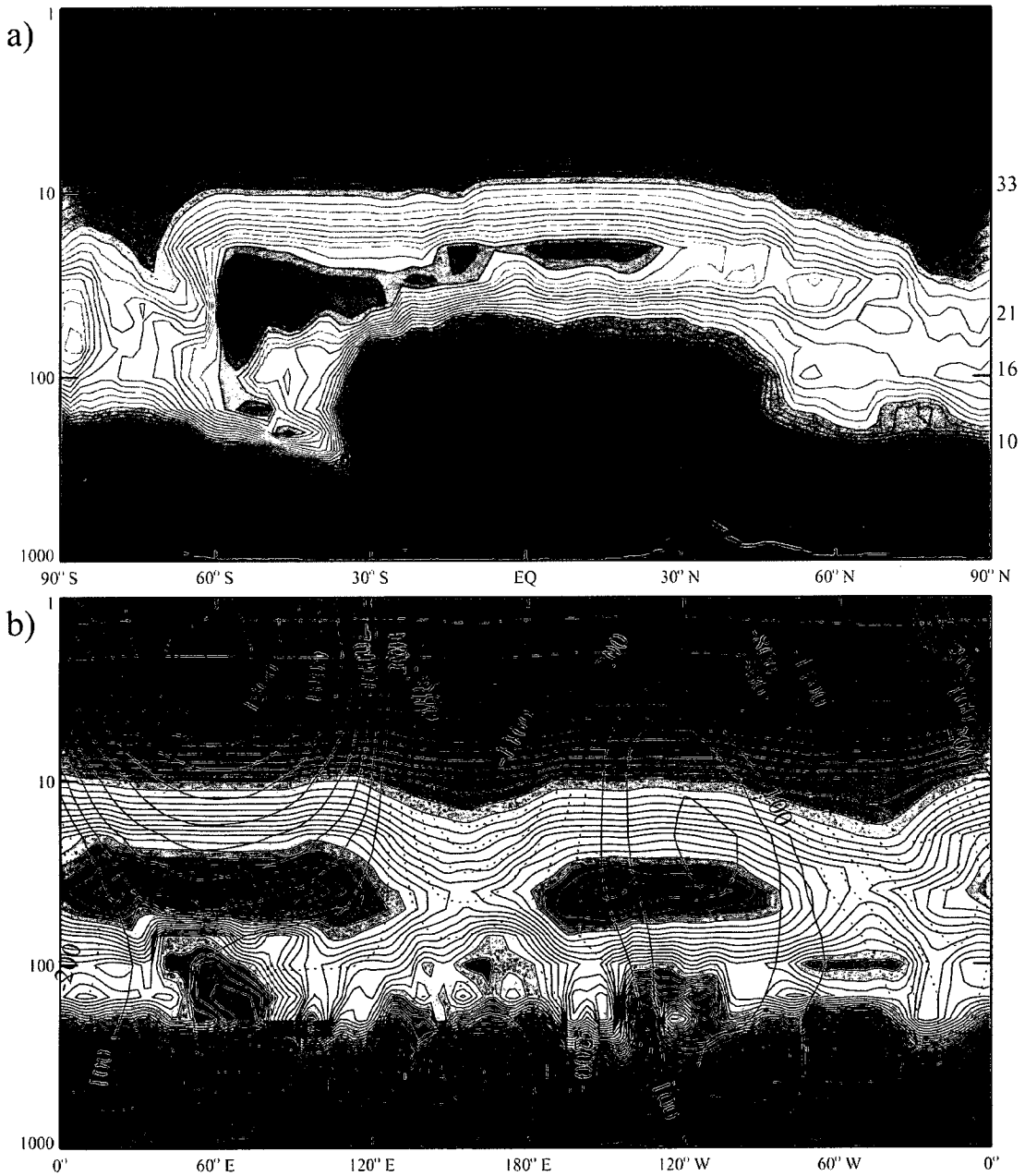

Figure 4.9. Sections through the ozone transport event at 1200 UT on 24 August 2000: a) GMAO ozone concentration at 95°E, contour interval 1.5 x 10^{18} molecules m^{-3}, and b) eddy geopotential height, contour interval 150 m, and GMAO ozone concentration at 47°S, contour interval 1.5 x 10^{18} molecules m^{-3}, with ozone highlighted in color. The approximate altitude in km is shown at right in panel a).

Reproduced with permission of the copyright owner. Further reproduction prohibited without permission.

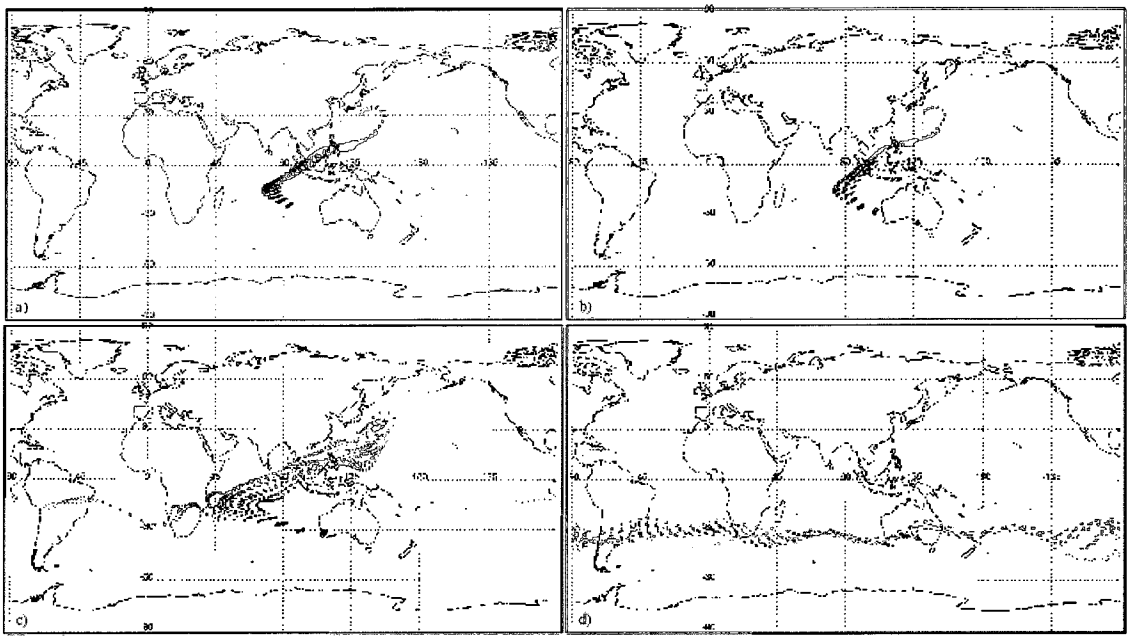

Figure 4.10. Eight day back-trajectories at 350 K ending on 0000 UT 24 August 2000 at 25°S and longitudes a) 100°E, b) 120°E, c) 130°E, and d) 140°E, using twice-daily gridded ECMWF data. Locations are plotted every six hours, with color changing from black (less than one day prior to arrival time) to purple (2 days), dark blue (3 days), light blue (4 days), dark green (5 days), light green (6 days), yellow (7 days), and orange (8 days prior).

Reproduced with permission of the copyright owner. Further reproduction prohibited without permission.

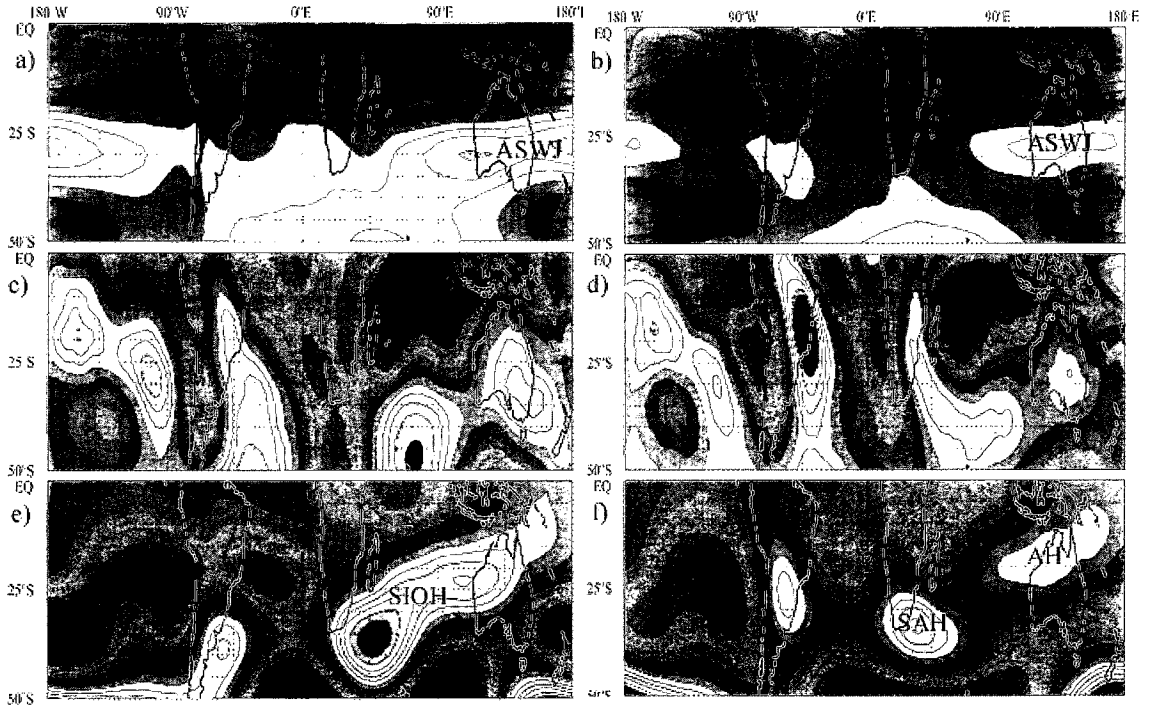

Figure 4.11. ECMWF 10 year average (1995-2004) 150 hPa a) and b) zonal wind (-30 to 50 m/s every 5 m/s), c) and d) meridional wind (-12 to 8 m/s every 1 m/s), and e) and f) geopotential height anomaly (-1400 to 1900 m every 100 m). Note the zonal contraction of the ASWJ from August (left) to October (right) and the statistical separation of the SIOH into the SAH and AH.

Reproduced with permission of the copyright owner. Further reproduction prohibited without permission.

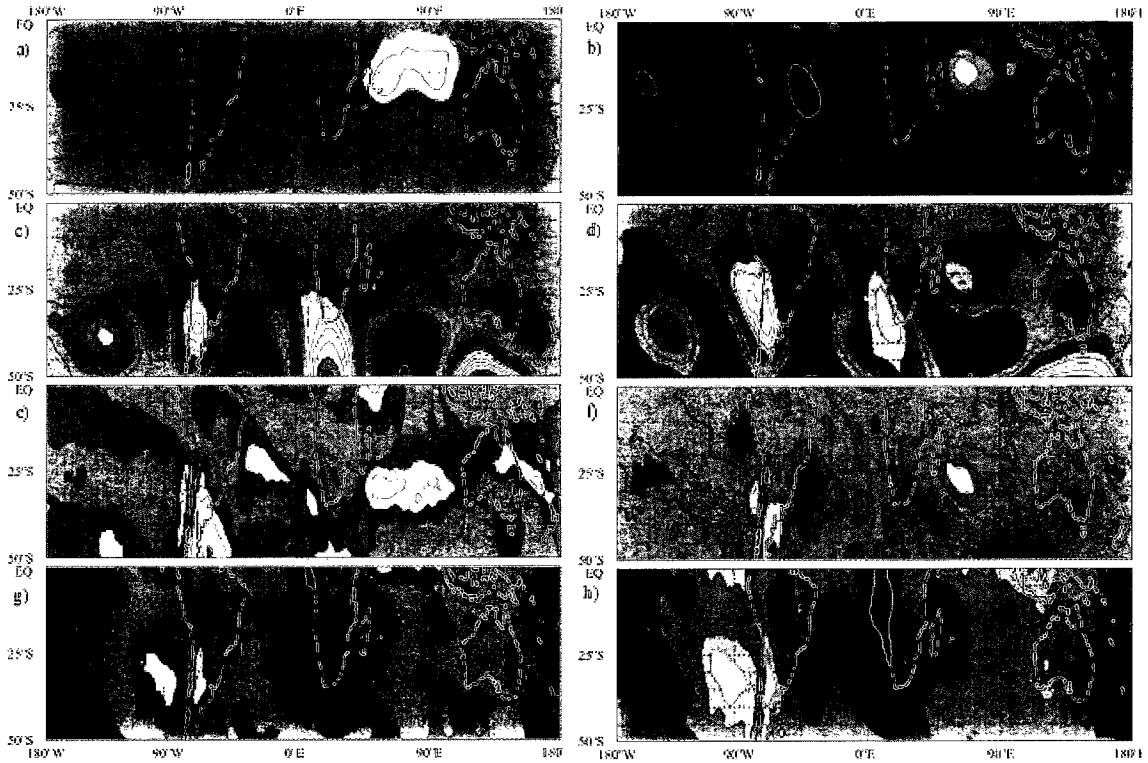

Figure 4.12. ECMWF 10 year average (1995-2004) 150 hPa terms in the zonal momentum budget for August (left) and October (right): a) and b) meridional advection of absolute vorticity (-1.0 to 1.1 every 0.1), c) and d) Coriolis torque on ageostrophic meridional flow (-1.6 to 1.6 every 0.2), e) and f) zonal wind advection (-1.3 to 1.0 every 0.1), and g) and h) residual term (-1.0 to 1.0 every 0.1), units in 10^{-3} m s^{-2} or ~100 m s^{-1} day^{-1}.

Reproduced with permission of the copyright owner. Further reproduction prohibited without permission.

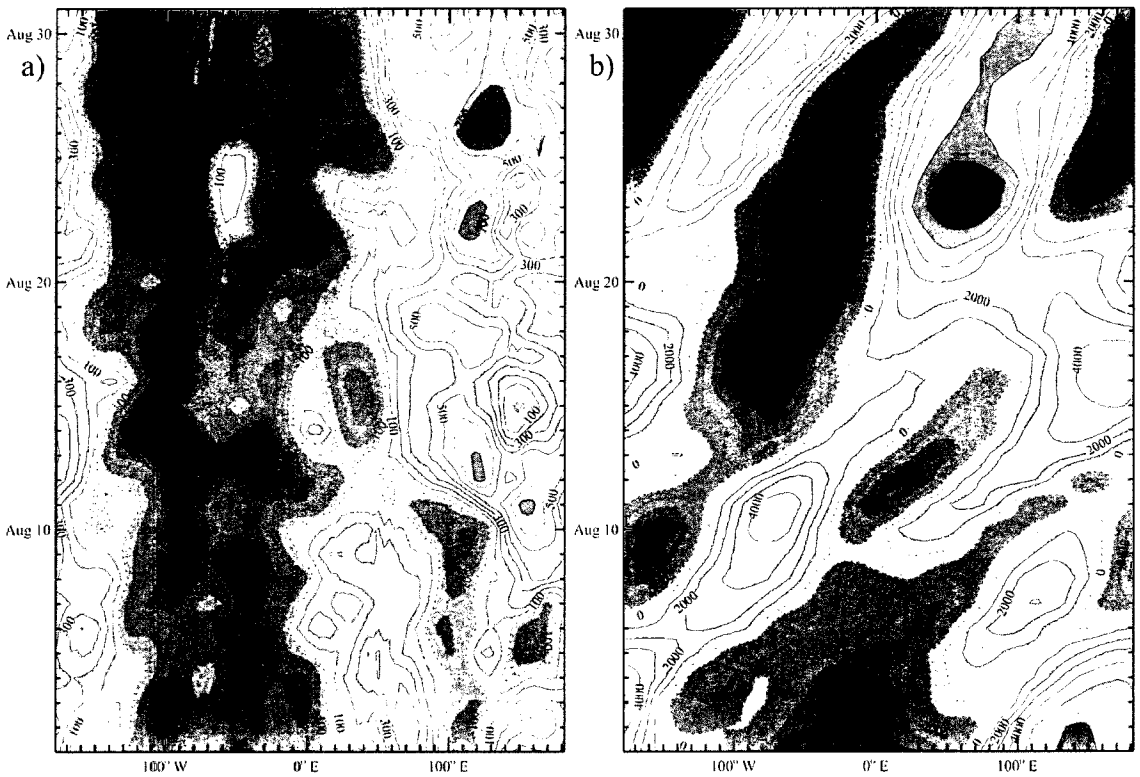

Figure 4.13. Longitude-time sections of UKMO eddy Montgomery streamfunction during August 1-31, 2000 at a) 16°S, 350 K, contour interval 100 m^2 s^{-2} and b) 46°S, 700 K, contour interval 1000 m2 s^{-2}.

Reproduced with permission of the copyright owner. Further reproduction prohibited without permission.

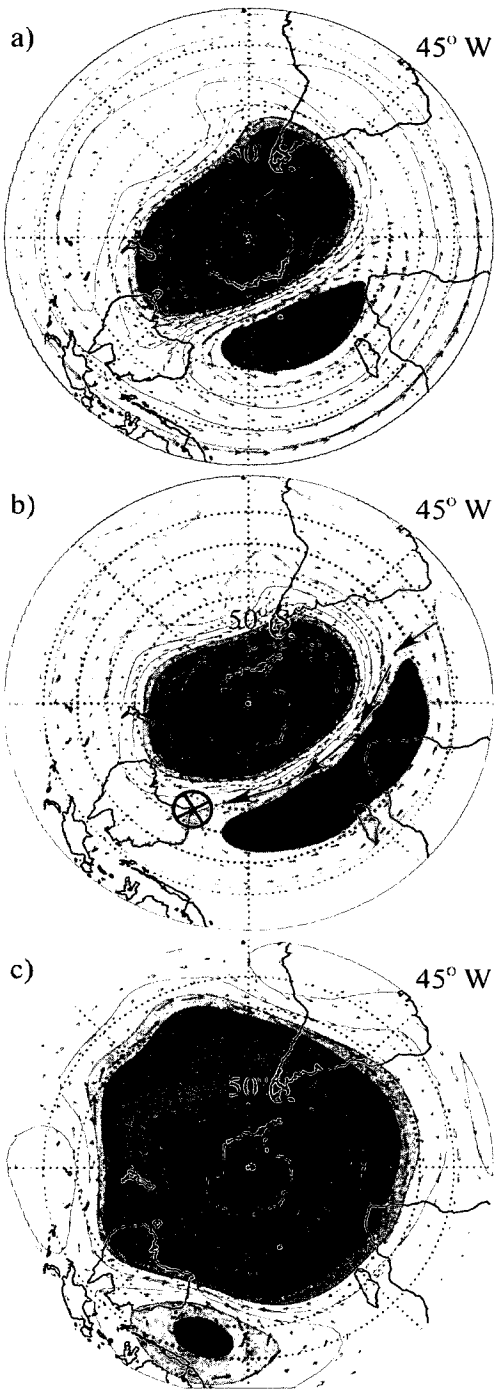

Figure 4.14. ECMWF Montgomery streamfunction and wind vectors at 1200 UT on 24 August 2000 at a) 800 K, contour interval 4.5 x 10^7 m^2 s^{-2}, b) 525 K, contour interval 3 x 10^7 m^2 s^{-2}, and c) 360 K, contour interval 4 x 10^7 m^2 s^{-2}. Arrows in b) suggest ozone transport along the poleward side the ridge to the top of the synoptic trough near Australia in c).

Reproduced with permission of the copyright owner. Further reproduction prohibited without permission.

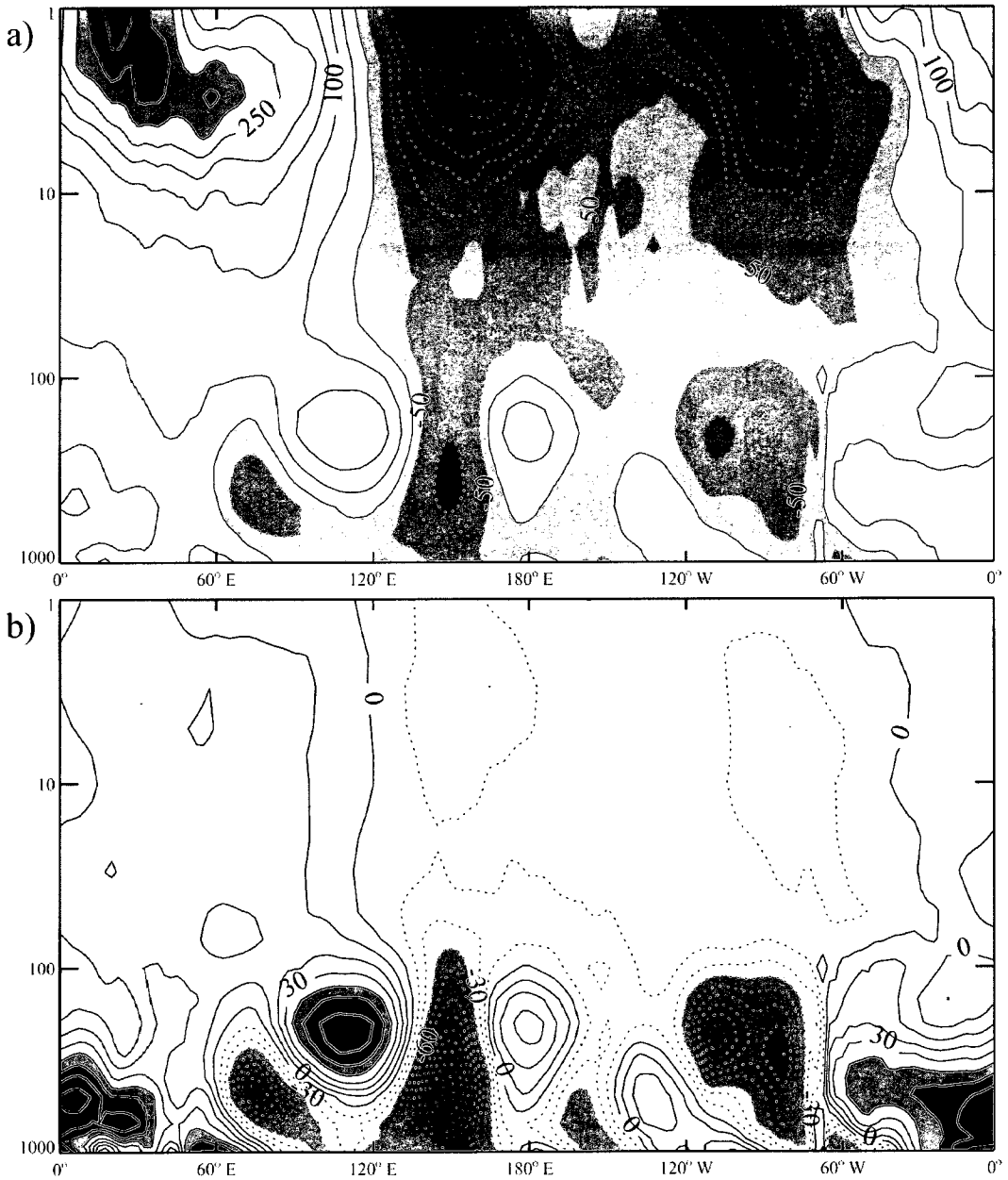

Figure 4.15. Altitude-longitude section at 22°S of ECMWF a) eddy geopotential height, Z′, contour interval 50 m, and of b) $Z' / p^{1/2}$, contour interval 10 m, at 1200 UT 24 August 2000.

Reproduced with permission of the copyright owner. Further reproduction prohibited without permission.

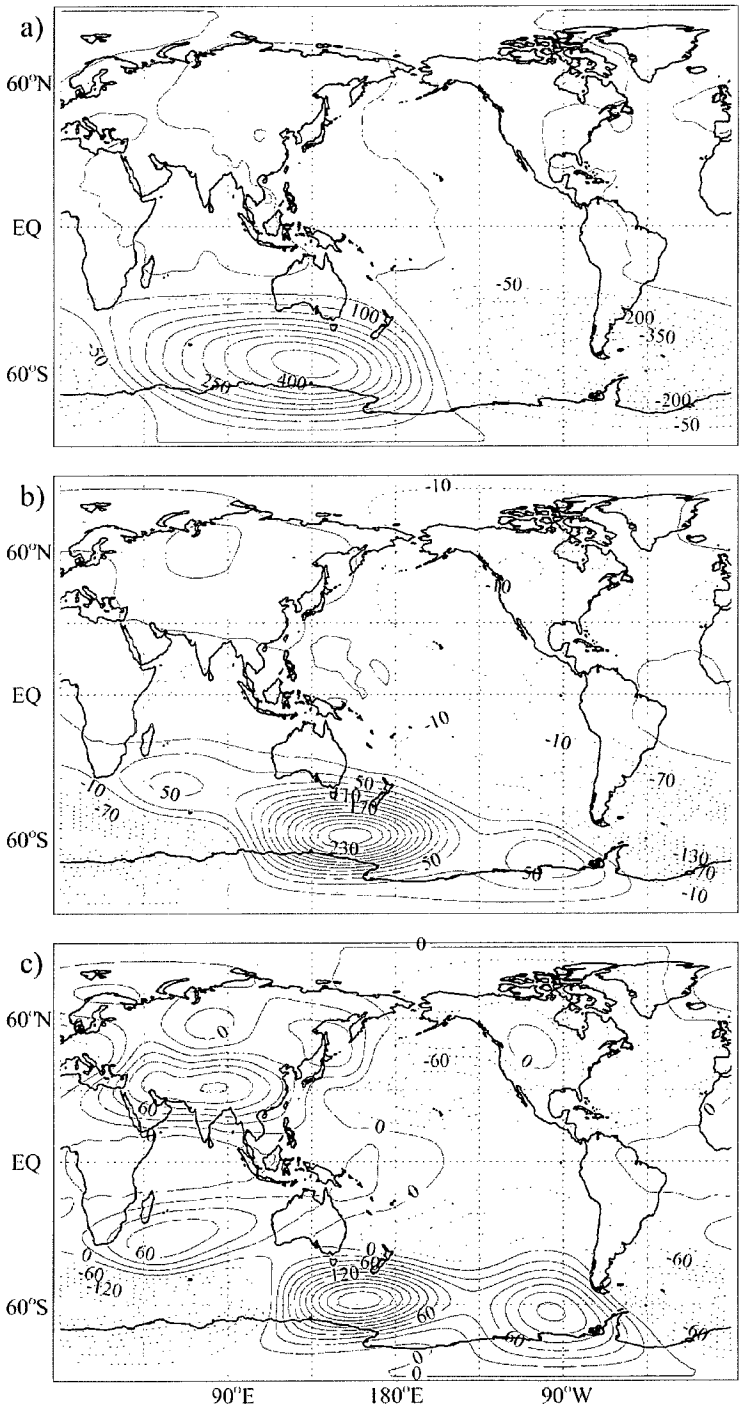

Figure 4.16. ECMWF JAS 2000 average eddy geopotential height at a) 10 hPa, contour interval 50 m, b) 50 hPa, contour interval 20 m, and c) 100 hPa, contour interval 20 m, showing the upward evanescence of the TH into summer easterlies and upward influence of the SIOH into winter westerlies. (The 150 hPa level is shown in Fig. 4.4b).

Reproduced with permission of the copyright owner. Further reproduction prohibited without permission.

Chapter 5

Climatology, part I

5.1 Introduction

The 1995-2004 period was divided into temporal composites according to the relative strength of the Austalian High (AH), the South African High (SAH) and Indian Ocean Highs (IOH) near 20°S to differentiate the convective forcing and dynamical regimes. The three temporal subsets were extracted to span periods of AH dominance (Type 1, 260 days), IOH (Type 2, 481 days) and the relatively high magnitude of both the AH and SAH anticyclones (Type 3, 179 days). All days in the 720 day August to October period over 10 years were binned into either type of case, depending on the activity of anticyclones over the Indian Ocean. Further details on the exact dates and their placement within the types is specified in table 5.1. Table 5.2 contains the breakdown of datasets into types for each month of the year of our analysis. These temporal composite subsets are analyzed in chapter six and seven in terms of variability of meteorological variables like geopotential heights, OLR and winds, as well as power spectra and Eliassen-Palm fluxes, in order to explain different dynamical regimes the SH circulation undergoes.

Sections 5.2, 5.3 and 5.4 investigate the behaviour of convection over the Southeast Asia (SEA) and MC during the August to September period. The temporal evolution is analyzed with hovmoller diagrams of OLR to underscore dynamical link between the SH hemisphere anticyclones and the convection over the SEA. The southward migration of

Reproduced with permission of the copyright owner. Further reproduction prohibited without permission.

convective centers together with zonal contraction that occurs as the boreal winter transitions into spring is analyzed through monthly means. Differences between type of events highlight the spatial changes in convection leading to the strengthening of AH instead of the IOH for example.

Sections 5.4, 5.5 and 5.6 look into the structure of geopotential height anomalies, temperature and zonal winds in the SH at the 150 hPa level during the August-October period. In the manner similar to the OLR analysis, this sections show a gradual decrease of the AH strength as time marches toward the October leading to the gradual decay of the ASWJ. The increase of the activity of the SAH and SAmH in the early spring is also highlited. The column ozone is shown to closely mimic the spatial and temporal distribution of the troughs associated with the AH, SAH, IOH, SAmH.

Sections 5.7 through 5.10 provides the analysis of the geopotential height anomalies in terms of the vertical extent of the SAH, AH and SAmH systems which do reach well into the stratosphere interacting with ridges prevalent in the midstratosphere, often leading to the stalling of the wave 2, which was described in chapter four. The seasonal progression in underscored by the gain in the vertical extent of the SAH and SAmH systems and opposite situation for the AH.

5.2 Analysis of the convection over the South East Asia.

Daily means of OLR for the analyzed period were chosen as a proxy allowing us to study the behavior of convection over the MC during different dynamical regimes included

Reproduced with permission of the copyright owner. Further reproduction prohibited without permission.

in designated typological subsets. Deep convection was defined to occur when values of OLR were below 120 W/m^2, while typical convective patterns were less than 240 W/m^2 range of values (Kousky, 1988, Horel et al., 1989, Collimore et al., 1998, 2003). Following sections will show the wide range of changes in the strength and placement of deep convection centers. The zonal contraction and soutward shift of convection regions over the MC and SEA, concurrent with enhancement of convection over the Africa and South America will be described. Different modes of convective activity leading to dynamical structures described in later sections will be highlited.

5.3. Time evolution of convective systems over the Southeast Asia and MC region.

The tropical convective pattern over 10°S-20°N is characterized by three main convective zones anchored on average over Amazonia, Equatorial Africa and the MC. However, its structure is not uniform spatially and in time. The day to day changes in the zonal extent of maxima as well as their latitudinal expansion play a major role in modulation of the anticyclones immediately southwest of it. Therefore their time evolution was important factor, together with temporal behaviour of the SAH-IOH-AH triplet, when selecting the dates for different composites.

The longitude-time plots of OLR (Figs. 5.1 - 5.5), projected for Equator and 10°N reveal well know pattern of three main convective areas anchored over continents of South America (around 60°E), Africa (0-35°E) and the MC, together with the eastern Indian Ocean. The last one is responsible for the existence of the AH system. Upon closer inspection of

Reproduced with permission of the copyright owner. Further reproduction prohibited without permission.

OLR minima at 0° (panels a and c) and 10°N (panels b and d) a migratory nature of convective systems over the MC region is clearly distinguishable, with convection maxima moving eastward from their starting points at approximately 60°E toward 110°E. Typical phaselines are represented on Figure 5a and b by white lines. The wavelike feature is closely resembling the equatorially trapped eastward propagating Kelvin wave (Matsuno, 1966, Wallace and Kousky, 1968, Andrews, 1987, Hitchman and Leovy, 1988, Tsuda et al., 1994, Shiotani et al., 1997, Holton et al., 2001, Mote et al., 2002), first observed in radiosonde data. Period of these "convectively coupled" waves ranges from 15 days in the lower troposphere, 10 days near the tropopause and 4-8 days in the lower stratosphere (Tsuda et al., 2006, Canziani et al., 1995, Shimizu and Tsuda, 1997, Salby et al., 1984, Wheeler and Kiladis, 1999, Wheeler et al., 2000, Straub and Kiladis, 2002). Their vertical lengths vary between 5 and 12 km. Convection in these waves propagated eastward at nearly 17 m/s and the horizontal scale for these disturbances can be 3000 km (60-110°E). The observed Kelvin wave pattern is consistent with the time evolution of the anticyclones in the MC region of the SH but additional spectral analysis of OLR patterns is needed to prove that relationship. These equatorially trapped Kelvin waves (together with Rossby waves) are known to be the driving mechanism of the Madden-Julian Oscillation (MJO, Madden and Julian, 1971, 1994; Wang, 1988; Rui and Wang, 1990; Hayashi and Golder, 1993, Geerts and Wheeler, 1998, Zhang, 2005; Kim et al., 2009).

When compared with the time evolution of anticyclones at 20°S (Hovmoller diagrams at 20°S for years 1995-2004, Fig. 5.6-5.8), three main phases were destinguished. Type I events, with the AH being relatively most important system at this latitude is characterized

Reproduced with permission of the copyright owner. Further reproduction prohibited without permission.

by convection maxima shifted eastward to around 90°E and further, coinciding with relatively subdued convection over the equatorial Africa (15-30°E). Type II events, when the whole Indian Ocean basin experiences anticyclonic positive geopotential high anomaly occur during initial pulse, when the convective maximum is still within 50°-90°E the whole equatorial region of 50-110°E is convectively active. These events may also show the increased convection over the Africa. Type III cases, occuring with less frequency than previous type include days that have a clear convective maxima in both the African and 90-110°E (or further east) at the Equator and much stronger OLR signal over the 50-90°E region. The correlation analysis showed a good first order agreement between the OLR pattern and the geopotential height anomalies to the southeast of it. The correlation coefficients computed for timeseries of 920 days each in the two regions of OLR (0°N,70°E and 0°,105°E) and Z' (20°S, 65°E and 20°S, 100°E) without any timelag were found to be 0.67 and 0.83 respectively.

5.4 Analysis of converction pattern in time composites.

The convection regions in August with OLR values within prescribed threshold (less than 240 W/m^2) covered most of the northern MC and Malaya as well as greater part of the central Indian Ocean and area of the Pacific east of Philippines (Fig. 5.9a). The eastern Pacific east to Central America and tropical Africa and Atlantic were also mostly covered by cumulus convection. The type I subset during August was characterized by decreased convection over the Micronesia and east of the Philippines as well as the Bay of Bengal (Fig.

Reproduced with permission of the copyright owner. Further reproduction prohibited without permission.

5.9b). The opposite was true for the equatorial Indian Ocean with vast expanses west of Sumatra undergoing decrease of 10 W/m^2 (10% of maximum value) or more in the OLR. Notable was the 10 W/m^2 decrease in convection over eastern equatorial Africa and the Indian Ocean immediately east of it as well as increased convection over the central continent of South America (with corresponding high southeast of increased convection). The type II scenario (Fig. 5.9c) brought little visible change from the 10-year average, with only small patches of the Western Pacific and central Indian Ocean experiencing an increase in the convective activity of 5 or more W/m2. The dual AH-SAH subtype time composite for August showed increased cumulus convective activity over the whole central Africa and over the South China Sea, which proved to be opposite to the Type I scenario (Fig. 5.9d). That phenomenon is a result of the eastward shift in the convective zone over the northern MC, which is simultaneously indicated by decreased convection in the Southern Bay of Bengal and west of Sumatra. The New Guinea- Celebes Sea area showed an increase of 10-25 W/m^2 (15% of maximum value). The African and central Indian Ocean sectors displayed generally expanded convective zones, deeper and stretching further poleward.

September OLR contours (Fig. 5.10a) show diminished regions of the convective activity throughout the tropical belt. The OLR signal is stronger by 20 W/m^2 over the convective region of the Western Pacific. The deep convection centers in concert with the annual cycle, experience southward shift toward the Sumatra as well as the more active region of New Guinea, while there is less convection visible over the northern Australian territories. The African and Central American sector continue to be strong contributors to the convection activity. The decrease in convective activity over the part of the MC as well as

Reproduced with permission of the copyright owner. Further reproduction prohibited without permission.

South China Sea (Fig. 5.10b) is further enhanced during the strong AH days (Fig. 5.10b), with OLR signal stronger by 5-10 W/m^2 throughout most of the tropical SH. The type II periods (Fig. 5.10c) do not show notable differences in the OLR signal in comparison to the September's average during analyzed years, similarly to the previous month. During the type III (Fig. 5.10d) events the tropical Indian Ocean, parts of the western Pacific north of New Guinea and the tropical Atlantic maritime region north of the Equator show relative increase in the convective activity when related to the average of September's days. There is also a notable increase of convection over the Malaya and Indochina resulting from northward expansion of deep convective zones over these regions. The convection is deepening also over most of the subequatorial Indian Ocean- MC region (up to 25 W/m^2 decrease of the OLR signal) as well as over the Central America (OLR decreased by approximately 10 W/m^2).

Unlike September, which exhibited the northwestward expansion of deep convection zone over the Indochina, the October's average OLR (Fig. 5.11a) shows low signal areas migrated southward and whole region experiencing decrease in convective activity. The South American convective regions are expanded well to the south of their August's positions, which is again attributable to the increasing solar zenith angle. Figure 5.11b shows decreased convection throughout the northern MC, with scattered negative difference patches indicating decrease of OLR on the order of 5 W/m^2. The OLR signal is stronger over the Celebes Sea and Micronesia pointing to the relative northeastward shift of the convective zone during the Type I event when compared with the month average (Fig. 5.11b). At the same time, the negative OLR differences over the central Indian Ocean are indicative of

Reproduced with permission of the copyright owner. Further reproduction prohibited without permission.

moderate southwestern expansion of low OLR zones as well. Higher OLR (5-10 W/m^2) values point to diminished convection over the tropical Africa, while the opposite is true for the central South America. The type II, unlike during previous months, displays significant differences from the monthly means (Fig. 5.11c). The whole Maritime Continent manifests a general decrease in OLR (~ 10 W/m^2) resulting from increasingly convective character. The increase in convection encompasses the whole eastern Indian Ocean Basin to the east of the New Guinea. Dissimilarly to the Type I, these events also display relatively decreased OLR signal over the Sub-Saharan Africa and the eastern Amazon Basin (5-10 W/m^2). The convective centers over the Central America also deepen and expand eastward into the Atlantic. A relative decrease in convection is visible over the Central Indian Ocean during Type III events (Fig. 5.11d), with OLR values lesser than the October's average by ~10 W/m^2. General decrease of convection in the regions north of the Equator is compatible with the annual cycle, with sun moving "southward" toward the southern spring. In concert with the sun's movement across the sky, there is an resultant increase of convection over the Indonesia, western Sub-Saharan Africa and the central South America. These areas of relative increases in convection are shown to be sort of wave-makers, sparking wave activity differently for each of the subtypes of events.

Reproduced with permission of the copyright owner. Further reproduction prohibited without permission.

5.5 Analysis of anomalies of geopotential height, temperature and zonal wind according to case subtypes at 150 hPa.

The average of geopotential height anomalies during all analyzed Augusts (Fig. 5.12a) show four prominent anticyclonic systems over the SH; the Australian High, the IOH immediately to the southeast of the AH, the high latitude Southern Pacific High (SPH, southeast of Australia) and the anticyclonic system over the South Atlantic, east of South America. Notable is a large trough encompassing the high latitude Southern Atlantic and Indian Ocean. The type I cases were characterized not only by the strenghtened AH (Fig. 5.12b, by approximately 20-30 gpm), but also by southeasterly shifted anicyclonic center over the southwestern Indian Ocean as well as increased geopotential height anomaly over the Weddell Sea and Patagonia. Relatively high strength of the AH is also underscored by large negative difference in anomalies southwest of the Australia (up to 40 gpm). The combined SAH-IOH-AH events showed opposite structure when compared to type I cases (Fig. 5.12c). The positive differences in geopotential height anomalies during type II events reside precisely in the positions of negative differences for case I, pointing to a similarity with the dipole mode seen when analyzing travelling waves (k=4 in this case). The magnitude of these differences is only approximately a third of levels observed in the type I events (30 gpm vs 90 gpm). The Mercator projection of the Type III events' deviation from the monthly mean (Fig. 5.12d) emphasise the strengthened anticyclonic center over the horn of Africa (70 gpm) and over the eastern part of the Australia (20 gpm). Furthermore, latitudes 45-65°S experience largest magnitude positive difference of all cases in August, pointing to

Reproduced with permission of the copyright owner. Further reproduction prohibited without permission.

strengthened highs in the region of Southern Seas (both Atlantic and Pacific areas) as well as buildup of high over the Antarctica.

The temperature anomalies at 150 hPa during the August (Fig. 5.13a) show a broad pool of negative anomalies stretching from the eastern South America to the central Indian Ocean at mid to high latitudes, with wave 1 pattern being consitent with previous studies (Hartman, Randel, Wirth). There is also a negative patch over the northwestern Australia which is colocated with the AH (compare to Fig. 5.12a). Deviations of the temperature anomalies from the monthly mean during Type I events (Fig. 5.13b) reveal a whole south Indian Ocean basin anomalously warmer (up to 2K), consistently with diminished anticyclonicity in the area between the AH and the high southeast of the Africa, which in itself manifests as a negative difference. Type II (Fig. 5.13c) differs by less than 1K from the averaged of analyzed Augusts. The broad differences resurface during Type III events (Fig. 5.13d) with a deep (2K) negative pool over the area of the SAH and lesser values covering the whole southern Indian Ocean and well over the Antarctica. The increased strength of anticyclone southeast of the South Africa is underscored by the negative patch in corresponding location, with positive differences over 1K almost wholly encasing it.

The monthly averaged zonal wind component (Fig. 5.14a) show the dual streak Australian Subtropical Westerly Jet (ASWJ) residing over the 25-35°S. This feature is set up and maintained by the outflow from the Tibetan High into the SH and the need for angular momentum conservation during these events (*Hitchman*, 2009). There is also a weak (barely over 40 m/s) low altitude extension of the Polar-Night Jet (PNJ) visible over the central Indian Ocean at approximately 50°S. As seen from panel b, there is a substantial

Reproduced with permission of the copyright owner. Further reproduction prohibited without permission.

strengthening of ASWJ by a 5 m/s during the type I events., which occurs in concert with strengthening of the AH. Further strengthening of the PNJ is also apparent from the differences field in the 50-70°S latitudinal band around 60°E. This enhancement coexists with stronger anticyclonic center just north of this positive difference in zonal wind. Changes of zonal wind field during the type II cases (Fig. 5.14c) are similar to corresponding differences in geopotential height anomalies shown before (Fig. 5.13c). They do not exceed 3 m/s but apparent is a negative difference in the area of ASWJ showcasing a weaker jet during the type II days in August. Type III events are characterized by uniform strengthening of the AH and ASWJ (Fig. 5.14d). The positive difference field at 30°S stretches well over the central Indian Ocean Basin pointing to the jet itself being displaced westward. An increase of more than 8 m/s south of the tip of Africa points to wider, while also shifted westward, lower extension of the PNJ, with the secondary extension set up northeast of the Antarctic Peninsula.

September is characterized by a similar activity of IOH, including the AH and SAH (Fig. 5.15a). The high latitude high pressure system in the Southern Pacific is stronger (by 100 gpm) than in the previous month and has a secondary center located immediately west to the Antarctic Peninsula. This secondary center is further underscored by the broad pool of positive differences in height anomalies over the Antarctic Peninsula that appears during type I events (Fig. 5.15b). Together with increased circulation in the AH (differences of ~40 gpm) it is the most dominant feature of type I events. The active IOH periods (Fig. 5.15c) are characterized by relatively small differences from the mean (10-30 gpm), with increased geopotential height anomalies over the southern central Indian Ocean and decreased over

Reproduced with permission of the copyright owner. Further reproduction prohibited without permission.

both the Australian sector and south of the Africa. The increase in height anomalies over the Australian, south central Indian Ocean and the southern Africa marks the type III events during the analyzed Septembers (fig. 5.15d). Also notable is mid-latitude spin up of the anticyclone east of the South America, pattern very similar to August. Other similarities with the previous months' type III include enhanced geopotential height anomalies over the south-central Pacific, with a broad decrease of anticyclonicity over the Antarctic Peninsula. However magnitudes of changes are greatly increased during September and the positive difference over the Indian Ocean region is dissimilar with the previous month's situation. August tended to favor enhancement more south, over the Antarctica while the positive anomaly spans 30° in latitude over the central Indian Ocean during September.

The September's temperature anomalies undergo similar cycles to these of previous month. Panel a (Fig. 5.16) reveals the deep pool of colder air residing over the South Seas, between 120°W and 60°E. It is colder by ~1 K and shifted westward in comparison with August, in concert with deepened negative geopotential height anomaly, which is also broader and reaches further west during this part of winter to spring conversion of the UTLS region. In comparison with the monthly mean, the type I events (Fig. 5.16b) are characterized by a colder air (by up to 1.5K) over the Australia (collocated with the enhanced AH), and south of the Africa, with warmer air stretching through the whole western and central Indian Ocean as well as immediately southeast of the Australia. Positive differences are also observed off both coasts of the South America consistent with the strengthened anticyclonicity over the central part of this continent. The colder air over most of the central Indian Ocean, indicative of enhanced anticyclones (Fig. 5.15c), characterizes the type II

Reproduced with permission of the copyright owner. Further reproduction prohibited without permission.

events (Fig. 5.16c). Again, differences are not exceeding 1K. While type II did not differ from the mean much, the type III emphasized large departures from it (Fig. 5.16d). All three continents display areas of air colder by 1K or more (Australia, South Africa and South America), there is also a k=2 structure around 60K with interchanging colder and warmer air departures from the monthly mean. The large amplitude of these differences stands in good agreement with the differences in geopotential height anomalies that are observed during September's type III cases.

The mean zonal winds during Septembers of 1995-2004 period (Fig. 5.17a) show a wind values diminished by up to 10m/s in the ASWJ while there is some enhancement of the PNJ, which tends to be broader (by 20° in longitude) than in August. This is consistent with the period of strengthening of the Polar Vortex (PV) in the SH. The periods of enhanced AH (Fig. 5.17b) show the tendency of the core of ASWJ to be strengthened by 2-3 m/s. The increased zonal wind just south of the position of the PNJ and negative difference over its mean position indicates the poleward shift of this jet and contraction of the PV. The relative expansion of the ASWJ is again feature of the type II events (Fig. 5.17c), with positive difference of up to 2m/s stretching over the Indian Ocean. However, no real strengthening of this jet can be seen, just the westward expansion. PNJ also benefits from the westward expansion as indicated from the patch of winds stronger wings (by ~2 m/s) over the southern part of Atlantic, but changes are relatively small and do not include any shifts in latitude. Again, the type III bears largest changes in the SH wind pattern (Fig. 5.17d). The dual cores of ASWJ are both enhanced by up to 10m/s, while the jet is also expanding southward. Similarly to the flow in August, September's type III also experience the secondary lower

Reproduced with permission of the copyright owner. Further reproduction prohibited without permission.

extension of PNJ even though by almost 10 m/s weaker than its predecessor. The wavelike (k=3) pattern of intermeshing positive and negative anomalies in the high latitudes points to the disturbed PV which is also shifted off the Pole.

October monthly means of the geopotential height anomalies (Fig. 5.18a) show the diminished AH (by 25 gpm) and the centre of SAH shifted to position over the eastern coast of Africa. There is a third anticyclone established over the South America. The high latitude anticyclonic anomalies are more robust than in previous month. The type I differences in height anomalies (Fig. 5.18b) reveal the limited geographically AH, here seen as a negative difference neighboring a positive one located over the Australia. The positive patch in the central Indian Ocean basin and corresponding negative area south of African continent points to the anticyclone being shifted eastward from its mean position toward the central Indian Ocean. The eastward shift is also true for the whole 20°-45°S band and include the anticyclone over the South America as well as the anticyclonic anomaly over the Southern Pacific centered around 60°S. The Type II deviations from the monthly mean (Fig. 5.18c) show a ~25 gpm decrease in the AH and over the South Africa with a coinciding 75 gpm increase over the central Indian Ocean. Notable is a westward expansion of the IOH even though it is weaker. The large (100 gpm) difference in height over the South Africa and south of it sets the type III apart from type II (Fig. 5.18d). The negative height difference over the Antarctic Peninsula points to a relative weakening of the high in this area which is opposite to the type II which favors the anticyclone.

The temperature anomaly mean in October for analyzed period (Fig. 5.19a) at 150 hPa feature a deep pool of cool air residing between the South America and central Indian

Reproduced with permission of the copyright owner. Further reproduction prohibited without permission.

Ocean from 30°S poleward, similar to previous month but colder (by 0.5K). The type I (Fig. 5.19b) events experience a structure of intermeshed positive and negative departures from monthly mean in the SAH-AH areas. Note the positive difference southeast of the Africa and west of the Australia , indicative once again of a decrease in anticyclonicity and an eastward shift in the position of the SAH and AH. The colder air area over the Australia lies within the strengthened AH. Figure 5.19c shows a positive difference in the southern Atlantic-Indian Ocean with its western part being opposite to the type I cases, closely to a dipole mode. The positive anomalies over the Australia and South Africa point to the diminished SAH and AH, with corresponding negative anomaly lying in the IOH activity area in the central Indian Ocean. The Type III difference map of temperature anomalies (Fig. 5.19d) shows the negative pool filled with cooler air in the southern central Indian Ocean, which is exactly a negative of the type II in this area. This cooler anomaly stretches northwestward and northeastward to encompass the enhanced SAH and AH. The most western extension of this colder pool resides over the Southern America coinciding with an anticyclone there.

The October's zonal winds (Fig. 5.20 a) show signs of abating, with the ASWJ being 10 m/s weaker than during the previous month and longitudinally limited between 100° and 180°E as opposed to stretching from 70°E to 110°W in the August. The footprint of the PNJ undergoes similar changes, even though it still retains its longitudinal span. The type I events (Fig. 5.20b) favored the relatively southwardly expanded Australian Jet, as visible from the positive zonal wind anomaly over the southwest Australia. The eastward shift of the PNJ lower extension is also visible by the way of negative anomaly south of the Africa and a

Reproduced with permission of the copyright owner. Further reproduction prohibited without permission.

positive just westward of it. While there is a noted increase in a zonal wind velocity in the ASWJ for type I, the type II (Fig. 5.20c) experiences the breakdown of the jet with a 3 m/s deceleration as well as 2 m/s deceleration in the area of PNJ. There is a general flow acceleration between 30° and 45°S, throughout the whole SH. Type III (Fig. 5.20d) unlike type II experiences accelerated zonal winds (by 5m/s) in the ASWJ zone as well as relative elongation of its core. This proves to be true to the PNJ section as well, as acceleration reaches a 4 m/s. The zonal wind signal in the 15°-45°S band, similarly to geopotential height and temperature anomalies, is of opposite sign to type II.

5.6 The 10 year climatology of column ozone during the late winter to spring transition according to the types of synoptic situation.

The column ozone roughly follows the geopotential height anomalies, with less ozone coinciding with anticyclones. This fact is accentuated in the distribution of TOMS ozone in August (Fig. 5.21a). The 300 DU solid isoline adheres to the outline of the 3 anticyclonic systems, namely the AH, SAH and South American High. The ozone maximum southwest of the Australia lies on the poleward side of the AH and southeast of the SAH systems. The enlarged ozone maximum in same locale during the type I events is attributable to strengthening of the AH (Fig. 5.21b) to the north of it. This is further reinforced by the difference panel (Fig. 5.22a) showing a 20 DU positive difference in the column ozone around 50°-60°S. There is also a positive anomaly around 45°S south of Africa and east of the South America, which factor into the northern extension of the 300 DU line in between

Reproduced with permission of the copyright owner. Further reproduction prohibited without permission.

the SAH and the high over the South America. The events characterized by the simultaneous activity of all IOH anticyclones (Fig. 5.21c) emphasize the maximum being smoothed out and weaker by 30 DU than the monthly mean. A stronger nature of the South American High (SAmH) is mirrored by the decreased ozone content within its location and more northerly extension of 300DU isoline to the west of it, visible also as a positive anomaly (Fig. 5.22b) as well as to the southeast of it. The SAH system contributes to the positive anomaly southeast of Africa. The more northern position of the enhanced SAH and the Australian High is accentuated by northerly expansion of the column ozone maximum. Type III events (Fig. 5.21d) lead to the broad smooth maximum in ozone, with values ranging from 360 to 372 DU south and southeast of the Australia, similar to type II but shifted eastward. The 300 DU isoline again closely matches contours of the AH, SAH and SAmH. The strenghtening of the SAmH which coincides with its poleward displacement introduces the intrusion of lower ozone content air 5-10° to the southeast almost braking the 300 DU collar feature. The activity of this anticyclonic system is emphasized by the negative patch of the column ozone difference (Fig. 5.22c) centered over 45°S, 50°W with corresponding positive anomalies to the southeast and northeast of it. The noted in the previous chapter strenghtening and longitudinal elongation of the SAH is emphasized by the large area of negative ozone anomaly within this system and increased ozone content area immediately to the east of it, located in the trough between the SAH and AH. The AH contibutes to the this anomaly as well as introduces further positive anomaly zone tracing the southern contour of this system as well as the braod pool of positive differences in column ozone to the southeast of it.

Reproduced with permission of the copyright owner. Further reproduction prohibited without permission.

The gradual increase in the column ozone during late winter to spring transition is underscored by the September's mean column ozone (Fig. 5.23a), with values inside the maximum exceeding 400 DU. The notable lack of the SAmH in the montly mean geopotential height anomalies (Fig. 5.15a) led to the 300 DU contour anchored over the South America more northerly than during previous month. The 345 DU contour extends well into the Southern Atlantic, emphasizing the increased ozone content in the SH, while the core of the maximum is still roughly in its climatological longitudinal band of 60°E-180°E. The enhanced AH brings more ozone into the trough southeast of it during type I events (Fig. 5.23b), which is also recognizable by the positive column ozone anomaly visible south of the Tasmania (Fig. 5.24a). A similar anomaly can be seen to the west of the anomaly associated with the AH system, though this one is a result of the SAH activity. The enlarger 405 DU contour (red) points to the further increase in an ozone content in the maximum during the enhanced AH type cases. Panel c (Fig. 5.23) shows the strong resemblance of the Type II events to the monthly mean column ozone distribution during the September. The similarity is further reinforced by the difference field (Fig. 5.24b), with three relatively small anomalies maxima of 10-15DU centered south of the AH, southeast of the SAH and to the west of the SAmH. The type III reintroduces strong singular AH, SAH and SAmH systems. However this situation does not translates into enhanced column ozone (Fig. 5.23d), the values of which are 10 DU lower in the maximum area during these events. The strong positive anomaly to the southeast of the anticyclone over the South America (Fig. 5.24c) is a dominant feature, its eastern part attributable to the AH while western is a result of the enhanced SAmH. This anticyclone allows for the western elongation of the 360 DU contour, while all maxima are relatively smaller in magnitude than the monthly mean for the decade.

Reproduced with permission of the copyright owner. Further reproduction prohibited without permission.

The SAH tends to weaken during October in comparison with August, while the AH stays to be a prominent feature of subrtopical SH. This leads to eastward shift in the core of the column ozone maximum during this month (Fig. 5.25a) due to the dimineshed ozone loading from the edges of the SAH. This is further distinguishable by the 360 DU column ozone isoline being moved to 60°E from its position in the central southern Atlantic a month earlier (Fig. 5.26a). The type I events (Fig. 5.25b), consistently with the enhanced AH bring a stronger (by 15 DU) ozone maximum south and eoutheast of the Australia. The 345 DU closely follows the SAH, which is weaker than climatologically with its center shifted to the southeast of the Madagascar. The stronger ozone transport at the edges of these anticyclones shows as positive column ozone anomalies to the south of the SAH and AH (Fig. 5.26a) where enhancements reach 30 DU in case of the SAH and 20 DU due the AH activity. The equal relative strength of all anticyclones in the Indian Ocean basin, together with the weakening of the AH during type II (Fig. 5.25c) events leads to decrease of the column ozone in the core of the maximum in the OC (Ozone Croissant). The only positive anomaly in the column ozone south of 40°S (Fig. 5.26b) results from the relatively intensified SAmH and brings a local maximum, a patch of column ozone increased by 40 DU in comparison to the climatological mean in the southern Atlantic. This local maxima is also visible on Figure 17c as oval extension of western part of the 345 DU contour. The TOMS ozone during Type III events (Fig. 5.25d) in October undergoes small intensification of the maximum south of the AH system as well as to the east and southeast of the enhanced anticyclone over the southern tip of Africa which manifests in the 330 DU contour being stretched to the northwest relatively to October's mean. This enhancement of ozone is also seen as a positive anomaly stretching from the Madagascar to the Australia (Fig. 5.26c), while the AH

Reproduced with permission of the copyright owner. Further reproduction prohibited without permission.

intensification signal is revealed over the southeastern portion of Australia and south of this continent. Notable is the large patch of positive anomaly centered over the southeastern Pacific, near the western Antarctic Peninsula. This ozone enhancement is collocated with the eastern end of the high latitude anticyclonic perturbation at the edge of the SPV. The strong SAmH system once again contributes to the positive anomaly to the southeast and negative difference over its position. Once again this system, together with quasistationary anticyclone over the Antarctic Peninsula is responsible for the minimum in the column ozone that brings zonal assymetry to the OC.

5.7. Analysis of the vertical structure of anomalies of the geopotential height, temperature and zonal wind in 10 year climatology of ASO.

This chapter deals with vertical characteristics of the anticyclones and the interactions between anomalies active at different levels of the atmosphere. These interactions lead to local modulation of the anticyclones at different heights and in some cases stalling events (*Hitchman and Rogal*, 2009). Three latitudes were analyzed because of their importance to the anticyclones; the 20°S which is relevant for the AH and to a lesser extent for the SAH. The 35°S and 45°S which are of premier importance for the SAH and Indian Ocean Highs as well as for the anticyclonic system over the Patagonia. The vertical profiles were organized into monthly means and means of days included in three major event types described before.

Reproduced with permission of the copyright owner. Further reproduction prohibited without permission.

5.8. Vertical structure of geopotential height anomalies in August

The August mean vertical profile of geopotential height anomaly at 20°S (Fig. 5.27a) shows the strong AH between 200 and 100 hPa centered over the 110°E and stretching from 70°E to 140°E. The anticyclones over the Africa and Indian Ocean do not reach into the UTLS region. There is also a visible wave 1 signal in the lower stratosphere centered over the African region. The difference between type I events and the mean (Fig. 5.27b) is underscored by the enhanced AH and a pool of negative difference in geopotential height just west of it, encompassing whole western Indian Ocean basin. The increased anticyclonicity over the tropical eastern Pacific is visible as two positive differences stretching from the surface up to the 70 hPa level over 150°W and 90°W. The type II (Fig. 5.27c) shows an increase of 15 gpm over the western Indian Ocean and opposing negative pool in the longitude of the AH, both centered over 200-100 hPa region. The third type of events (Fig. 5.27d) underscores the anticyclogenesis inherent to the three main regions of quasistationary anticyclones, bringing a system of intermeshing positive and negative differences in geopotential height, with a major one being a 40 gpm enhancement of the SAH in the UTLS region. The AH anticyclone is strengthened from the surface up to a 100 hPa by ~10 gpm, and a further downstream development of anticyclonic features may be seen eastward. The enhancements over the South America and Africa have vertical structure expanding well into the lower stratosphere.

The 35°S profile (Fig. 5.28a) shows the strong SAH, 200 gpm in the center as well as the SAmH (140 gpm in the center). Notable is the wave 1 structure in the lower stratosphere. The difference fields show the 35 gpm enhancement in the western Indian Ocean area as well

Reproduced with permission of the copyright owner. Further reproduction prohibited without permission.

as similar improvement in the eastern part of the AH region during the type I events (Fig. 5.28b). The positive anomaly in the SAH region has a direct connection with the anticyclone aloft. Interestingly, the positive geopotential height difference west of the South America is also linked with similar enhancement in aloft. Type II events (Fig. 5.28c) bring a 20 gpm increase in anticyclonicity over the Indian Ocean, with corresponding small decreases over the eastern AH and SAH regions. The IOH, which is a very active feature during this type of events, is vertically connected with the ridge in the lower and middle stratosphere. The increase of 50 and more gpm over the SAH area marks the type III cases (Fig. 5.28d). These periods are also associated with the slight increase of the AH activity, notably on and below 150 hPa levels as well as increased activity of SAmH and anticyclones over the Southeastern Pacific. This coincides with the enhanced ridge in the stratosphere (an increase of more than 60 gpm in comparison to other cases) and the connection between UTLS region and higher levels is visible for the SAH, SAmH and eastern Pacific anticyclonic anomaly.

The vertical structure of geopotential height anomalies at 45°S in August brings the relatively equal strength of the SAH and SAmH systems (Fig. 5.29a), both extending into the stratosphere and feeding the wave 1 ridge centered over 150°E. The southeastern shift of the SAH system, noted in previous chapters, marks the type I difference with respect to the monthly mean (Fig. 5.29b). The enhancement of more than 80 gpm and its vertical extent, well into the stratospheric ridge is a prominent feature during these events. This vertical connection may lead to frequent stalling events and enhances the quasistationary nature of the anticyclones over the Indian Ocean region. In comparison to the previous type, events associated with the type II (Fig. 5.29c) bring small scale changes (around 30 gpm). The two

Reproduced with permission of the copyright owner. Further reproduction prohibited without permission.

main regions marked with enhancement include the area of the IOH and the southeastern Atlantic. The 45°S latitude belt experiences strong increases in anticyclonicity in the SAmH and over the central and eastern Pacific zones during the type III cases (Fig. 5.29d). The eastward shift of the stratospheric wave 1 ridge is underlined by the vertical extensions of these two enhanced anticyclones centered over 50°W and 120°W. The southernmost extension of the SAH is diminished while the system moves westward and northward to the Africa (compare with Fig. 5.4d).

5.9. The vertical structure of geopotential height anomalies in September

The monthly mean anomalies at 20°S (Fig. 5.30a) show the AH stretching over the 70°E to 150°E region in the UTLS, with an elongated core. This system is weaker by 30 gpm in comparison with the August. The negative anomalies lying over the western Indian Ocean and eastern Pacific are shallower than month before, otherwise the vertical structure in height looks very similar. The enrichment of the AH system during the Type I events reaches 20 gpm (Fig. 5.30b) and occurs simultaneously with the strengthening of the anticyclonic system over the South America which is similar in magnitude. There is a broad pool of negative geopotential height difference over the Africa and western Indian Ocean region pointing to the relatively weaker surface anticyclones in this area at 20°S. The opposite is true during type II events (Fig. 5.30c) when the AH is weaker than the highs over the central Indian Ocean which manifests itself in a dipole feature with positive anomaly where the IOH reside and negative one in place of the AH. Differences from the monthly mean do not

Reproduced with permission of the copyright owner. Further reproduction prohibited without permission.

exceed 20 gpm throughout the atmosphere. The type III events (Fig. 5.30d) is characterized by simultaneous enhancement of the AH (by 25 gpm), SAH (~15 gpm) and the SAmH (up to 20 gpm). Both last highs show relatively strong vertical connection with the wave 1 ridge aloft, while the AH seems to be vertically limited to the UTLS region like a month before.

The monthly mean geopotential height anomalies at 35°S (Fig. 5.31a) show the relatively strong SAH with its smaller western counterpart, the SAmH. The SAH extends well into the stratosphere connecting with the ridge of the wave 1. The stratospheric system is stronger by 100 gpm than during the August. The SAmH system tends to be weaker in September (compare Fig. 5.20 a and 5.23a). The strengthening of the AH during the type I events (Fig. 5.31b) occurs simultaneously with the westward shift and weakening of the SAH system, seen here as a negative difference over 40°-80°E region and positive one to the west of it. At the same time, the SAmH undergoes similar relocation toward the coast of South America. The type II events (Fig. 5.31c) show opposite signal, with respect to the type I. However the magnitude of changes is roughly half of that typical for type I, being 10 gpm rather than 20-25 gpm. The positive anomaly over the central Indian Ocean stretches from 500 hPa up to 50 hPa, pointing to the connection of UTLS IOH with the wave 1 ridge at 20 hPa, which in itself is elongated westward. The enhancements of the SAH, together with even greater strengthening of the SAmH system, characterize the type III events (Fig. 5.31d). This occurs with the westward shift of the wave 1 phase in the stratosphere and additionally with the enrichment and southern expansion of the AH system, which is seen here as a positive anomaly at 130°E.

Reproduced with permission of the copyright owner. Further reproduction prohibited without permission.

The 45°S mean September vertical structure of Z' (Fig. 5.32a) shows strong stratospheric anticyclone over 60-180°E (by 400 gpm stronger than in August), with the SAH displaced eastward and poleward from the South Africa and equally strong to its predecessor in the August. The SAmH is a well defined structure centered over the South America. Furthermore, the South Pacific High (SPH) is stronger than a month before and extends well into the stratosphere. The type I events (Fig. 5.32b) marked a relative westward shift of the SAH system, complimentary with its strengthening by 100 gpm. While the SAH underwent expansion, the SAmH was moved westward, with its strength remaining at a monthly mean level. Interestingly, still visible is a positive anomaly signal, southeast of the Australia, marking the extension of the southward expansion of the enhanced AH system. The type II events (Fig. 5.32c) bears close resemblance to the monthly mean for the September, with relatively low (up to 40 gpm) differences from it. The SAmH is the only system benefiting from enhancement greater than 40 gpm. Type III events, visible on paned d (Fig. 5.32) emphasize the strengthening of the South Pacific High (at 130°W, difference of more than 180 gpm) coincidental with enhancement of the SAmH and SAH. Notable is a positive difference of more than 200 gpm in the 10-50 hPa over the Atlantic marking the westward shift in phase of the wave 1 discussed already during the analysis of 35°S situation.

5.10 The vertical structure of the geopotential height anomalies in October.

The AH and SAmH systems are enhanced during the October at 20°S (Fig. 5.33a), with the AH stronger by 10 gpm and the SAmH being well developed climatologically

Reproduced with permission of the copyright owner. Further reproduction prohibited without permission.

system with a core stronger by 30 gpm in comparison with the September. Similarly, like in the previous month, the wave 2 structure in lower to mid-stratosphere is a prominent feature, with anticyclonic centers residing at the longitudes of Atlantic and Australia. There is a SAH signal visible at this latitude centered in the mid troposphere at 20°E. Type I events (Fig. 5.33b) bring a simultaneous enhancement of the AH, SAH and SAmH systems, with the anticyclones being enriched by 15-20 gpm for the AH and 5-10 gpm for the second and third respectively. The IOHs are strengthened by 15 gpm throughout the whole basin of Indian Ocean during the type II events (Fig. 5.33c). Simultaneously, the northernmost extension of the SAH moves westward, a shift which is marked by a positive 5-10 gpm difference over the 0°-20°W area. The SAmH shows signs of decrease in anticyclonicity, pointing to the northward migration during these events as discussed previously during the 150 hPa analyses. The contemporary enhancement of the AH, SAH and SAmH mark the vertical structure changes during the type III events (Fig. 5.33d), with strongest improvement in the SAH anticyclonicity (10-15 gpm). Notable is also the vertical expansion of this system, which unlike during other types of events does connect with the stratospheric ridge over it, while the SAmH was the only one vertically burrowing its way into the lower stratosphere during type I and II events.

The 35°S vertical structure shows the boosted strength of the SAH and SAmH systems (Fig. 5.34a) especially in comparison with the September. The Wave 1 in the mid stratosphere shows signs of abating at this latitude, being on average 60 gpm weaker in its core than a month before. The more equal partitioning in October between cases in terms of the length shows in their comparison. The type I events (Fig. 5.34b) underscore the relative

Reproduced with permission of the copyright owner. Further reproduction prohibited without permission.

increase in anticyclonicity in the AH, SAH and SAmH region, with equal enhancement shown for the anticyclone over the southern Pacific. The type II (Fig. 5.34c) provides a contrast to the previous case, with the SAmH weakened and shifted westward simultaneously with the SAH and IOH systems, the IOH being diminished by 10-15 gpm from its climatological mean. The case III (Fig. 5.34d) events show large enhancement of the SAH (by 40 gpm) and the AH system, which is stronger by 25 gpm in its core. The longitudinal expansion of the SAmH, visible during these periods goes together with its strengthening by approximately 15 gpm. Type I and III events also show the enhancement in the wave 1 stratospheric structure, while the vertical connection between the UTLS SAH and SAmH and the ridge in the stratosphere is not featured during type III cases.

The 45°S mean of geopotential height anomalies during the October (Fig. 5.35a) show a wave 1 ridge in the stratosphere shifted to the east from its September's position. The southernmost extension of the SAH system is no longer vertically connected with that feature and the system itself is diminished by 20 gpm from its September's climatological strength. Type I cases (Fig. 5.35b) at this latitude show a strengthening of the anticyclones over the Indian Ocean and expansion of the SAmH, while the Eastern Pacific High undergoes greatest relative enhancement in comparison with the climatological mean. This system connects with a stronger ridge aloft. The decay of the wave 1 amplitude in the stratosphere characterizes the type II events (Fig. 5.35c) and is marked by the positive anomaly in geopotential height residing in a center of the trough together with a negative difference to the west and east of it. This leads to a westward shift in phase of the wave 1 as well as similar migration of the anticyclonic centers in the troposphere and UTLS region marked by a series of interlocked

Reproduced with permission of the copyright owner. Further reproduction prohibited without permission.

negative and positive differences in the geopotential height. A signal opposite in phase is revealed during type III cases in the stratosphere (Fig. 5.35d), where there is a slight eastward shift (in comparison with climatology) in phase of the wave 1, while the IOH, SAH and SAmH are in positions similar to the type II and climatological means. The SAH is stronger by approximately 30 gpm during these events and extends further south.

5.11. Discussion

As the winter to spring transition progresses, the relative strength of the AH generally diminishes, while the SAH and its western Indian Ocean manifestation grows. This is shown not only by the mean of type III but also by the changing partition between types in the 3 months analyzed. The ten Augusts include 80, 186 and 44 days of type I, II and III events, respectively, while September shows a similar partition of 91, 183 and 26 days, reflecting a very active period for the IOH. The partition is then changed into 89, 112 and 109 days in the October showing unchanged number of days when the AH was the major active anticyclone at 22°S but triple the number of days with clear enhancement of the SAH and relative calm over the central Indian Ocean.

The analysis of geopotential height, temperature and zonal wind anomalies, as well as column ozone distribution resulted in following findings:

a) The core of the ASWJ during type I and III events tends to undergo enhancement. A gradual overall decay as time proceeds is worth noting and agrees with previous studies of the SH flow structure.

Reproduced with permission of the copyright owner. Further reproduction prohibited without permission.

b) The apparent two-core structure of the ASWJ is also attributable to the type I and III geopotential height structure.

c) Type III events show a larger activity of the SAmH which also undergoes enhancement during the late transition period in October.

d) The TOMS data analysis showed a general tendency for the column ozone to increase from August to October for each year. This is due to increased availability of ozone in its production regions as time marches toward October as well as the cumulative transport processes in the wave active SH midlatitudes.

e) The dependence of the column ozone on the type of events as well as the geometry of the TH outflow was also established, with the type I preference of a sharp ozone maximum south of the ASWJ, the elongated and weakened ozone maximum shifted toward the central Indian Ocean inherent with type II, and finally type III events which are similar to type II but with higher ozone maximum, characterized by the 300 DU contour closely following the SAH and SAmH contours.

Reproduced with permission of the copyright owner. Further reproduction prohibited without permission.

	August		
Year	**Type I**	**Type II**	**Type III**
1995	13-22	5-12, 23-31	1-4
1996	10-15, 28-31	1-9, 16-27	
1997	8-12	1-7, 12-21, 26-31	13-15
1998	1-7	8-11, 18-23, 24-31	12-17
1999	20-23	1-15, 24-31	16-19
2000	25-30	1-11, 18-24, 31	12-17
2001	19-21	3-6, 13-18, 27-31	1-2, 7-12, 22-26
2002	1-3, 9-11, 23-31	4-8, 12-22	
2003	4-12	13-31	1-3
2004	21-31	1-10, 16-20	11-15
	September		
Year	Type I	Type II	Type III
1995	11-22	1-10, 23-30	
1996	23-30	8-22	1-7
1997	6-11, 16-23	1-5, 12-15,24-30	
1998		4-30	1-3
1999		4-17, 22-30	1-3, 18-21
2000	7-14, 22-27	1-6, 15-21, 28-30	
2001		1-30	
2002	1-10, 17-23, 30	11-16, 24-29	
2003	5-6, 14-30	1-4, 7-13	
2004	1-6	7-13, 23-30	14-22
	October		
Year	Type I	Type II	Type III
1995	6-12, 23-31	16-22	1-5, 13-15
1996	22-25	1-5, 12-21, 26-31	6-11
1997	6-11, 26-31	1-5	12-25
1998	4-10, 21-25	1-3, 11-20, 29-31	26-28
1999		1-31	
2000	4-14, 23-25	1-3	15-22, 26-31
2001	15-19		1-14, 20-31
2002	1-9	10-13, 24-31	14-23
2003	1-3, 24-27		4-23, 28-31
2004	3-6, 13-18	1-2, 7-12, 23-31	19-22

Table 5.1. Detailed index of dates included in each of the event types during the 1995-2004 period.

Reproduced with permission of the copyright owner. Further reproduction prohibited without permission.

	Event type		
August	I	II	III
1995	10	17	4
1996	10	21	0
1997	5	23	3
1998	7	18	6
1999	4	23	4
2000	6	19	6
2001	3	15	13
2002	15	16	0
2003	9	19	3
2004	11	15	5
	80	**186**	**44**
September			
1995	12	18	0
1996	8	15	7
1997	14	16	0
1998	0	27	3
1999	0	23	7
2000	14	16	0
2001	0	30	0
2002	18	12	0
2003	19	11	0
2004	6	15	9
	91	**183**	**26**
October			
1995	16	7	8
1996	4	21	6
1997	12	5	14
1998	12	16	3
1999	0	31	0
2000	14	3	14
2001	5	0	26
2002	9	12	10
2003	7	0	24
2004	10	17	4
	89	**112**	**109**
Total day count for the type	**260**	**481**	**179**

Table 5.2. Number of days per event during 1995-2004 period.

Reproduced with permission of the copyright owner. Further reproduction prohibited without permission.

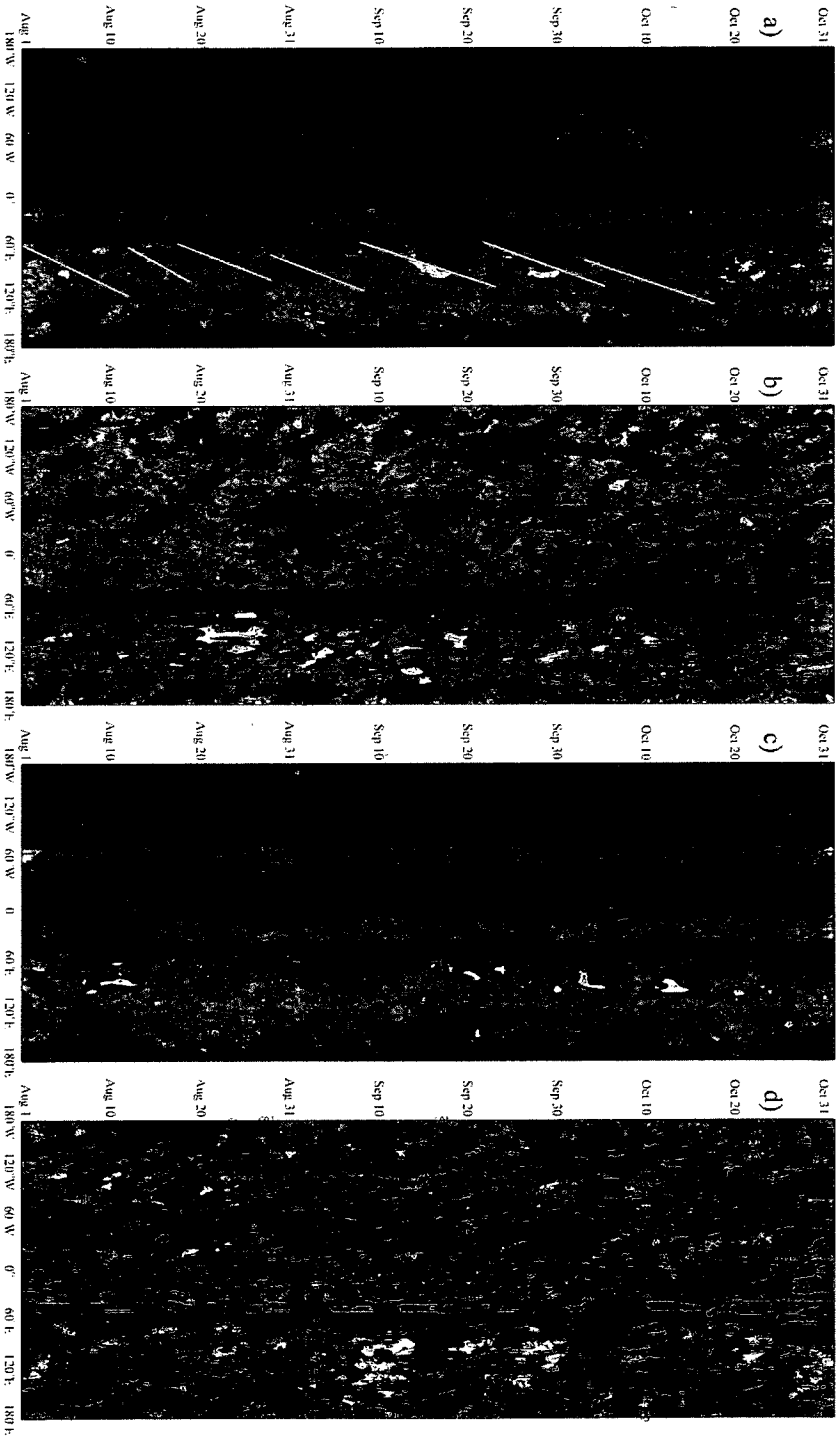

Figure 5.1. Time-Longitude Hovmöller diagram of NCAR daily OLR from August through October for years: a) 1995 (0°), b) 1995 (10°N), c) 1996 (0°) and d) 1996 (10°N). Contour interval is 25 W/m^2, with values ranging from 50-250 W/m^2.

Reproduced with permission of the copyright owner. Further reproduction prohibited without permission.

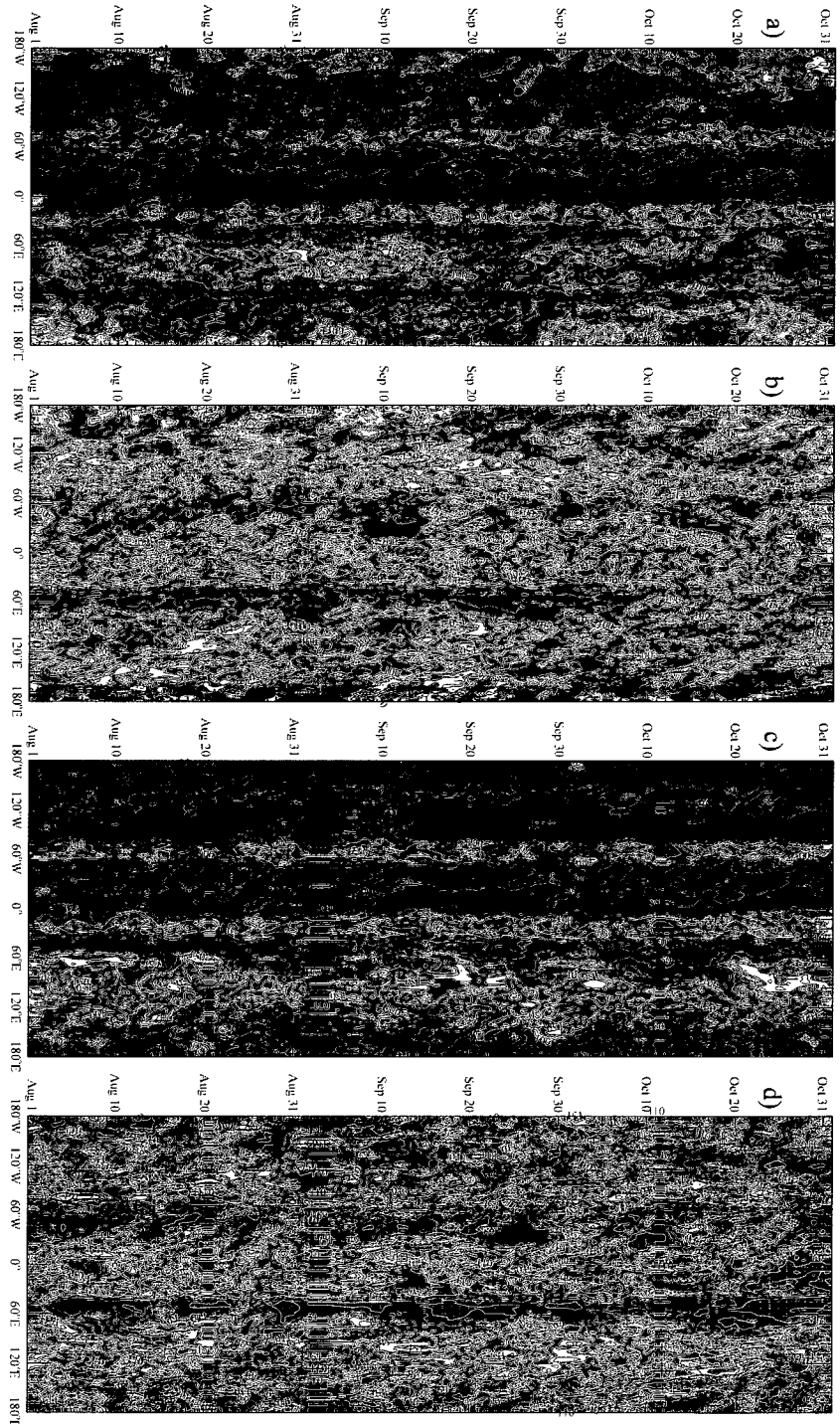

Figure 5.2. Time-Longitude Hovmöller diagram of NCAR daily OLR from August through October for years: a) 1997 (0°), b) 1997 (10°N), c) 1998 (0°) and d) 1998 (10°N). Contour interval is 25 W/m^2, with values ranging from 50-250 W/m^2.

Reproduced with permission of the copyright owner. Further reproduction prohibited without permission.

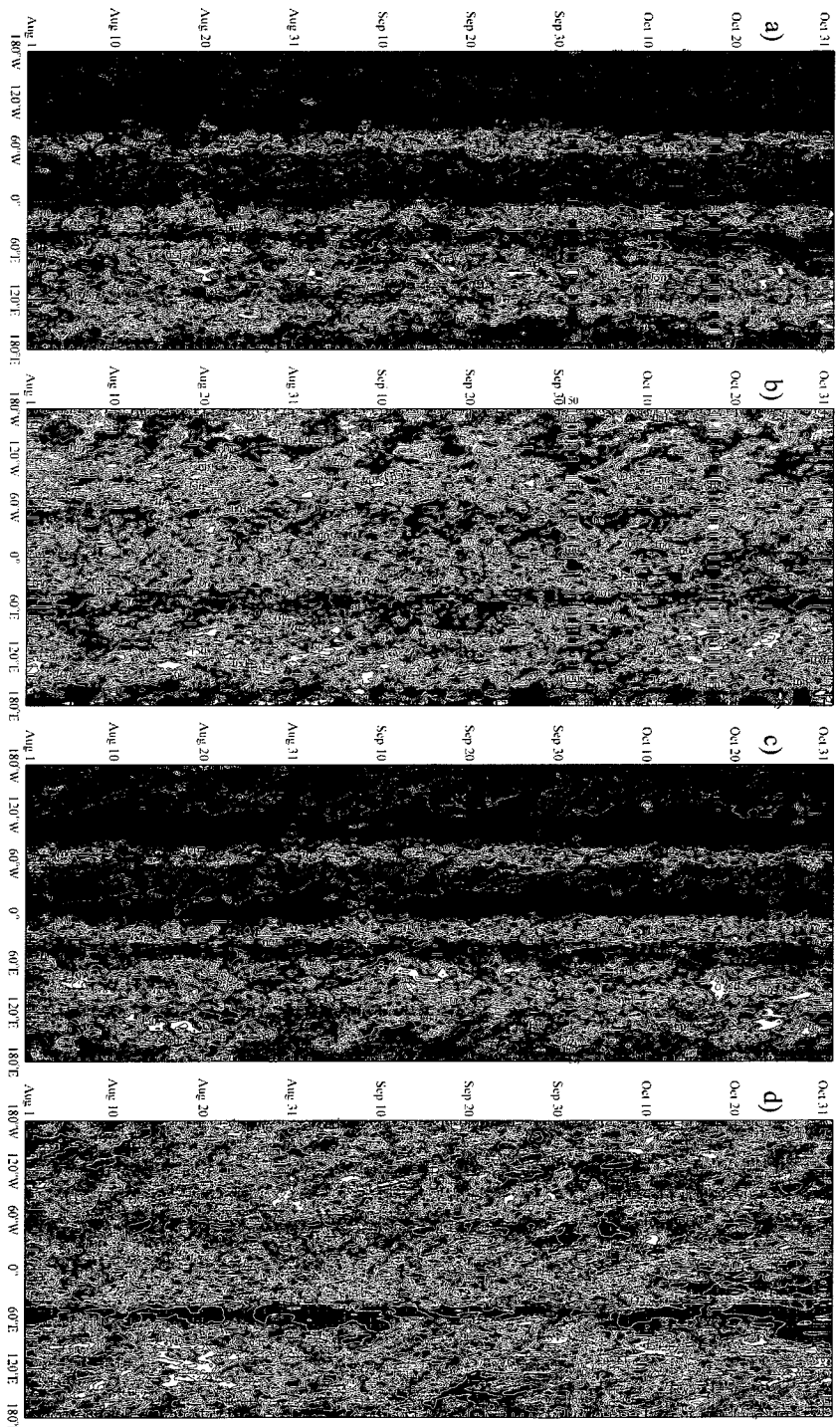

Figure 5.3. Time-Longitude Hovmöller diagram of NCAR daily OLR from August through October for years: a) 1999 (0°), b) 1999 (10°N), c) 2000 (0°) and d) 2000 (10°N). Contour interval is 25 W/m^2, with values ranging from 50-250 W/m^2.

Reproduced with permission of the copyright owner. Further reproduction prohibited without permission.

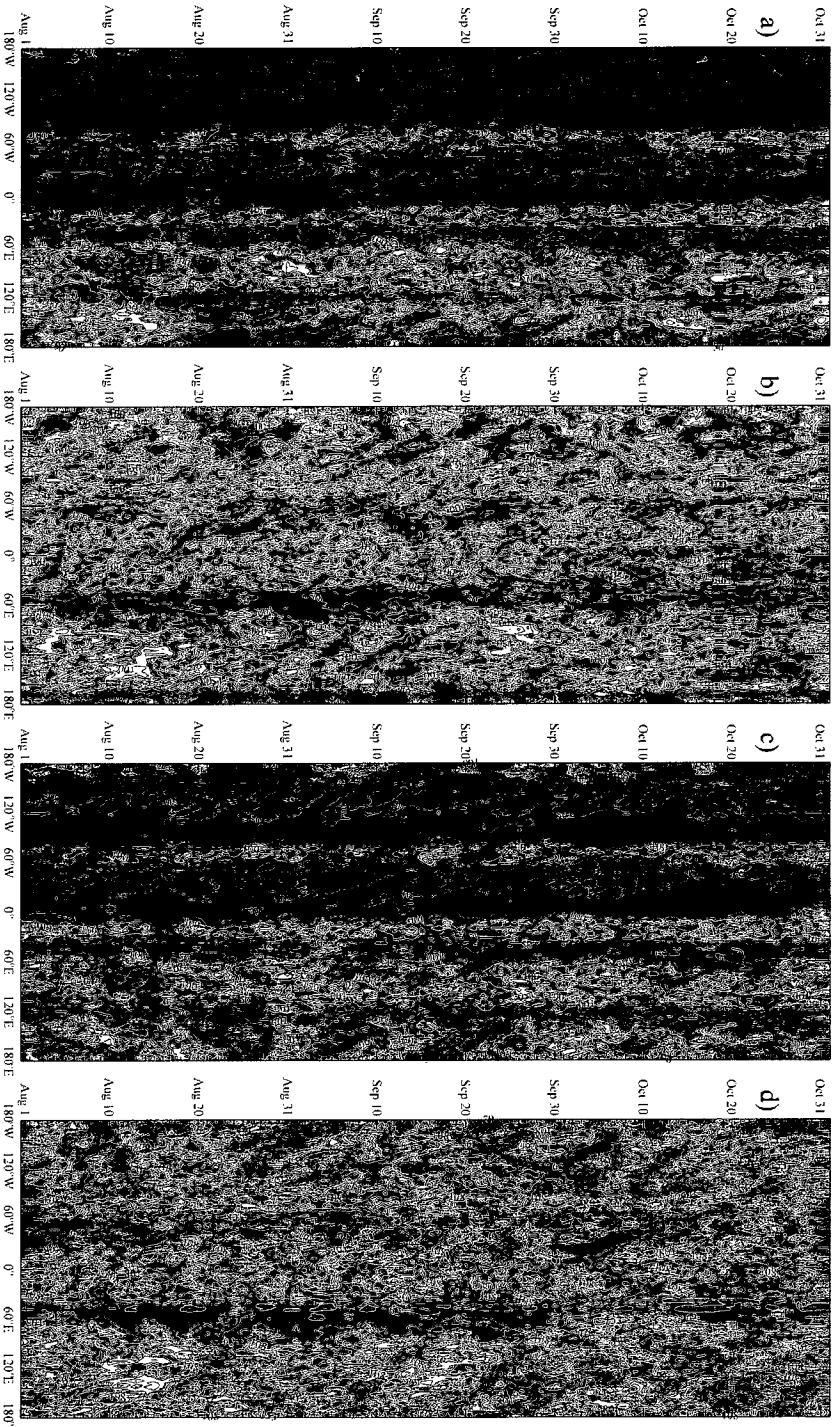

Figure 5.4. Time-Longitude Hovmöller diagram of NCAR daily OLR from August through October for years: a) 2001 (0°), b) 2001 (10°N), c) 2002 (0°) and d) 2002 (10°N). Contour interval is 25 W/m^2, with values ranging from 50-250 W/m^2.

Reproduced with permission of the copyright owner. Further reproduction prohibited without permission.

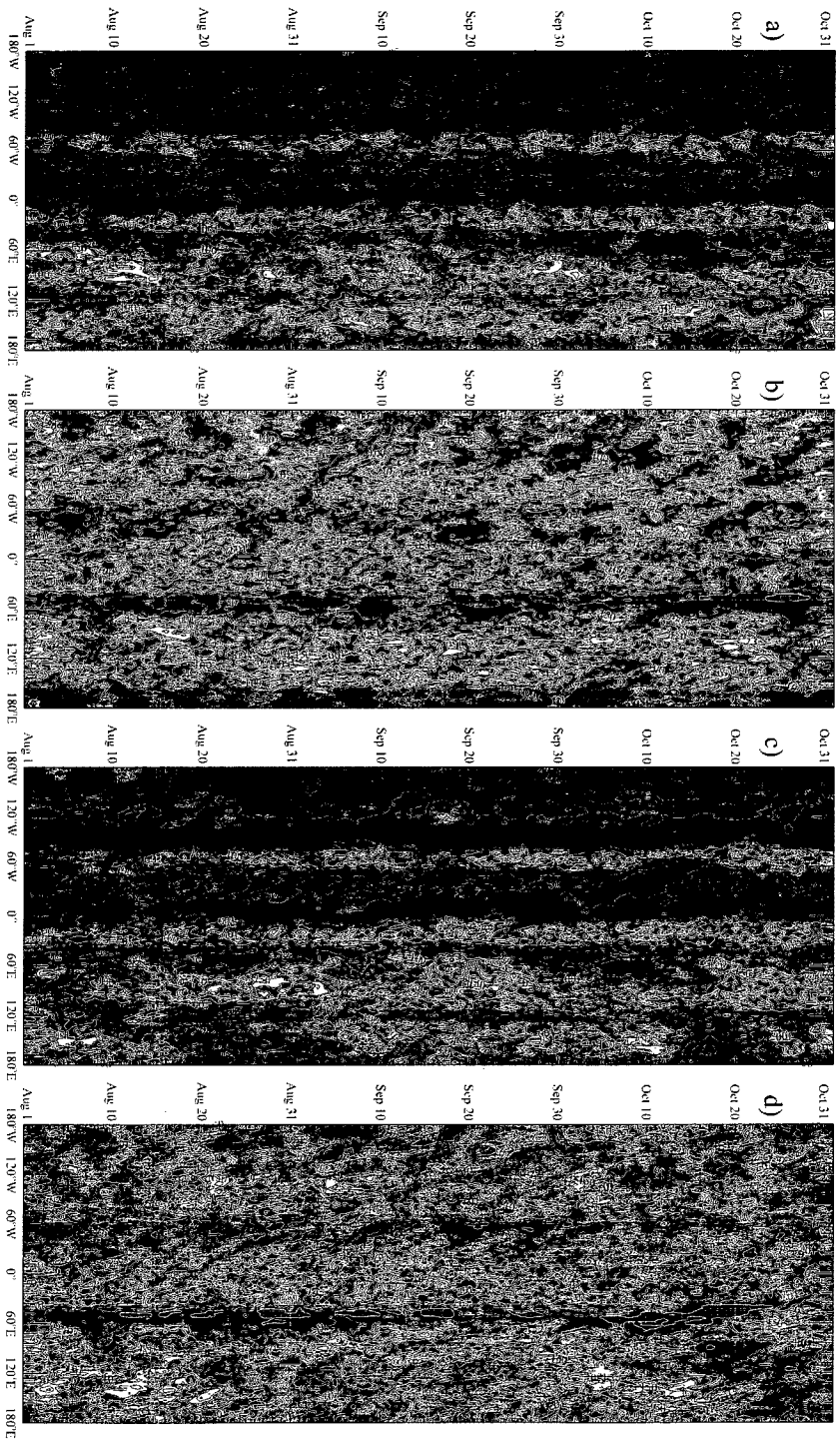

Figure 5.5. Time-Longitude Hovmöller diagram of NCAR daily OLR from August through October for years: a) 2003 (0°), b) 2003 (10°N), c) 2004 (0°) and d) 2004 (10°N). Contour interval is 25 W/m^2, with values ranging from 50-250 W/m^2.

Reproduced with permission of the copyright owner. Further reproduction prohibited without permission.

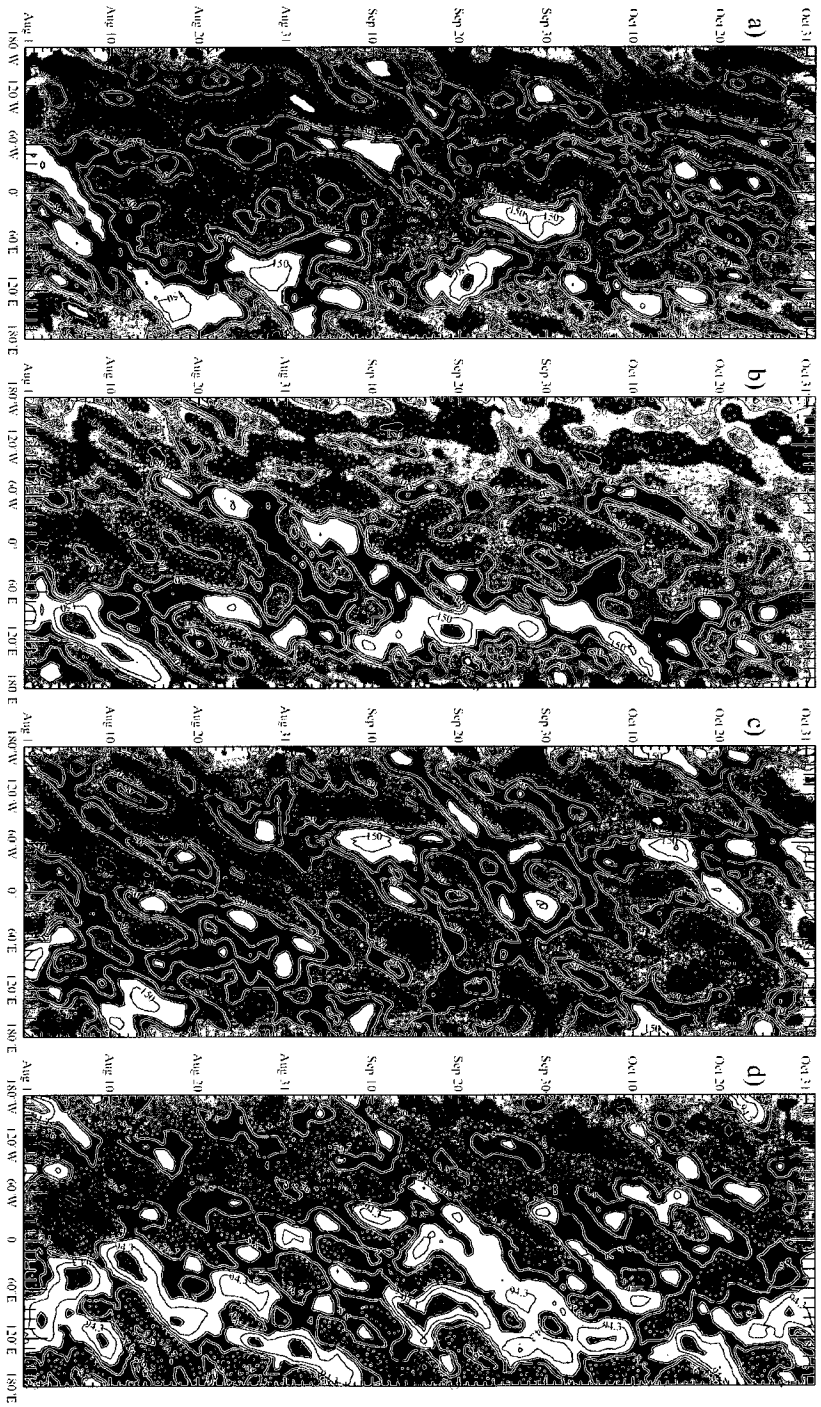

Figure 5.6. Time-Longitude Hovmöller diagram of ECMWF daily geopotential height anomalies at 25°S for August - October for years: a) 1995, b) 1996, c) 1997 and d) 1998. Contour interval is 50m, with values ranging from -250 to 250 m.

Reproduced with permission of the copyright owner. Further reproduction prohibited without permission.

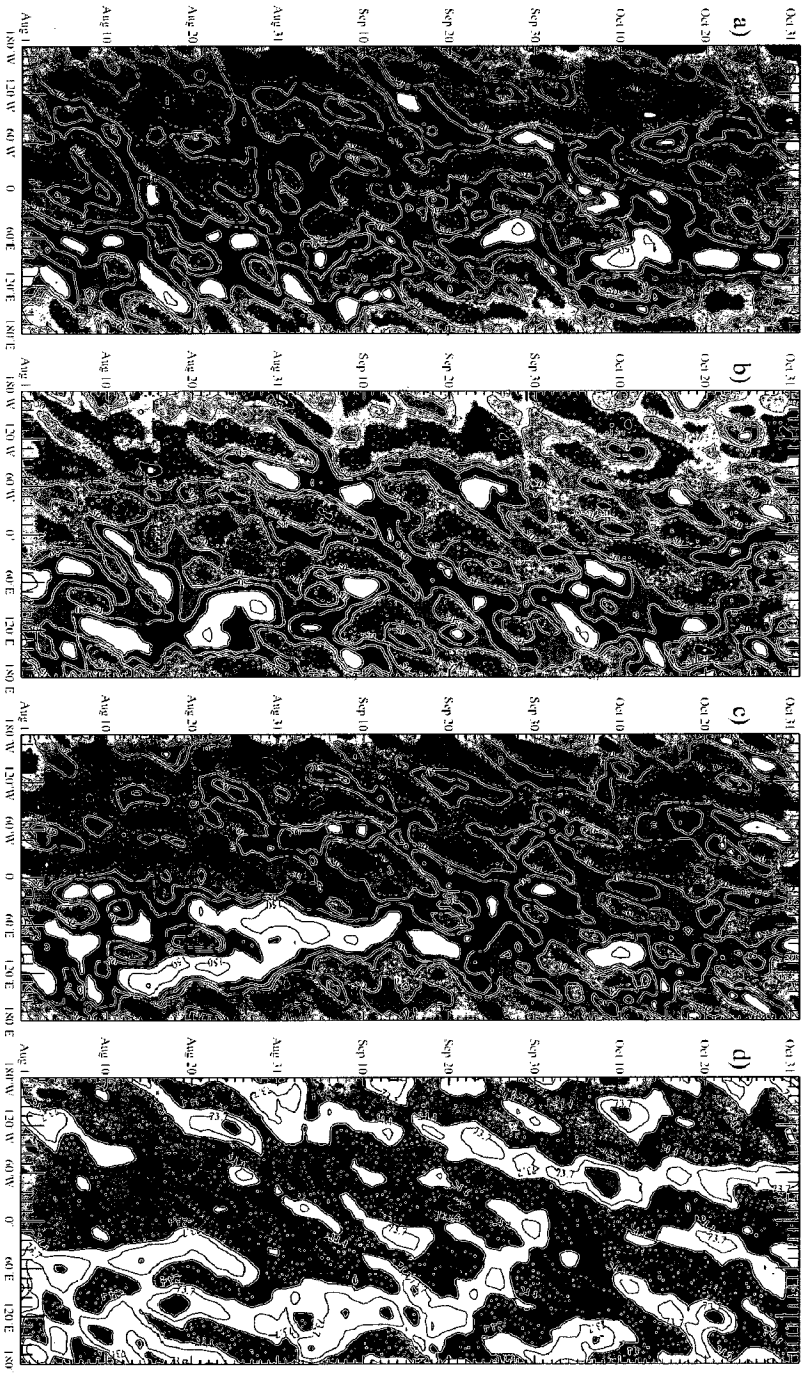

Figure 5.7. Time-Longitude Hovmöller diagram of ECMWF daily geopotential height anomalies at 25°S for August - October for years: a) 1999, b) 2000, c) 2001 and d) 2002. Contour interval is 50m, with values ranging from -250 to 250 m.

Reproduced with permission of the copyright owner. Further reproduction prohibited without permission.

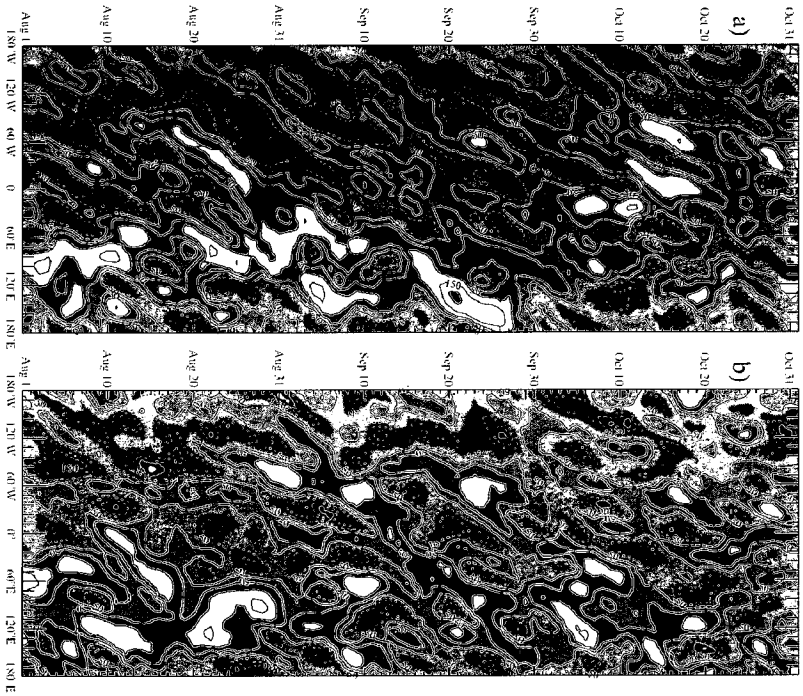

Figure 5.8. Time-Longitude Hovmöller diagram of ECMWF daily geopotential height anomalies at 25°S for August - October for years: a) 2003, b) 2004. Contour interval is 50m, with values ranging from -250 to 250 m.

Reproduced with permission of the copyright owner. Further reproduction prohibited without permission.

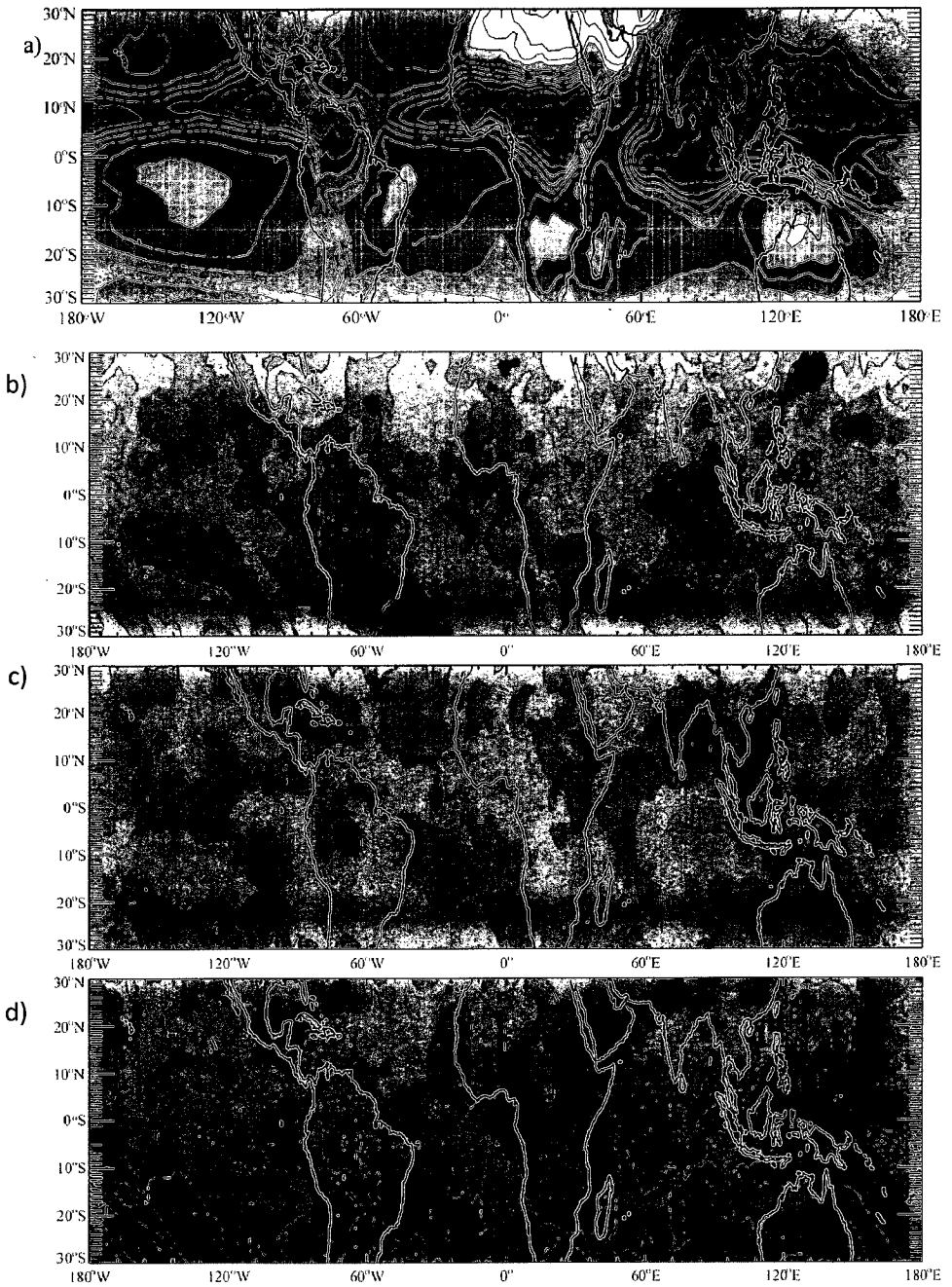

Fig. 9 Figure 5.9. NOAA OLR composite averages for August during years 1995-2004: a) monthly, b) difference Type I cases – monthly average, c) Type II cases – monthly average, d) Type III cases – monthly average. Contour interval is 20 W/m^2 for a) and 5 W/m^2 for differences with values ranging from 80-340 W/m^2 and -35/+35 W/m^2 respectively.

Reproduced with permission of the copyright owner. Further reproduction prohibited without permission.

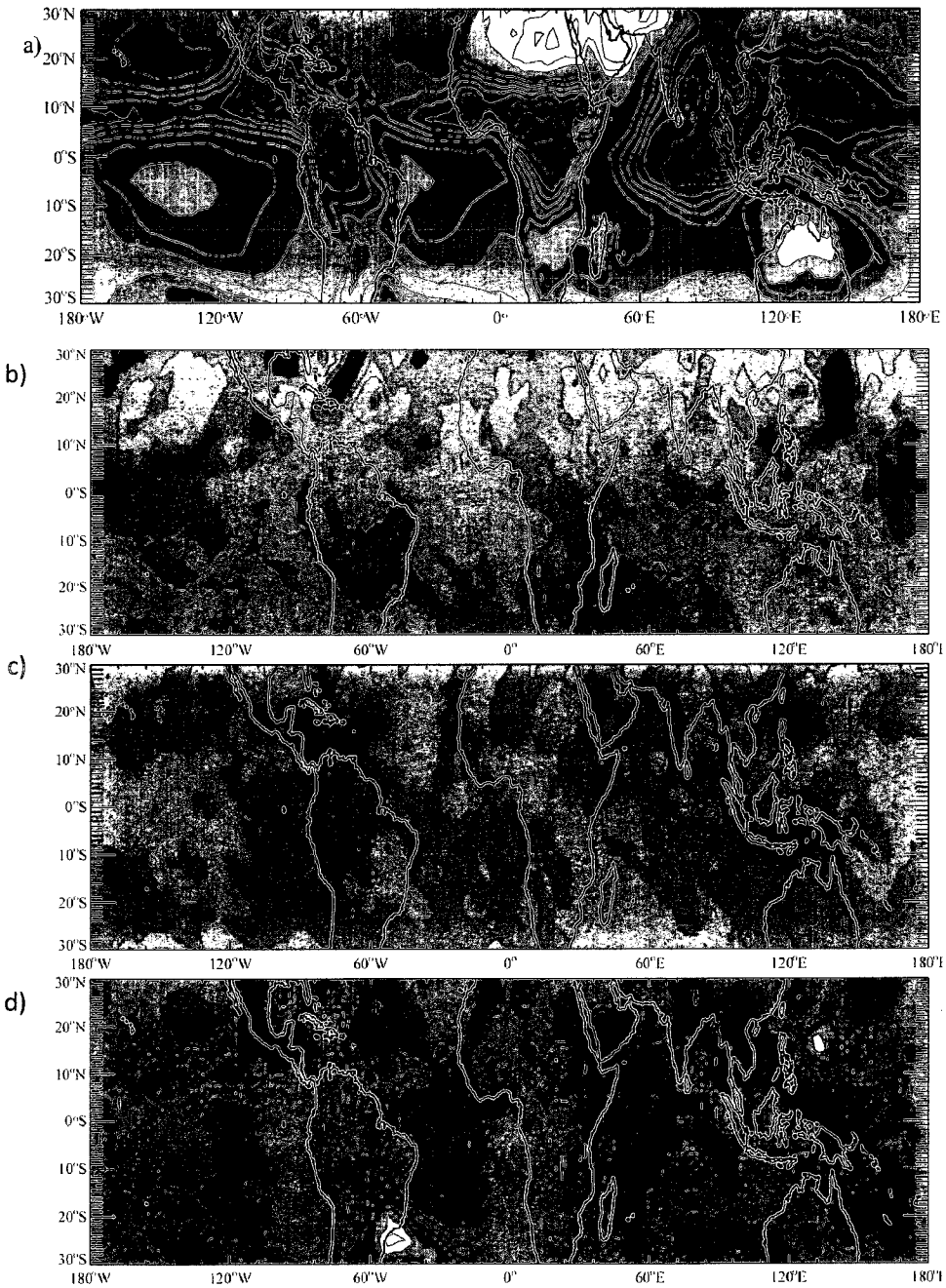

Figure 5.10. NOAA OLR composite averages for September during years 1995-2004: a) monthly, b) difference Type I cases – monthly average, c) Type II cases – monthly average, d) Type III cases – monthly average. Contour interval is 20 W/m^2 for a) and 5 W/m^2 for differences with values ranging from 80-340 W/m^2 and -35/+35 W/m^2 respectively.

Reproduced with permission of the copyright owner. Further reproduction prohibited without permission.

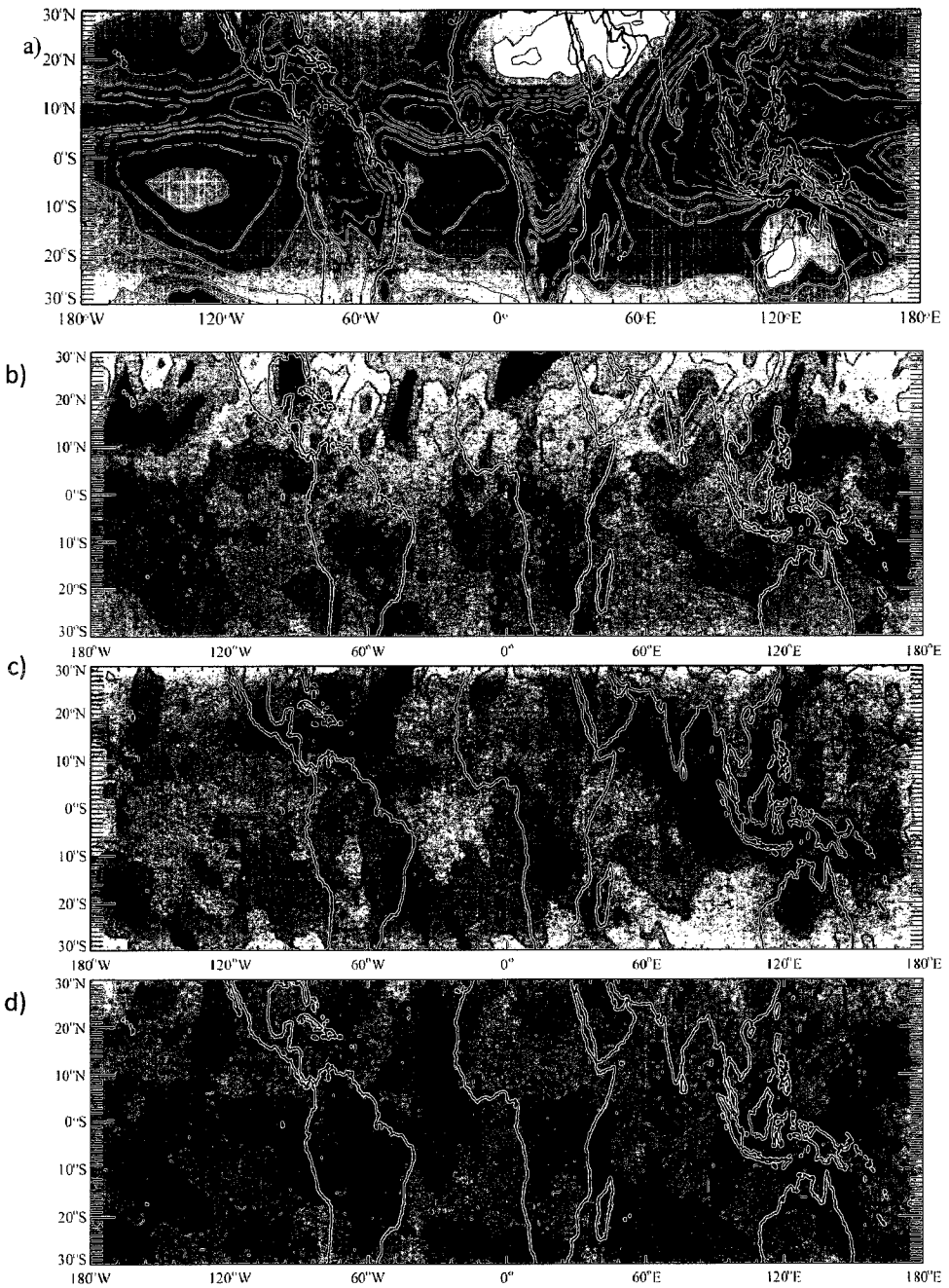

Figure 5.11. NOAA OLR composite averages for October during years 1995-2004: a) monthly, b) difference Type I cases – monthly average, c) Type II cases – monthly average, d) Type III cases – monthly average. Contour interval is 20 W/m^2 for a) and 5 W/m^2 for differences with values ranging from 80-340 W/m^2 and -35/+35 W/m^2 respectively.

Reproduced with permission of the copyright owner. Further reproduction prohibited without permission.

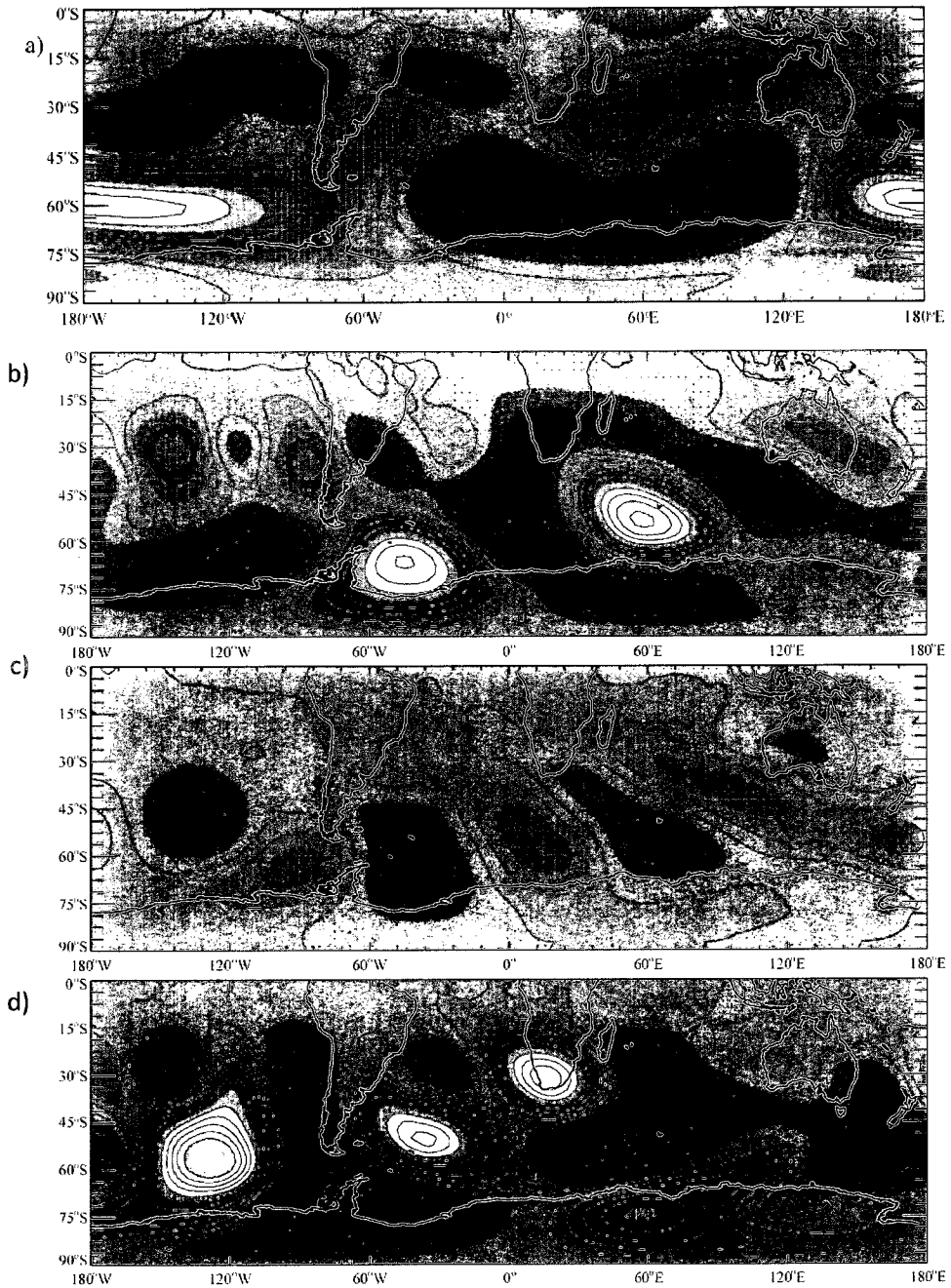

Figure 5.12. ECMWF geopotential height anomalies composite averages for August during years 1995-2004: a) monthly, b) difference Type I cases – monthly average, c) Type II cases – monthly average, d) Type III cases – monthly average. Contour interval is 25m for a) and 10 m for differences with values ranging from -200/+250 m and -100/+100 m respectively.

Reproduced with permission of the copyright owner. Further reproduction prohibited without permission.

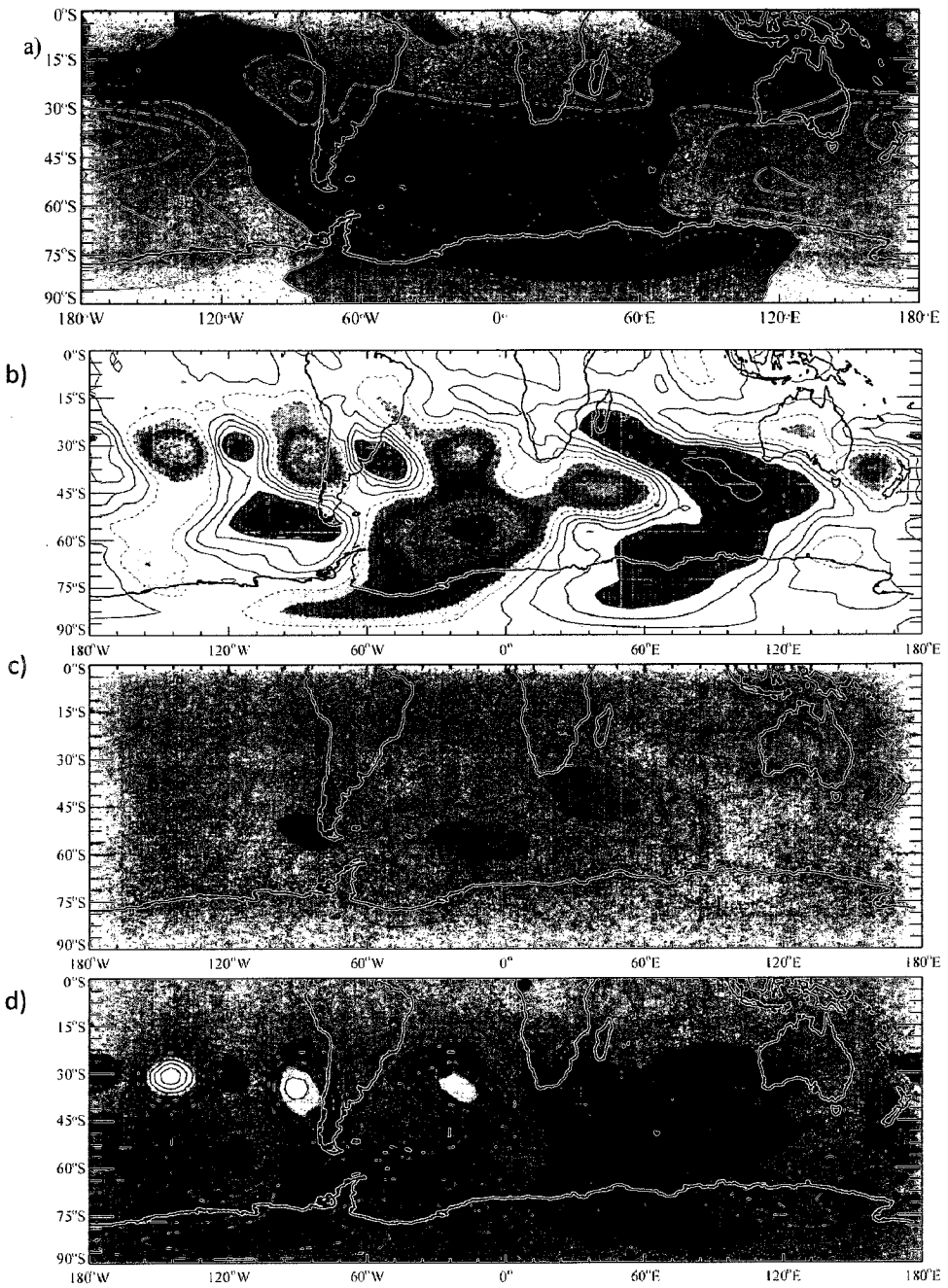

Figure 5.13. ECMWF temperature anomalies composite averages for August during years 1995-2004: a) monthly, b) difference Type I cases – monthly average, c) Type II cases – monthly average, d) Type III cases – monthly average. Contour interval is 1K for a) and 0.25K for differences with values ranging from -9/+10 K and -4/+4 K respectively.

Reproduced with permission of the copyright owner. Further reproduction prohibited without permission.

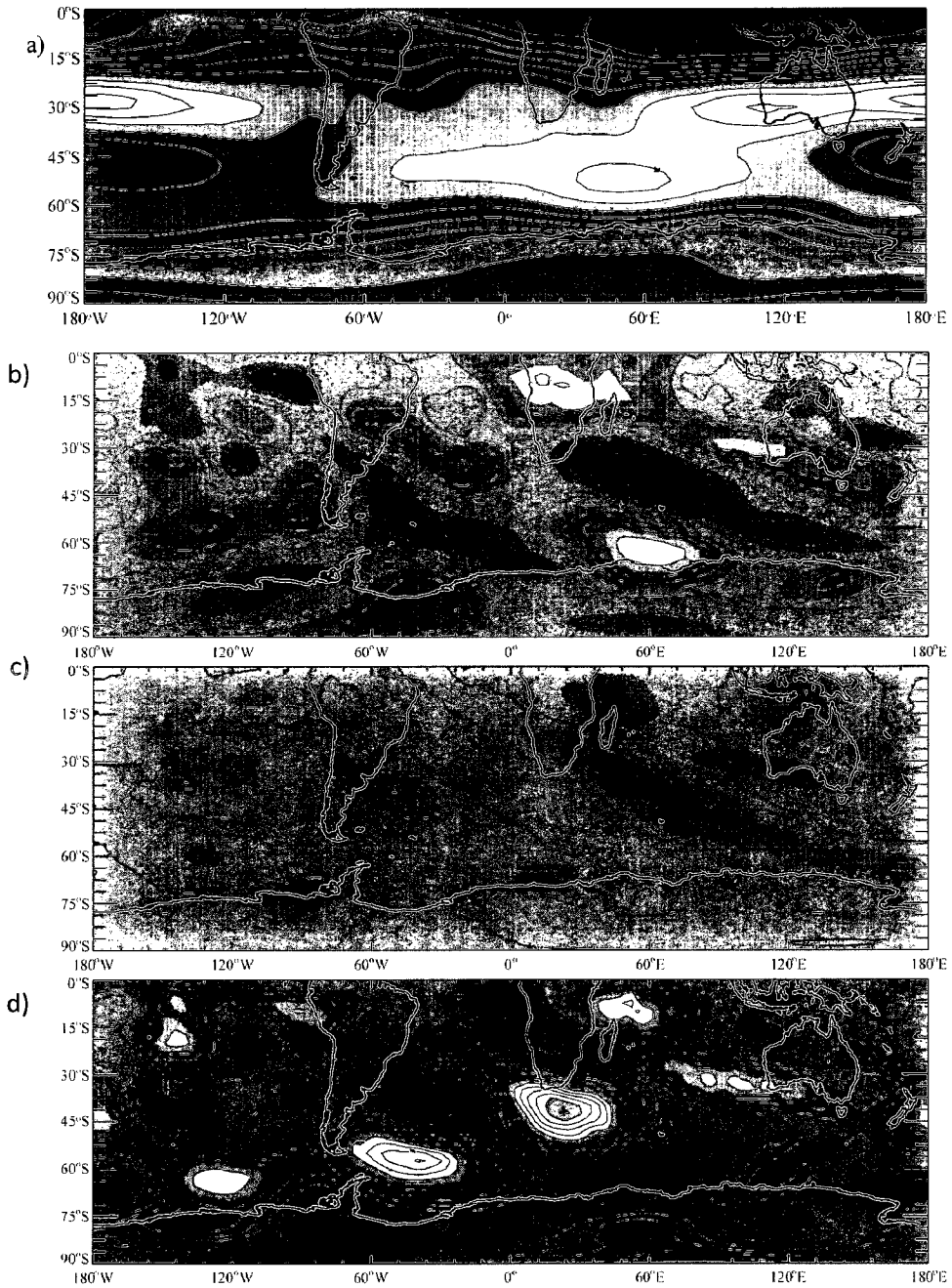

Figure 5.14. ECMWF zonal wind composite averages for August during years 1995-2004: a) monthly, b) difference Type I cases – monthly average, c) Type II cases – monthly average, d) Type III cases – monthly average. Contour interval is 5 m/s for a) and 1 m/s for differences with values ranging from -30/+50 m and -11/+11 m respectively.

Reproduced with permission of the copyright owner. Further reproduction prohibited without permission.

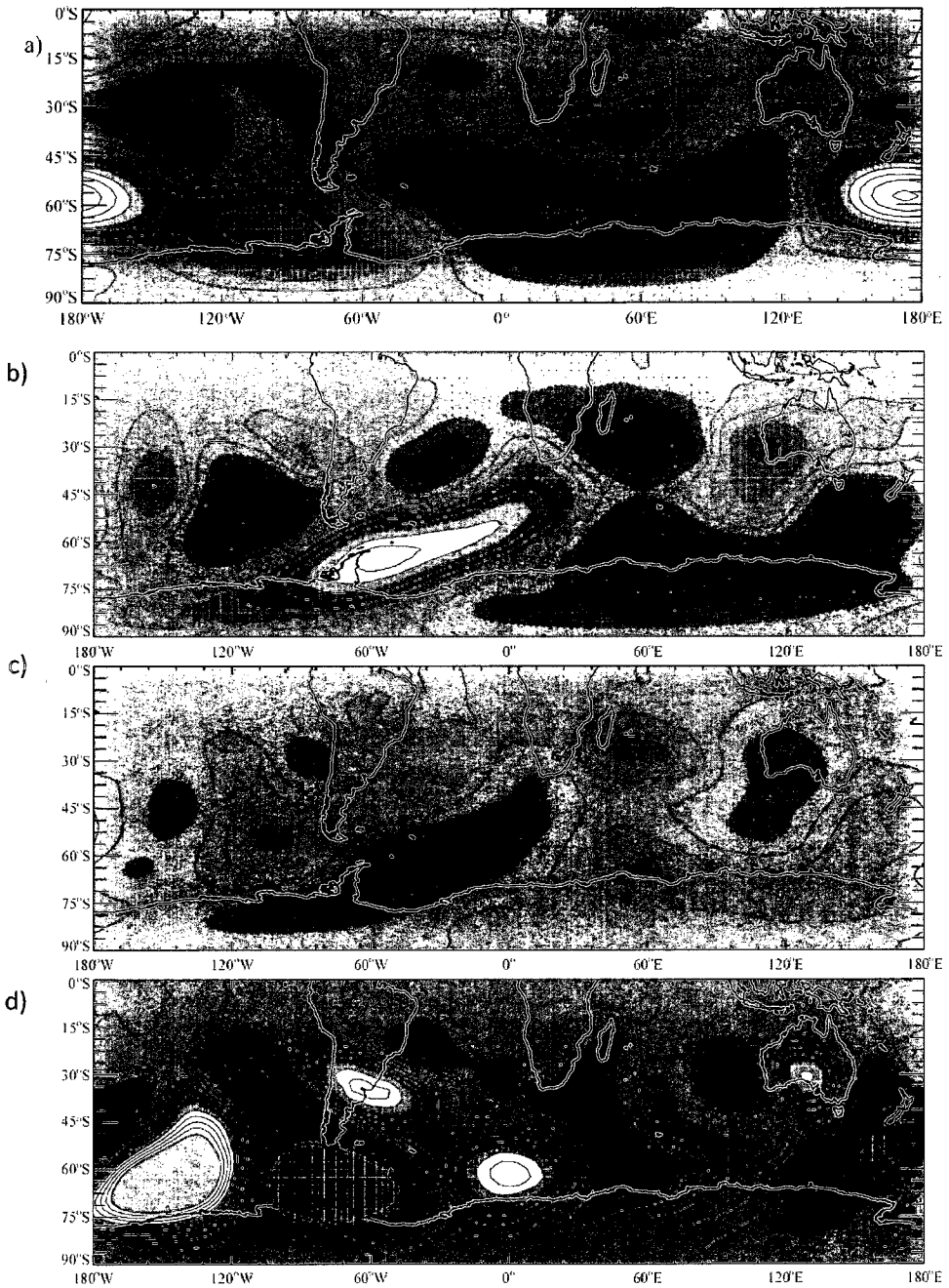

Figure 5.15. ECMWF geopotential height anomalies composite averages for September during years 1995-2004: a) monthly, b) difference Type I cases – monthly average, c) Type II cases – monthly average, d) Type III cases – monthly average. Contour interval is 25m for a) and 10 m for differences with values ranging from -200/+250 m and -100/+100 m respectively.

Reproduced with permission of the copyright owner. Further reproduction prohibited without permission.

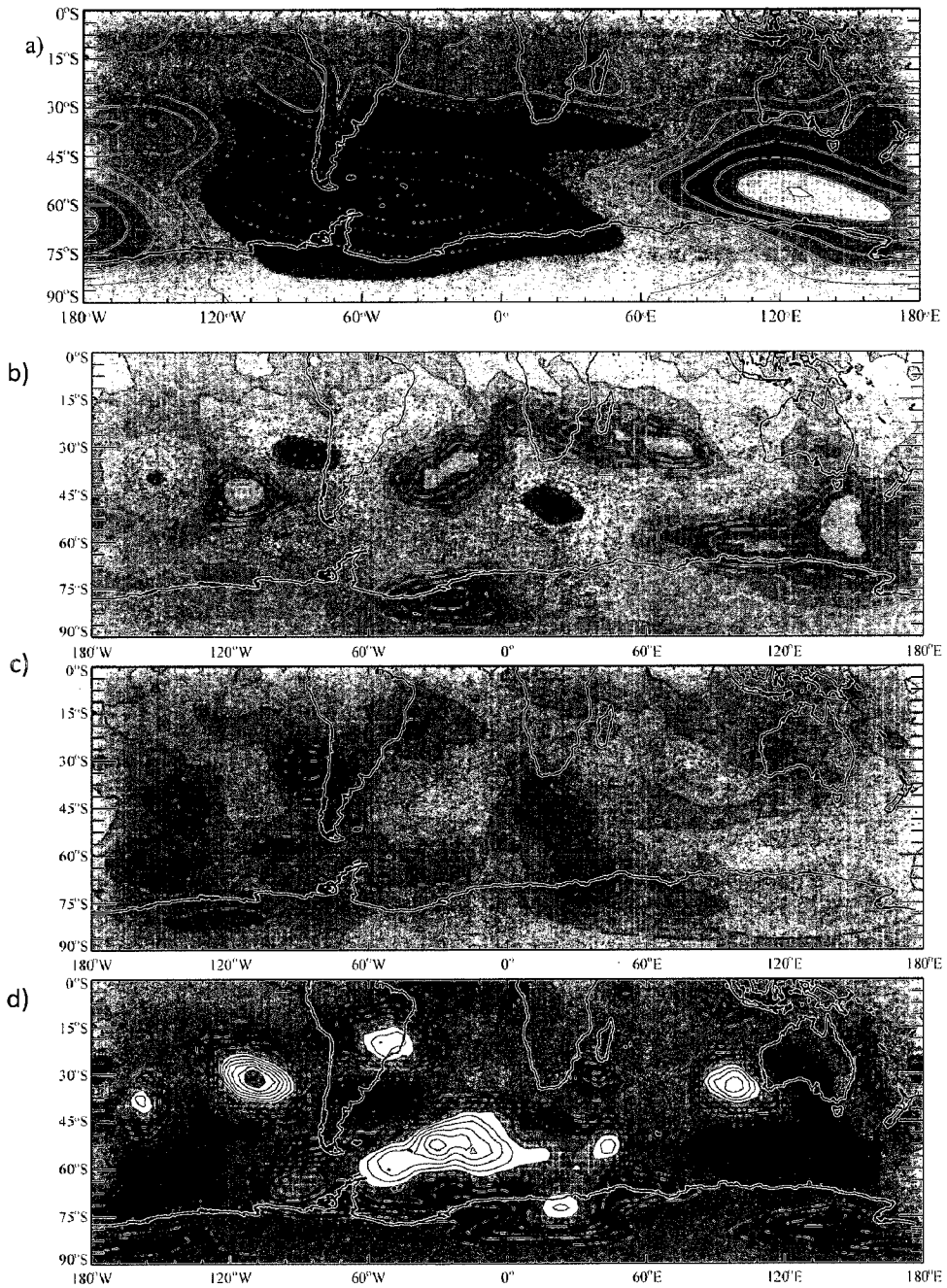

Figure 5.16. ECMWF temperature anomalies composite averages for September during years 1995-2004: a) monthly, b) difference Type I cases – monthly average, c) Type II cases – monthly average, d) Type III cases – monthly average. Contour interval is 1K for a) and 0.25K for differences with values ranging from -9/+10 K and -4/+4 K respectively.

Reproduced with permission of the copyright owner. Further reproduction prohibited without permission.

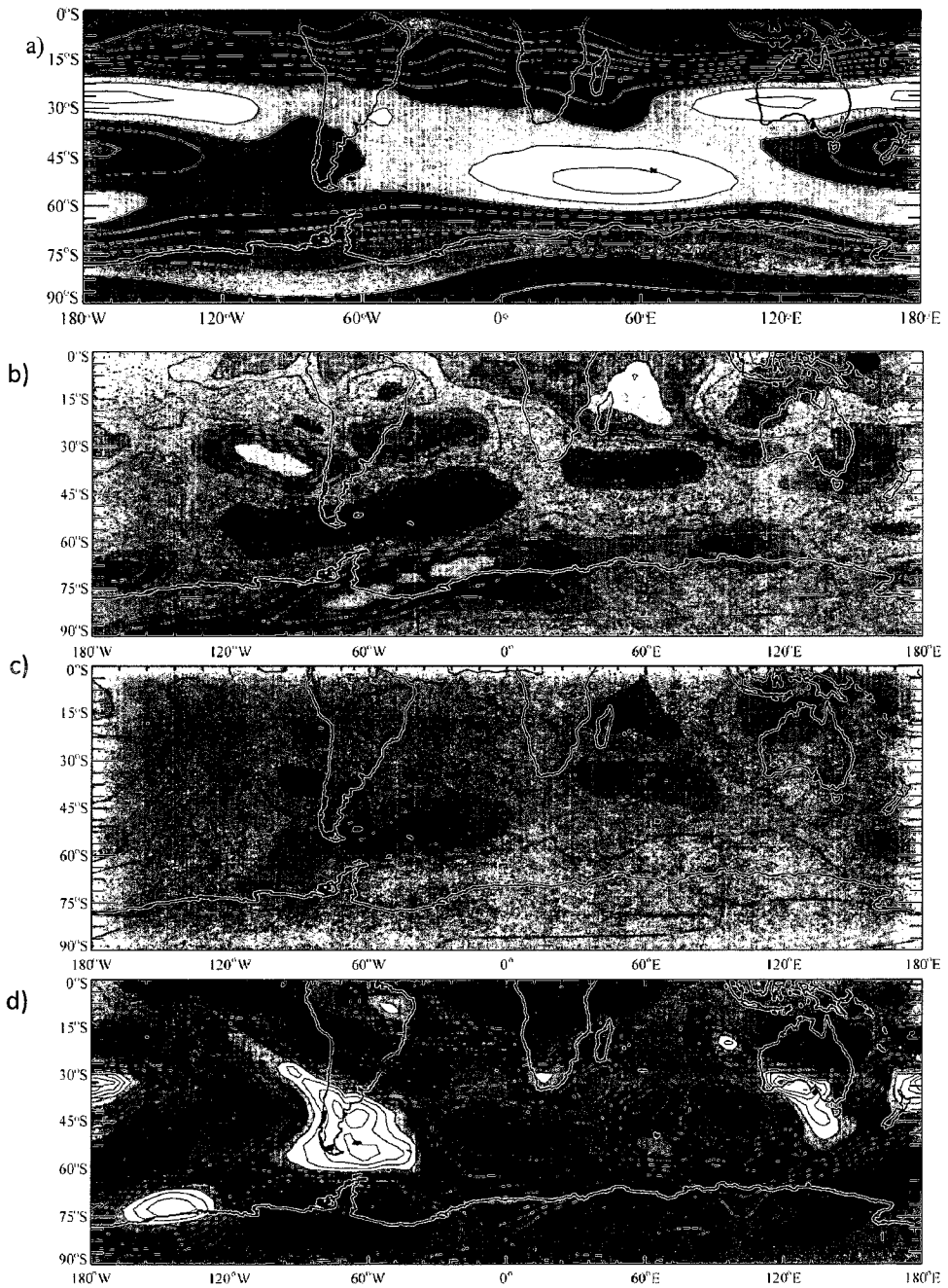

Figure 5.17. ECMWF zonal wind composite averages for September during years 1995-2004: a) monthly, b) difference Type I cases – monthly average, c) Type II cases – monthly average, d) Type III cases – monthly average. Contour interval is 5 m/s for a) and 1 m/s for differences with values ranging from -30/+50 m and -11/+11 m respectively.

Reproduced with permission of the copyright owner. Further reproduction prohibited without permission.

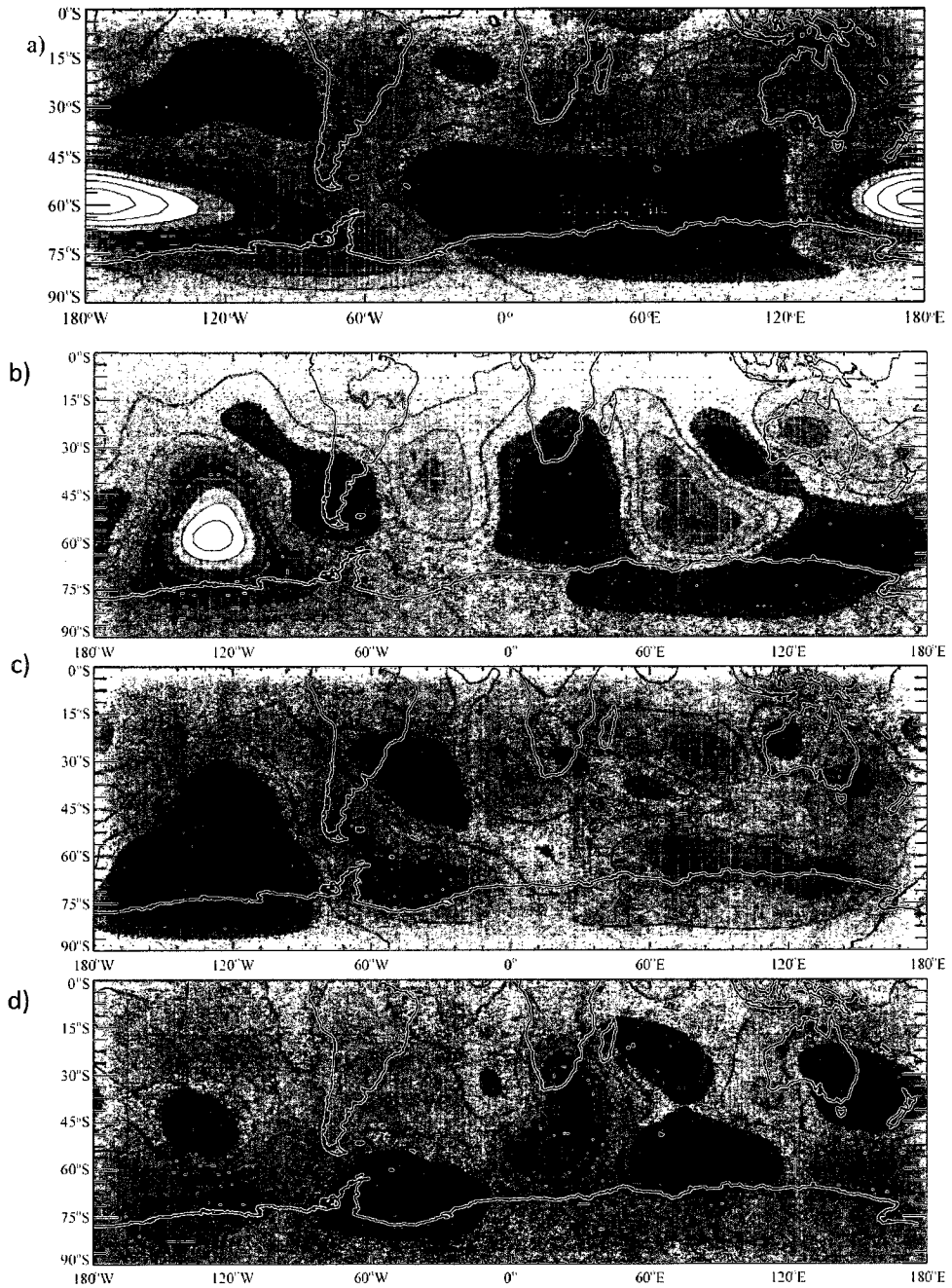

Figure 5.18. ECMWF geopotential height anomalies composite averages for October during years 1995-2004: a) monthly, b) difference Type I cases – monthly average, c) Type II cases – monthly average, d) Type III cases – monthly average. Contour interval is 25m for a) and 10 m for differences with values ranging from -200/+250 m and -100/+100 m respectively.

Reproduced with permission of the copyright owner. Further reproduction prohibited without permission.

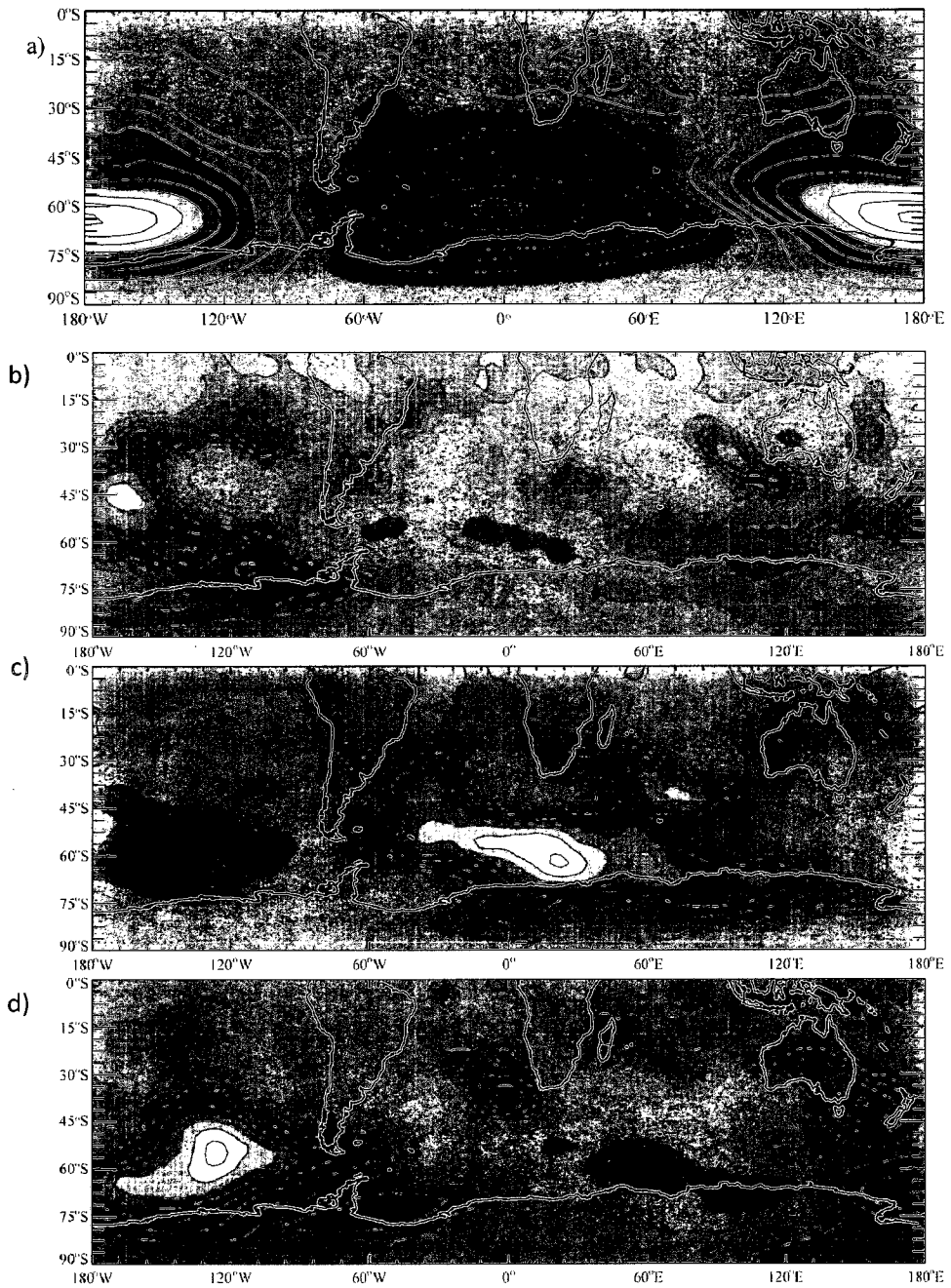

Figure 5.19. ECMWF temperature anomalies composite averages for October during years 1995-2004: a) monthly, b) difference Type I cases – monthly average, c) Type II cases – monthly average, d) Type III cases – monthly average. Contour interval is 1K for a) and 0.25K for differences with values ranging from -9/+10 K and -4/+4 K respectively.

Reproduced with permission of the copyright owner. Further reproduction prohibited without permission.

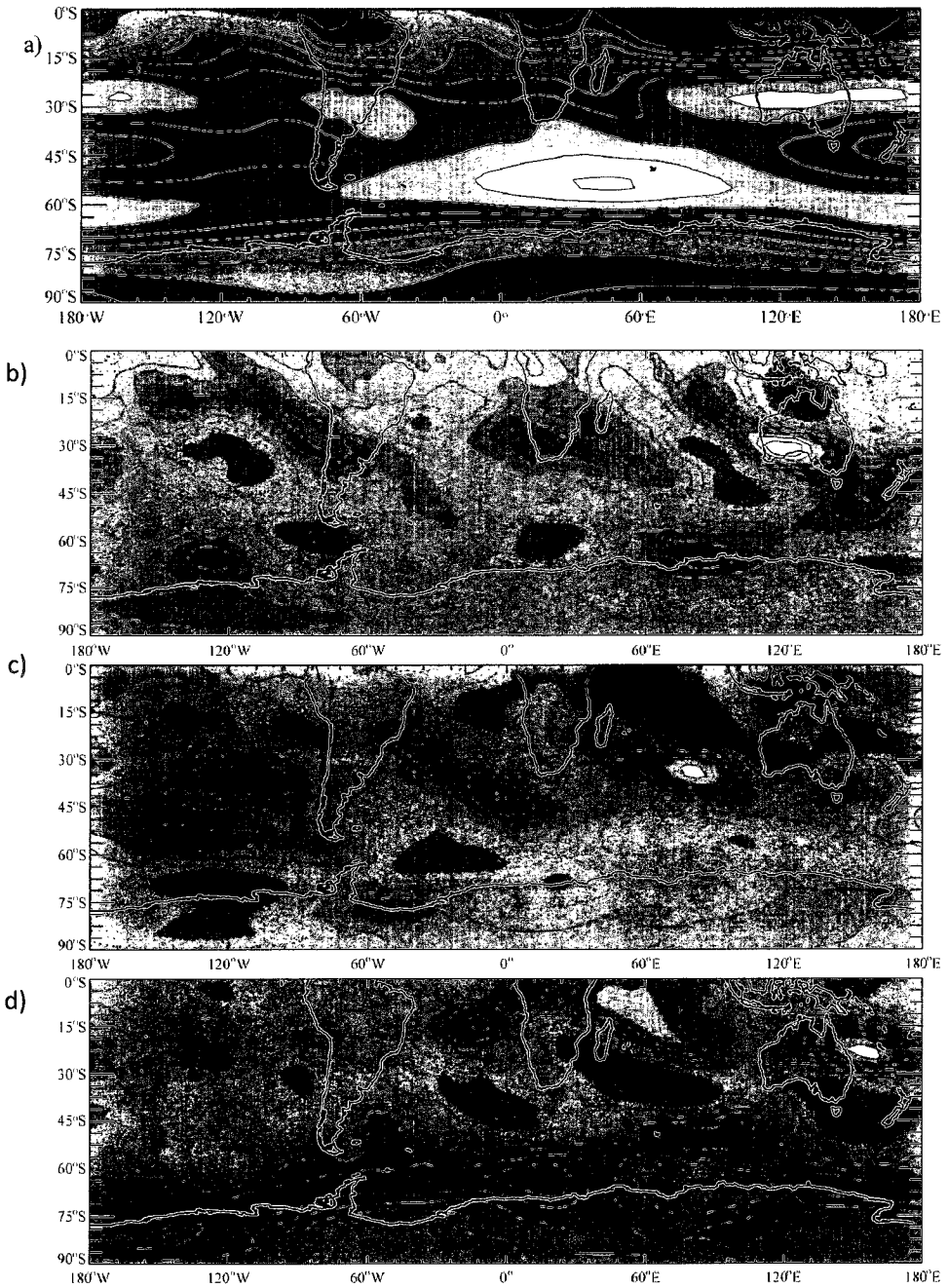

Figure 5.20. ECMWF zonal wind composite averages for October during years 1995-2004: a) monthly, b) difference Type I cases – monthly average, c) Type II cases – monthly average, d) Type III cases – monthly average. Contour interval is 5 m/s for a) and 1 m/s for differences with values ranging from -30/+50 m and -11/+11 m respectively.

Reproduced with permission of the copyright owner. Further reproduction prohibited without permission.

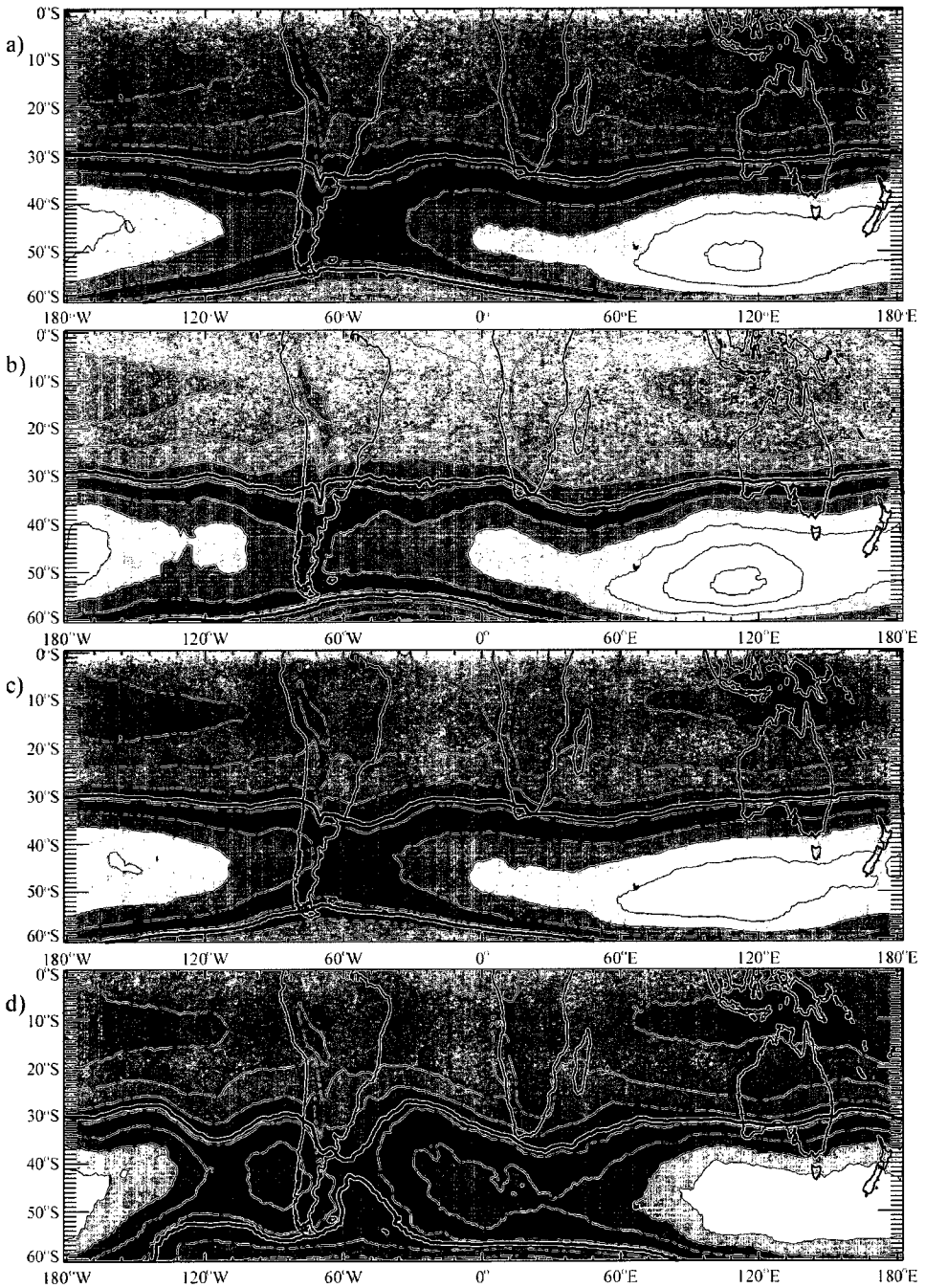

Figure 5.21. TOMS column ozone composite averages for August during years 1995-2004: a) monthly, b) Type I cases, c) Type II cases, d) Type III cases. Contour interval is 30 DU. The 300 DU contour is depicted with wide isoline.

Reproduced with permission of the copyright owner. Further reproduction prohibited without permission.

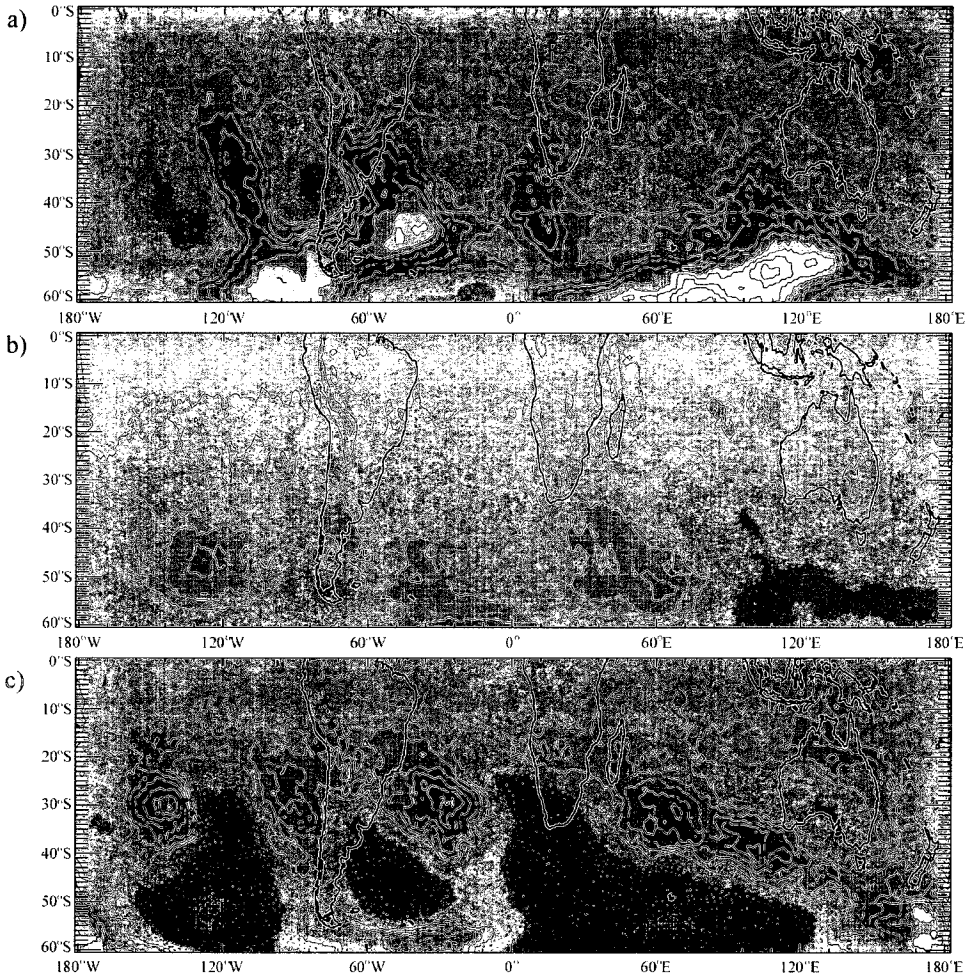

Figure 5.22. Differences in TOMS column ozone composites for August during years 1995-2004: a) Type I cases – monthly average, b) Type II cases – monthly average, c) Type III cases – monthly average. Contour interval is 2 DU, values range from -20 DU to 20 DU.

Reproduced with permission of the copyright owner. Further reproduction prohibited without permission.

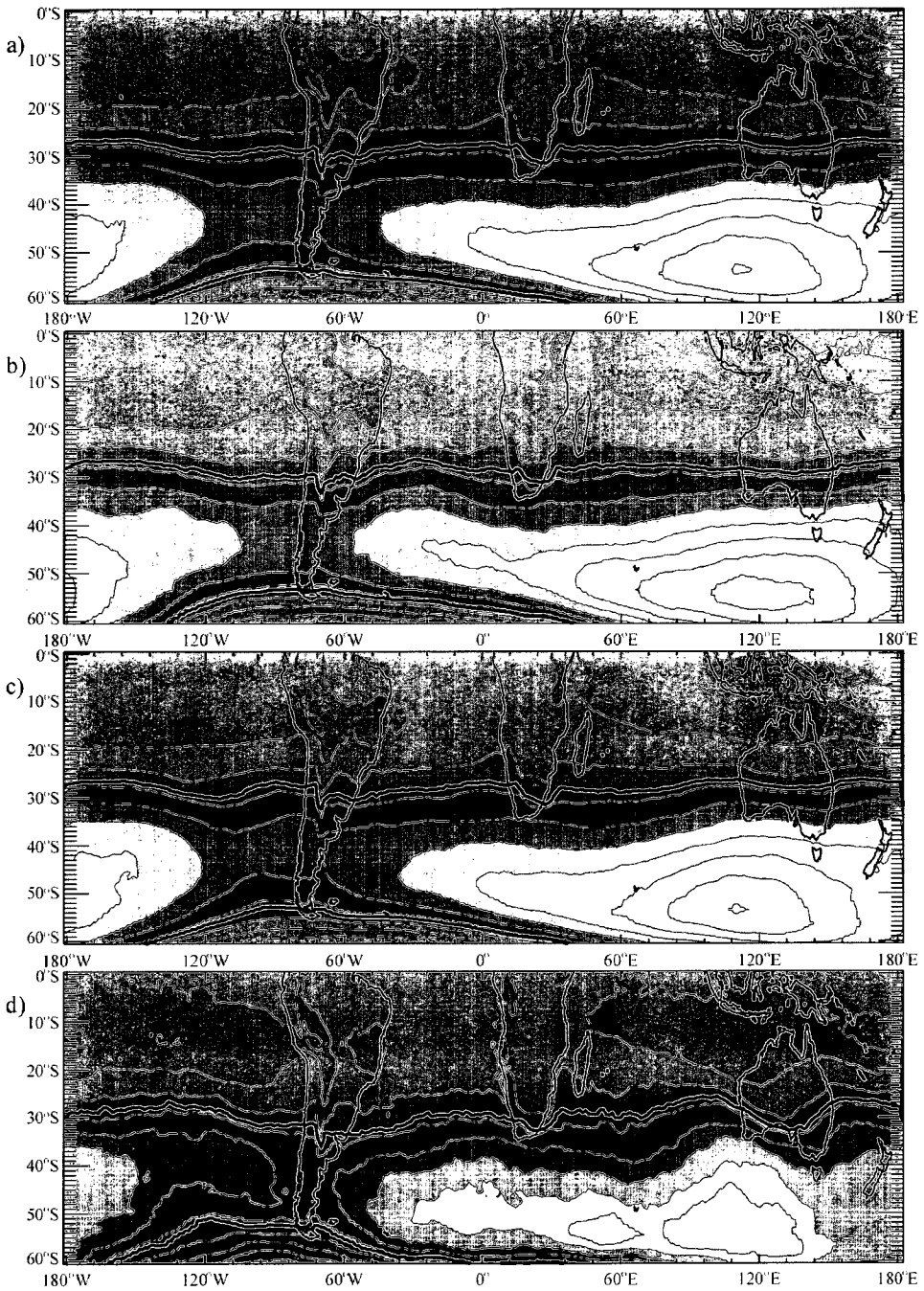

Figure 5.23. TOMS column ozone composite averages for September during years 1995-2004: a) monthly, b) Type I cases, c) Type II cases, d) Type III cases. Contour interval is 30 DU. The 300 DU contour is depicted with wide isoline.

Reproduced with permission of the copyright owner. Further reproduction prohibited without permission.

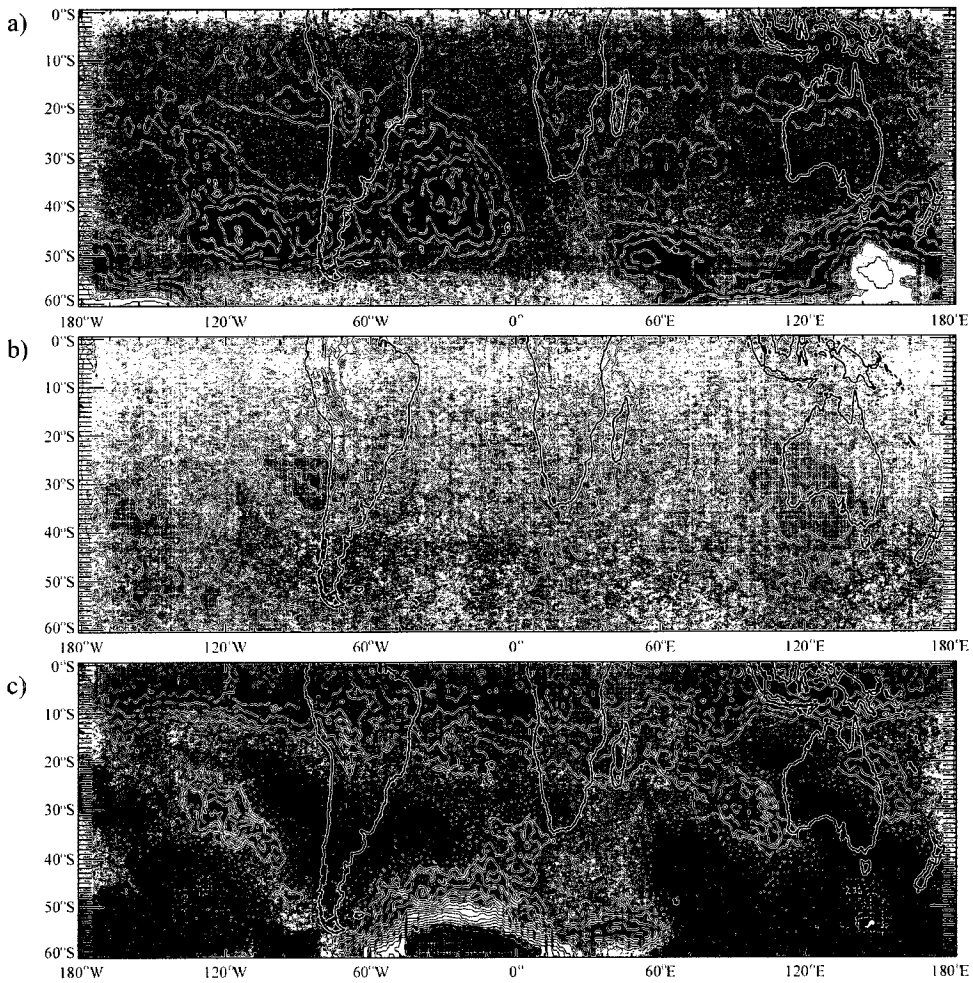

Figure 5.24. Differences in TOMS column ozone composites for September during years 1995-2004: a) Type I cases – monthly average, b) Type II cases – monthly average, c) Type III cases – monthly average. Contour interval is 2 DU, values range from -40 DU to 40 DU.

Reproduced with permission of the copyright owner. Further reproduction prohibited without permission.

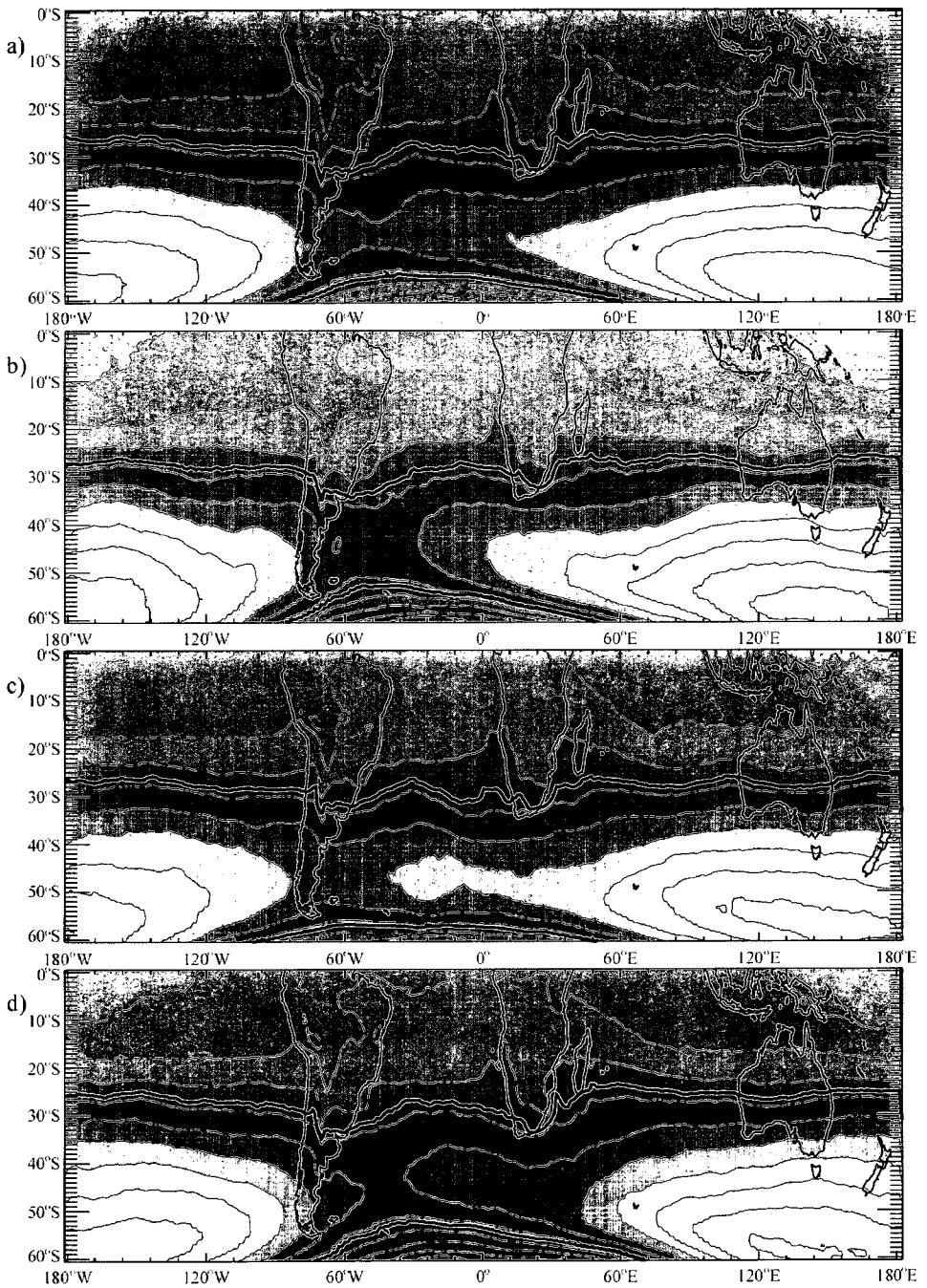

Figure 5.25. TOMS column ozone composite averages for October during years 1995-2004: a) monthly, b) Type I cases, c) Type II cases, d) Type III cases. Contour interval is 30 DU. The 300 DU contour is depicted with wide isoline.

Reproduced with permission of the copyright owner. Further reproduction prohibited without permission.

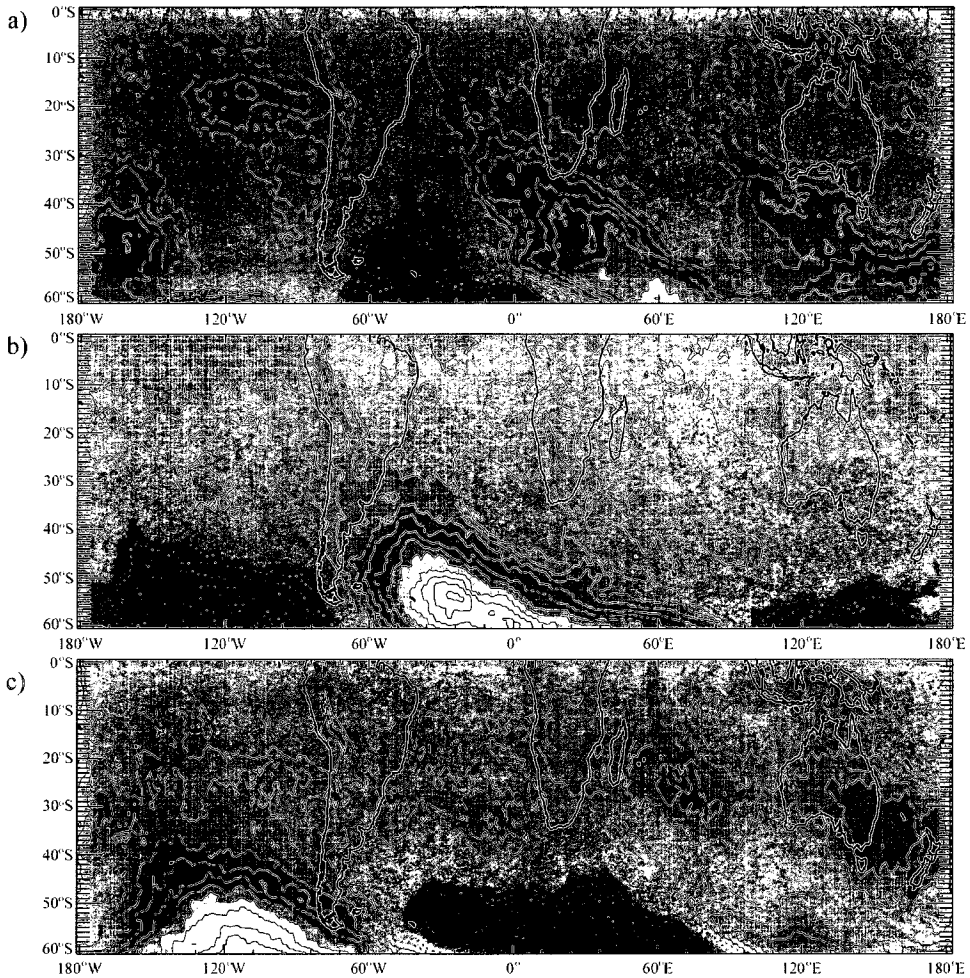

Figure 5.26. Differences in TOMS column ozone composites for October during years 1995-2004: a) Type I cases – monthly average, b) Type II cases – monthly average, c) Type III cases – monthly average. Contour interval is 2 DU, values range from -20 DU to 20 DU.

Reproduced with permission of the copyright owner. Further reproduction prohibited without permission.

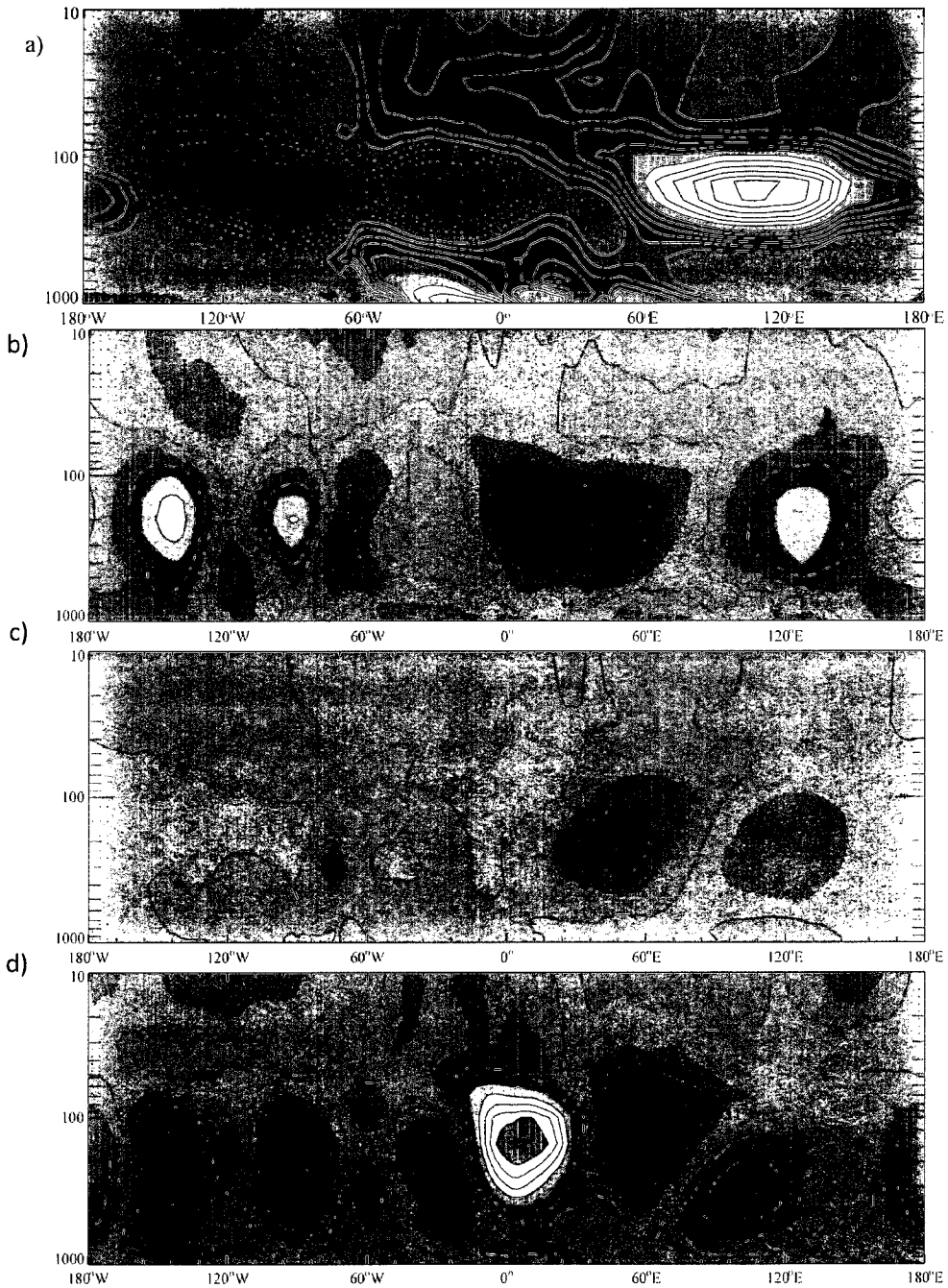

Figure 5.27. Longitude-Altitude averages of ECMWF geopotential height anomalies composites for August during years 1995-2004 and their difference from the monthly mean at 20°S: a) monthly mean b) Type I cases – monthly average, c) Type II cases – monthly average, d) Type III cases – monthly average. Contour interval is 10 m (a) and 5 m (b,c,d). Values range from -80 m to 80 m (a) and -40 to 40 m (b,c,d).

Reproduced with permission of the copyright owner. Further reproduction prohibited without permission.

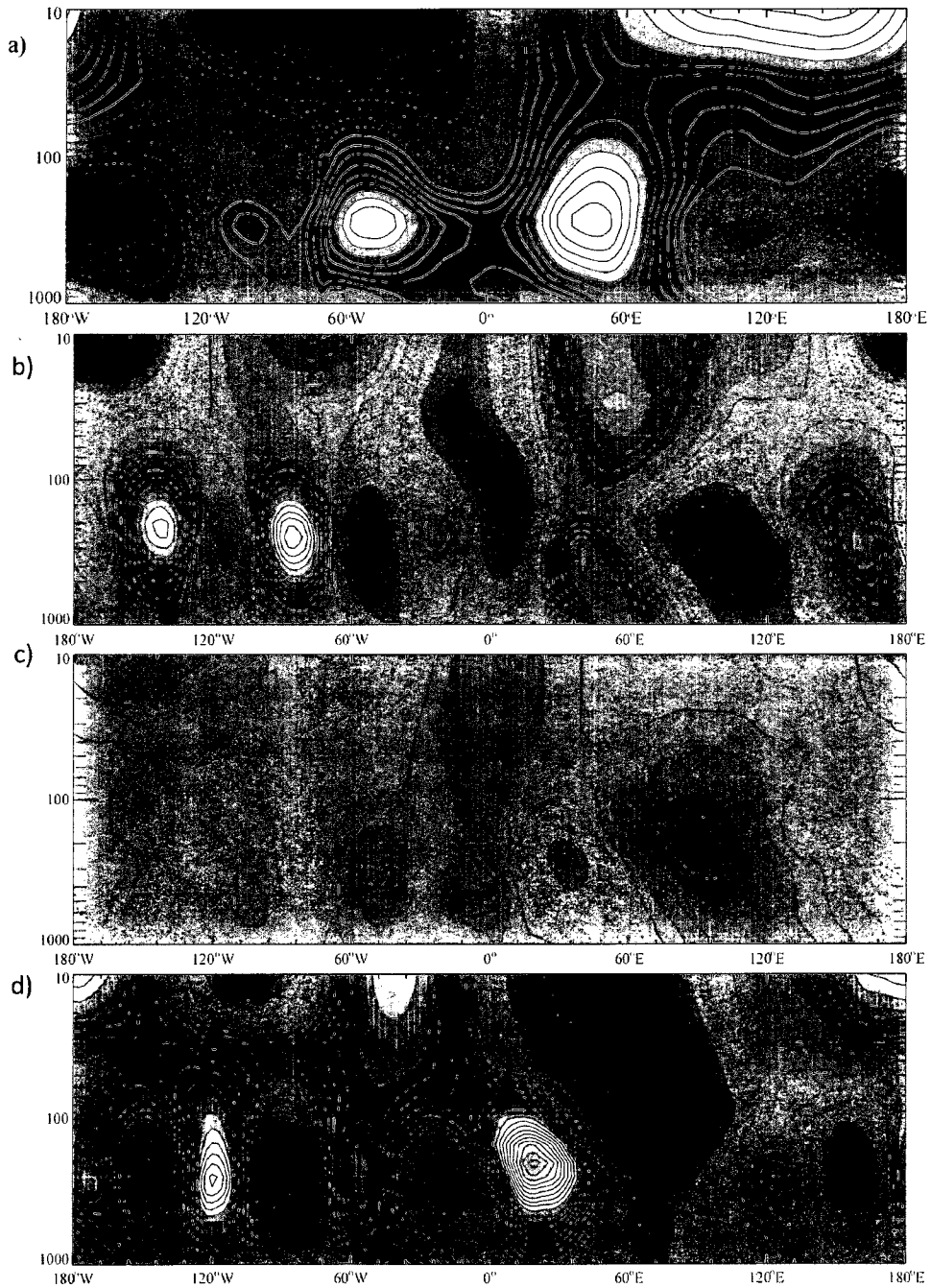

Figure 5.28. Longitude-Altitude averages of ECMWF geopotential height anomalies composites for August during years 1995-2004 and their difference from the monthly mean at 35°S: a) monthly mean b) Type I cases – monthly average, c) Type II cases – monthly average, d) Type III cases – monthly average. Contour interval is 20 m (a) and 5 m (b,c,d). Values range from -200 m to 180 m (a) and -40 to 40 m (b,c,d).

Reproduced with permission of the copyright owner. Further reproduction prohibited without permission.

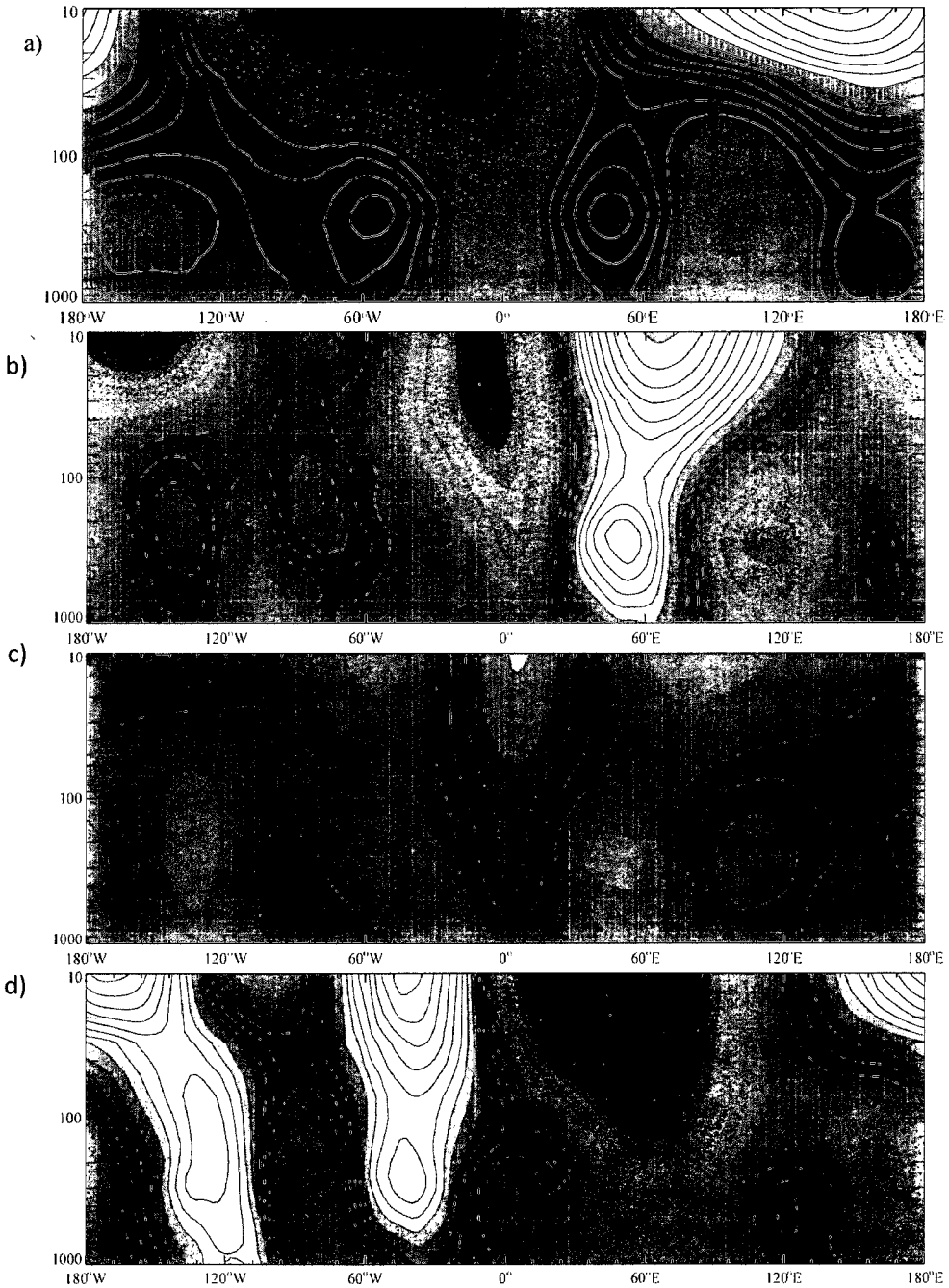

Figure 5.29. Longitude-Altitude averages of ECMWF geopotential height anomalies composites for August during years 1995-2004 and their difference from the monthly mean at 45°S: a) monthly mean b) Type I cases – monthly average, c) Type II cases – monthly average, d) Type III cases – monthly average. Contour interval is 50 m (a) and 10 m (b,c,d). Values range from -450 m to 400 m (a) and -200 to 150 m (b,c,d).

Reproduced with permission of the copyright owner. Further reproduction prohibited without permission.

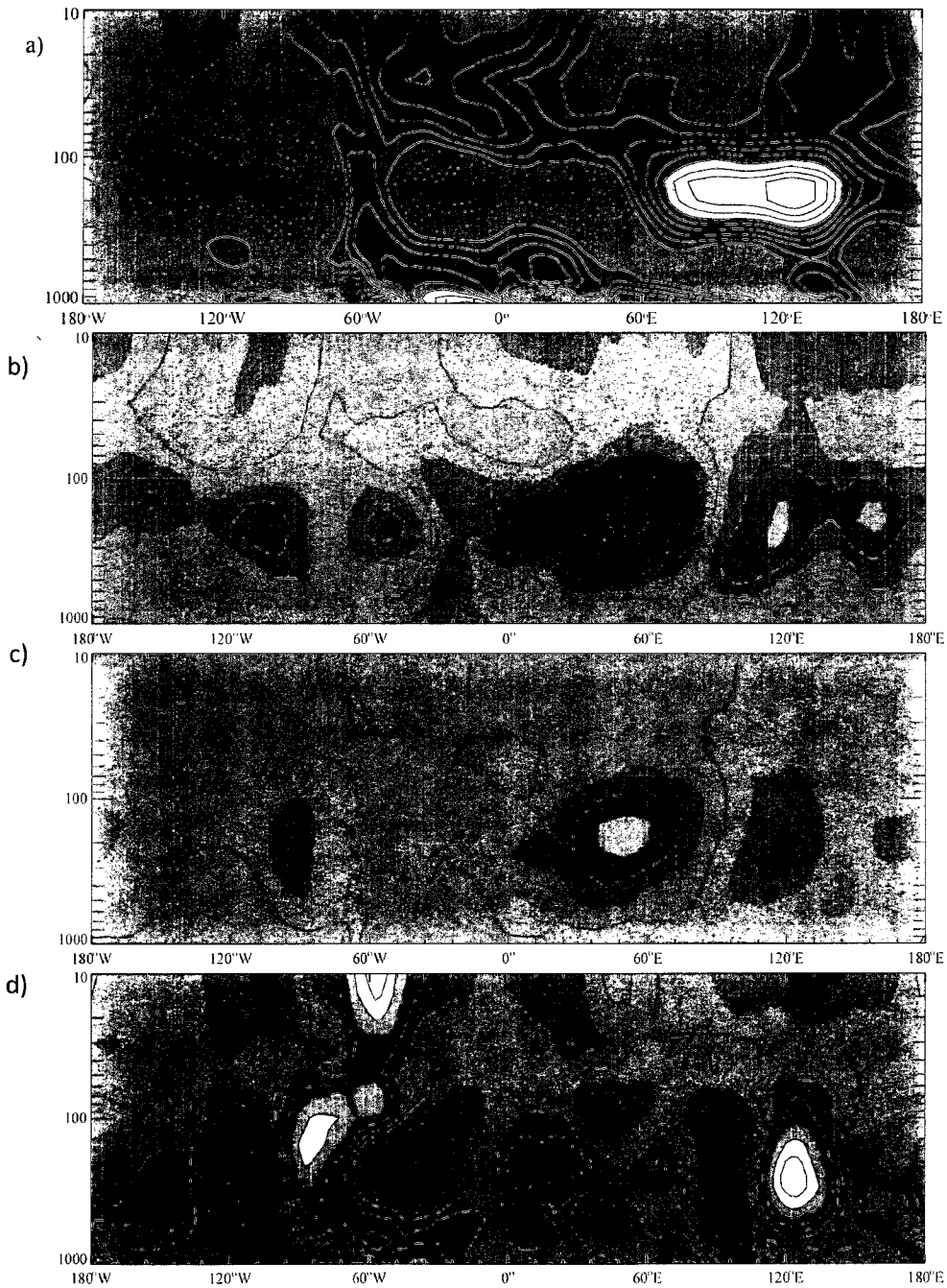

Figure 5.30. Longitude-Altitude averages of ECMWF geopotential height anomalies composites for September during years 1995-2004 and their difference from the monthly mean at 20°S: a) monthly mean b) Type I cases – monthly average, c) Type II cases – monthly average, d) Type III cases – monthly average. Contour interval is 10 m (a) and 5 m (b,c,d). Values range from -80 m to 80 m (a) and -40 to 40 m (b,c,d).

Reproduced with permission of the copyright owner. Further reproduction prohibited without permission.

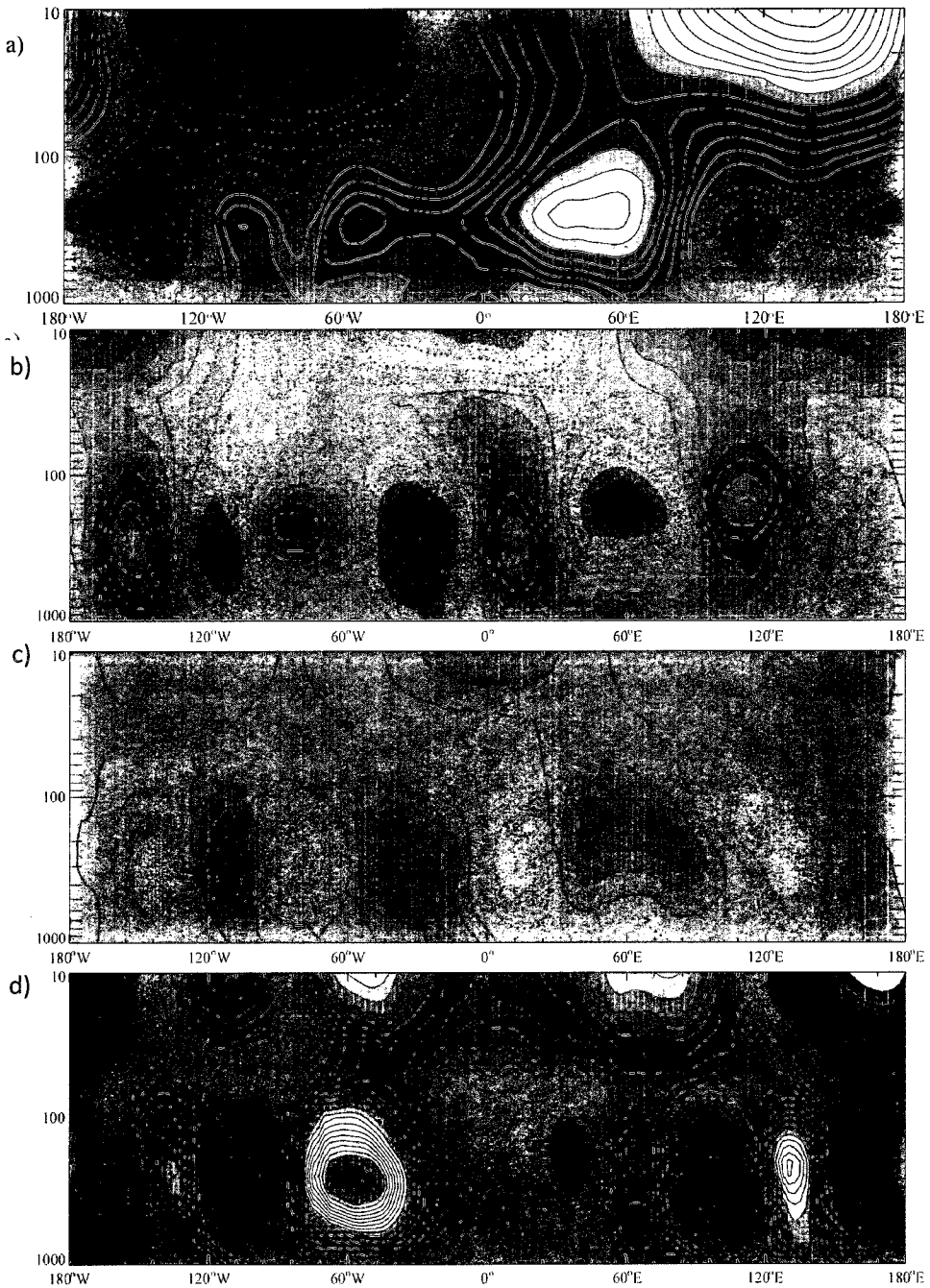

Figure 5.31. Longitude-Altitude averages of ECMWF geopotential height anomalies composites for September during years 1995-2004 and their difference from the monthly mean at 35°S: a) monthly mean b) Type I cases – monthly average, c) Type II cases – monthly average, d) Type III cases – monthly average. Contour interval is 20 m (a) and 5 m (b,c,d). Values range from -200 m to 180 m (a) and -40 to 40 m (b,c,d).

Reproduced with permission of the copyright owner. Further reproduction prohibited without permission.

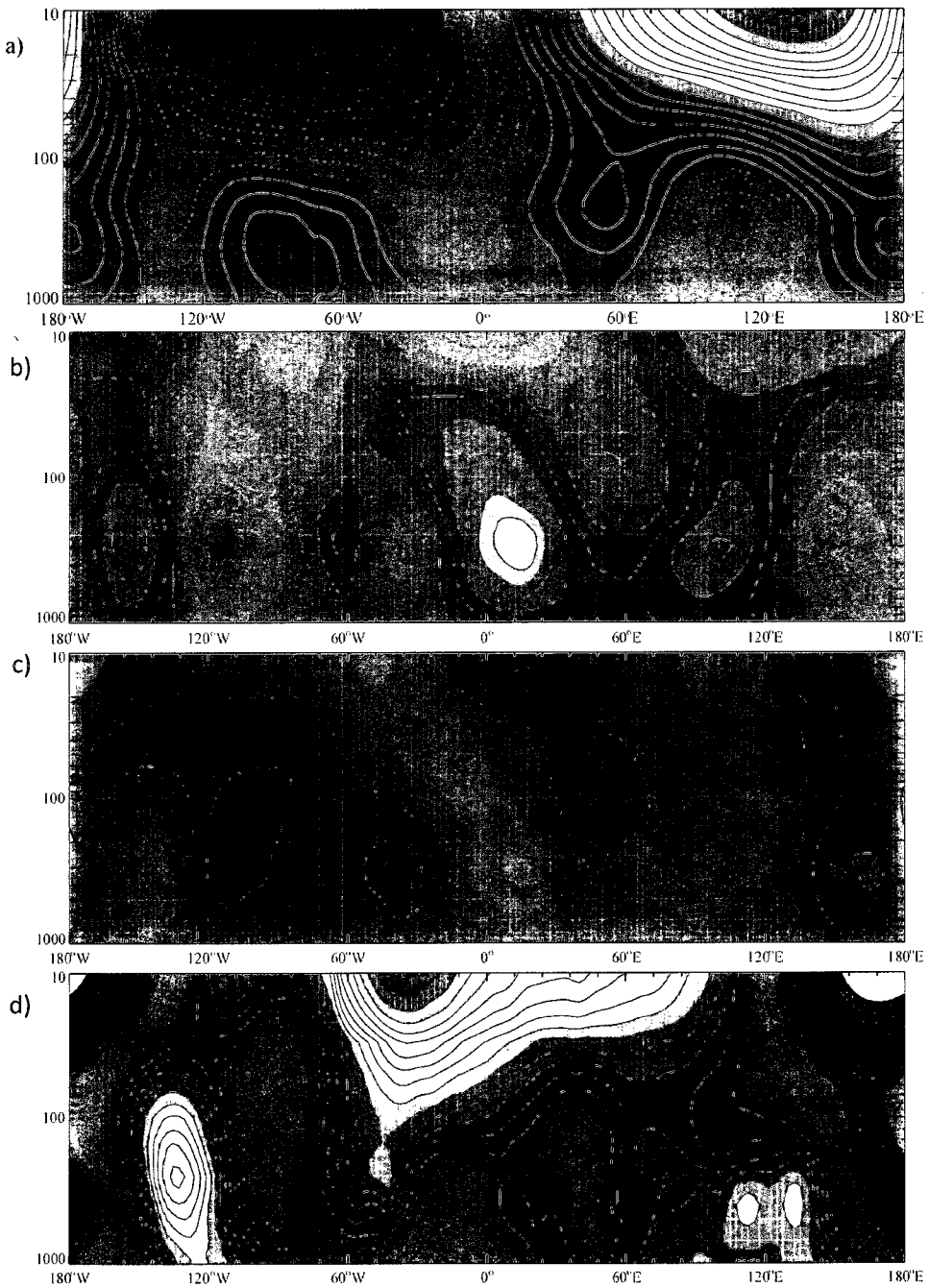

Figure 5.32. Longitude-Altitude averages of ECMWF geopotential height anomalies composites for September during years 1995-2004 and their difference from the monthly mean at 45°S: a) monthly mean b) Type I cases – monthly average, c) Type II cases – monthly average, d) Type III cases – monthly average. Contour interval is 50 m (a) and 10 m (b,c,d). Values range from -450 m to 400 m (a) and -200 to 150 m (b,c,d).

Reproduced with permission of the copyright owner. Further reproduction prohibited without permission.

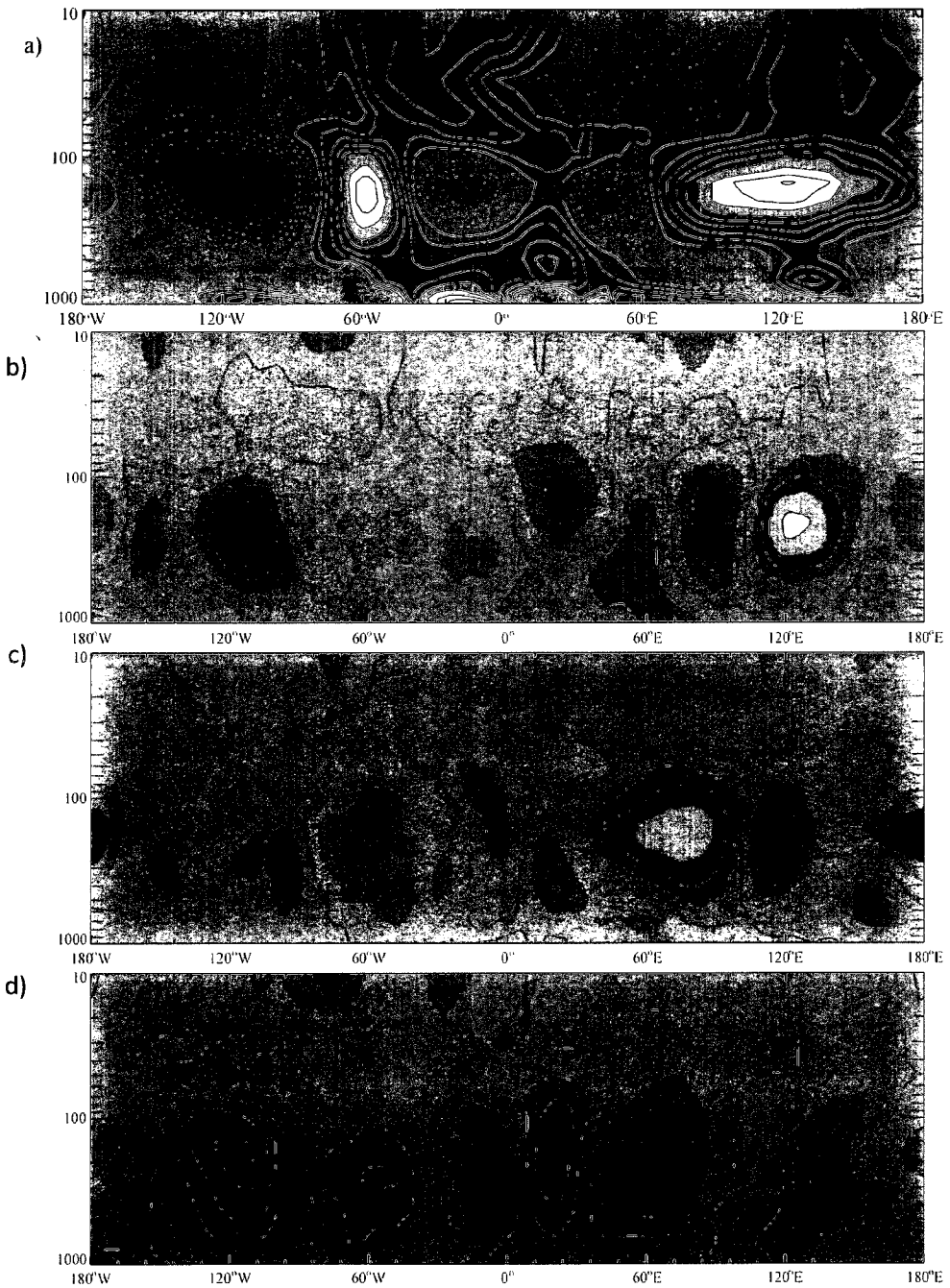

Figure 5.33. Longitude-Altitude averages of ECMWF geopotential height anomalies composites for October during years 1995-2004 and their difference from the monthly mean at 20°S: a) monthly mean b) Type I cases – monthly average, c) Type II cases – monthly average, d) Type III cases – monthly average. Contour interval is 10 m (a) and 5 m (b,c,d). Values range from -80 m to 80 m (a) and -40 to 40 m (b,c,d).

Reproduced with permission of the copyright owner. Further reproduction prohibited without permission.

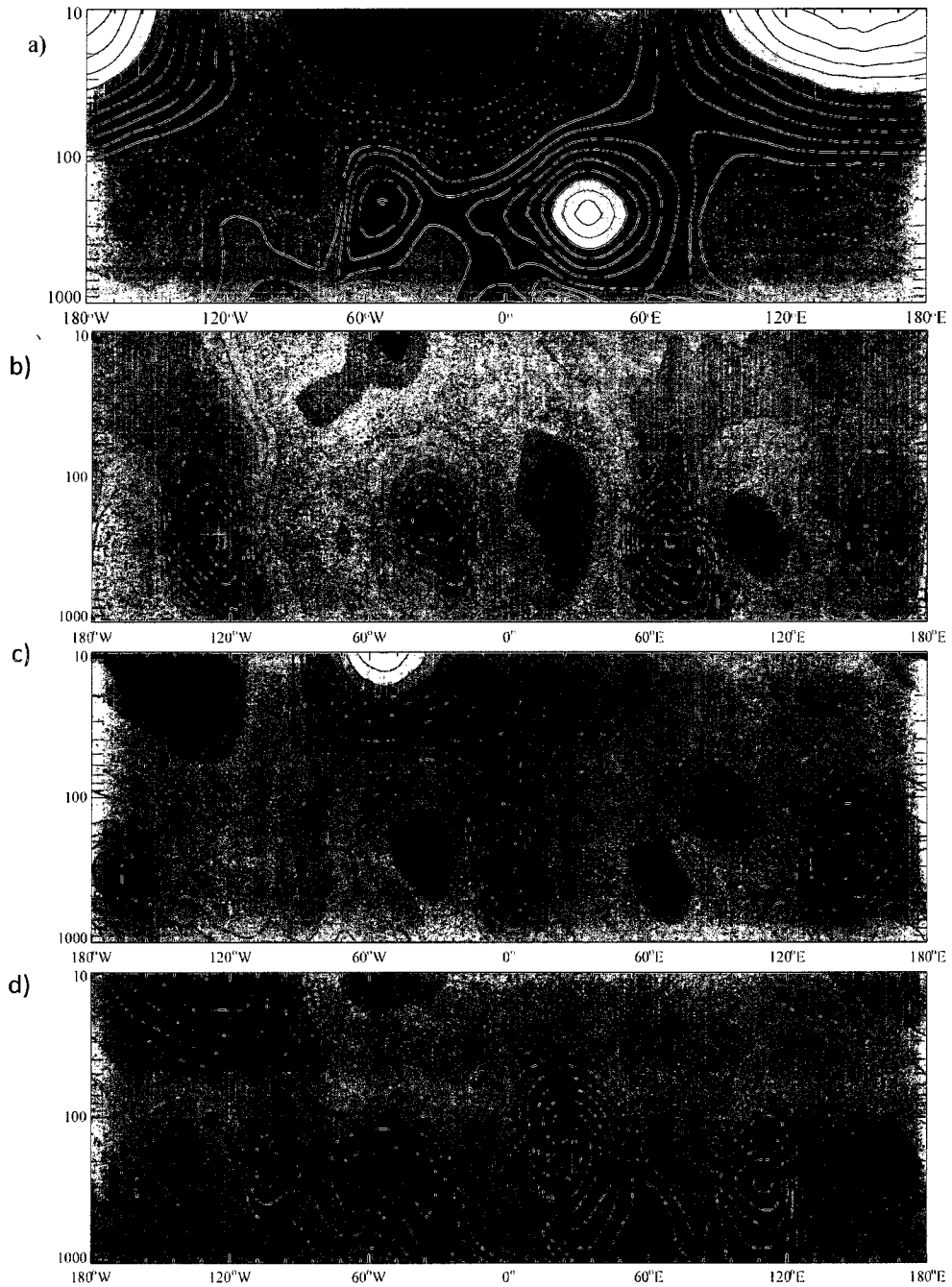

Figure 5.34. Longitude-Altitude averages of ECMWF geopotential height anomalies composites for October during years 1995-2004 and their difference from the monthly mean at 35°S: a) monthly mean b) Type I cases – monthly average, c) Type II cases – monthly average, d) Type III cases – monthly average. Contour interval is 20 m (a) and 5 m (b,c,d). Values range from -200 m to 180 m (a) and -40 to 40 m (b,c,d).

Reproduced with permission of the copyright owner. Further reproduction prohibited without permission.

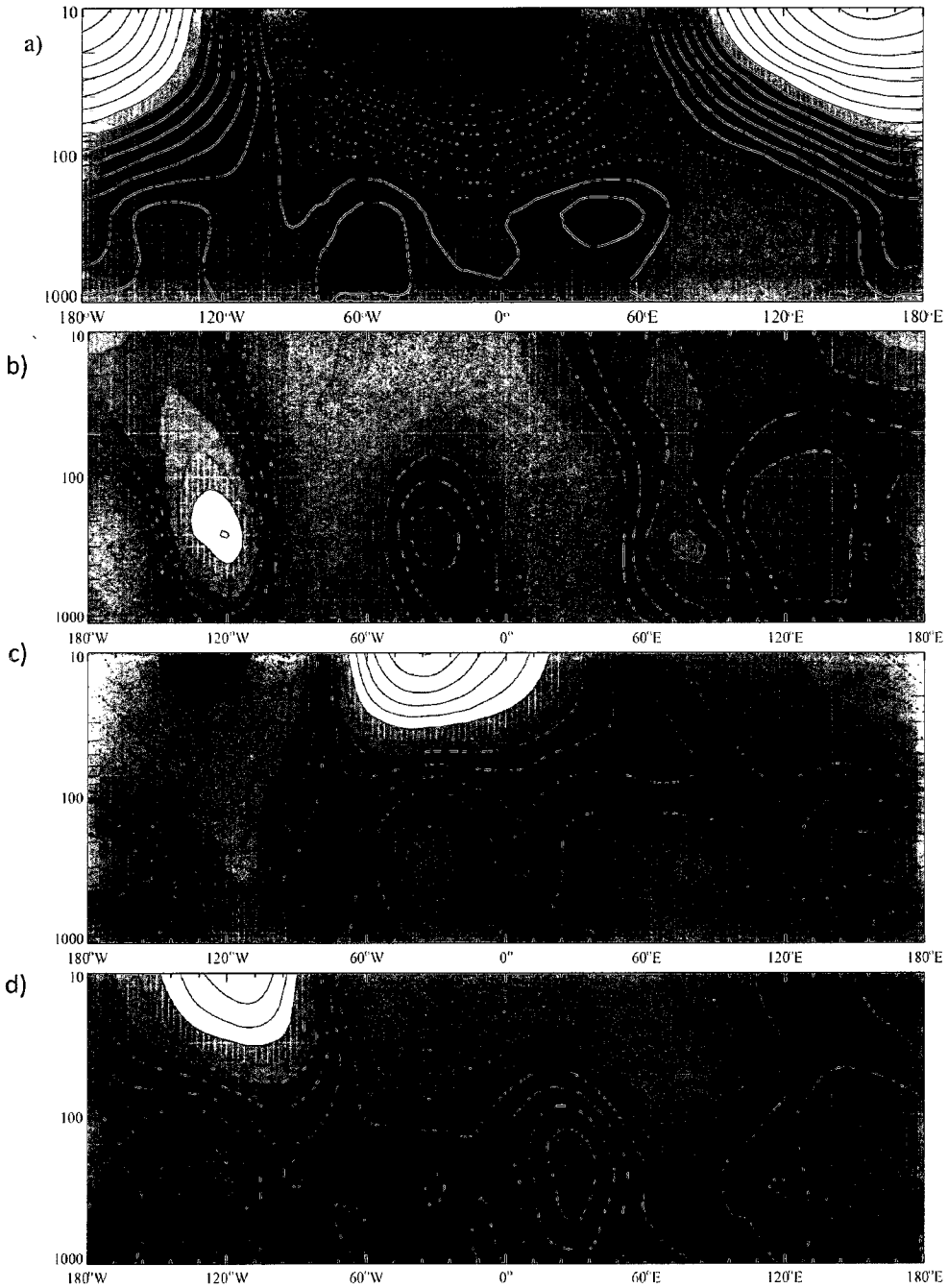

Figure 5.35. Longitude-Altitude averages of ECMWF geopotential height anomalies composites for October during years 1995-2004 and their difference from the monthly mean at 45°S: a) monthly mean b) Type I cases – monthly average, c) Type II cases – monthly average, d) Type III cases – monthly average. Contour interval is 50 m (a) and 10 m (b,c,d). Values range from -450 m to 400 m (a) and -200 to 150 m (b,c,d).

Reproduced with permission of the copyright owner. Further reproduction prohibited without permission.

Chapter 6

Analysis of the SH structure in waves, E-P flux and its divergence in a 10 year climatology for ASO

An E-P flux analysis was performed for ASO monthly means during the 10 year period (1995-2004) and additionally for the time-composite cases as in Chapter 5. E-P fluxes and their divergences were calculated for the total power spectrum as well as separately for wavenumbers 1, 2, 3 and 4-7. This allowed us to further understanding of the contribution of different wavenumbers to wave-mean flow interactions during the late winter to spring transition as well as differences that each case displays in wave activity and forcing in comparison to monthly means.

6.1 The vertical structure of zonal wind

In order to analyze the driving influences of wave activity on the zonal mean flow we have to first establish the structure of the flow as seen during the months of August, September, and October in monthly means and in time composites as described in previous chapters.

The monthly mean zonal mean flow for August (Fig. 6.1a) shows the typical dual jet structure for the SH winter, with the ASWJ centered at 150 hPa near 30°S and much stronger westerlies in the stratosphere at 60°S. The core of the PNJ is at approximately 10 hPa with zonal winds exceeding 80 m/s, while the ASWJ reaches 40 m/s. The case I events (Fig. 6.1b)

Reproduced with permission of the copyright owner. Further reproduction prohibited without permission.

show a poleward shift of the stratospheric jet, visible here as a dipole structure with an increase of 2.5 m/s on the poleward side of the jet and a 6 m/s decrease on the equatorward side of it. There is virtually no change in the position and strength of the ASWJ. Type II events (Fig. 6.1c) bring relatively small differences in comparison with the monthly mean, not exceeding 1 m/s. Type III cases show the opposite structure of the flow changes seen in type I, being 10 m/s faster on the northern side of the PNJ and 5 m/s slower on its poleward side. Again, the ASWJ seems to be stable regardless of the type of event in August.

The zonal mean flow averaged over the all Septembers in the 1995-2004 dataset (Fig. 6.2a) shows diminished PNJ relative to August, with velocities not exceeding 65 m/s in the lower to mid-stratosphere and the ASWJ also reduced in strength by 5 m/s relatively to August (maximum flow velocity 35 m/s). The difference between Type I cases and the monthly mean (Fig. 6.2b) shows the poleward shift of the PNJ again as well as equatorward shift of the ASWJ. Migration of the PNJ in the opposite direction characterizes Type II events (Fig. 6.2c), without any changes to the ASWJ. The strong AH-SAH type events (Fig. 6.2d) reveal a downward and slightly equatorward descend of the PNJ, with maximum differences reaching 8 m/s at the 10 hPa level, the upper boundary of our analysis.

The downward and poleward migration of the PNJ is a prominent feature of the October zonal mean flow structure (Fig. 6.3a). Weakening of the upper stratospheric jet associated with weaker temperature gradients in middle latitudes is a well-documented feature of the PNJ life cycle during the late winter to spring transition (*Butchart et al.*, 1982, *O'Neill and Youngblut*, 1982, *Hartman,* 1984, *Mechoso et al.*, 1985). There is virtually no change in the zonal wind speed in the vicinity of the ASWJ in comparison with the averaged structure for the September. Type I events (Fig. 6.3b) show a lack of differences between the modal and

Reproduced with permission of the copyright owner. Further reproduction prohibited without permission.

monthly mean flows that exceed 1 m/s except for the ASWJ which undergoes slight acceleration. Deceleration in the lower and poleward side of the PNJ is characteristic of Type II events (Fig. 6.3c). Coupled with a strengthening of westerlies in the 30-60°S region in the lower stratosphere there is an upward migration of the PNJ in comparison with the monthly mean. The dipole-like structure, with slight increase in westerlies on the poleward side of the ASWJ and corresponding deceleration of the equatorward side of this jet result in a southward shift of ASWJ core. Both the ASWJ and PNJ undergo opposite modulation during type III events (Fig. 6.3d). The diminished PNJ core is displaced downward as well as poleward, with an overall decrease in wind speed of 3-4 m/s, while winds are 2 m/s weaker over 30-40°S area in the UTLS region. There is a corresponding acceleration north of 30°S, as the ASWJ is displaced equatorward.

Due to relatively short period of analyzed data, the tropical latitudes (15°N-15°S) show vertical dipole structures in the zonal wind field that are an artifact of the QBO which was not filtered out from this dataset. While this kind of aliasing does not influence directly monthly means of zonal wind in the 100-10 hPa region, it does however introduce unwanted biases in time-composites manifesting with anomalous differences similar in pattern to dipoles (Figs. 6.2b and d, 6.3c and d) over the Equator. For example all type III events in September did show easterlies in the equatorial 100-70 hPa region and westerlies (stronger than 10-year September average) above which shows clearly as an anomalous dipole (Fig. 6.2d) in difference field.

Reproduced with permission of the copyright owner. Further reproduction prohibited without permission.

6.2. Spectral analysis of wave structure

The relative importance of wavenumber 1 and 2 as major structures in the SH upper troposphere and stratosphere is well-established. Additionally, waves up to k=8 contribute significantly to the extratropical and midlatitude regions of the SH.

The k=1 structure in August (Fig. 6.4a) displays a double maximum, with a strong peak around 55-60°S and a lesser maximum near 20-40°S. Type I events show a generally weakened amplitude with respect to the other types of events and the monthly averages. Wave one during Type III events tends to be 10 m larger than the average in the maximum which is shifted equatorward. Type I shows a poleward shift of 5° in both maxima during September (Fig. 6.4b), while all other types of events follow closely the average. September's amplitude is 10-15 m less for all events than in August, before being enhanced in October (Fig. 6.4c). Unlike during August, the type I k=1 shows amplitude over the 60°S region strengthened by approximately 10m in comparison to the monthly average, followed by type III events with amplitude larger as well. In the 20-40°S band, Type III amplitude is enhanced in October and diminished for Type I. Types I and III show a hint of a double structure in the extratropical and midlatitude maximum throughout all months pointing to the AH and SAH anticyclones.

The k=2 structure resembles the k=1 in amplitude and behavior during different types of events. August's structure (Fig. 6.5a) shows again the relatively larger amplitude of the type III events near 40-70°S, with type I being largest poleward of

Reproduced with permission of the copyright owner. Further reproduction prohibited without permission.

70°S. Type II events, with whole Indian Ocean Basin being active show a 5 m stronger amplitude for k=2 in the 25-40°S region. September's (Fig. 6.5b) k=2 structure shows a shifted poleward (to 65°S) maximum for Type III as well as a latitudinally stretched type I maximum near 60-70°S, both stronger by 20 and 10 m respectively than the average, which itself indicates a 10 m drop in the amplitude in this region. Similarly to k=1, October's latitudinal structure (Fig. 6.5c) shows a hint of a double maximum over the 20-40°S region for type I and III events and their amplitude in the 60°S region higher by 5-10 m than that of the monthly average.

The structure of k=3 during August (Fig. 6.6a) shows notable differences between different types of events and the monthly average. Type I is larger at most latitudes during August, being strongest of all between 35° and 55°S. The difference reaches 25 m, near 50°S again is strongest of all poleward from that latitude. Type III events are distinguishable by amplitude smaller than average by 20 m in the 35°-55°S zone, with 2 peaks, at 35°S and 65°S respectively. September (Fig. 6.6b) brings 5 m stronger amplitude for the Type I events at 25°S, while the type III peaks 10° more poleward. While Types I and II are similar to the average in the mid to high latitudes, Type III exhibits a high latitude peak in amplitude at 65°S, with magnitudes higher by 40 m than the monthly average. All types show much abated amplitudes in the high latitude region during the October (Fig. 6.6c), with Type III peaking at 30m around 55°S, while Type II peaks around 65°S at 35m.

Reproduced with permission of the copyright owner. Further reproduction prohibited without permission.

The k=4 structure shows double peaks in August (Fig. 6.7a) for Type III events at 40°S and 55°S respectively. The strongest amplitude occurs for Type I events, which peak at 55m at 50°S, 20 m higher than the monthly average. Type III events produce a double peak at 35°S and 65°S respectively in September (Fig. 6.7b), while types II and I peak at 50°-55°S with 37m and 22m respectively. The amplitude of Type III events is higher from the Equator to 45°S and from 58°S poleward while the opposite is true between 45° and 58°S. October (Fig. 6.7c) brings diminished amplitudes for all types of events and while they tend to show latitudinal variations similar to the previous month, the overall amplitude is 10-20 m less.

The k=5 structure shows the prominence of Type I and III events (Fig. 6.8a) in August. The strength of their peaks stretching from 35°-50°S averages at 22 and 29 m respectively, 10 m higher than the monthly average. September's structure (Fig. 6.8b) shows Type III peaking at 25 m around 35°S and a double peak for Type I events, at 25°S and 45°S. The relatively poleward peaking (40°S) of type I event k=5 and strong amplitude maxima of 20 m produced by type III events at 30°S are highlights of October's k=5 latitudinal structure (Fig. 6.8c). The average and Type II events peak at 10m around 20-25°S and then decrease poleward almost monotonically.

The cumulative k=6-8 band structure as seen in August (Fig. 6.9a) reveals higher amplitude during Type III events, with a peak at 30°S reaching 50 m, more than 30 m larger than the next strongest counterpart, the mean of Type I events. All types of events tend to peak around 30-40°S also during September (Fig. 6.9b), with Type III

Reproduced with permission of the copyright owner. Further reproduction prohibited without permission.

again displaying 25 m larger amplitude as well as a secondary, much smaller (less than 10 m) maximum around 60°S. October's latitudinal structure for k=6-8 amplitude (Fig. 6.9c) shows diminished amplitude for Type III events, and an almost uniform distribution of amplitude of all types of events with latitude.

The relatively high importance of the wavenumbers 3-5 at 40°-60°S is also shown on the latitude-wavenumber diagram displaying wave amplitudes during August (Fig. 6.10a). Waves 1- 3 display strong signals in the 20°-40°S region. Type I events bring an even stronger signal from k=3-5 in the 40-60°S region (Fig. 6.10b), Type II (Fig. 6.10c) show diminished amplitudes of k=3-5 with respect to the monthly mean in the same region but a stronger signal from k=2 near 30-40°S. Type III (Fig. 6.10d) show somewhat diminished k=3-5 in the 40-60°S but a strong signal from higher wavenumbers in the extratropics and midlatitudes.

The same type of plot for averaged September (Fig. 6.11a) reveals diminished amplitudes of all lower wavenumbers 1-3 acting in concert with the lesser amplitudes of k=4-5 in the 40-60°S region. The stronger k=4 at 45-60°S region during Type II events is clearly visible on panel c). The increased activity of all wavenumbers 1-8 during type III events in the 20-40°S region as well as their increased strength during these events are highlighted by panel d).

October shows (Fig. 6.12a) a stronger k=2 (in comparison to the k=1) contribution to the SH wave structure at high latitudes, as well as a relatively weak signal spread throughout wavenumbers 1-5 at 15-30°S. This low latitude signal is enhanced,

Reproduced with permission of the copyright owner. Further reproduction prohibited without permission.

especially for the k=2 and 3 during Type I events (Fig. 6.12b), while 60°S latitude exhibits a parity between the strengths of k=1 and 2. Type II events (Fig. 6.12c) show weakening of the amplitudes across the spectrum and latitudes, with spatial structure similar to the monthly average, while Type III events (Fig. 6.12d) exhibit stronger k=2 at 60°S, a strong signal from k=1 and 2 in the 30-40°S band, as well as unusually strong amplitude k=5 at 25°-30°S.

The extratropical and low latitude signals described above are projections of the mesoscale features described in this thesis, namely the AH, IOH, SAH and the SAmH. When comparing phases of wave 1 to 3 (Fig. 6.13a) of the geopotential height anomalies in the monthly mean, at 22°S, to the climatological positions of the main anticyclones, a collocation of the climatological ridge positions of k=1 and 2 (near 110°E) with the AH becomes a highlighted feature. The k=3 ridges at 22°S are placed over the central Indian Ocean, central Pacific and the Atlantic. During the type I events (Fig. 6.13b) at 22°S the k=1 ridge is shifted eastward precisely over the position of the strong AH, similarly to k=2 and 3. The second ridge of k=2 lays over the position of the SAmH. The westward shift in the position of k=1 to 3 ridges characterizes Type II events (Fig. 6.13c) at 35°S, with the ridges of k=2 and 3 overlaying the Indian Ocean area and k=1 is positioned over the African continent. It remains there during Type III events (Fig. 6.13d at 33°S), together with a collocated k=3 ridge when the SAH undergoes amplification.

Reproduced with permission of the copyright owner. Further reproduction prohibited without permission.

6.3. E-P fluxes and their divergences.

6.3.1. Total E-P flux divergence for the August – September period.

As noted in multiple previous studies (*Hartmann,* 1984, *Mechoso et al.*, 1985, *Randel,* 1987) tropospheric E-P fluxes constitute mostly the signal of synoptic-scale baroclinic wave disturbances. E-P flux divergence anomalies are associated with acceleration of the westerlies in the lower to mid troposphere while having the opposite influence in the UTLS region. The strongest EP vectors in August (Fig. 6.14a) are visible to originate in the midlatitudes, as expected from the relatively strong baroclinic zone present in these latitudes. One major group tends to bend equatorward when reaching the middle and upper troposphere in the ASWJ region, resulting in the deceleration of westerlies in it. The divergence in the UTLS region reaches approximately 5m s^{-1} day^{-1}. The other E-P flux vector group originates more south, around 45-55°S and tends to propagate energy well into the stratosphere and while the stratospheric values of divergence does not exceed the 1.5 m/s/day value in August, we can observe strong equatorward and weaker poleward bending of wave energy propagation on both sides of the PNJ, due to strong westerlies. Type I events (Fig. 6.14b) bring expansion of the convergence regions with values of 4 m s^{-1} day^{-1} and more in the midlatitudes in the UTLS region as well as the stratospheric divergence near 50°S strengthened by 0.5 m s^{-1} day^{-1} when compared with monthly mean. When compared with zonal flow (Fig. 6.1b) the collocation of the decrease in westerlies in the 45-60°S region is well correlated with enhanced wave activity. The opposite is true during Type II events (Fig. 6.14c) when the stratospheric divergence is on par with the monthly mean and the midlatitude UTLS region is relatively weakened. The stratospheric westerlies during

Reproduced with permission of the copyright owner. Further reproduction prohibited without permission.

corresponding times are enhanced (Fig. 6.1c). Type III events (Fig. 6.14d) bring stronger vertical E-P fluxes into the ASWJ region and less activity propagating into the stratosphere. This is underscored by weaker than monthly mean divergence in the high latitudes stratospheric region and strengthened westerlies over the broad 30-50°S stratospheric region (Fig. 6.1d).

September mean E-P flux divergence fields (Fig. 6.15a) show weakened negative divergence in the stratosphere over the high latitudes region of 1 m/s/day in concert with the diminished positive divergence (maximum of 4 m s^{-1} day^{-1}) in the ASWJ region which, unlike in August, is combined with a relative lack of the negative divergence region immediately underneath. The comparison with zonal mean flow (Fig. 6.2a) shows weakened westerlies in the PNJ region as well as the ASWJ core. Type I events (Fig. 6.15b) show further diminution in the negative divergence region around 60°S at levels 50 hPa and higher, with the UTLS region virtually intact. This corresponds with decreased westerlies in the stratosphere near 60°S and increased westerlies poleward of 60°S line (Fig. 6.2b). Type II events (Fig. 6.15c) show some reconstitution of the divergence region in the PNJ area with stronger vertical propagation of wave energy in comparison with the monthly mean state. This increase in the vertical wave propagation occurs in stronger westerlies (Fig. 6.2c) in the 30-60°S stratosphere. Type III events (Fig. 6.15d) display a negative divergence region in the stratosphere diminished by 0.5 m s^{-1} day^{-1} throughout the PNJ area of influence. In ASWJ region divergence is enhanced by 2 m s^{-1} day^{-1} on the poleward side of the jet. There is a region of marked negative divergence below which did not occur during the previous types and monthly mean. The stratospheric region undergoes strengthening of westerlies (Fig.

Reproduced with permission of the copyright owner. Further reproduction prohibited without permission.

6.2d) by more than 7 m/s while the ASWJ core is moved poleward during corresponding time.

The downward and poleward movement of PNJ in October is correlated in time with greatly diminished negative divergence region in this stratospheric zone (to approximately .5 m s^{-1} day^{-1}, Fig. 6.16a). The further diminished positive divergence region in the vicinity of the ASWJ is characterized by greater meridional and equatorward direction of the E-P fluxes than in August and is lying on top of a 2 m s^{-1} day^{-1} or more pronounced pool of negative divergence. Type I events (Fig. 6.16b) are characterized by an enlarged lower stratospheric negative divergence region, with no corresponding change in other important areas of the atmosphere. Changes in zonal flow (Fig. 6.3b) do not exceed 1 m/s in both the PNJ and ASWJ zones. The lack of a distinguishable area of negative divergences of .5 m s^{-1} day^{-1} in the PNJ region marks Type II events (Fig. 6.16c) and coexists with the broad strengthening of westerlies aloft in the 30-60°S region (Fig. 6.3c). Type III events (Fig. 6.16d) bring enhanced vertical E-P flux vectors and a convergence pool (around 60°S) in the stratosphere, which is stronger in comparison with the monthly mean. This occurs in concert with enhancement of westerlies on the poleward side of the PNJ and a corresponding weakening of zonal wind on its equatorward side (Fig. 6.3d).

6.3.2. E-P flux divergence for wavenumbers 1 and 2

August. Wavenumbers 1 and 2 are important components of the wave-mean flow interaction since their wavelengths allow them to propagate well into the stratospheric westerlies. The August k=1 E-P flux divergence cross-section (Fig. 6.17a) reveals its contribution to the negative divergence field in the vicinity of the PNJ, giving a maximum of

Reproduced with permission of the copyright owner. Further reproduction prohibited without permission.

approximately 1 m s^{-1} day^{-1} in the around 20 hPa at 60°S. The region of the ASWJ is at the same time characterized by two positive divergence maxima located at 250 hPa, 30°S (1.4 m s^{-1} day^{-1}) and 150 hPa, 20°S (m s^{-1} day^{-1}) and corresponding negative divergence regions to the north and south respectively.

The E-P divergences due to k=2 bear a close resemblance to k=1 (Fig. 6.18a) but with smaller ranges. The negative divergence in the high latitude stratosphere achieves values of approximately 0.5 m s^{-1} day^{-1}. While there is a similar double maximum structure in the UTLS region, the positive divergences achieve only around 0.4 m s^{-1} day^{-1} in both positions. The lower maximum is positioned more poleward than for k=1, while the upper is approximately collocated with the corresponding feature for k=1. The unabated vertical propagation at 50°S allows the wave energy to reach almost 50 hPa level before being refracted equatorward. Type I events for k=1 (Fig. 6.17b) do not display any deviations from the monthly mean, while the k=2 E-P vectors (Fig. 6.18b) bend poleward throughout the tropospheric region of 50-70°S, before propagating upward, with the vertical component being stronger than that for monthly mean. There is also more intense upward propagation in the 20°S UTLS region. The dual positive divergence regions in the UTLS regions do exceed 0.6 m/s/day, a thirty % increase from the monthly mean. Type II events favor UTLS maxima in the positive divergence stronger by 0.2-0.4 m s^{-1} day^{-1} for k=1 (Fig. 6.17c) and their weakening for the k=2 by 0.2 m s^{-1} day^{-1} (Fig. 6.18c). Otherwise the E-P divergence cross-sections for k=1 and 2 are fairly similar to their respective monthly mean.

Type III events for k=1 (Fig. 6.17d) show diminished negative divergence in the stratospheric PNJ region (by 0.2 m s^{-1} day^{-1}), a weakened upper, equatorward positive divergence maximum in the UTLS, region with a corresponding stronger lower maximum

Reproduced with permission of the copyright owner. Further reproduction prohibited without permission.

(by 0.4 m s^{-1} day^{-1}) and a more robust negative divergence pool separating these features. E-P flux vectors display a strong poleward component and greatly diminished vertical propagation in the mid-high latitudes region. Unlike for k=1, August's Type II events k=2 (Fig. 6.18d) display an enhanced vertical component with a slightly equatorward veer over the broad region between 30-70°S from the 250 hPa level up. Almost gone is the double positive divergence maximum structure in the UTLS region, with the lower maximum shifted poleward and weakened by 0.2 m s^{-1} day^{-1}. There are two upper maximum centers, with the addition of a 150 hPa maximum at 35°S. Interestingly, it coincides with the stronger double-core ASWJ.

September. The wavenumber 1 cross-section of monthly mean E-P flux divergence (Fig. 6.19a) shows a double structure of maximum negative divergence in the stratosphere over 60°S. Similarly to the August mean, there is a double maximum positive divergence feature in the UTLS region but these maxima are weakened by approximately 0.6 m s^{-1} day^{-1} in comparison with the previous month. Notable is the increase in vertical wave energy propagation, with strong vectors originating well below 250 hPa level. The monthly mean k=2 E-P fluxes (Fig. 6.20a) show an vertical offset in the position of the lower UTLS positive divergence center over 30°S and a notable lack of distinguishable upper UTLS maximum. Like during the previous month, the E-P vectors in the 50-60°S region originate well within the middle troposphere and propagate upwards, with the slight hint of a poleward veer, unabated until approximately the 70 hPa level, being then refracted equatorward. Type I events for k=1 (Fig. 6.19b) show a relative increase in positive divergence inside both of the UTLS maxima, with the upper, equatorward maximum being enhanced by 0.4 m s^{-1} day^{-1}. During these events the wavenumber 2 (Fig. 6.20b) displays a similar enhancement of the

Reproduced with permission of the copyright owner. Further reproduction prohibited without permission.

lower maximum (by 0.2 m s^{-1} day^{-1}) and creation of an additional negative divergence center just south of it and adjacent to the stratospheric negative divergence pool. There is an enhanced vertical and poleward wave energy propagation in comparison with the monthly mean. Type II events for k=1 (Fig. 6.19c) are similar to the monthly mean which is also true for wavenumber 2 (Fig. 6.20c). Unlike Type II, the wavenumber 1 Type III events (Fig. 6.19d) bring further enhancement of the positive divergence maximum around 250 hPa at 30°S (by 0.4 m s^{-1} day^{-1}) while the divergence values inside the upper center (150 hPa, 20°S) are only slightly greater. The 50 hPa stratospheric negative divergence center, the lower of the duo is contracted and does not extend to 70 hPa level.

Wavenumber 2 E-P fluxes (Fig. 6.20d) display great changes from the monthly mean. The lower maximum in the positive divergence centered at 30°S is replaced by a zone of negative divergence and a very pronounced positive divergence maximum aloft, between 250 and 100 hPa. Unlike during the mean September, Type III events further differ by the establishment of a large middle tropospheric positive divergence center at 60°S. This is reflected in a complete recomposition of E-P vector propagation in the whole 30-60°S region. The wave energy propagates upward and poleward form the 40-50°S region and upward and equatorward from the 30-40°S originating around the 350 hPa level but much less propagates into the stratosphere relatively to the monthly average. The stratospheric divergence minimum in the PNJ region is greatly reduced in the extent and in values by 0.1 m s^{-1} day^{-1}.

October. The E-P flux cross-section for the k=1 monthly mean (Fig. 6.21a) shows further contraction and weakening and a simultaneous downward shift of the stratospheric negative divergence pool. At the same time, the UTLS maxima in positive divergence located on the upper equatorward side of the ASWJ and lower poleward ASWJ sides

Reproduced with permission of the copyright owner. Further reproduction prohibited without permission.

respectively are diminished by approximately 0.4 m s^{-1} day^{-1} each. The k=2 E-P fluxes (Fig. 6.22a) shows similar change of these features, with the further reduction in the energy propagation from troposphere to stratosphere in comparison with the previous month. The values of negative divergence maxima in the PNJ region do not exceed 0.2 m s^{-1} day^{-1}. The k=1 pattern during Type I events (Fig. 6.21b) does not differ noticeably from the monthly mean, with the exception of 0.1 m s^{-1} day^{-1} increase in the negative divergence zone in the 100-50 hPa region. The k=2 (Fig. 6.22b) brings marked differences with respect to the magnitudes of both the positive divergence maxima in the ASWJ region and the PNJ region stratospheric maximum in negative divergence. The former peaks at 0.4 m s^{-1} day^{-1} below 250 hPa and is centered near 30°S, with a secondary center over 20°S in the UTLS region with similar values and a structure resembling on the smaller scale the September's k=1 behavior in this region. The wave energy propagates unperturbed from the 250 hPa region into the stratosphere, with E-P vectors originating over the 45-60°S region, bending poleward before reaching the 50 hPa region then being deflected toward the Equator. Notable is the descending positive divergence field over the 45-60°S region in the upper levels (50-20 hPa), which is stronger than during all other types of events and the monthly mean. The k=1 during type II events (Fig. 6.21c) again mirrors the monthly mean for the October. Similarly, k=2 (Fig. 6.22c) follows the path of monthly mean except for a 0.2 m s^{-1} day^{-1} increase in the magnitudes of both UTLS positive divergence maxima, with the 500-250 hPa center shifted southward toward 40°S. Type III events show 0.2 m s^{-1} day^{-1} enhancement of the positive divergence maximum over 30°S at 250 hPa for k=1 (Fig. 6.21d) as well as 0.1 m s^{-1} day^{-1} enhancement in negative divergence values in the lower stratospheric PNJ area. Notable is a weakened southward energy propagation in the UTLS region into the ASWJ region from the

Reproduced with permission of the copyright owner. Further reproduction prohibited without permission.

Equator in comparison with two former types of events. The k=2 (Fig. 6.22d) E-P divergence cross-section shows an additional center of maximum negative divergence at 50°S, 250 hPa, while the stratospheric center seems to be diminished by 0.1 m/s/day in comparison with the monthly mean. This additional negative center coincides with enhanced westerlies in the same region shown on panel d) of figure 6.3. The UTLS positive divergence centers around the ASWJ are almost gone.

6.3.3. E-P flux divergence for wavenumber 3 and 4-10

August. The inability of the shorter waves to penetrate into the stratosphere is immediately visible when analyzing the behavior of k=3 E-P flux divergence (Fig. 6.23a). A low level (500-250 hPa) maximum in positive divergence resides over the broad area between 40° and 60°S. A second maximum is located at the 150 hPa level at 30°S, more poleward than the corresponding maxima characteristic of wavenumbers 1 and 2. There is a small (0.1 m s^{-1} day^{-1} or less) maximum in negative divergence in the 50-20 hPa level in the PNJ region. The wave energy propagates equatorward from this area. The vertical propagation is mostly confined to the mid to upper troposphere, with strong upward and poleward vectors originating around 50-60°S near the surface. The wave energy propagation in the UTLS region around the ASWJ bears a strong meridional equatorward component.

The k=4-7 E-P flux divergence field (Fig. 6.24a) shows similarity in position of the positive maxima in the UTLS region with magnitudes of divergence lesser than 1 m/s/day. The wave energy propagates right from the surface in the 30-60°S belt up to the tropopause region, bending around the 425 hPa level toward the equator. The type I events bring for the wavenumber 3 (Fig. 6.23b) an enhancement (0.4 m s^{-1} day^{-1}) of the positive divergence field

Reproduced with permission of the copyright owner. Further reproduction prohibited without permission.

over the 40-60°S region and simultaneous weakening of the UTLS maximum south of the ASWJ at 30°S. The wave energy vectors propagate more meridionally in the ASWJ area than their monthly mean counterparts. The k=4-10 wave-set exhibits a similar E-P flux divergence pattern (Fig. 6.24b), except for stronger vertical propagation of wave energy in the poleward ASWJ region, as well as an increased magnitude of the divergence by 1 m s^{-1} day^{-1} relatively to k=3. Type II (Fig. 6.23c) wavenumber 3 behavior is a close approximation of the monthly mean except for a stronger center of negative divergence underneath the 40-60°S maximum and more poleward bending E-P vectors in the 500-250 hPa region. Similarly, the k=4-10 pattern during the same times (Fig. 6.24c) remains unchanged. The Type III events are unusual in that there is a broad negative divergence field in the stratosphere at 45-55°S and the vertical wave energy propagation continues well into the stratospheric region, being deflected equatorward near 70 hPa. Most of this energy originates in the 50-60°S area near the surface. The relatively large value of divergence (approximately 1.5 m s^{-1} day^{-1}) on top of simultaneous activity by k=1 and 2 may be a direct reason for the enhanced westerlies in the 30-60°S region (Fig. 6.1d). There is no notable change in the k=4-10 E-P flux divergence fields during that kind of event (Fig. 6.24d).

The September's E-P flux divergence field for k=3 (Fig. 6.25a) shows similar structure in the middle to upper troposphere between 20 and 60°S to that of the previous month, with smaller magnitudes of positive divergence maxima amounting to roughly 0.5 m s^{-1} day^{-1} less in the 500-250 hPa region and 1 m s^{-1} day^{-1} in the UTLS area poleward of the ASWJ. The stratosphere is already patched with positive divergences except for a small negative divergence zone near the tropopause between 50° and 60°S. The wave energy propagates upward slightly over the tropopause in this region. The k=4-10 (Fig. 6.26a) divergence field

Reproduced with permission of the copyright owner. Further reproduction prohibited without permission.

and the E-P vector field are virtually unchanged structurally from the previous month except for positive divergence maxima being 0.5 m s^{-1} day^{-1} less. Type I events show an interesting 4 piece structure of positive divergence centers for k=3 (Fig. 6.25b) There is an usual positive divergence maximum at the tropopause level at 30°S accompanied by one immediately downward and poleward from it at 350 hPa, 35-40°S. The 45-60°S latitudinal band experiences two maxima: a tropospheric at 500-250 hPa and a stratospheric one centered at 70 hPa and stretching upward and poleward. The E-P vectors show magnified upward wave energy propagation in the UTLS region throughout the extratropics and midlatitudes. Once again, no changes are notable for the k=4-10 wave E-P divergence fields (Fig. 6.26b), which is also true for the type II events (Fig. 6.26c). The cross-section of E-P fluxes and their divergence for k=3 during the type II events (Fig. 6.25c) show a lack of the stratospheric maximum of positive divergence in the 50-60°S region and a general structure similar to the monthly mean in both the E-P vectors propagation as well as their divergence field. There is little change in the divergence structure for the k=4-10 (Fig. 6.26c). Panel d) on Fig. 6.25 shows the E-P flux divergence for the type III events of k=3. Strikingly, there are four divergence maxima, this time clearly isolated vertically by the negative divergence maxima in the mid-upper troposphere. Both mid tropospheric maxima at 30° and 60°S are greatly enhanced by 1 m s^{-1} day^{-1}. Similarly the UTLS maximum over the 30°S latitude is strengthened by 0.5 m s^{-1} day^{-1} while the 60°S, 50-20 hPa shows a 0.5 m s^{-1} day^{-1} signal. The E-P vectors show strong vertical propagation form 50°S to 60°S with a slight poleward slant. There is reversed, downward wave energy propagation visible at the 250 hPa region, between 30°S and 40°S. The momentum deposition by this feature leads to the enhanced (by approximately 1 m/s) westerlies in that region (Fig. 6.2d). Similarly, there is a great

Reproduced with permission of the copyright owner. Further reproduction prohibited without permission.

enhancement of westerlies in the stratospheric region over 40-60°S, associated with the observed positive divergence region there. The k=4-10 (Fig. 6.26d) show the tropospheric midlatitude E-P divergence enhanced by 0.5 m s^{-1} day^{-1}, but no visible change in wave energy propagation.

October's k=3 (Fig. 6.27a) cross-section of E-P flux divergence shows a decline of the sharp upper tropospheric positive divergence maxima (by 0.5 m s^{-1} day^{-1}) and their change into a dual structure of two positive divergence centers anchored over the 20°S and 45°S respectively. Because of this broad arrangement there is enhanced upward wave energy propagation in the UTLS region, without a real breakout into the stratosphere. The k=4-10 E-P fluxes and their divergences (Fig. 6.28a) show remarkable similarity to September's situation. Type I events bring an poleward and upward expansion to the 45°S positive divergence zone (Fig. 6.27b) at the tropopause which includes now the additional maximum center at 70 hPa over 60°S latitude. This positive divergence region introduces increased poleward E-P flux in the 70-20 hPa region. Again, there is no change in the k=4-10 structure of E-P flux divergence and vector propagation (Fig. 6.28b), which stays unchanged during all types of events (compare with Fig. 6.28c and d). The k=3 E-P flux divergence during Type II events (Fig. 6.27c) bears a close resemblance to the monthly mean, with the notable exception of the 45°S positive divergence maximum being strengthened by 0.5 m s^{-1} day^{-1}. Interestingly the UTLS region experiences the three maximum centers structure of positive E-P divergence during Type III events (Fig. 6.27d). The mid-troposphere maximum at 60°S is weakened by 0.5 m s^{-1} day^{-1} and the E-P vectors propagate upward in the broader set of latitudes, between 45°S and 65°S, than during the monthly mean. There is also a strengthened equatorward component to the E-P vectors in the stratosphere. Slightly

Reproduced with permission of the copyright owner. Further reproduction prohibited without permission.

enhanced is the most equatorward positive divergence pool at 150 hPa over 20°S collocated with enhanced westerlies in the AH zone (Fig. 6.3d) during those times.

6.4. A zonal momentum budget for the winter to spring transition during 1995-2004.

Following similar methodology to Chapter 5, a simple momentum budget was constructed for each month of the transition period as well as for the three types of events. The focus has been on the analysis of differences in the meridional advection of angular momentum, the ageostrophic advection of angular momentum, the zonal acceleration and the residual term, which by itself should point to areas of strong convection and increased wave drag.

August's 'overworld' outflow from convection over the MC and Southeast Asia creates a large pool of excess westerly momentum over the tropical and extratropical regions of the Indian Ocean (Fig. 6.29a) thus creating large area of westerly acceleration upstream of the ASWJ (compare with Fig. 14a). The maximum of the meridional angular momentum advection has a distinctive dual structure with two centers, east of the Madagascar and northwest of Australia. Type I events are characterized by an increased maximum northwest of Australia (Fig. 6.29b), as well as a deepened minimum east of it, a signal compatible with the enhanced AH. The opposite is true during Type II events (Fig. 6.29c) when both maxima are weakened and contracted in concert with the somewhat abated and broadened outflow. The expanded and enhanced dual maximum structure over the Indian Ocean, with an additional westerly acceleration region west of South Africa is a feature of Type III events (Fig. 6.29d).

Reproduced with permission of the copyright owner. Further reproduction prohibited without permission.

The monthly mean [f(v-v_g)] term representing the ageostrophic meridional advection of angular momentum has a wave 4 structure associated with troughs of AH, SAmH, SAH, plus a localized maximum over Madagascar (Fig. 6.30a). The maximum over the South Africa is replaced with two centers (Fig. 6.30b) northeast and southwest of the enhanced and displaced westward SAmH during Type I events (Fig. 5.12b). The strengthened AH and SAH systems bring the enhancement of the ageostrophic terms south of the Australia and the South Africa. Type II events (Fig. 6.30c) bring no changes in the [f(v-v_g)] except for a broader and stronger maximum over the Madagascar in comparison with the monthly mean. The events characterized by enhanced AH and SAH show (Fig. 6.30d) a boosted positive ageostrophic meridional advection of angular momentum over the Indian Ocean basin east of Madagascar with simultaneous enhancements southwest of Africa, over South America and the eastern Pacific.

The zonal acceleration in August (Fig. 6.31a) shows a relatively accurate collocation of maximum position over the Indian Ocean with the ASWJ entrance. The jet exit region is marked by a negative patch as well. The strengthening of the jet west of Australia during Type I events is marked by an enhanced maximum in the westerly acceleration over the Indian Ocean (Fig. 6.31b). The enhancement in zonal acceleration south of the Africa (at around 50°S) converges in time with a stronger lower PNJ extension located there. Type II events (Fig. 14c) show a weakened ASWJ which is also mirrored in abated zonal acceleration maximum over the Indian Ocean (Fig. 6.31c), while the positive patch over the tip of South America brings enhanced westerlies well into the eastern Atlantic (compare with Fig. 5.14c). The dual nature of the ASWJ is further underlined during Type III events (Fig. 5.14d), when there are three major zonal acceleration maximum centers (Fig. 6.31d): over the

Reproduced with permission of the copyright owner. Further reproduction prohibited without permission.

southeastern Indian Ocean, over the eastern part of the Australia and in the southeastern Atlantic. The last one is associated with anomalously strong westerlies south of the Africa during those events.

The residual resulting from the summation of terms described above shows relatively good balance in the budget. Panels a through d (Fig. 6.32) show residual the term for monthly mean and event types respectively. There are three chronic disagreement regions, Over the equatorial Indian Ocean – MC, southwest of the Australia and over the western South America. While the wave-drag over the last location is mostly static and unchanged regardless of the event type, the Indian Ocean maximum shows a tendency for an eastward shift during strong AH events, while the opposite is true for Type III events with strong SAH and AH. Type III events are also marked by a positive enhancement of the residual over the central Indian Ocean, which points to a stronger zonal acceleration and increased height gradient during these times in comparison with meridional advection of absolute vorticity.

Similarly to the situation in August, the September's meridional advection of zonal momentum (Fig. 6.33a) shows a two-pronged maximum over the central Indian Ocean with the western part relatively stronger than the eastern center. The overall decay of the ASWJ is also marked by weaker values of advection in comparison with the previous month. Again, Type I (Fig. 6.33b) shows an enhancement of the maximum in the Indian Ocean region corresponding to increased westerlies over the Australia. Unlike during August, the western part of the maximum shows a bigger enhancement. Type II events (Fig. 6.33c) show great similarity with the monthly mean, while Type III events (Fig. 6.33d) are marked by a clear dual maximum with centers over northeastern Madagascar and northwest of Australia. There is an additional maximum east of this continent which translated into a second ASWJ core

Reproduced with permission of the copyright owner. Further reproduction prohibited without permission.

shifted toward the western Pacific (Fig. 5.17d). The ageostrophic advection of meridional momentum during the September (Fig. 6.34a) remains reminiscent of the situation in the previous month. The lack of strengthening of $[f(v-v_g)]$ term during Type I events is a remarkable departure from the August's picture. Except for the positive enhancement over the central Indian Ocean, this term stays similar to the monthly mean. The increase in the ageostrophic advection of momentum over the regions south of Australia marks Type II events (Fig. 6.34c). This happens without notable amplification of other maxima anywhere else. Type III events (Fig. 6.34d) are characterized by simultaneous enhancement of the ageostrophic advection term on both sides of Australia and Africa as well as over the South America, similarly to August Type III events but with smaller magnitude.

The zonal acceleration term reflects the average weakening of the ASWJ during September (Fig. 6.35a) by having a smaller magnitude than during August. Again it picks up in the central Indian Ocean during Type I events (Fig. 6.35b), a fact which is reflected in an enhanced jet elongated longitudinally during these times. Type II events (Fig. 6.35c) show a secondary maximum SE of Madagascar but remain unchanged from monthly mean in overall. The ASWJ was shown to contract and strengthen its primary core over eastern and central Australia during Type III events (Fig. 6.35d) and that fact is also marking the zonal acceleration structure with a strong maximum just west and southwest of its entrance as well as a secondary strong maximum east of Australia (Fig. 6.35d). The PNJ extension is also longitudinally limited which is manifested here as sharp acceleration zones south of Africa bounded by a similarly sharp deceleration area over the south-central Indian Ocean. Again the small residuals (Fig. 6.36 a through b) show relative good cancellation of momentum equation terms, a preference for a westward displacement of the maximum during strong

Reproduced with permission of the copyright owner. Further reproduction prohibited without permission.

SAH events and for a eastward position of the residual maximum during Type I events. Likewise, the southwest corner of the Australia experiences a localized maximum during Type III events. Enhancement in the magnitude of the residual immediately to the west and over the South America during the winter-spring transition is a noteworthy feature of the residual fields.

Further decay of the ASWJ during October is also visible in the momentum budget for the SH. The meridional advection of angular momentum during this month is characterized by a weakened maximum with the eastern center almost nonexistent (Fig. 6.37a). The enhancement of the western part of the maximum characterizes Type I events (Fig. 6.37b), while the eastern region of the maximum is boosted during both, Type II and III events (Fig. 6.37c and d). Unlike during previous months, October's Type III events do not show the double maximum feature at all, which is consistent with the one-core ASWJ structure (as seen in Fig. 5.20d) which is elongated with a jet core over central Australia.

The monthly mean ageostrophic meridional advection of angular momentum field (Fig. 6.38a) looks fairly similar to the previous month, with a maximum east of Madagascar, south of Africa and over the western part of South America. Type I events (Fig. 6.38b) show an additional maximum west of Australia and an amplified maximum over South America, while Type II (Fig. 6.38c) mark a return to the state described by the monthly mean, with the exception of the maximum south of Africa being positioned more to the southwest from its monthly mean location. The simultaneous strengthening of maxima over the American and African continents as well as over the western half of the Indian Ocean characterizes Type III events (Fig. 6.38d). The negative pool over the Australia is expanded and deepened, similarly to the previous month's Type III events.

Reproduced with permission of the copyright owner. Further reproduction prohibited without permission.

The zonal acceleration fields during the October (Fig. 6.39a) show similar (to the September) values in the maximum over the central and western Indian Ocean, with simultaneous deceleration zones placed over the tip of Africa, southeastern Australia and over the southern Indian Ocean. The magnification of the westerlies in the ASWJ during Type I events is marked by a relatively strong maximum center shifted eastward toward the eastern coast of Australia (Fig. 6.39b), while the strong deceleration region immediately to the east marks the sharp nature of this jet during these events. Type II events (Fig. 6.39c) favor the position of the maximum zonal acceleration shifted towards the western Indian Ocean basin, with smaller magnitude a fact that has immediate implications for the position and strength of the ASWJ which is weak and relatively short during these periods, with its core positioned over the central Indian Ocean (Fig. 5.20c). The zonally elongated nature of the ASWJ during Type III events (Fig. 5.20d) is closely attributable to the strong maximum in the zonal acceleration east of the Madagascar, virtually no deceleration zone east of this feature and another localized maximum over the northeastern part of Australia (Fig. 6.39d). This secondary maximum in concert with average acceleration upstream results in the elongated jet and the position of its primary core being shifted eastward. The panels of residual (Fig. 6.40 a through d) reveal relative stability of the position of the equatorial maximum, regardless of the event type as well as a notable lack of the positive maximum southeast of Australia. The residual areas positioned west of the South America and over the Andes show a generally smaller magnitude than their counterparts from the previous month.

Reproduced with permission of the copyright owner. Further reproduction prohibited without permission.

6.5. Discussion

The spectral analysis shown in this chapter reveals interesting trends in the SH wavestructure, as well as differences between the types of events, namely:

a) k=1 and 2 are stronger during type III events around 60°S in August while both type I and III are shown to be stronger than average and type II during October.

b) Type I k=1 and 2 peaks more poleward at higher latitudes than all other types.

c) The amplitude of k=5 shows enhancement during between 20° and 50°S during Type III events for the ASO period.

d) Type I k=5 is characterized by enhancement in the 30-70°S band during August and October.

e) The strong signal coming from around 20°S latitude for both wavenumbers reflects the duo of the AH and SAH projected into wave-space.

f) The descent of the PNJ together with its poleward shift that was observed when comparing three months of the analyzed period. This is also reflected in the downward and equatorward shift of the E-P flux divergence region in the stratosphere around 60°S, with corresponding diminution of the upward wave energy propagation.

g) The k=1 E-P flux divergence plots show a strong source of wave activity near 30°S in the UTLS region in August pointing to the proposed "Australian connection" with higher latitude k=1.

h) The k=3 and 4 of type I shows double the amplitude at 50°S in August, while similar feature is exhibited by k=3 of type III at 65°S in September.

Reproduced with permission of the copyright owner. Further reproduction prohibited without permission.

i) The k=3 and 4 show relative enhancement of the tropospheric divergence maximum in the 500-250 hPa region and similar enhancement during the September Type III events, shifted poleward with respect to the monthly mean and other types of events.

j) The strong activity and poleward extension of the midlatitude anticyclones (AH, SAH) and the interaction between higher latitude anticyclones (SAmH and the Southeastern Pacific High) with the PV is reflected in the double maximum (35°S and 65°S) in k=4 amplitude during the September in type III.

k) The type III events show a remarkable preference for wavenumber 5 with much higher amplitudes in the 30-60°S latitudinal band, which narrows and shifts equatorward from August to October. A similar feature is shared by type III cumulative wavenumbers 6-8.

l) The E-P flux divergence analysis showed the contraction of the tropospheric and UTLS divergence regions and their equatorward shift for higher wavenumbers.

m) The fact of projection of the AH into k=1 and 2 near 20°S line during type I events as well as the SAH further south (35°S) was examined with the help of phase plot showing the dependence of a mean position of the ridge on the event type.

n) Generally smaller values of E-P divergence in the stratosphere near 60°S in August and September result in the stronger westerlies during Type III events.

Reproduced with permission of the copyright owner. Further reproduction prohibited without permission.

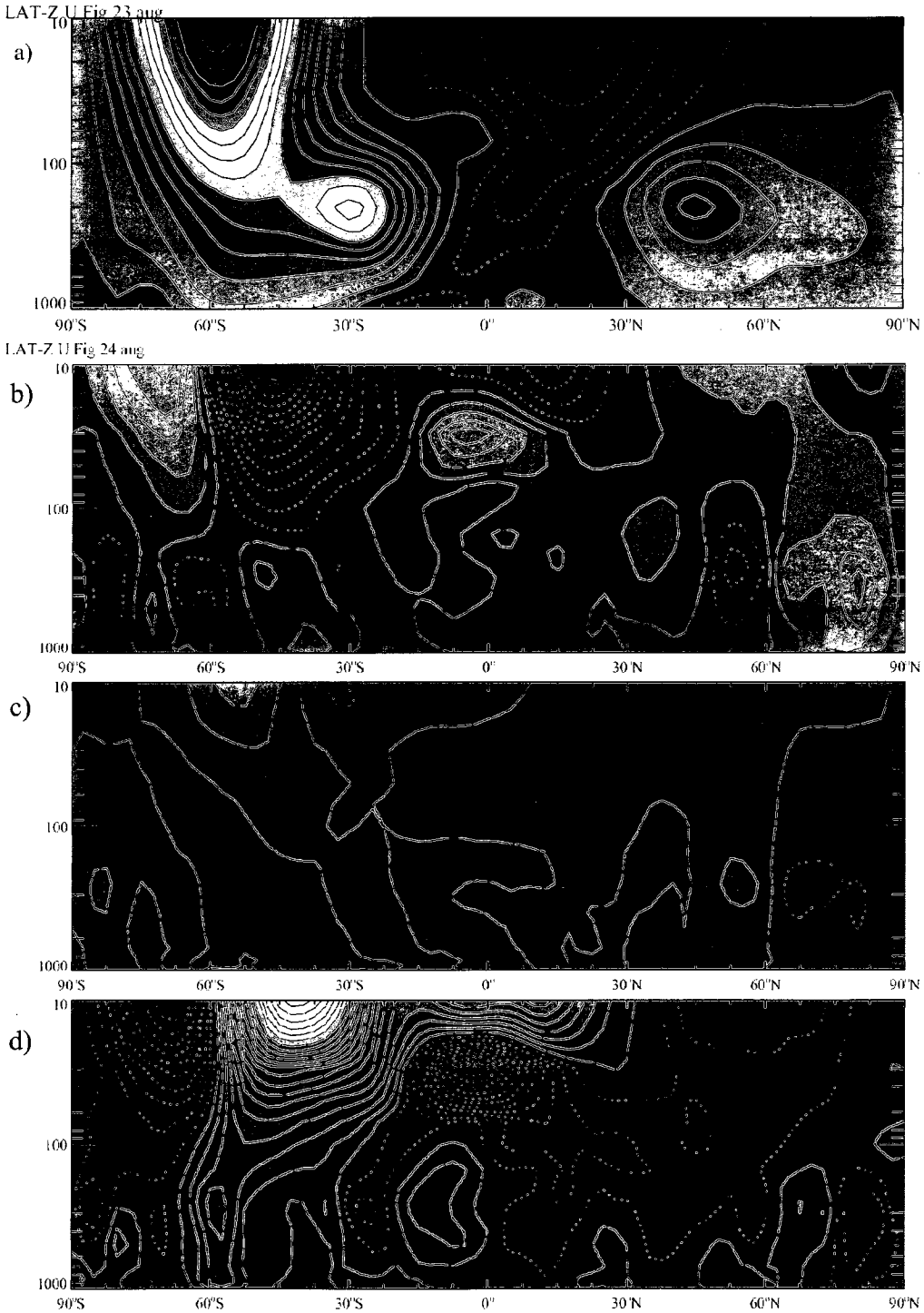

Figure 6.1. Altitude-Latitude mean August zonal winds: a) averaged, b) type I minus average, c) type II minus average, and d) type III minus average. Contour interval is a) 5 m/s and 0.5 m/s in b), c) and d).

Reproduced with permission of the copyright owner. Further reproduction prohibited without permission.

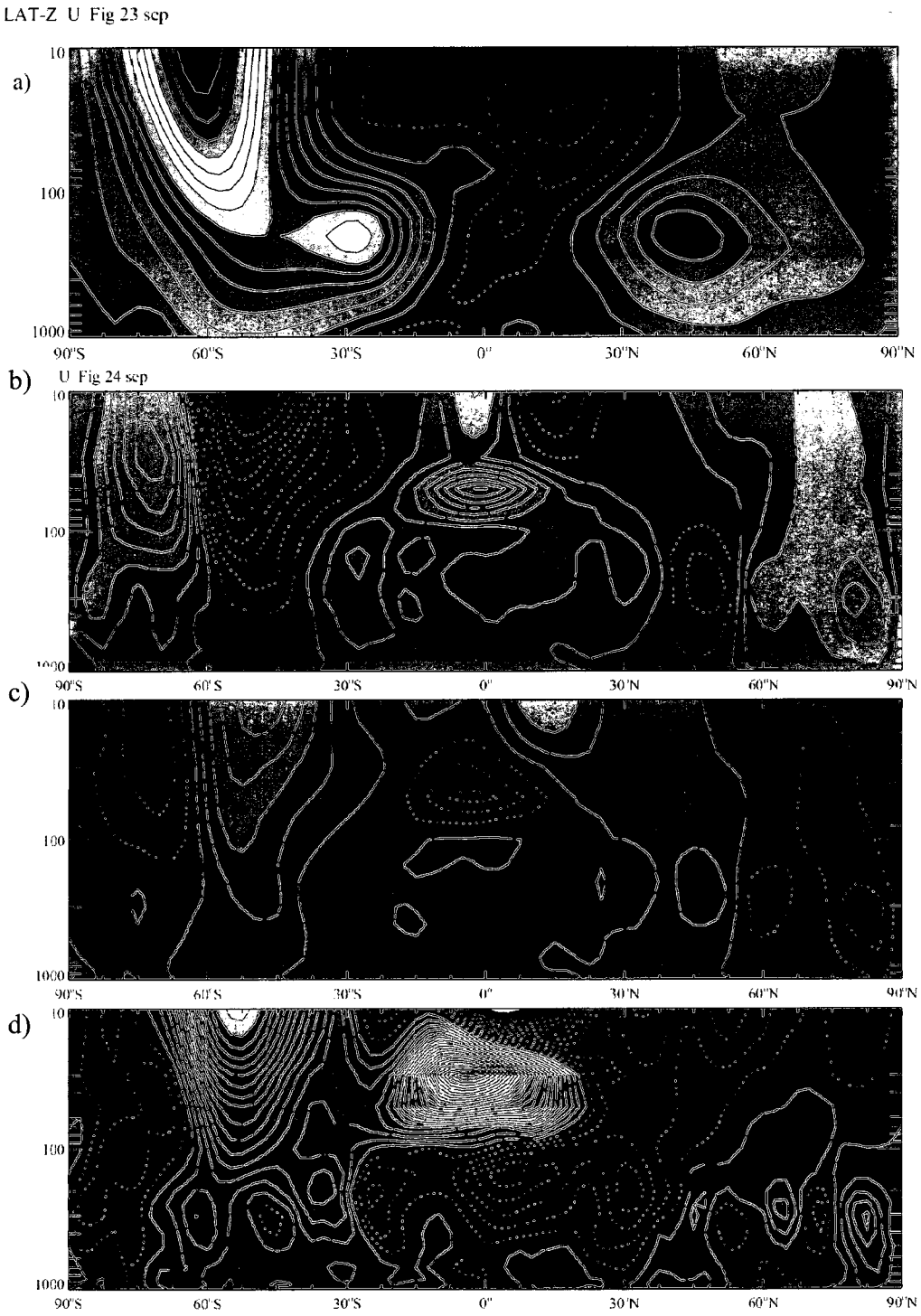

Figure 6.2. As in figure 6.1 but for September.

Reproduced with permission of the copyright owner. Further reproduction prohibited without permission.

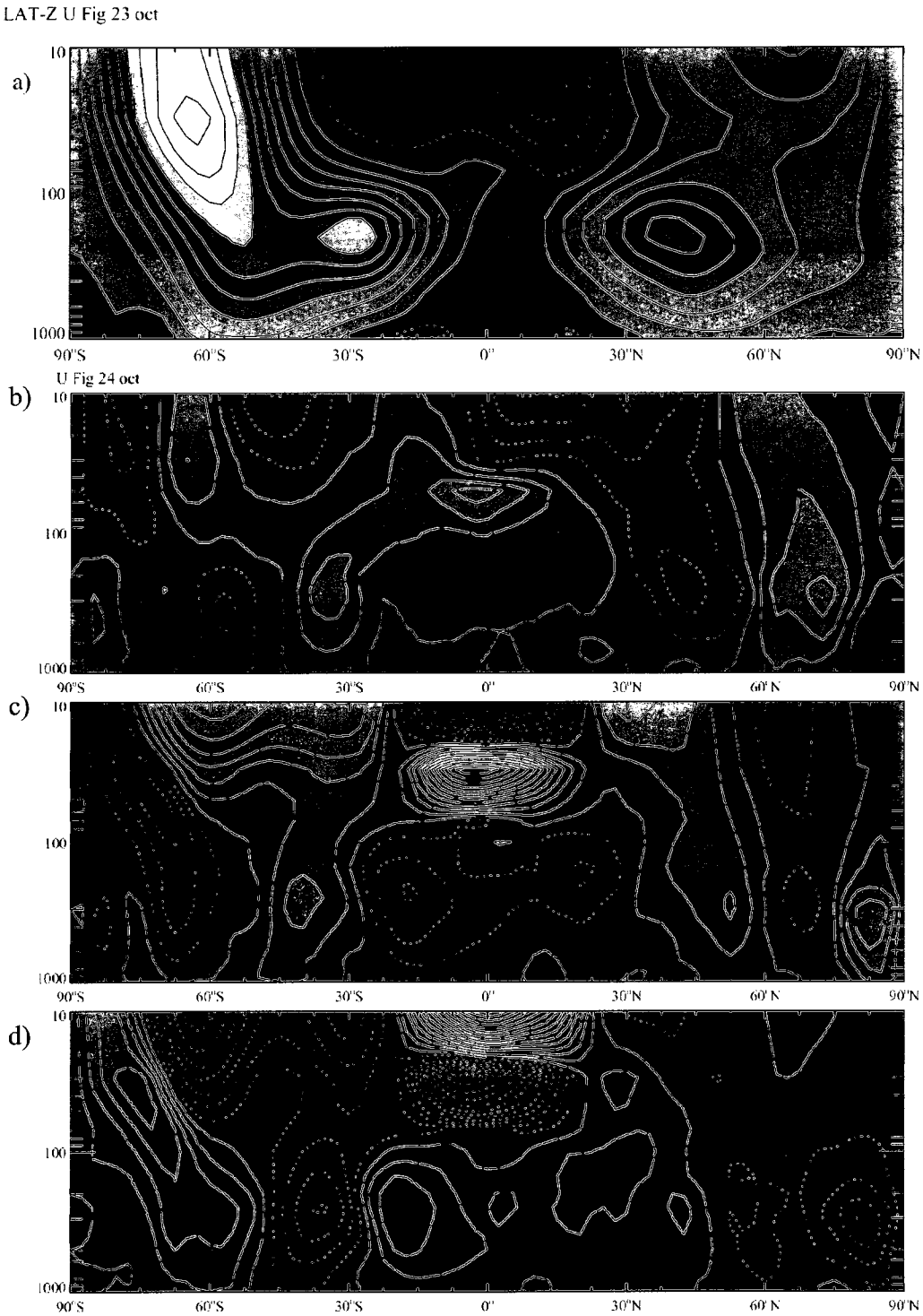

Figure 6.3. As in figure 6.1 but for October.

Reproduced with permission of the copyright owner. Further reproduction prohibited without permission.

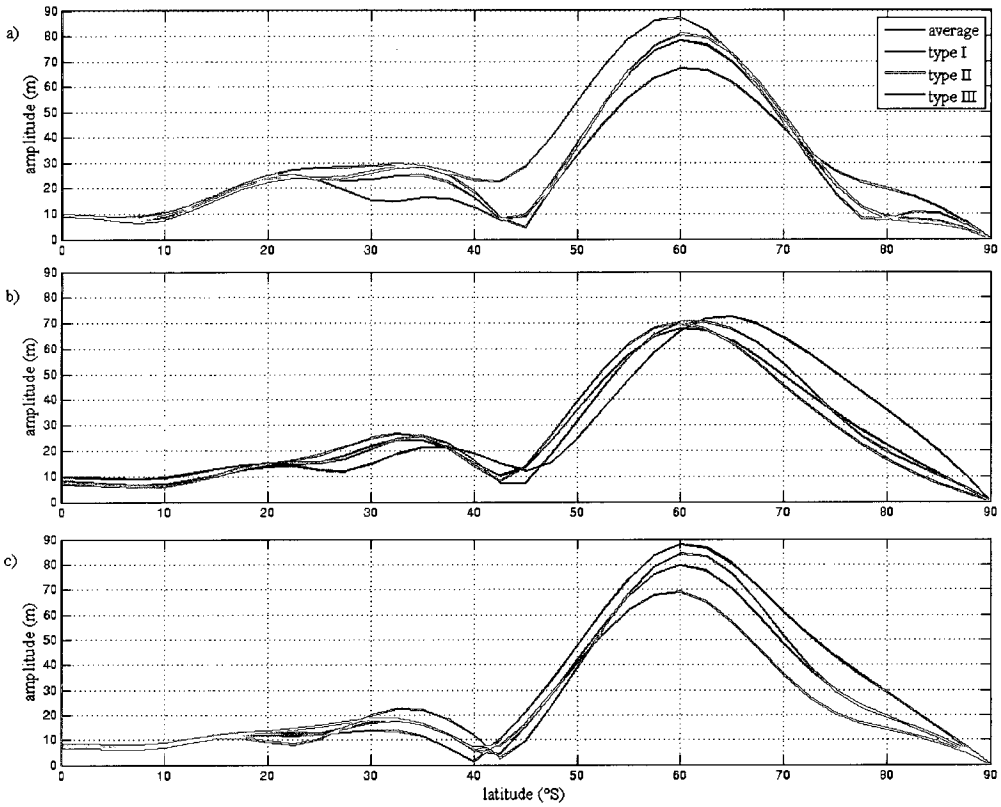

Figure 6.4. Amplitude of k=1 in the SH during a) August, b) September, c) October. Blue – average, green – type I, red – type II, teal – type III.

Reproduced with permission of the copyright owner. Further reproduction prohibited without permission.

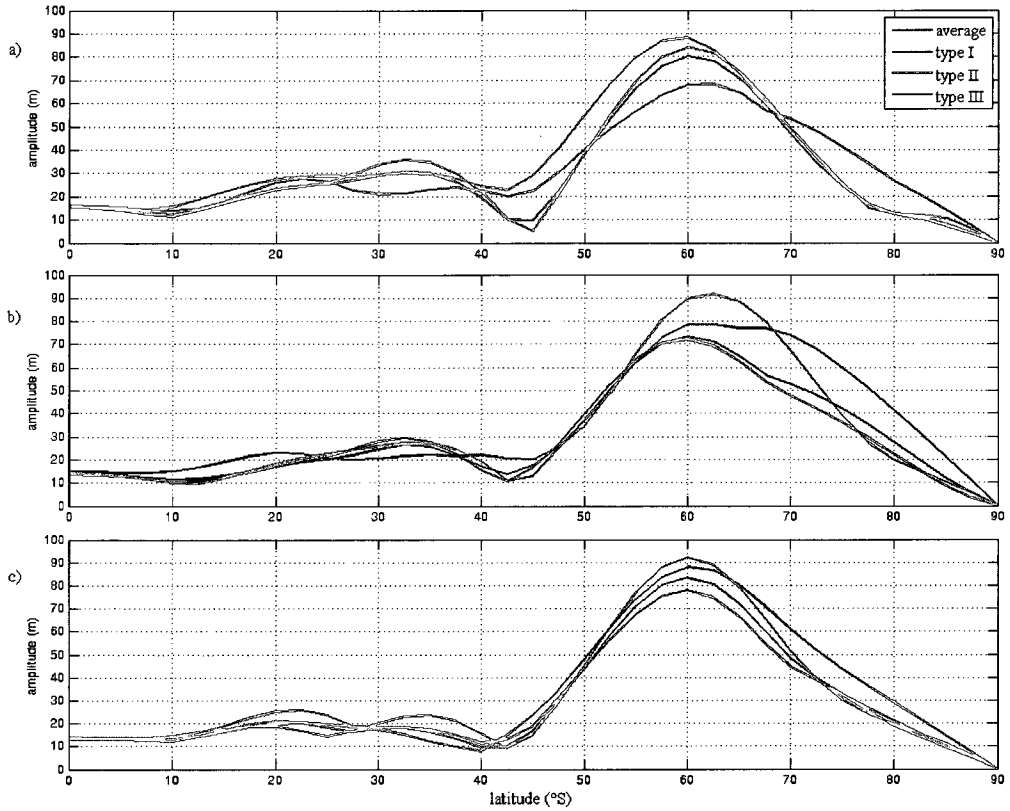

Figure 6.5. Amplitude of k=2 in the SH during a) August, b) September, c) October. Blue – average, green – type I, red – type II, teal – type III.

Reproduced with permission of the copyright owner. Further reproduction prohibited without permission.

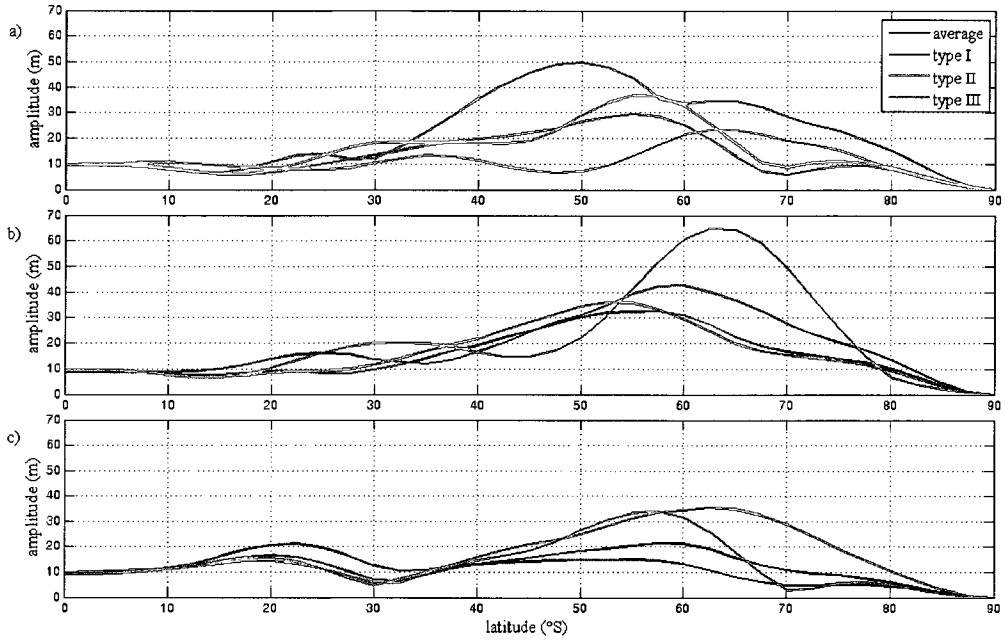

Figure 6.6. Amplitude of k=3 in the SH during a) August, b) September, c) October. Blue – average, green – type I, red – type II, teal – type III.

Reproduced with permission of the copyright owner. Further reproduction prohibited without permission.

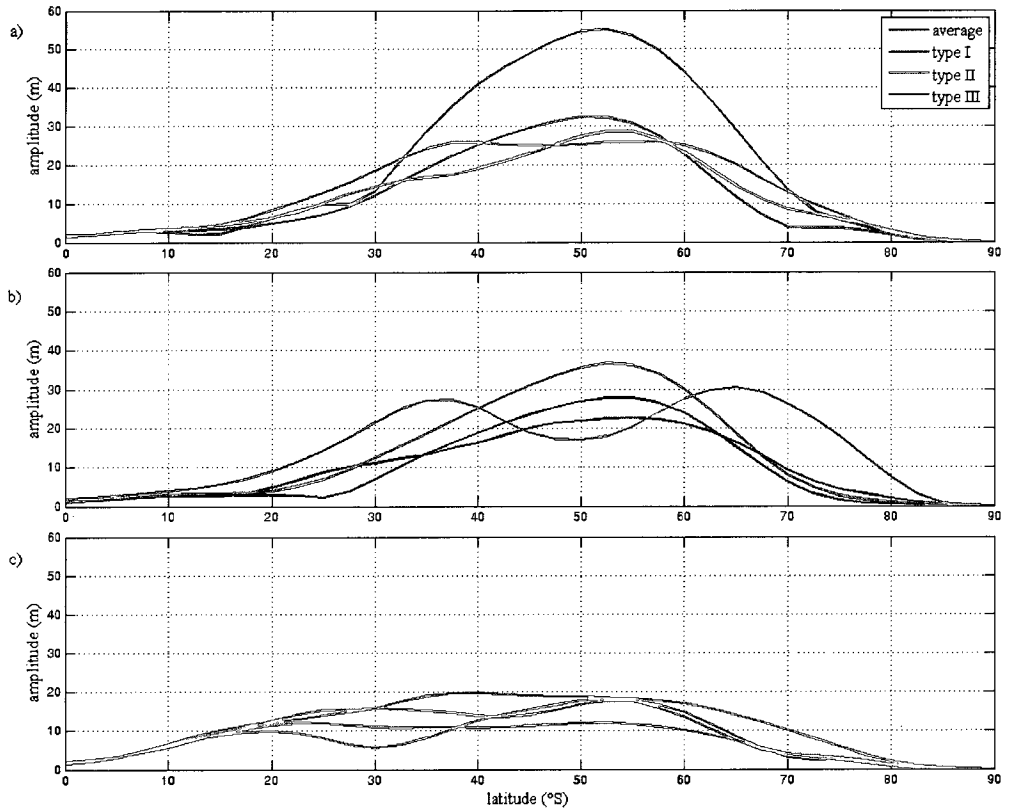

Figure 6.7. Amplitude of k=4 in the SH during a) August, b) September, c) October. Blue – average, green – type I, red – type II, magenta – type III.

Reproduced with permission of the copyright owner. Further reproduction prohibited without permission.

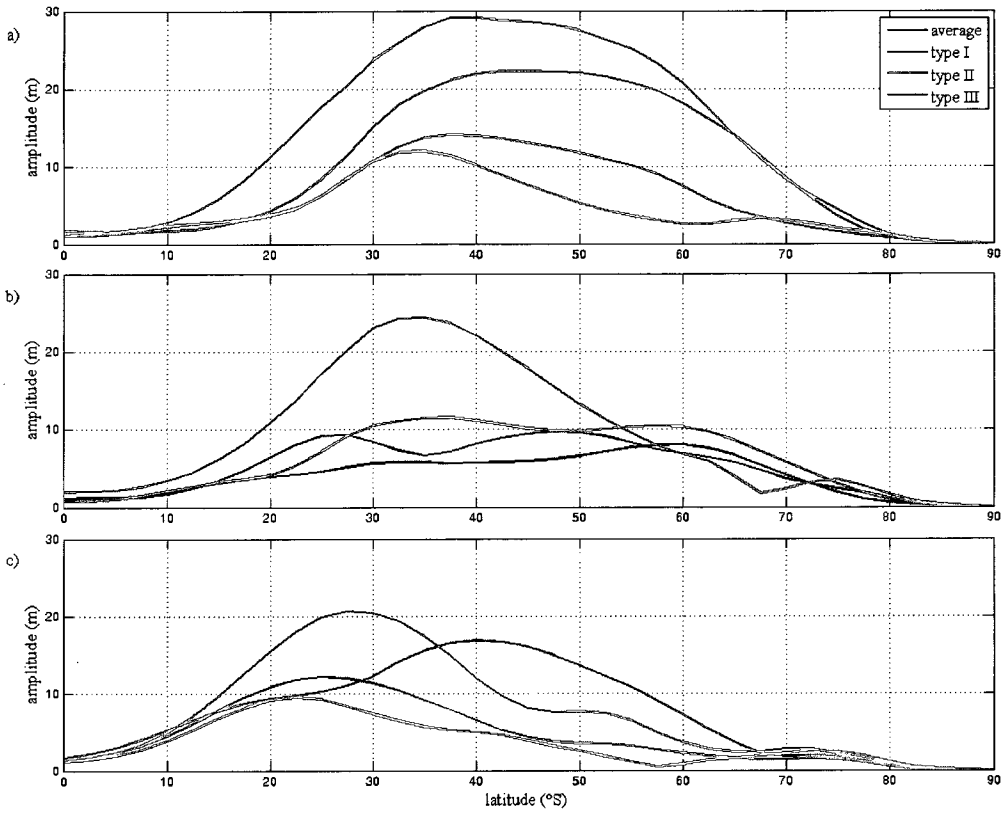

Figure 6.8. Amplitude of k=5 in the SH during a) August, b) September, c) October. Blue – average, green – type I, red – type II, teal – type III.

Reproduced with permission of the copyright owner. Further reproduction prohibited without permission.

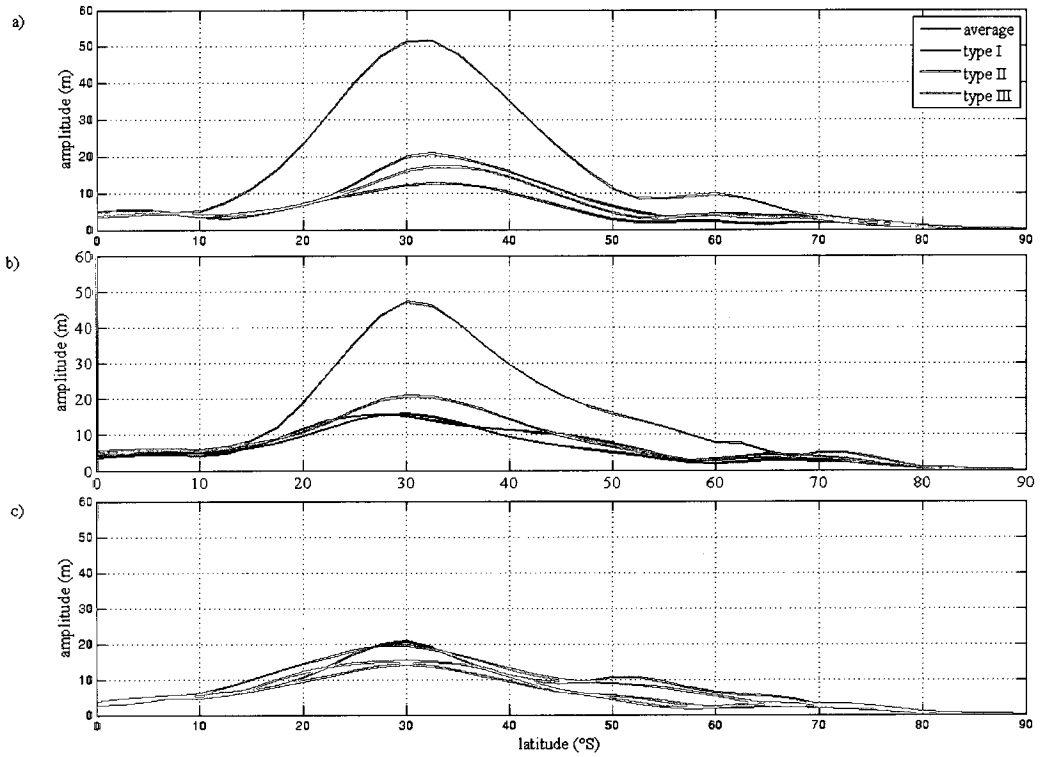

Figure 6.9. Amplitude of k=6-8 in the SH during a) August, b) September, c) October. Blue – average, green – type I, red – type II, teal – type III.

Reproduced with permission of the copyright owner. Further reproduction prohibited without permission.

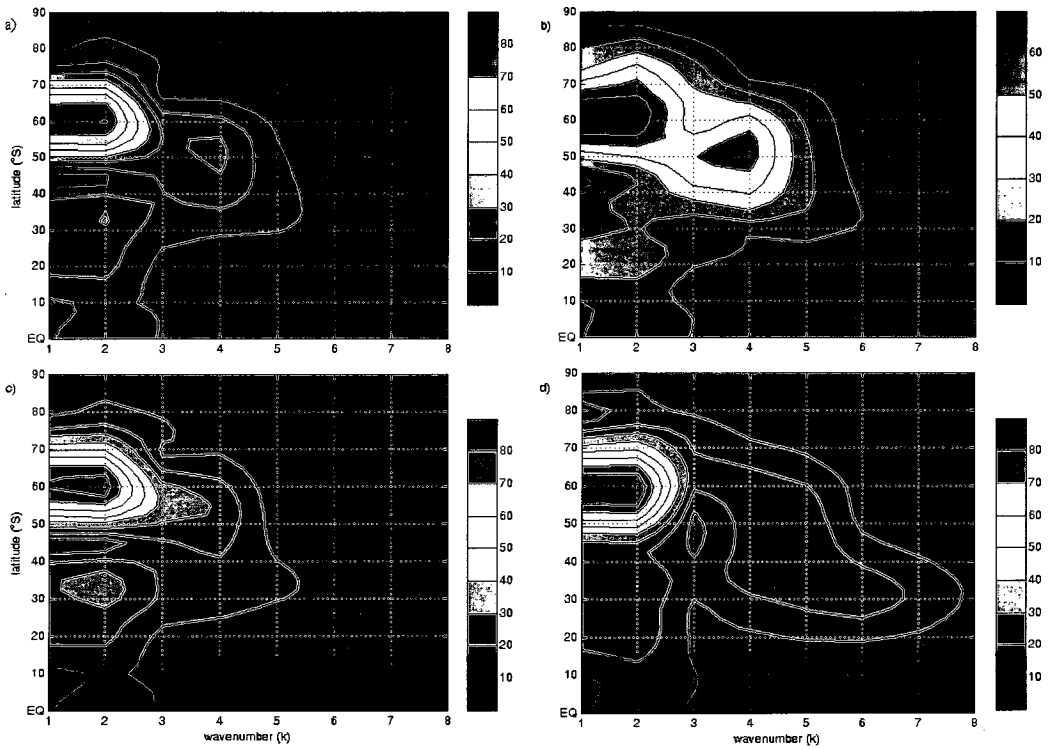

Figure 6.10. Latitude-wavenumber plot of amplitude for August a) averaged, b) Type I, c) Type II and d) Type III.

Reproduced with permission of the copyright owner. Further reproduction prohibited without permission.

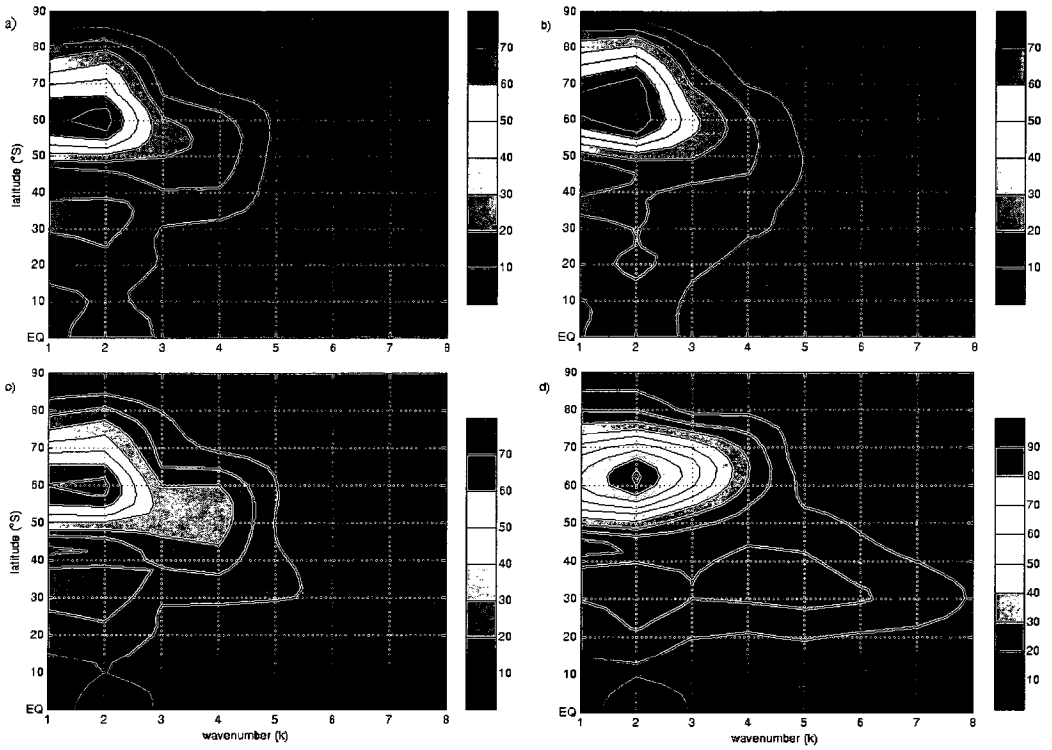

Figure 6.11. As in figure 6.10 but for September.

Reproduced with permission of the copyright owner. Further reproduction prohibited without permission.

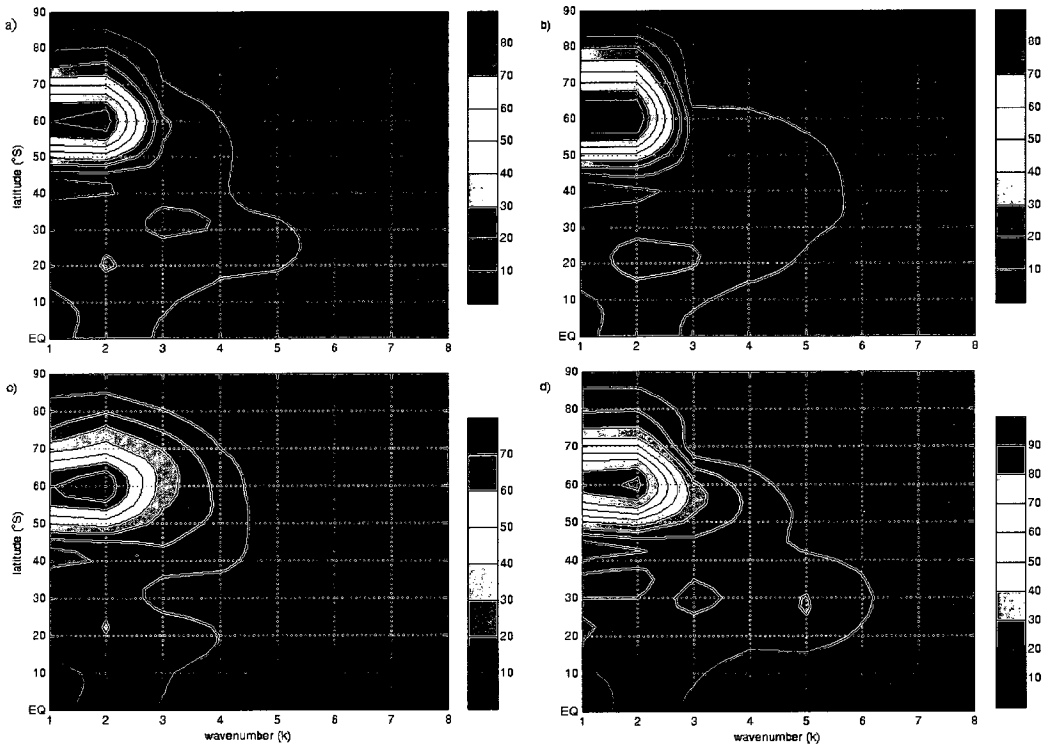

Figure 6.12. As in figure 6.10 but for October.

Reproduced with permission of the copyright owner. Further reproduction prohibited without permission.

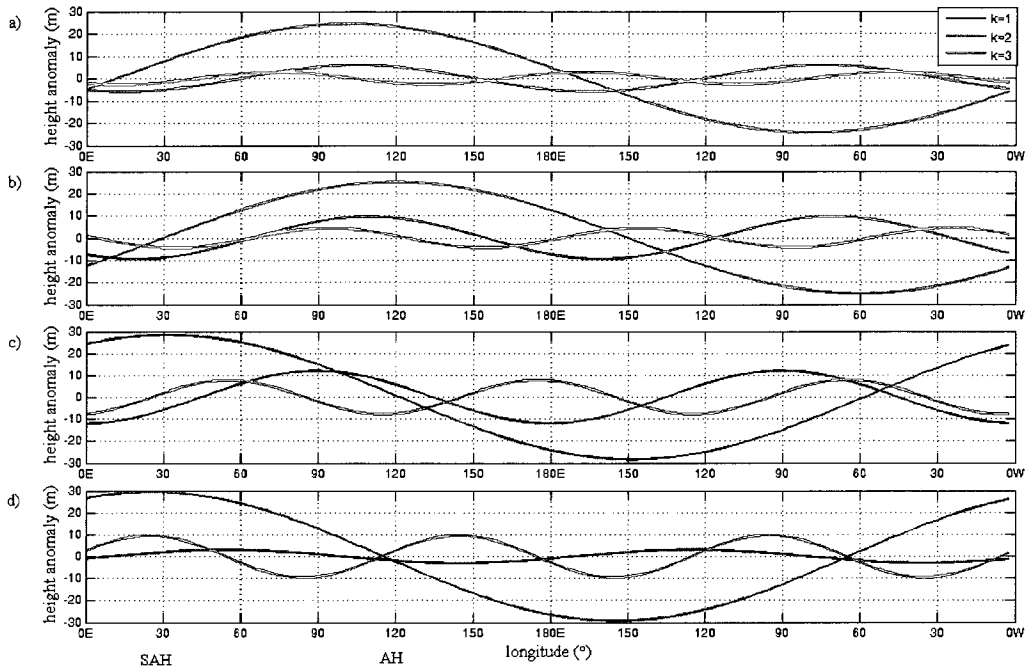

Figure 6.13. Longitude-Amplitude plot of k=1-3 for a) monthly averaged at 22°S, b) Type I at 22°S, c) Type II at 35°S, d) Type III at 33°S. Blue – k=1, green – k=2, red – k=3.

Reproduced with permission of the copyright owner. Further reproduction prohibited without permission.

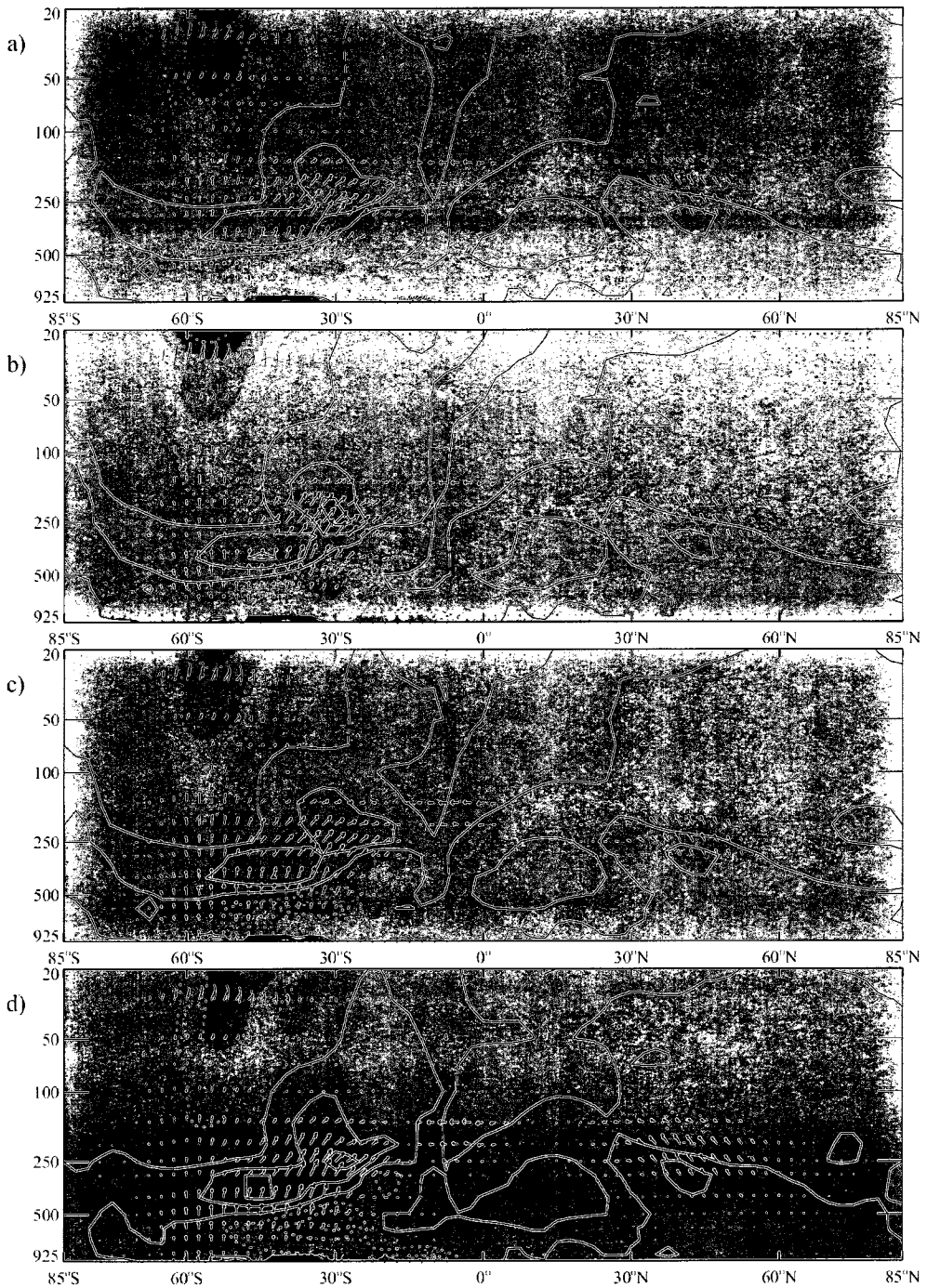

Figure 6.14. E-P flux divergence and vectors for all wavenumbers during the August for a) monthly average, b) Type I, c) Type II, d) Type III. Contour interval 0.5 m/s/day above 100 hPa and 2 m/s/day below. Green color depicts divergence, blue shows convergence

Reproduced with permission of the copyright owner. Further reproduction prohibited without permission.

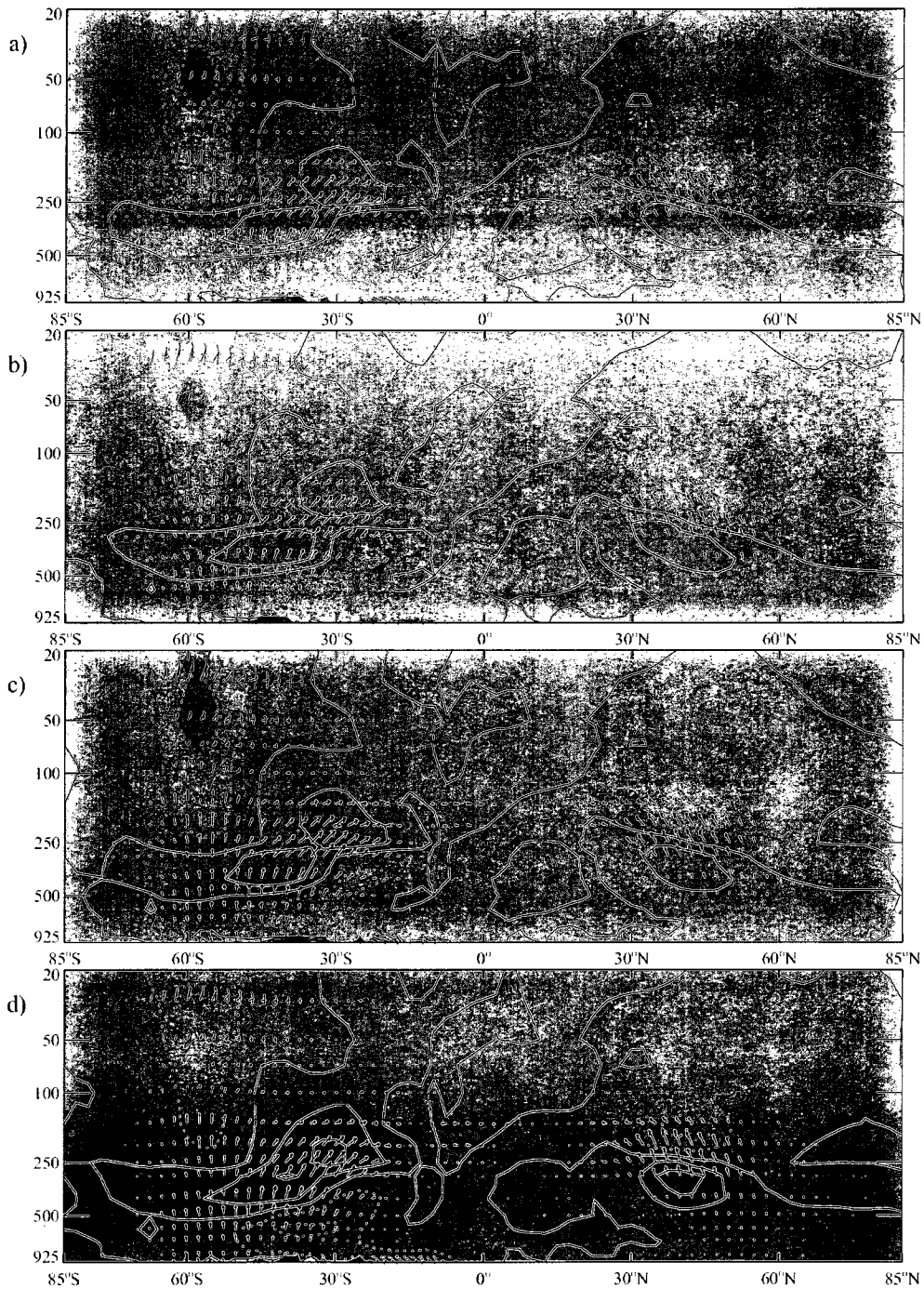

Figure 6.15. As in figure 6.14 but for September.

Reproduced with permission of the copyright owner. Further reproduction prohibited without permission.

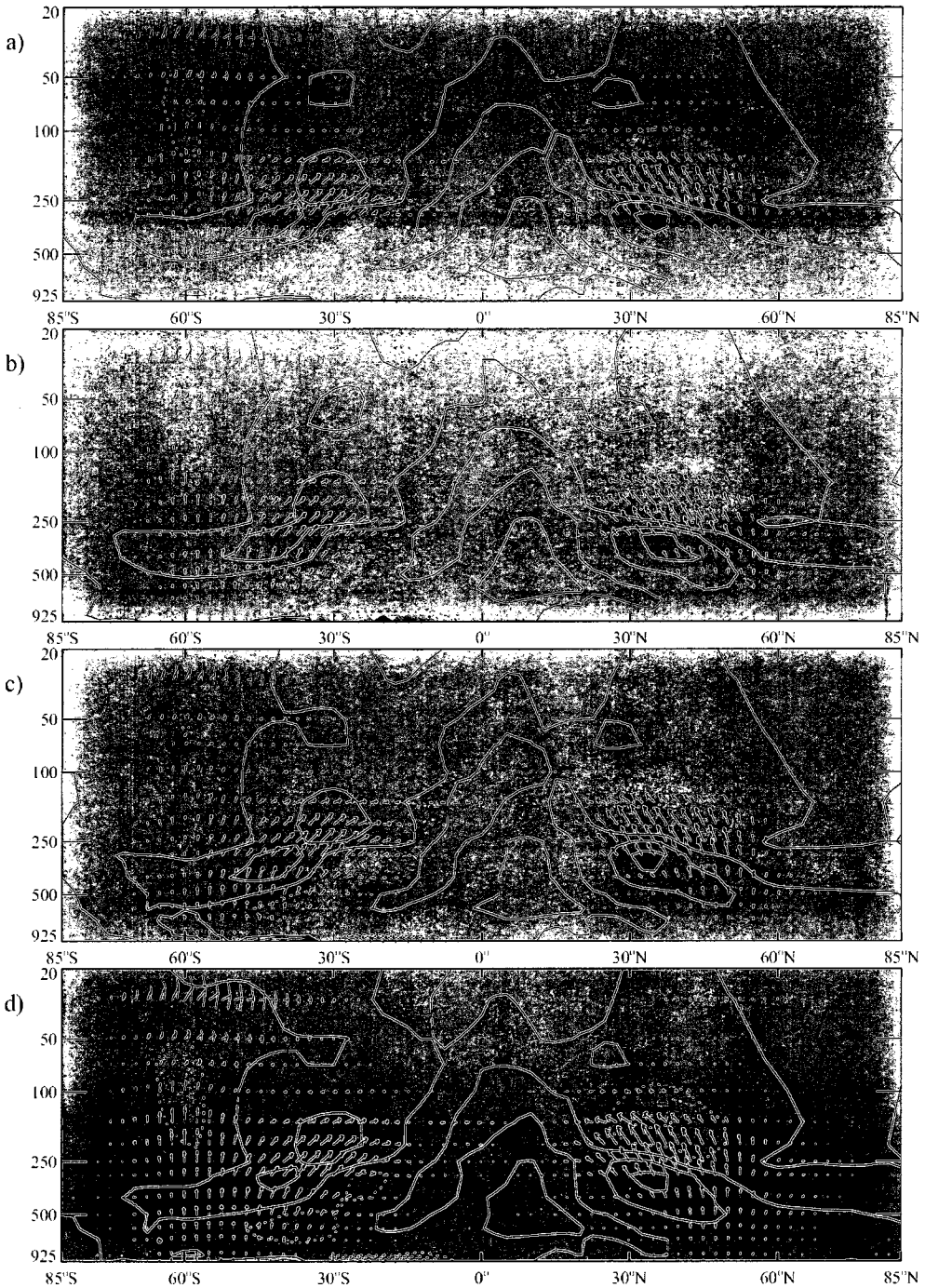

Figure 6.16. As in figure 6.14 but for October.

Reproduced with permission of the copyright owner. Further reproduction prohibited without permission.

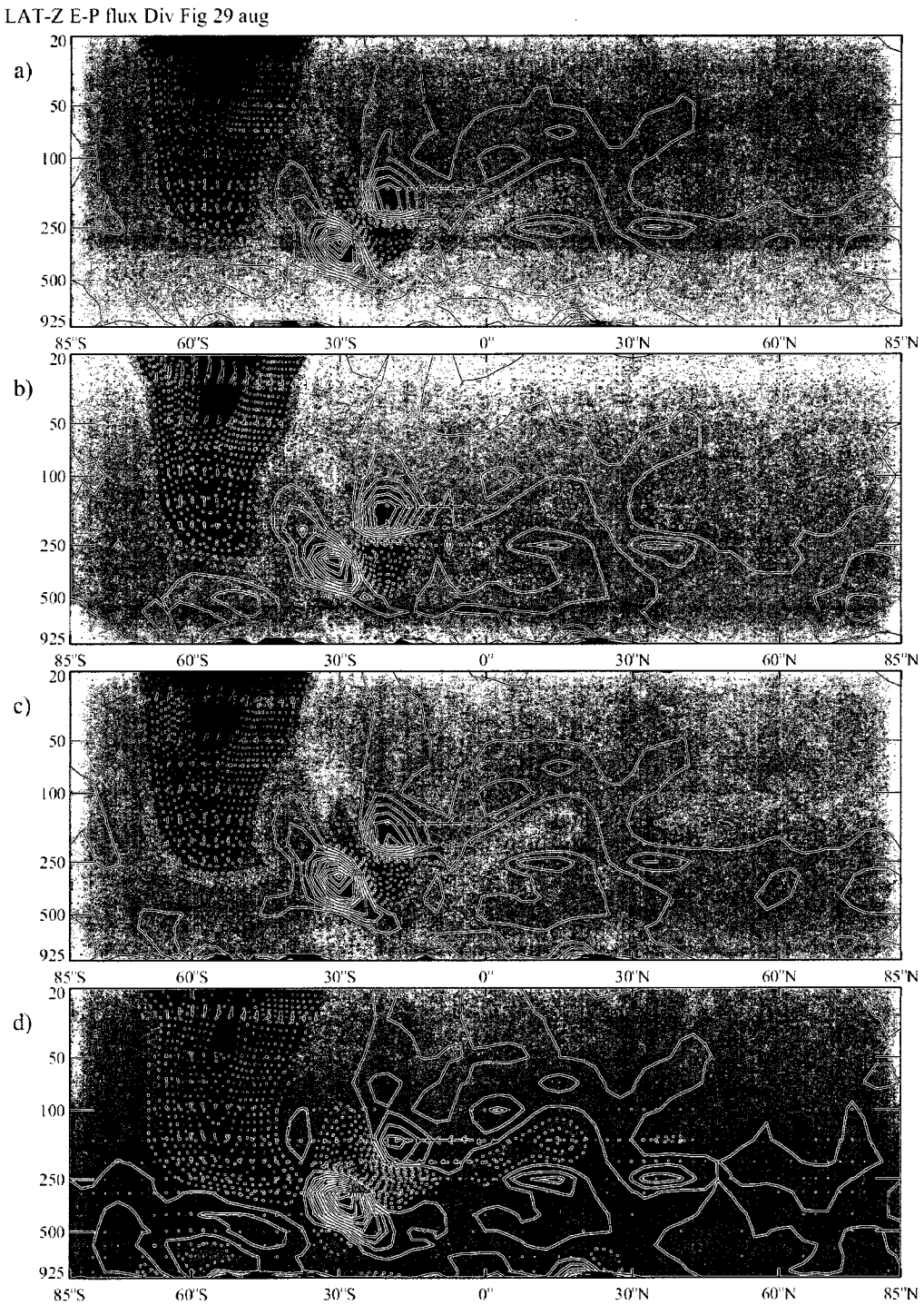

Figure 6.17. E-P flux divergence and vectors for k=1 during the August for a) monthly average, b) Type I, c) Type II, d) Type III. Contour interval 0.1 m/s/day above 100 hPa and 2 m/s/day below.

Reproduced with permission of the copyright owner. Further reproduction prohibited without permission.

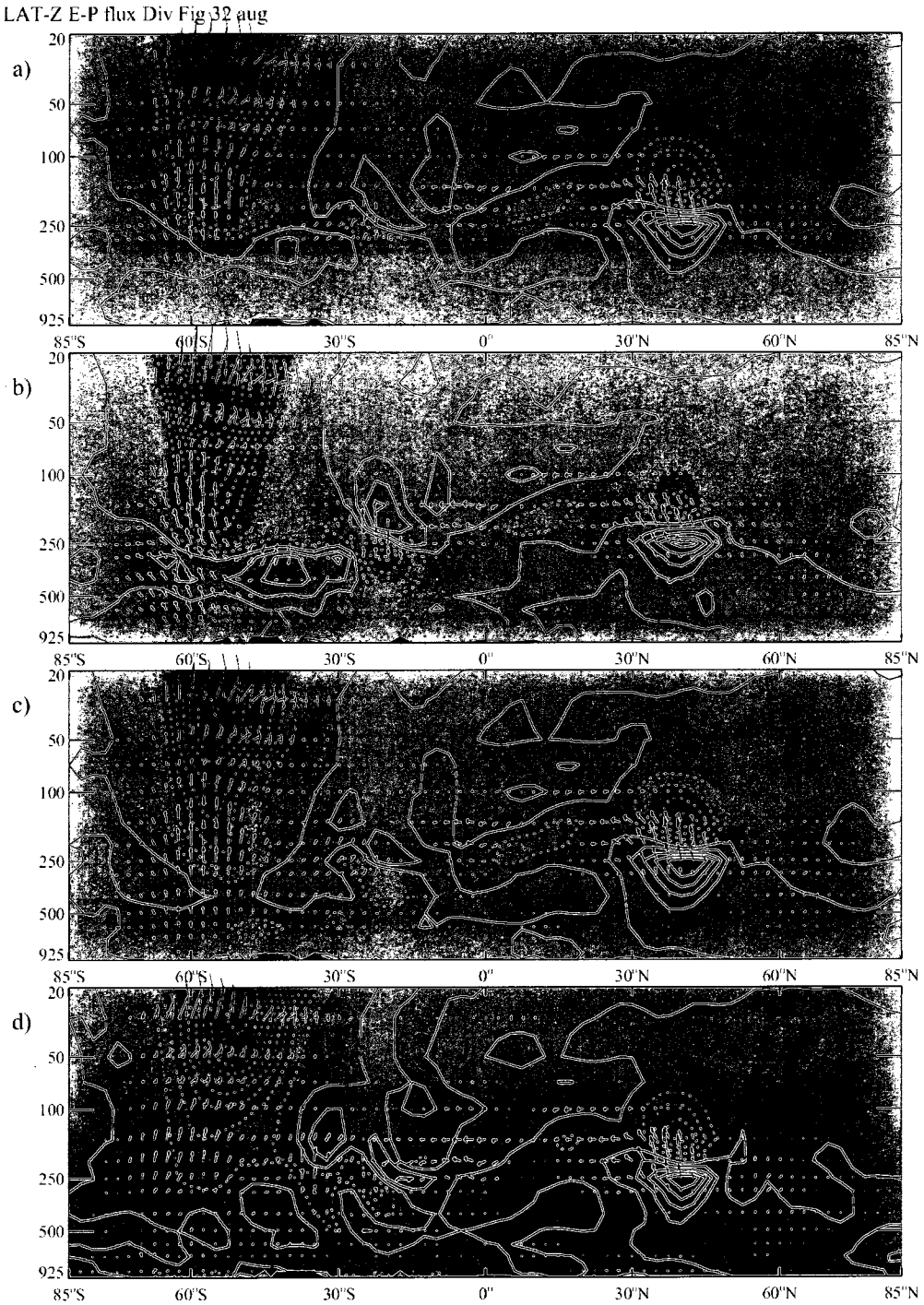

Figure 6.18. E-P flux divergence and vectors for k=2 during the August for a) monthly average, b) Type I, c) Type II, d) Type III. Contour interval 0.1 m/s/day above 100 hPa and 2 m/s/day below.

Reproduced with permission of the copyright owner. Further reproduction prohibited without permission.

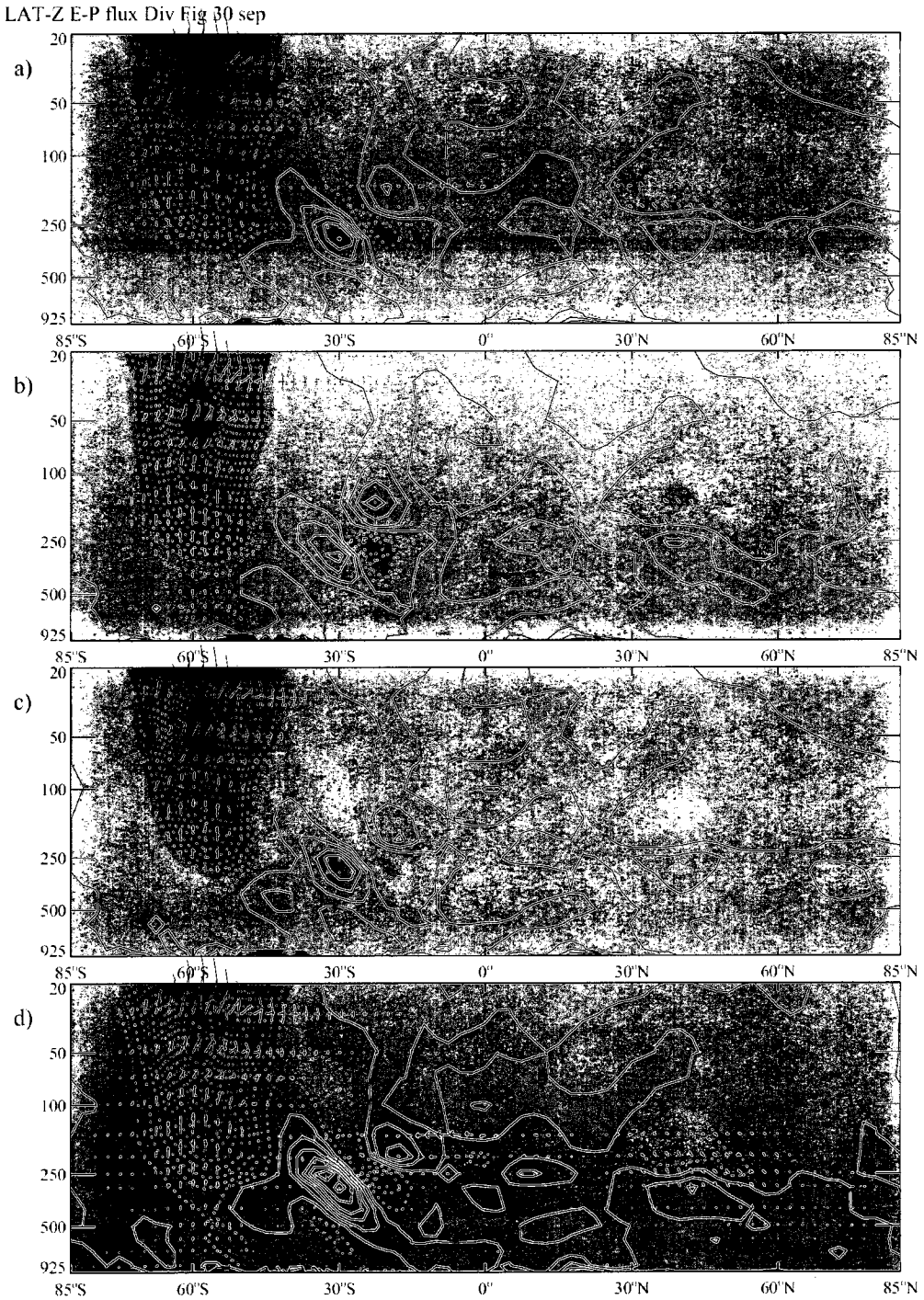

Figure 6.19. E-P flux divergence and vectors for k=1 during the September for a) monthly average, b) Type I, c) Type II, d) Type III. Contour interval 0.1 m/s/day above 100 hPa and 0.2 m/s/day below.

Reproduced with permission of the copyright owner. Further reproduction prohibited without permission.

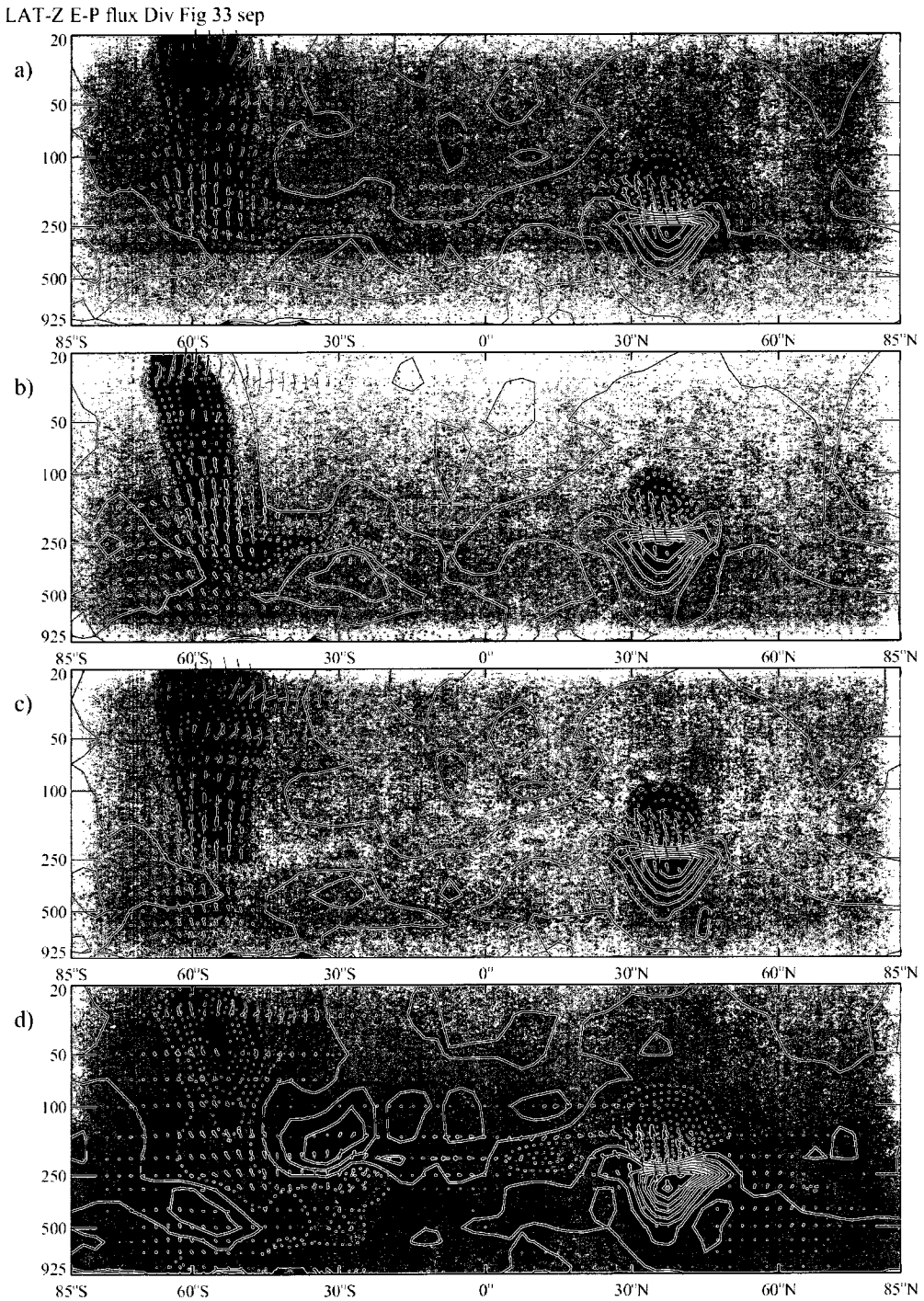

Figure 6.20. E-P flux divergence and vectors for k=2 during the September for a) monthly average, b) Type I, c) Type II, d) Type III. Contour interval 0.1 m/s/day above 100 hPa and 0.2 m/s/day below.

Reproduced with permission of the copyright owner. Further reproduction prohibited without permission.

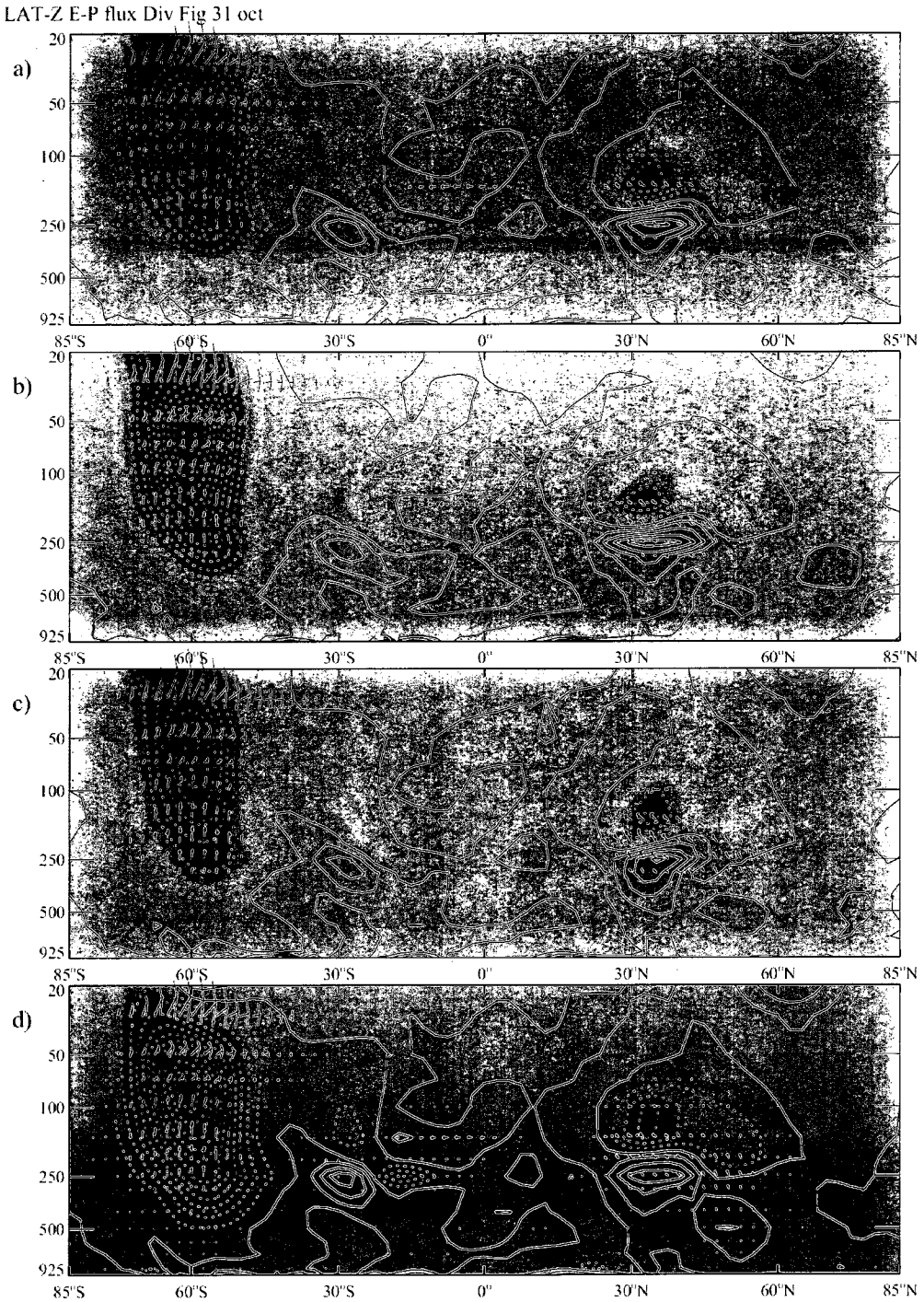

Figure 6.21. E-P flux divergence and vectors for k=1 during the October for a) monthly average, b) Type I, c) Type II, d) Type III. Contour interval 0.1 m/s/day above 100 hPa and 0.2 m/s/day below.

Reproduced with permission of the copyright owner. Further reproduction prohibited without permission.

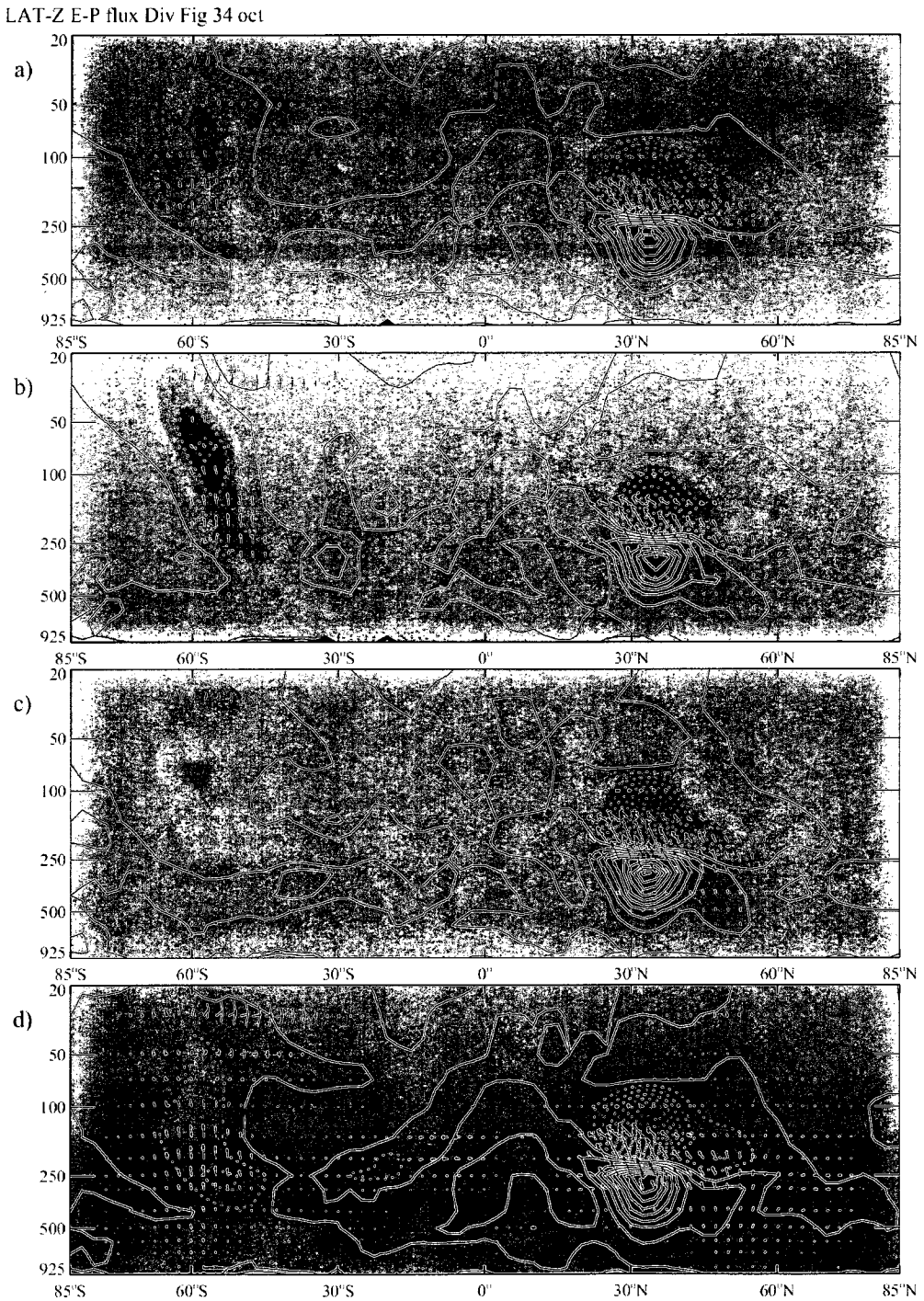

Figure 6.22. E-P flux divergence and vectors for k=2 during the October for a) monthly average, b) Type I, c) Type II, d) Type III. Contour interval 0.1 m/s/day above 100 hPa and 0.2 m/s/day below.

Reproduced with permission of the copyright owner. Further reproduction prohibited without permission.

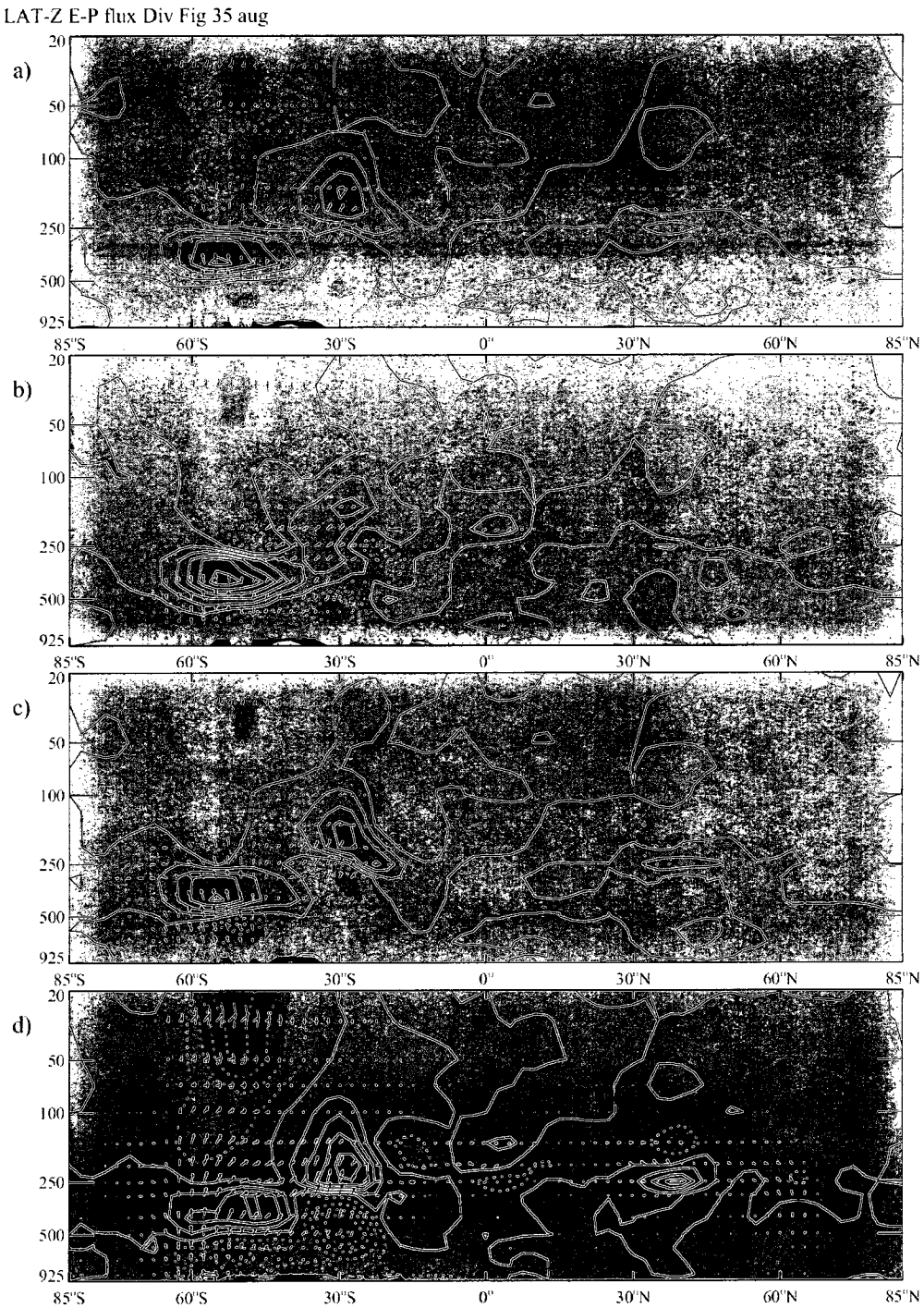

Figure 6.23. E-P flux divergence and vectors for k=3 during the August for a) monthly average, b) Type I, c) Type II, d) Type III. Contour interval 0.1 m/s/day above 100 hPa and 0.2 m/s/day below.

Reproduced with permission of the copyright owner. Further reproduction prohibited without permission.

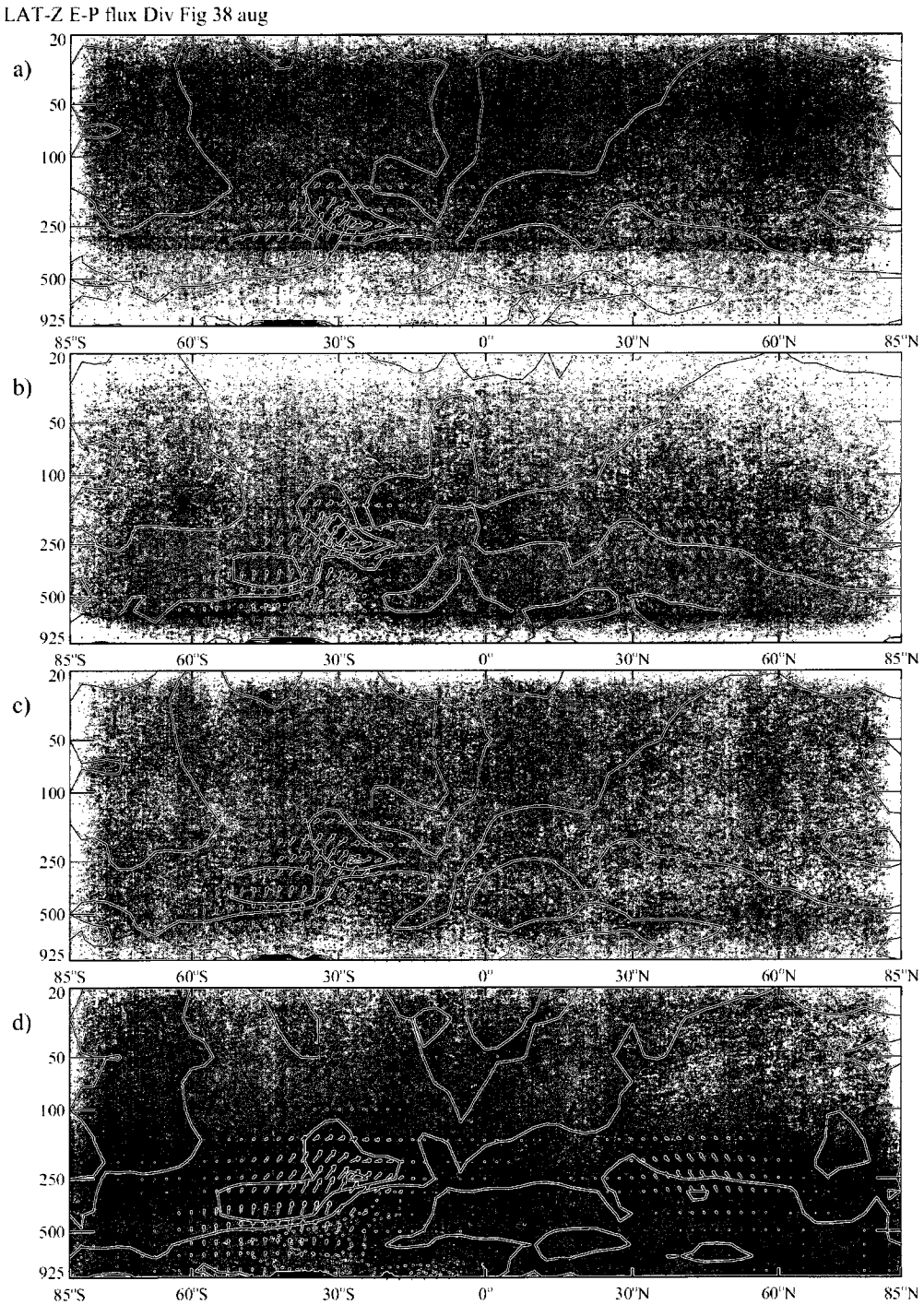

Figure 6.24. E-P flux divergence and vectors for k=4-10 during the August for a) monthly average, b) Type I, c) Type II, d) Type III. Contour interval 0.1 m/s/day above 100 hPa and 0.2 m/s/day below.

Reproduced with permission of the copyright owner. Further reproduction prohibited without permission.

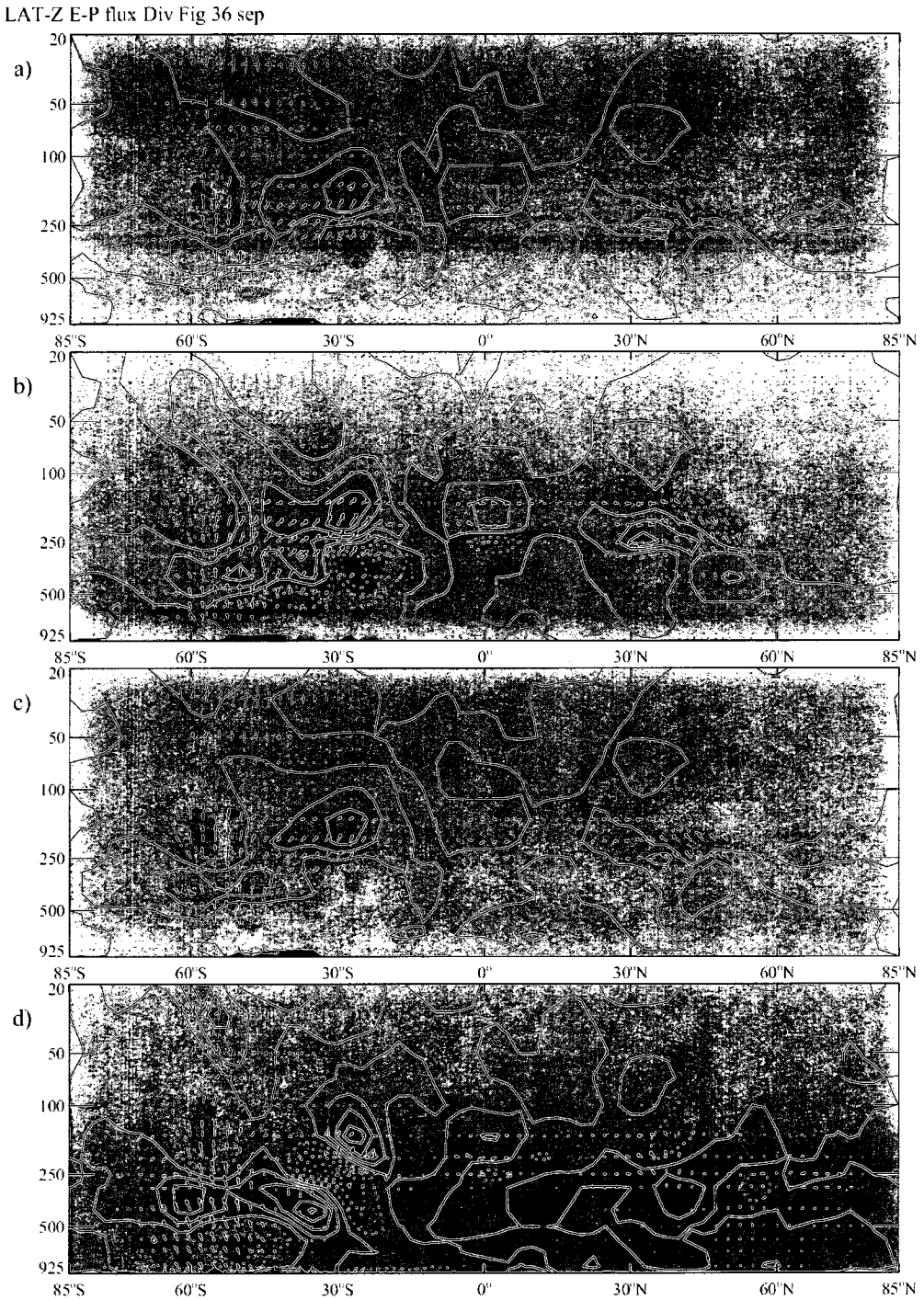

Figure 6.25. E-P flux divergence and vectors for k=3 during the September for a) monthly average, b) Type I, c) Type II, d) Type III. Contour interval 0.1 m/s/day above 100 hPa and 0.2 m/s/day below.

Reproduced with permission of the copyright owner. Further reproduction prohibited without permission.

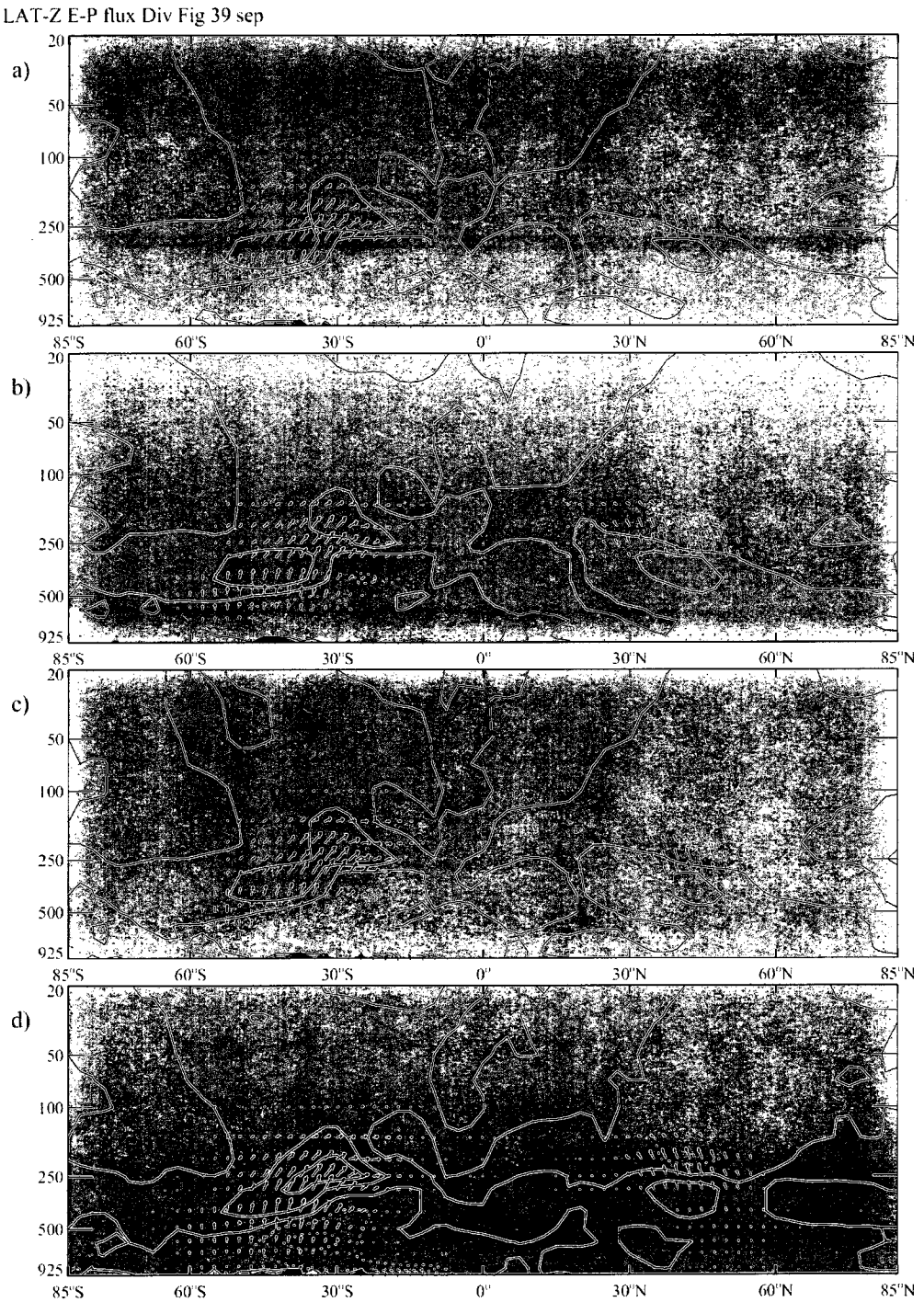

Figure 6.26. E-P flux divergence and vectors for k=4-10 during the September for a) monthly average, b) Type I, c) Type II, d) Type III. Contour interval 0.1 m/s/day above 100 hPa and 0.2 m/s/day below.

Reproduced with permission of the copyright owner. Further reproduction prohibited without permission.

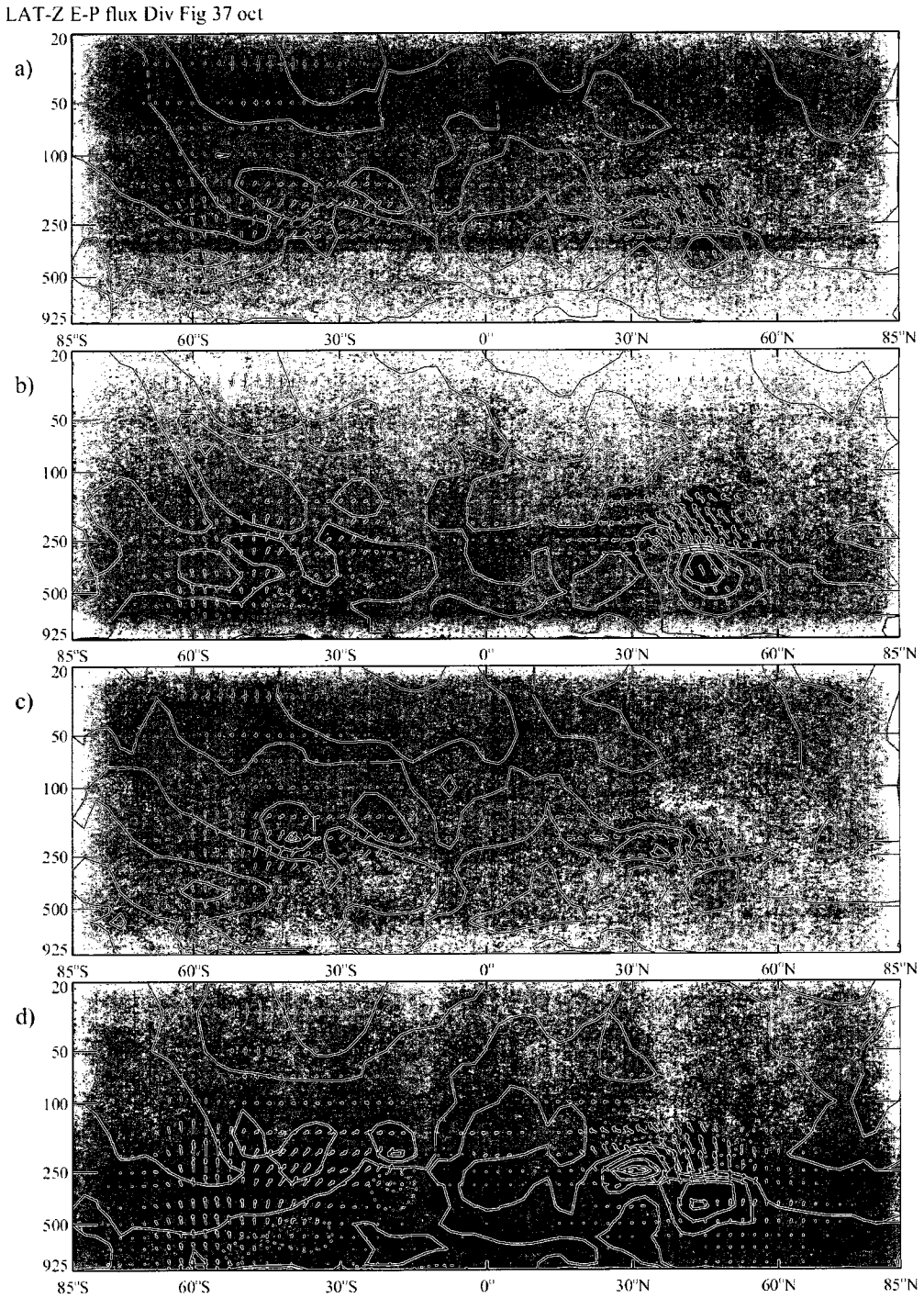

Figure 6.27. E-P flux divergence and vectors for k=3 during the October for a) monthly average, b) Type I, c) Type II, d) Type III. Contour interval 0.1 m/s/day above 100 hPa and 0.2 m/s/day below.

Reproduced with permission of the copyright owner. Further reproduction prohibited without permission.

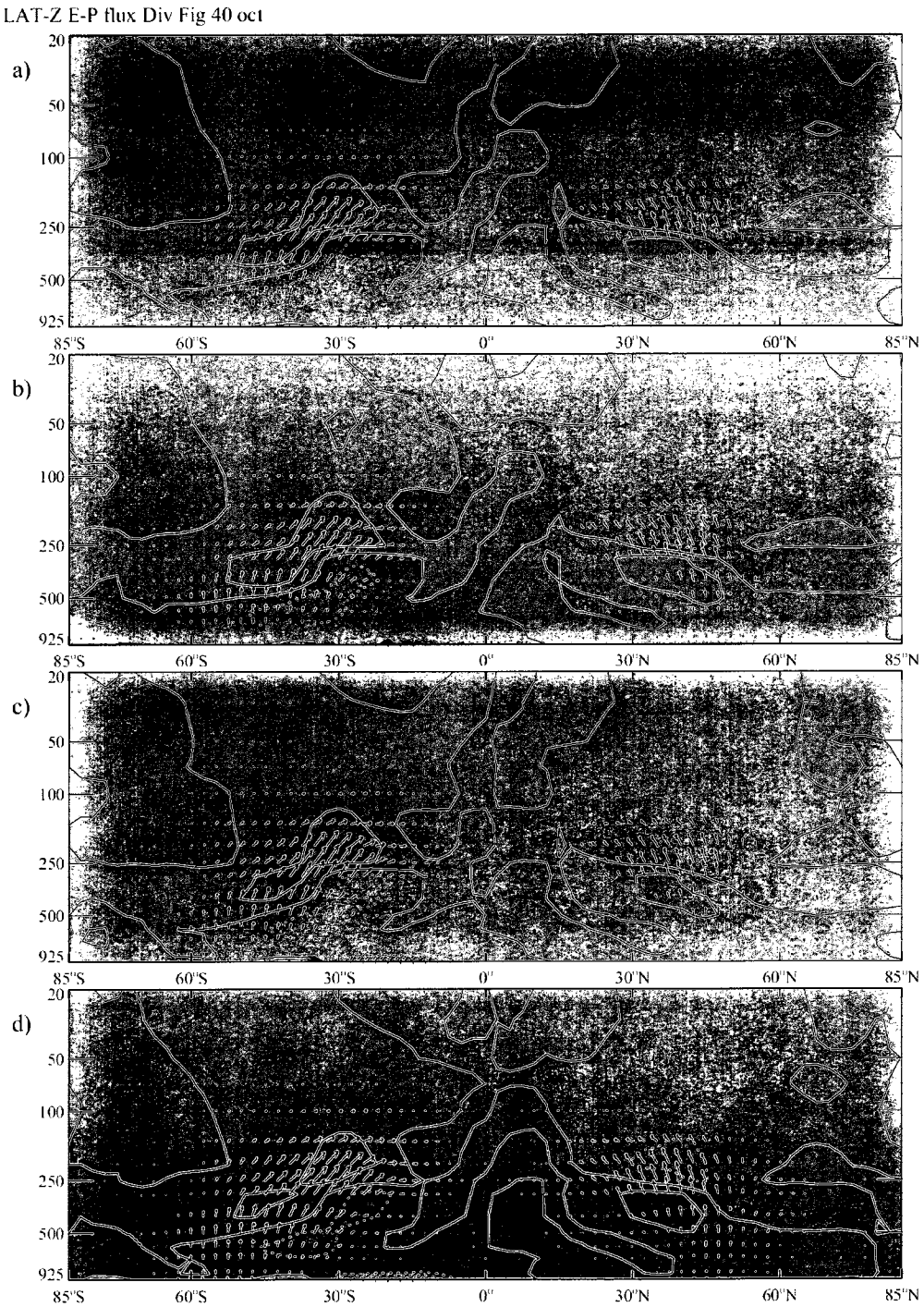

Figure 6.28. E-P flux divergence and vectors for k=4-10 during the October for a) monthly average, b) Type I, c) Type II, d) Type III. Contour interval 0.1 m/s/day above 100 hPa and 0.2 m/s/day below.

Reproduced with permission of the copyright owner. Further reproduction prohibited without permission.

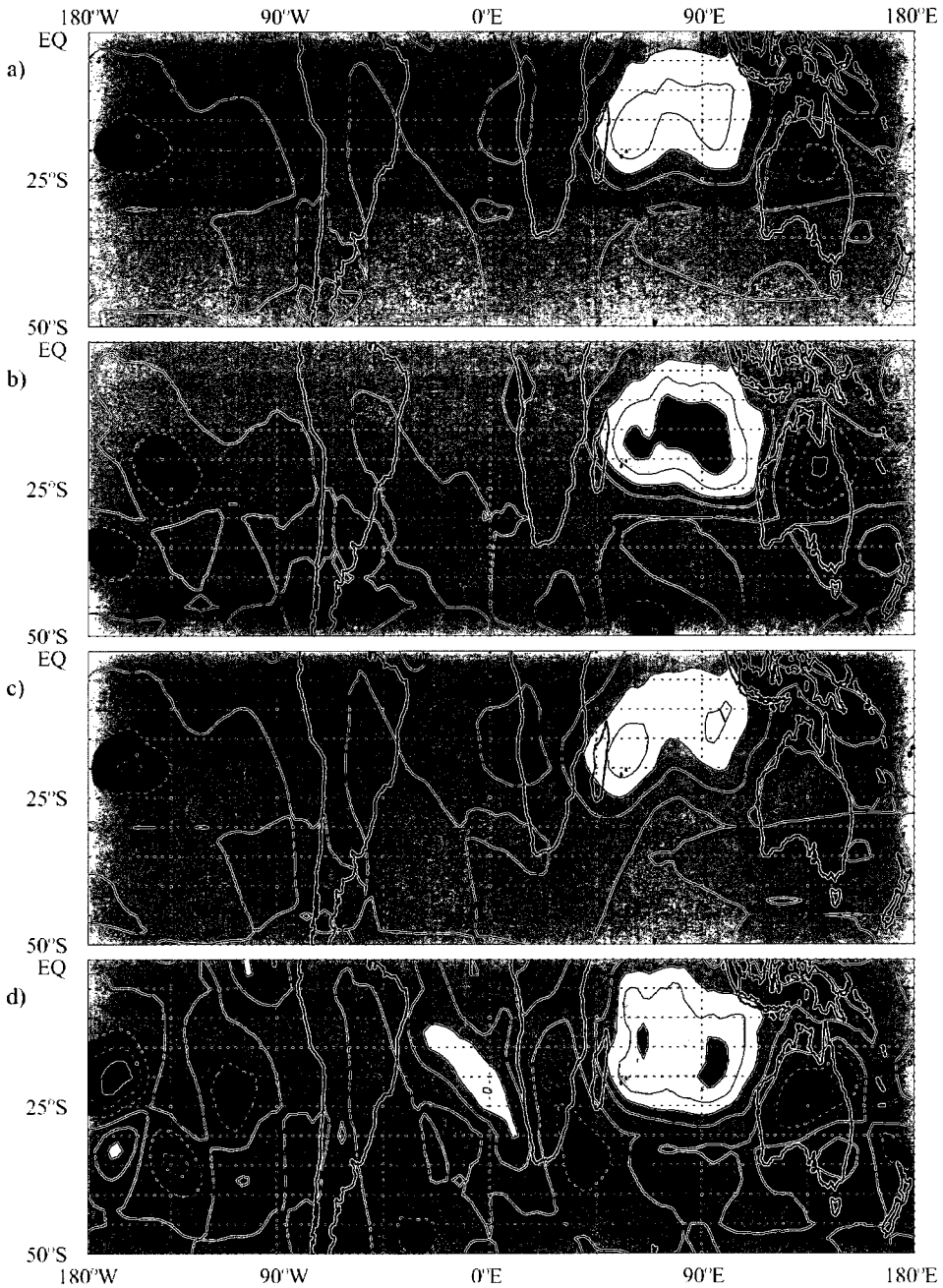

Figure 6.29. Meridional advection of absolute vorticity in August 1995-2004 for a) monthly average, b) Type I, c) Type II, d) Type III. Contour interval 0.2 x 100ms^{-1}day^{-1}, negative values depicted by dashed line.

Reproduced with permission of the copyright owner. Further reproduction prohibited without permission.

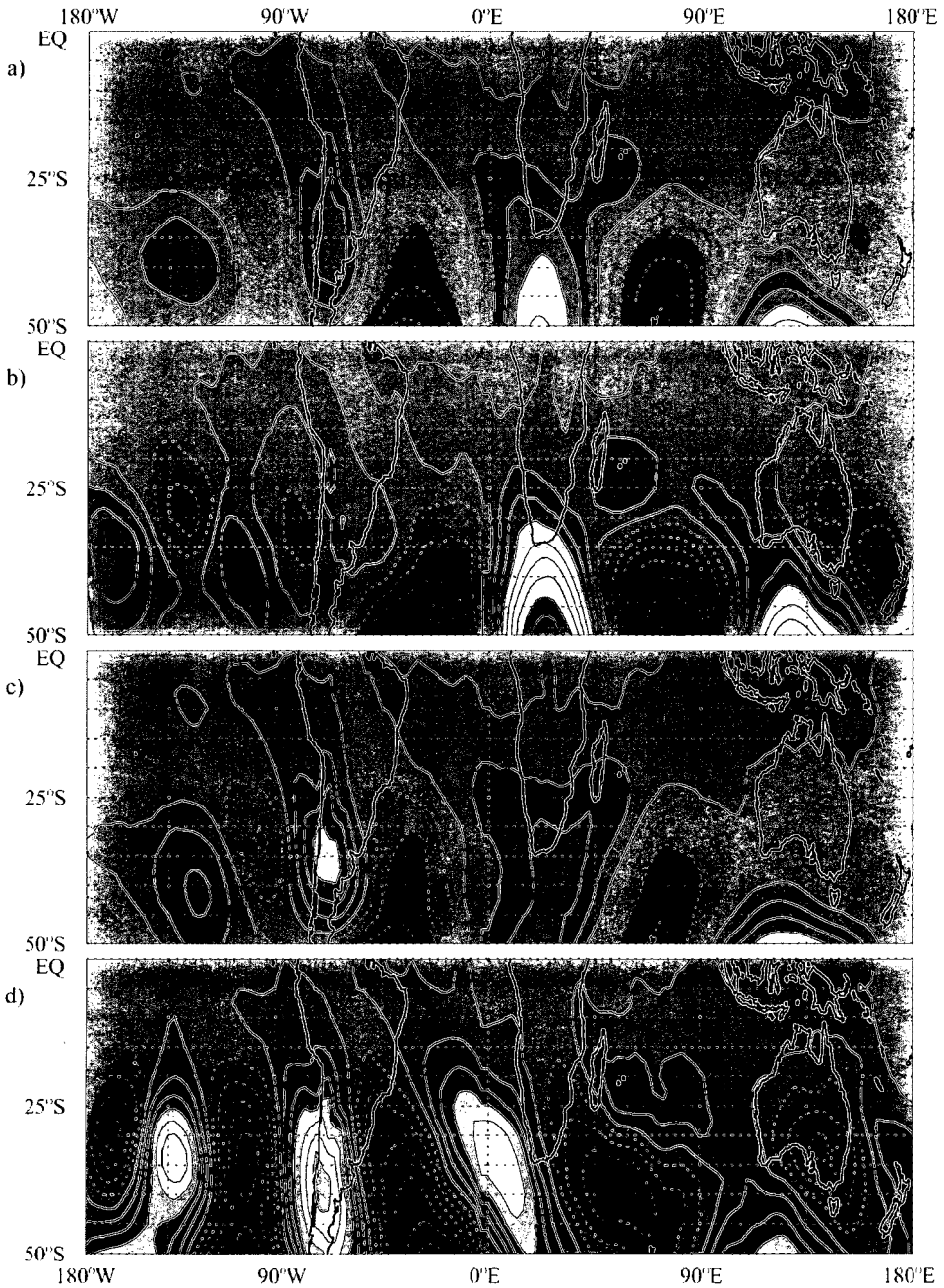

Figure 6.30. Coriolis torque on ageostrophic meridional flow in August 1995-2004 for a) monthly average, b) Type I, c) Type II, d) Type III. Contour interval 0.2 x 100ms^{-1}day^{-1}, negative values depicted by dashed line.

Reproduced with permission of the copyright owner. Further reproduction prohibited without permission.

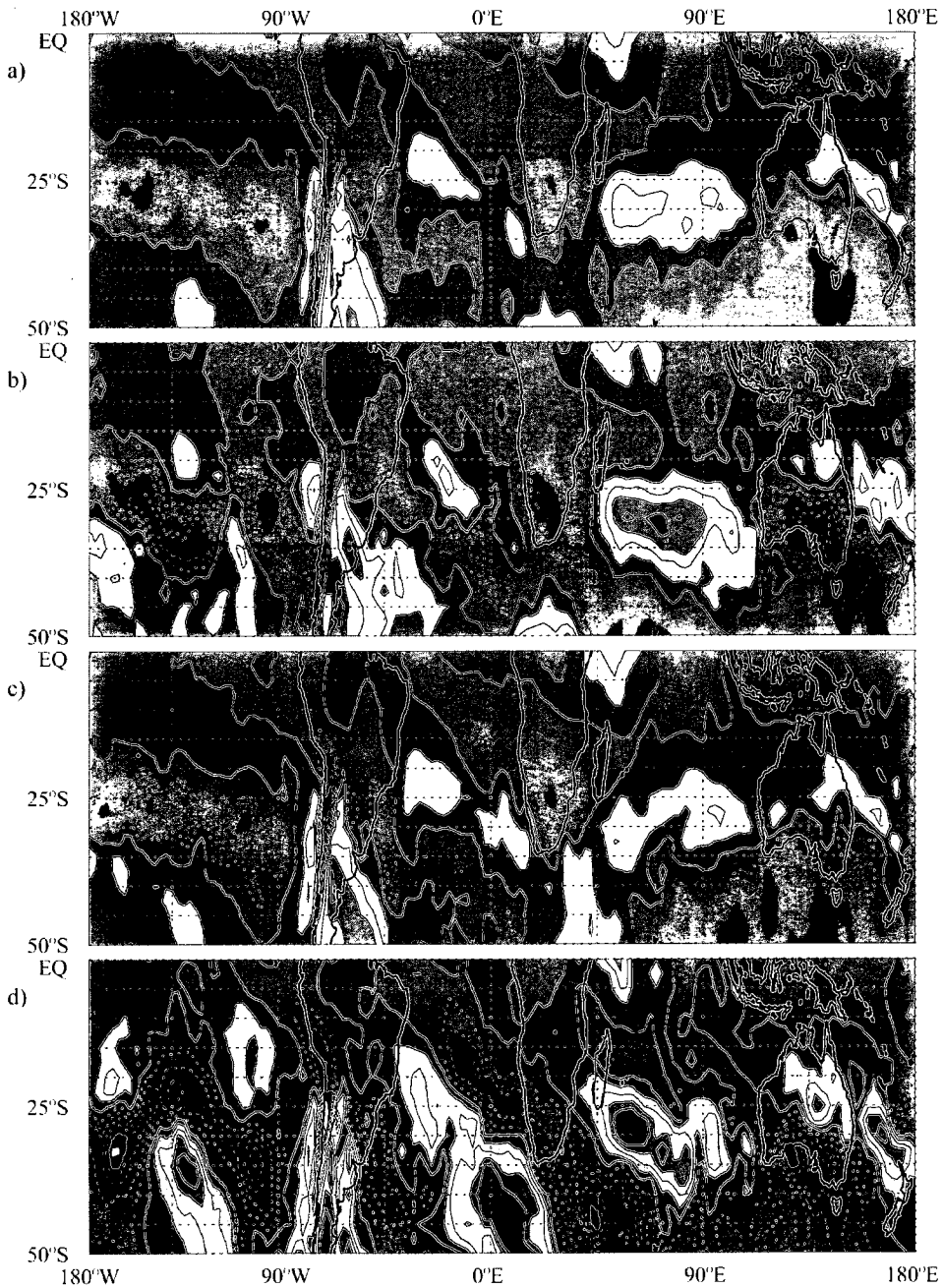

Figure 6.31. Zonal wind advection in August 1995-2004 for a) monthly average, b) Type I, c) Type II, d) Type III. Contour interval 0.2 x 100ms^{-1}day^{-1}, negative values depicted by dashed line.

Reproduced with permission of the copyright owner. Further reproduction prohibited without permission.

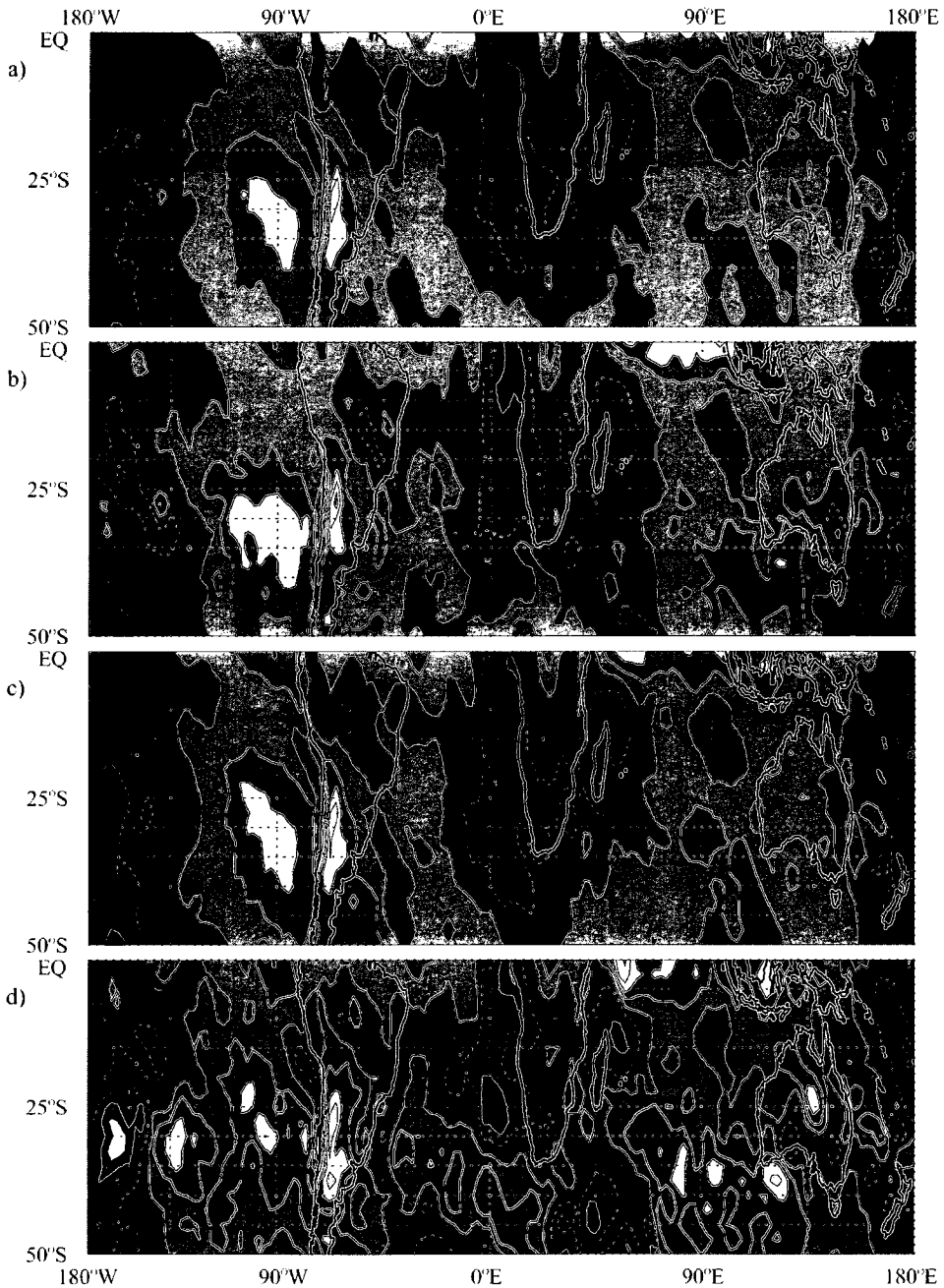

Figure 6.32. Residual term in August 1995-2004 for a) monthly average, b) Type I, c) Type II, d) Type III. Contour interval 0.2 x 100ms^{-1}day^{-1}, negative values depicted by dashed line.

Reproduced with permission of the copyright owner. Further reproduction prohibited without permission.

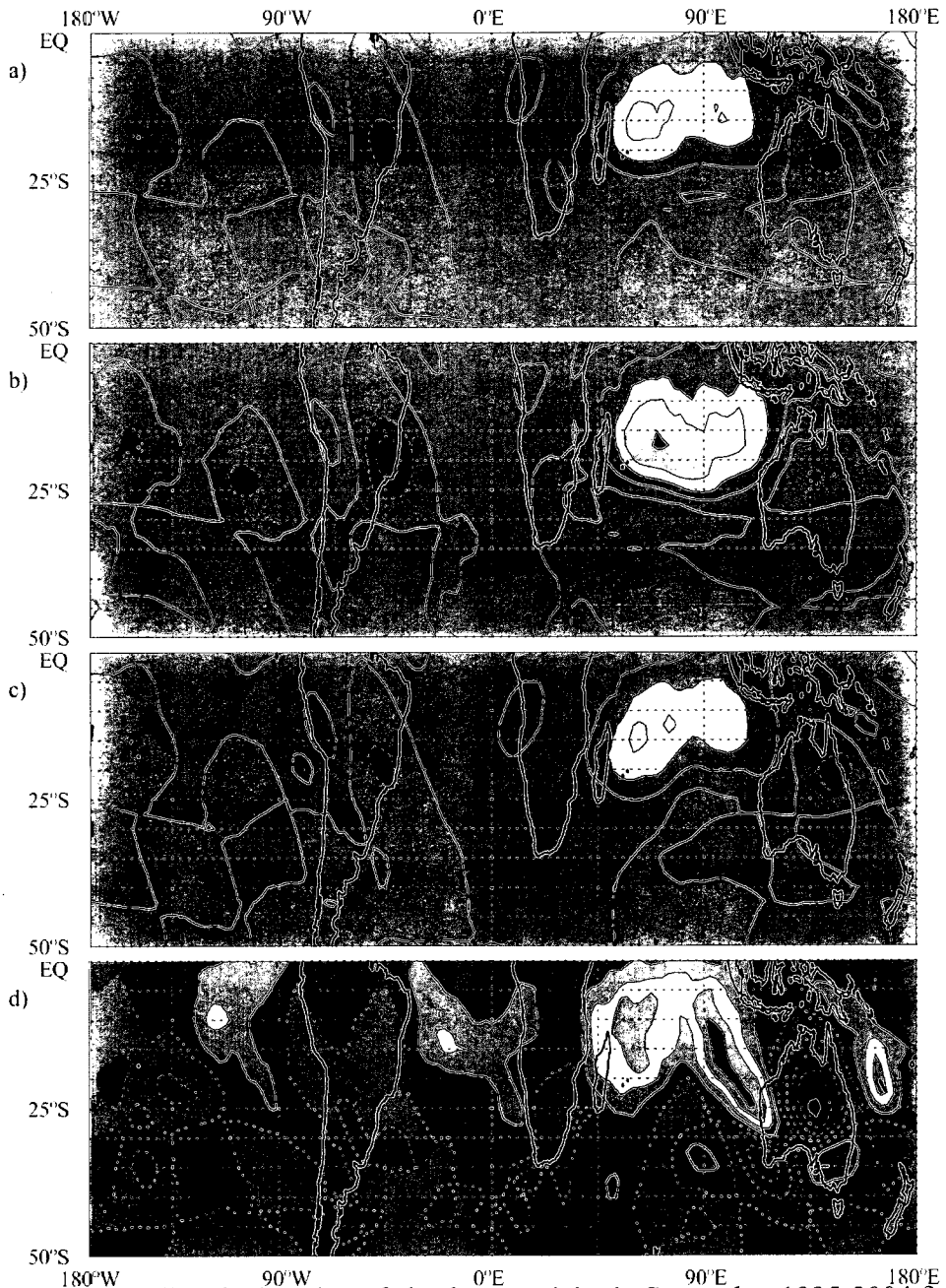

Figure 6.33. Meridional advection of absolute vorticity in September 1995-2004 for a) monthly average, b) Type I, c) Type II, d) Type III. Contour interval 0.2 x 100ms^{-1}day^{-1}, negative values depicted by dashed line.

Reproduced with permission of the copyright owner. Further reproduction prohibited without permission.

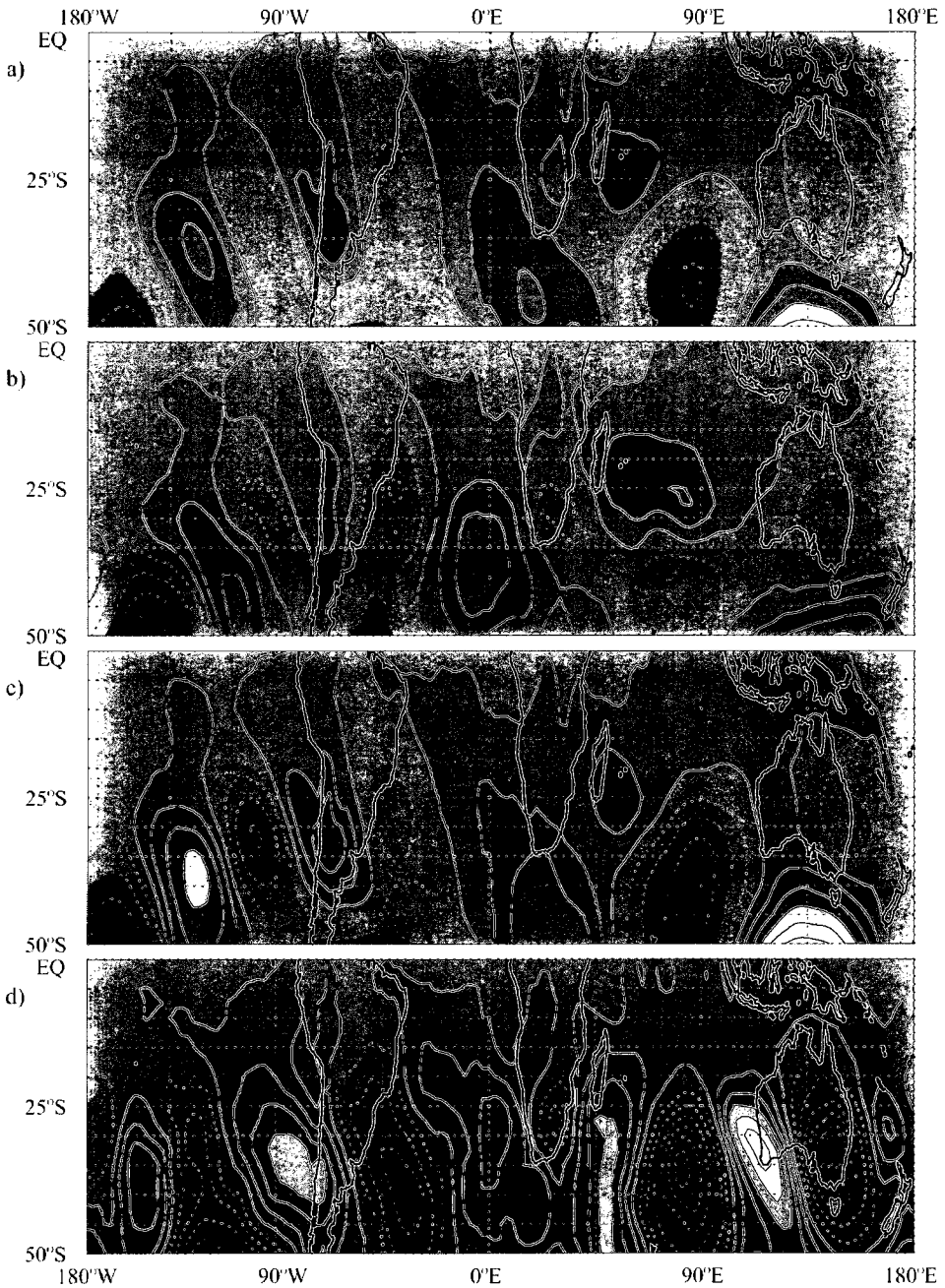

Figure 6.34. Coriolis torque on ageostrophic meridional flow in September 1995-2004 for a) monthly average, b) Type I, c) Type II, d) Type III. Contour interval 0.2 x 100ms^{-1}day^{-1}, negative values depicted by dashed line.

Reproduced with permission of the copyright owner. Further reproduction prohibited without permission.

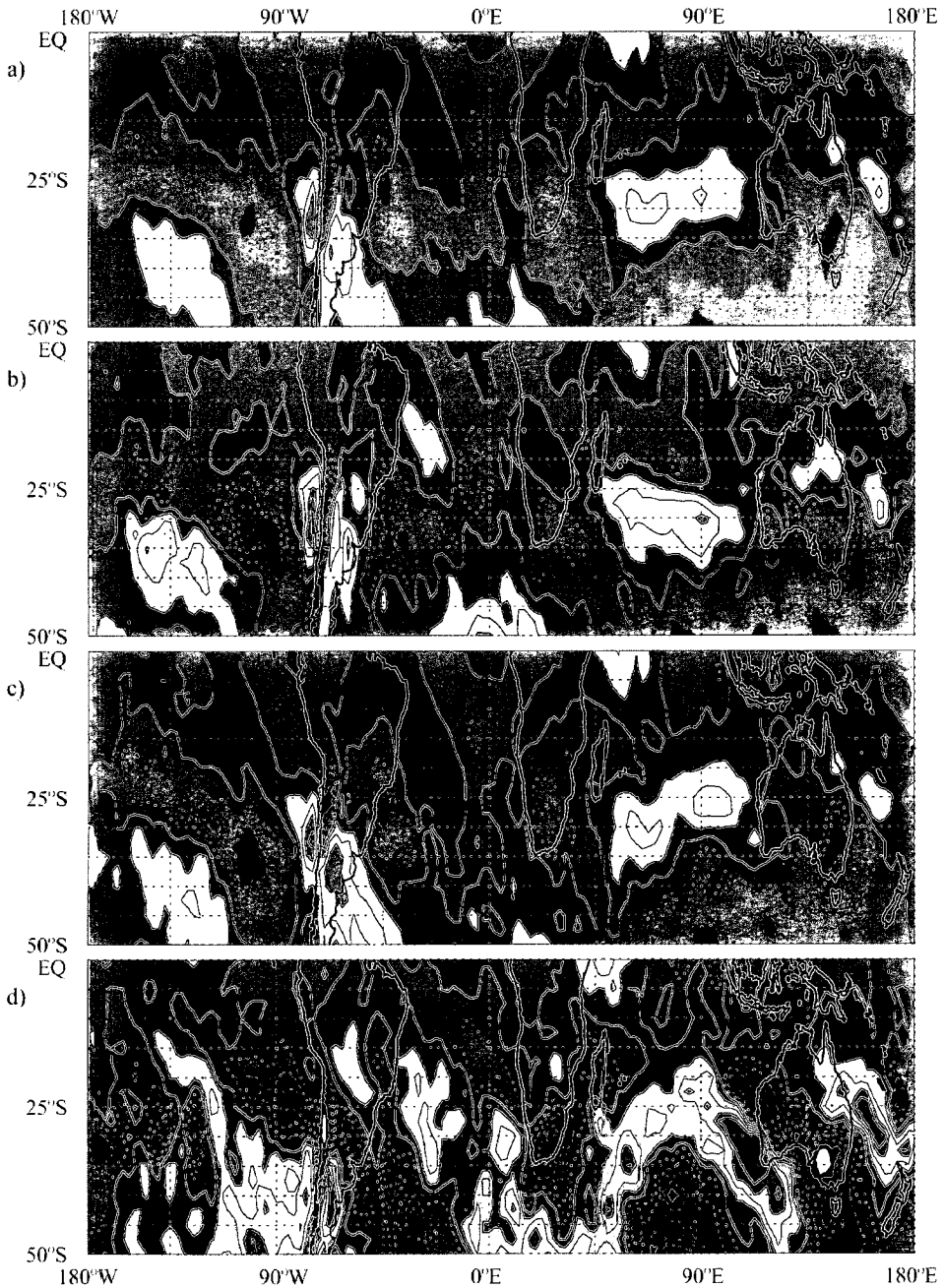

Figure 6.35. Zonal wind advection in September 1995-2004 for a) monthly average, b) Type I, c) Type II, d) Type III. Contour interval 0.2 x 100ms^{-1}day^{-1}, negative values depicted by dashed line.

Reproduced with permission of the copyright owner. Further reproduction prohibited without permission.

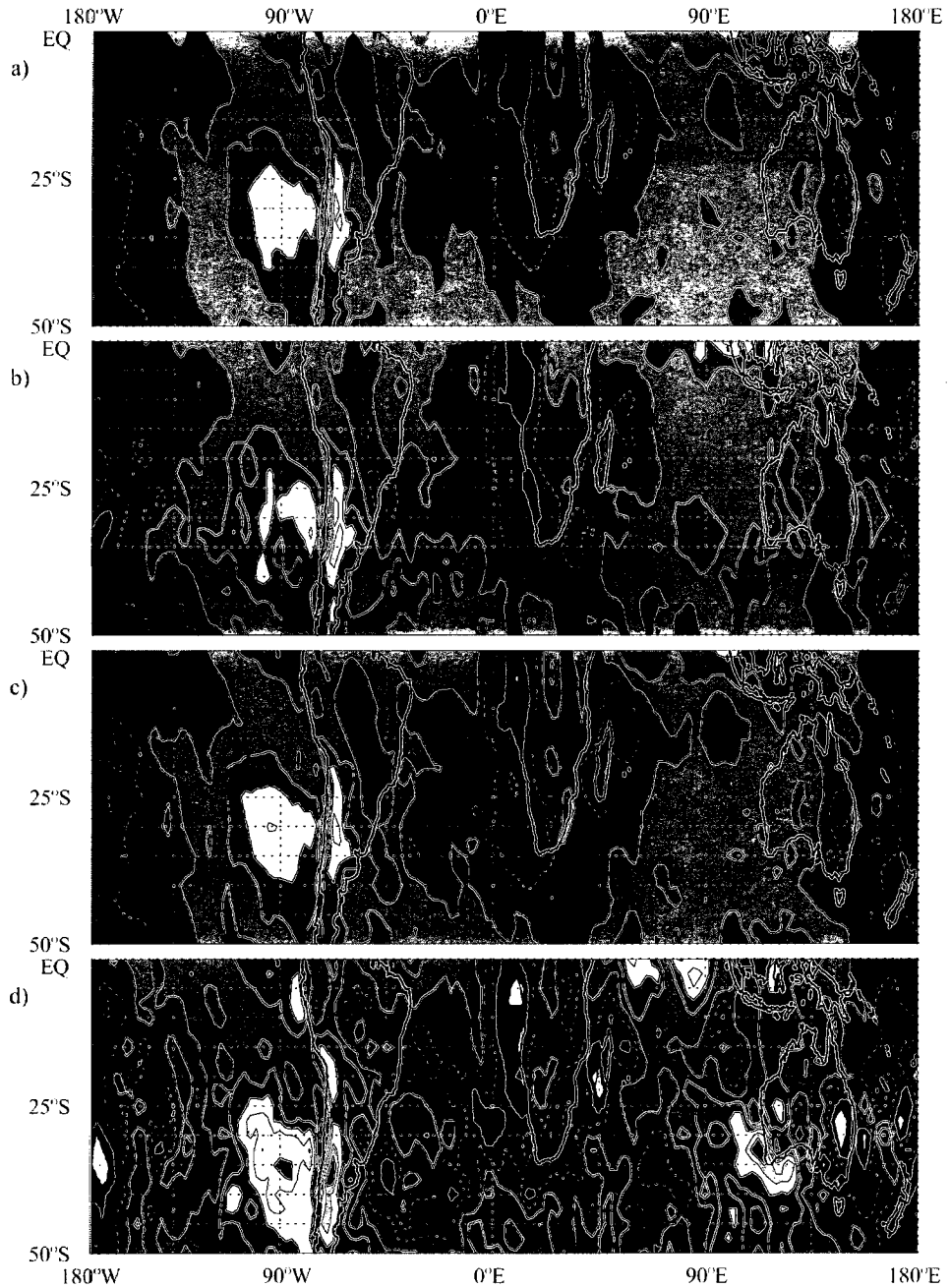

Figure 6.36. Residual term in September 1995-2004 for a) monthly average, b) Type I, c) Type II, d) Type III. Contour interval 0.2 x 100ms^{-1}day^{-1}, negative values depicted by dashed line.

Reproduced with permission of the copyright owner. Further reproduction prohibited without permission.

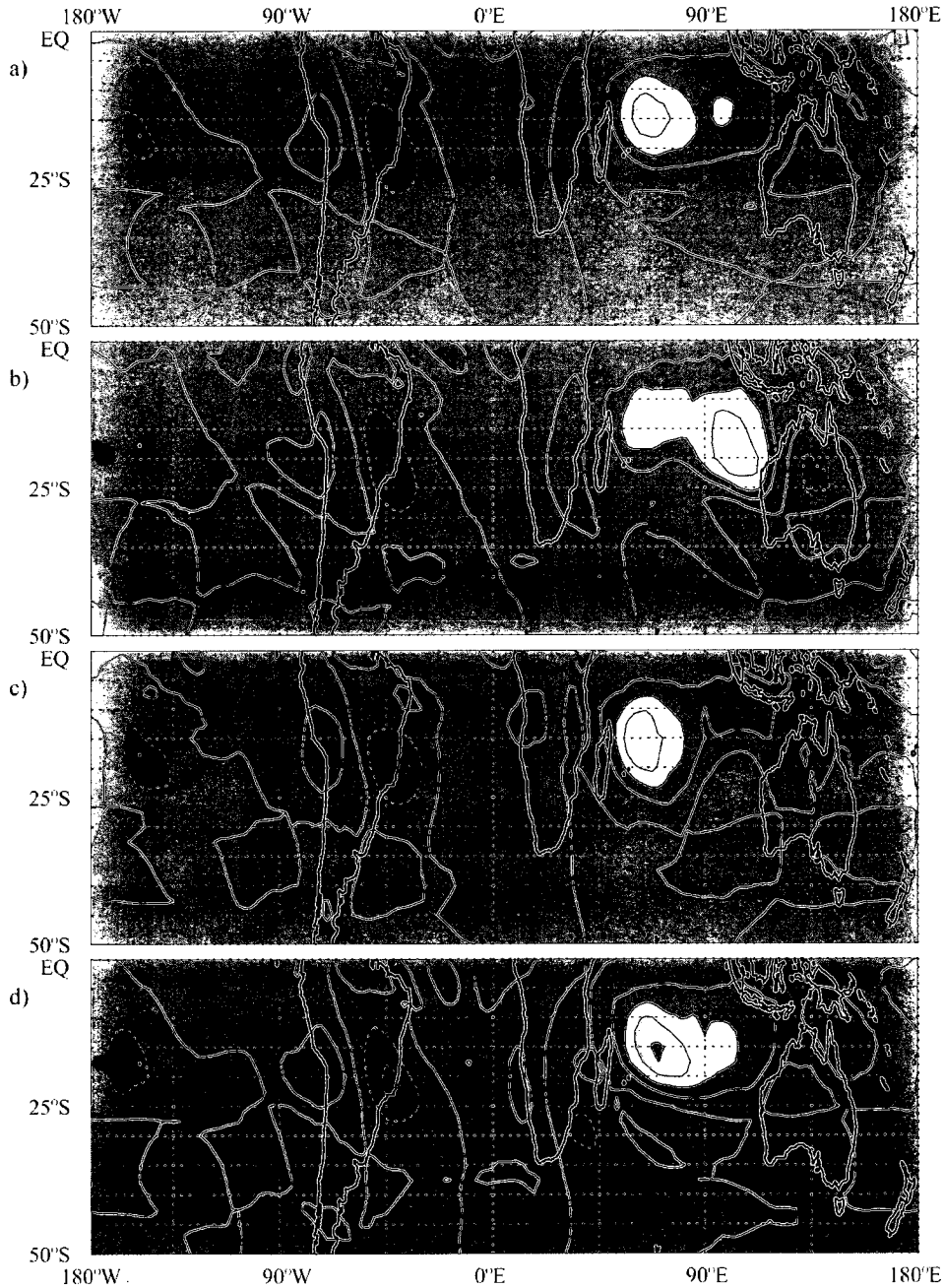

Figure 6.37. Meridional advection of absolute vorticity in October 1995-2004 for a) monthly average, b) Type I, c) Type II, d) Type III. Contour interval 0.2 x $100ms^{-1}day^{-1}$, negative values depicted by dashed line.

Reproduced with permission of the copyright owner. Further reproduction prohibited without permission.

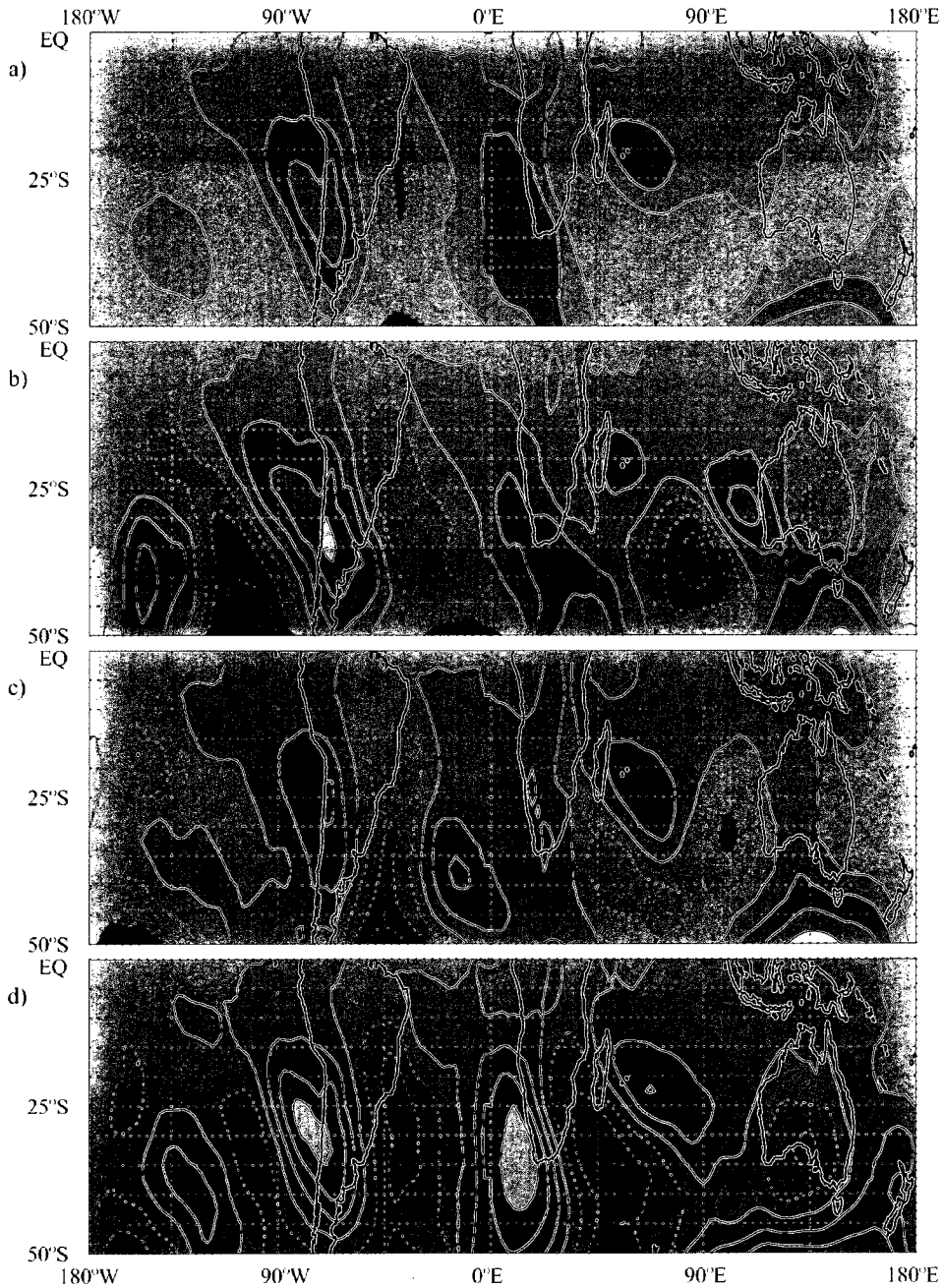

Figure 6.38. Coriolis torque on ageostrophic meridional flow in October 1995-2004 for a) monthly average, b) Type I, c) Type II, d) Type III. Contour interval 0.2 x 100ms^{-1}day^{-1}, negative values depicted by dashed line.

Reproduced with permission of the copyright owner. Further reproduction prohibited without permission.

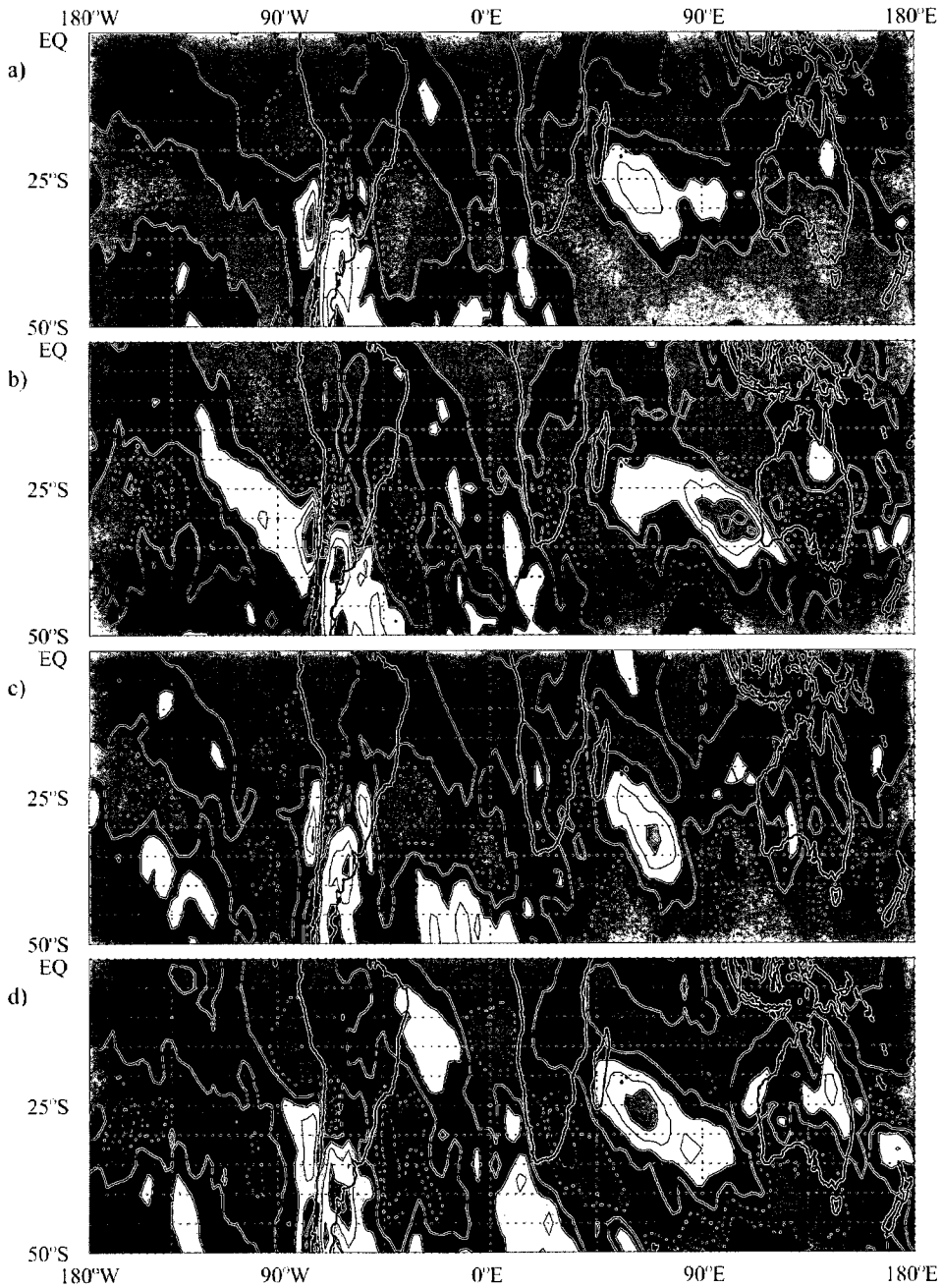

Figure 6.39. Zonal wind advection in October 1995-2004 for a) monthly average, b) Type I, c) Type II, d) Type III. Contour interval 0.2 x 100ms^{-1}day^{-1}, negative values depicted by dashed line.

Reproduced with permission of the copyright owner. Further reproduction prohibited without permission.

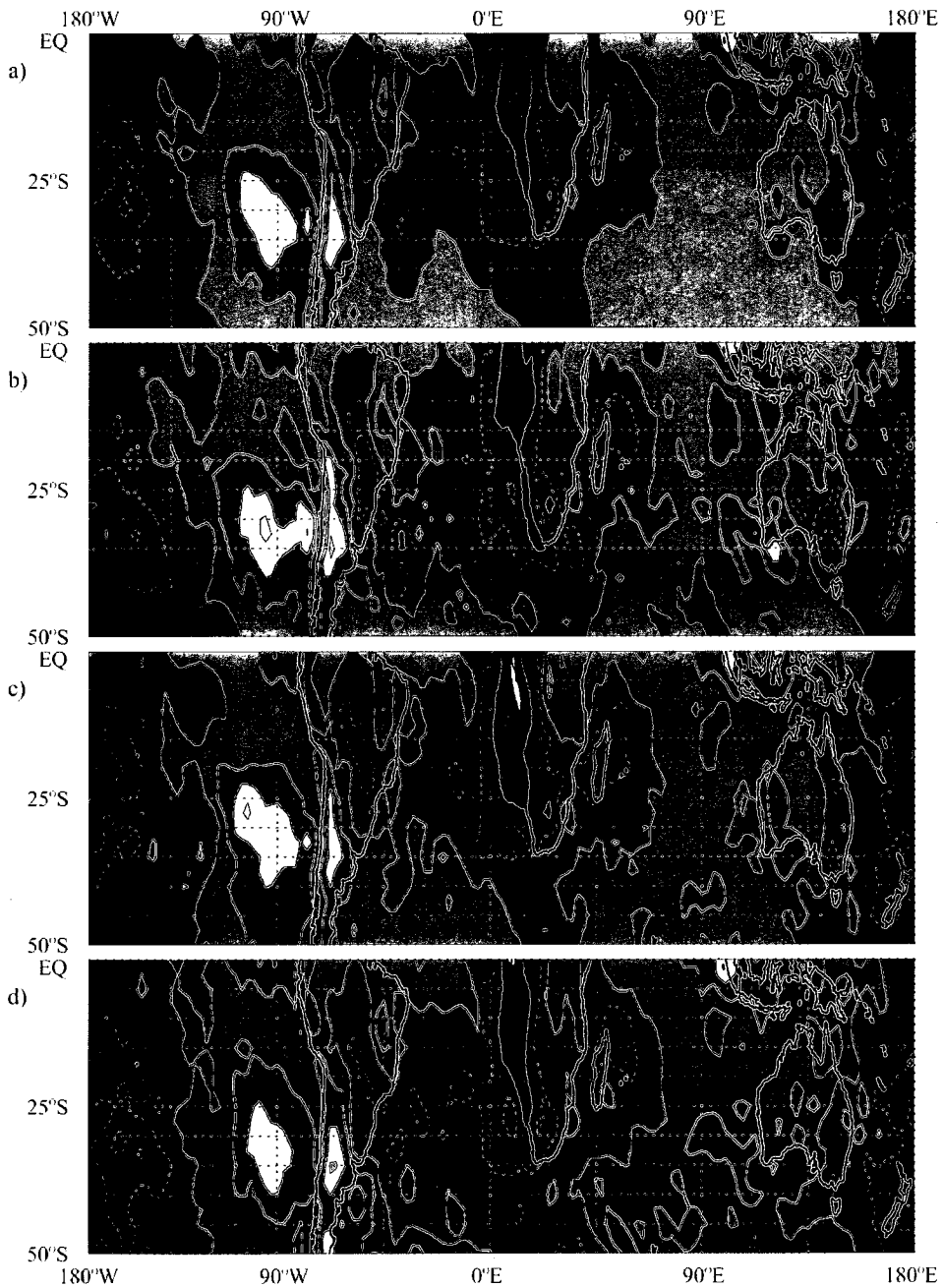

Figure 6.40. Residual term in October 1995-2004 for a) monthly average, b) Type I, c) Type II, d) Type III. Contour interval 0.2 x 100ms^{-1}day^{-1}, negative values depicted by dashed line.

Reproduced with permission of the copyright owner. Further reproduction prohibited without permission.

Chapter 7

ENSO influences on monthly mean column ozone and stratospheric geopotential height and temperature anomalies during the Southern Hemisphere winter to spring transition

Matthew H. Hitchman, Marek Rogal (2009), submitted to *J. Geophys. Res.*

7.1. Introduction

The global distribution of column ozone is strongly influenced by short and long term variability in meteorological fields. The position of the time-mean maximum in total ozone is highly correlated with the region of the maximum mean baroclinicity and the Southern Hemisphere (SH) storm track near 50-60°S [*Berbery and Vera,* 1996]. Strong correlations exist between column ozone and tropopause height [*Schubert and Muntenau,* 1988; *Steinbrecht et al.*, 1998], lower stratospheric temperature anomalies [*Labitzke and van Loon*, 1992] and lower stratospheric potential vorticity anomalies [*Hood et al.*, 1999]. Anthropogenic and natural trends in column ozone have been studied extensively [e.g., *Angel,* 1988, 1989, 1990; *Karoly et al.,* 1989; *Stolarski et al.*, 1990, 1991, 1992, 2005; *Randel and Cobb*, 1994; *McCormack and Hood,* 1994]. Variability in column ozone has been related to the 11 year solar cycle (~2-3 DU) [*Angel,* 1989; *Labitzke and van Loon*, 1992; *McCormack and Hood*, 1994; *Randel and Cobb*, 1994] and to the Quasi-Biennial Oscillation [QBO; *Hasebe*, 1980; *Bowman*, 1989; *Stolarski et al.*, 1991; *Shiotani*, 1992; *Randel and Cobb*, 1994]. In the tropics there is ~8 DU less ozone when QBO easterly shear is in the

Reproduced with permission of the copyright owner. Further reproduction prohibited without permission.

lower stratosphere compared to QBO westerly shear, due to an elevated tropopause and enhanced upwelling [*Shiotani*, 1992; *Randel and Cobb*, 1994]. The QBO influences the propagation of planetary waves from the troposphere into the stratosphere by changing the location of critical wind surfaces in the subtropics, in concert with the Charney-Drazin criterion. Various modeling studies [*Kinnersley and Tung*, 1998, 1999; *Pascoe et al.*, 2005; *Hampson and Haynes*, 2006] as well as observational data analysis studies [*Baldwin and Dunkerton*, 1998] have shown that QBO winds influence both the Antarctic and Arctic stratosphere. *Hitchman and Huesmann* [2009] provide a systematic survey of the influence of QBO wind regimes on the extratropical stratosphere as a function of altitude QBO wind regime, season, and hemisphere.

Another major planetary-scale oscillation relevant to the distribution of column ozone is the El Nino Southern Oscillation (ENSO). *Shiotani* [1992] documented zonal mean changes in tropical column ozone for the period 1979 – 1989 on the order of 6 DU, with less ozone during El Nino (EN). He also found an east-west tropical dipole in column ozone, with more ozone over Indonesia during EN and more over the Eastern Pacific during La Nina (LN), with amplitude ~6 DU. The midlatitude region contains what is generally referred to as the "Ozone Croissant" or "Ozone Collar" [e.g., *Randel et al.*, 2002], a longitudinally elongated column ozone maximum. *Bojkov* [1987] suggested that the east-west shift in the column ozone maximum in the SH midlatitudes between 1983 and 1985 was related to ENSO. *Kayano* [1997] analyzed Total Ozone Mapping Spectrometer (TOMS) data for the 12 year period 1979 – 1991, using empirical orthogonal functions with a low-pass filter which eliminated variability at time scales of less than about a year. An anti-phased ENSO dipole in column ozone in the SH midlatitudes relative to the tropical dipole was confirmed

Reproduced with permission of the copyright owner. Further reproduction prohibited without permission.

in this data record, with a westward shift in the midlatitude ozone maximum during LN. *Kayano* [1997] found that the ENSO signal in midlatitude total ozone was highly correlated with lower stratospheric temperatures. Here we show monthly mean composites of TOMS data over the 22 year record 1982 - 2004, with a focus on month to month changes during August – September – October (ASO).

Although it is difficult to distinguish the influences of ENSO from those of the QBO solely through analysis of observational data [*Garfinkel and Hartmann*, 2007; *van Loon et al.*, 1982; *van Loon and Labitzke*, 1987; *Hamilton*, 1993], modeling studies [e.g., *Sassi et al.*, 2004; *Garcia-Herrera et al.*, 2006] show significant differences in temperatures in the polar stratosphere between EN and LN events. Changes in tropical convection associated with ENSO are more profound than those associated with the QBO, yet there is reason to believe that the two phenomena are physically linked at particular times [*Angell*, 1992]. A brief discussion of the statistical coincidence of ENSO and QBO phases for our data sample is given in section 7.2.

In the present work the monthly evolution of the influence of ENSO on column ozone and dynamical fields is explored in detail during the SH winter to spring transition. Geographical variation in monthly mean geopotential height and temperature is emphasized, with a focus on how they relate to column ozone anomalies. A key dynamical principle is that ENSO exerts its influence on extratropical column ozone via longitudinal shifts in convective outflow and associated modulation of subtropical high pressure systems in the upper troposphere – lower stratosphere (UTLS). *Rogal et al.* [2009] provides a modeling case study of these mechanisms, with a focus on the relationship between subtropical anticyclones in the UTLS in the Southern Indian Ocean (SIO) basin and synoptic ozone

Reproduced with permission of the copyright owner. Further reproduction prohibited without permission.

maxima. ENSO also modulates the extratropical stratospheric planetary wave pattern. *Hitchman et al.* [2009] explores the seasonal intensification of the Ozone Croissant from August to October, emphasizing the zonal contraction of tropical convection on the subtropical westerly jet over Australia and the coupling between amplifying ULTS anticyclones and stalling of ozone-rich planetary wave ridges in the Australian sector.

7.2. Data and methodology

The TOMS column ozone dataset used in our study encompasses the 22 year record 1982-2004, including data from following spacecraft: Nimbus 7 (11/1/1978 – 5/6/1993), Meteor 3 (8/22/1991 – 11/24/1994) and Earth Probe (7/22/1996 – 12/14/2005) [toms.gsfc.nasa.gov]. There is a gap in 1996 due to calibration problems. We have limited analysis to the August-September-October (ASO) period to focus on the SH late winter to early spring transition.

Monthly mean meteorological data fields were derived from 2.5° gridded European Centre for Medium Range Weather Forecasts (ECMWF) global upper air analyses [*Trenberth*, 1992; *Hollingsworth et al.*, 1986; *Kallberg et al.*, 2005].

In order to analyze the interactions between ENSO and column ozone we created subsets of data using the Oceanic Nino Index (ONI), available from the National Oceanic and Atmospheric Administration Climate Prediction Center, to identify cold and warm events [www.cpc.noaa.gov]. The ONI index, which is based on a three-month running mean of sea surface temperature anomalies in the NINO 3.4 region (5°S-5°N, 120-170°W), is the core of the Multivariate ENSO Index (MEI), which is widely used in similar analyses. Correlations between the ONI and MEI indices are 0.927, 9.834 and 0.981 for August, September and

Reproduced with permission of the copyright owner. Further reproduction prohibited without permission.

October, respectively, supporting our decision to use the ONI. We assumed an index threshold value of -0.4 for EN and +0.4 for LN, which produced seven ASO EN periods (1982, 1986, 1987, 1991, 1997, 2002, 2004) and six ASO LN periods (1983, 1984, 1988, 1998, 1999, 2000).

Table 7.1 shows the 30-50 hPa QBO wind shear index for the months used in this study. This was created from 30 and 50 hPa monthly mean winds [www.cpc.noaa.gov]. In this 22 year sample, QBO westerly shear tends to coincide with EN, consistent with reduced convection over Indonesia, while QBO easterly shear usually coincides with LN, consistent with enhanced Indonesian convection [*Gray et al.*, 1992, 1993; *Collimore et al.*, 1998, 2003]. A reasonable conclusion is that specific QBO and ENSO phases are at times moderately coupled through the physical link of tropical convection. In addition to QBO modulation of deep convection being smaller than ENSO modulation, QBO effects on equatorial convection are more zonally symmetric [*Collimore et al.*, 2003]. During ASO, SH stratospheric winds are not especially sensitive to 30-50 hPa QBO wind shear [*Hitchman and Huesmann*, 2009]. We proceed in analyzing results with emphasis on ENSO – extratropical teleconnections, yet these results may also be relevant to QBO – extratropical teleconnections.

7.3. ENSO modulation of zonal mean column ozone

Zonal mean column ozone for the ASO period varies in a sinusoidal fashion with latitude (Fig. 7.1a), exhibiting a minimum of 260-270 DU just south of the equator, a maximum of ~350 DU around 50°S, then diminishing into the Southern Polar Vortex (SPV).

Reproduced with permission of the copyright owner. Further reproduction prohibited without permission.

Extratropical column ozone increases with time from austral winter to early spring, with maximum values in October at 55°S being ~20 DU higher than in August.

In order to explore behavior as a function of latitude, the distribution of column ozone was divided into three bands: tropical source region, 0-20°S; subtropical transport region, 20-40°S; and midlatitude accumulation region, 40-60°S. Although this division would not be valid were we to analyze the evolution of column ozone in a daily manner [*Hudson et al.*, 2003, 2006], it captures meteorologically distinct regimes in the context of monthly means (Table 7.2). Ozone is produced in the sunlit tropical middle stratosphere, and is then transported via planetary and synoptic waves toward higher latitudes. The ozone minimum near 10°S in the austral winter is due to a combination of a high tropical tropopause plus reduced photochemical production relative to the summer subtropics [*Perliski et al.*, 1989]. Planetary and synoptic waves reaching into the subtropical stratosphere transport ozone poleward and downward, where ozone gradually accumulates poleward of the subtropical westerly jet. Column ozone increases as winter transitions into early spring and wave activity increases, enabling more ozone to be transported southward and downward from its production regions. The evolution of column ozone observed during the ASO period leads to an average increase of 20 DU (from 333 in August to 353 DU in October) in the accumulation region (Table 7.2). The total hemispheric content increases by ~13 DU and the subtropical region stabilizes at 308 DU in September (Table 7.2).

7.4. ENSO modulation of the geographical distribution of column ozone

The differences found in column ozone between LN and EN modes generally do not exceed 5% of the average column ozone values for a given latitudinal band, but are

Reproduced with permission of the copyright owner. Further reproduction prohibited without permission.

nevertheless pronounced (Fig. 7.1b, Table 7.3). LN periods tend to have higher ozone content than EN events. Differences are greatest in August and September, when column ozone is 5-10 DU higher in the band 10-55°S (Fig. 7.1b). At the equator and in the SPV at 60°S column ozone is slightly lower during LN in September and October (Fig. 7.1b). This is consistent with greater transport out of the tropics and a stronger SPV during LN. In October the differences between LN and EN ozone are smaller than during August and September. This is also seen in band averages for LN and EN events in Table 7.3. The highest differences are found in the subtropical region in August and September: 9 DU and 8 DU respectively, while hemispheric differences for both months stay at the 6 DU level.

The longitudinal distribution of column ozone in the midlatitude band (Fig. 7.1c) displays an EN maximum of 377 DU near 135°E, shifted eastward relative to the LN maximum of 383 DU near 100°E. Minima for both LN and EN remain anchored around the longitude of the Palmer Peninsula at 70°W. During LN the midlatitude column ozone pattern is shifted westward, consistent with the results of *Kayano* [1997]. During LN there is ~ 20 DU more column ozone in the 70°W-135°E region and ~20 DU less in the 135°E-70°W region.

Figure 7.2 shows the progression of column ozone during LN (left column), EN (middle column), and LN – EN differences (right column) from August to October (top to bottom). There is a general eastward progression and amplification of the midlatitude ozone maximum from August to October [*Hitchman et al.*, 2009]. For each month the ozone maximum is displaced westward during LN. Differences between LN and EN (Figs. 7.2c, f, i) exhibit interesting geographical patterns that are distinct for each month, suggesting a complex evolution of underlying transport processes. The statistical significance of ENSO

Reproduced with permission of the copyright owner. Further reproduction prohibited without permission.

differences in column ozone exceed the 95% level everywhere throughout the SH, using the Students T-test (not shown). During August, LN – EN differences exhibit a poleward-spiraling wave two pattern, with maxima over the South Atlantic and Southern Indian Ocean (Fig. 7.2c). Less ozone is observed over the high latitude South Pacific Ocean during LN, consistent with a stronger, displaced SPV during LN compared to EN. Column ozone exhibits a relative maximum in the Eastern Pacific during LN, consistent with a colder, higher tropopause over Indonesia during LN [cf. *Shiotani*, 1992].

The tropical LN – EN differences during September and October are similar to those during August, but at middle and high latitudes, LN - EN differences reveal a poleward-spiraling wave 1 pattern and a marked eastward shift from September to October. During September there is a pronounced LN – EN column ozone maximum south of South Africa, with a LN – EN column ozone minimum over the high latitude South Pacific Ocean (Fig. 7.2f). During October this pattern rotates eastward, with a pronounced LN – EN column ozone maximum south of Australia and a LN – EN column ozone minimum near the Palmer Peninsula (Fig. 7.2i). Column ozone differences are quite significant in these two geographical locations, exceeding 30 DU. The high latitude LN – EN differences are consistent with a stronger SPV, but with notable westward rotation of the position of the enhanced LN trough from August through. Column ozone in the SPV is reduced by up to 45 DU during LN. We now examine LN – EN differences in geopotential height and temperature to explore the dynamical nature of the midlatitude differences in column ozone.

Reproduced with permission of the copyright owner. Further reproduction prohibited without permission.

7.5. ENSO differences in geopotential heights and temperatures

Geopotential height and temperature anomalies are shown for August, September, and October in Figs. 7.3-7.8 for LN (upper), EN (middle), and LN – EN (lower) at 150 hPa, 100 hPa, 70 hPa, and 50 hPa (left to right). During August (Figs. 7.3 and 7.4), differences between LN and EN are more subtle than during September (Figs. 7.5 and 7.6) and October (Figs. 7.7 and 7.8).

August geopotential height fields in the UTLS near the Indian Ocean feature a distinct Australian High (AH) at 25°S and a South African High (SAH) near 35°S during both LN and EN (Figs. 7.3a and 7.3e), which decay with increasing altitude. At higher latitudes, August geopotential height fields exhibit a wave one pattern, with an anticyclonic structure over the high latitude South Pacific, which does not decay with altitude (Figs. 7.3a-h). LN – EN differences in geopotential height for August shows a distinct wave 3 pattern in the extratropics that persists with altitude (Figs. 7.3i-l), but it is very difficult to relate this pattern to LN – EN differences in column ozone (Fig. 7.2c).

Geographical variations in temperature are much more clearly related to column ozone features, with the wave one in midlatitude column ozone (Figs. 7.2a, b) coinciding with a wave one in temperature which is barotropic in nature (Figs. 7.4a-h). LN – EN differences in midlatitude column ozone during August (Fig. 7.2c) appear to be related most fundamentally to the LN –EN wave two temperature pattern in the middle stratosphere (Figs. 7.4k,l), with warm LN anomalies coinciding with high column ozone.

In September the primary features in LN – EN differences in column ozone are the maximum off the tip of South Africa and minimum over the high latitude South Pacific (Fig. 7.2f). During September the height anomalies in the subtropical UTLS are somewhat

Reproduced with permission of the copyright owner. Further reproduction prohibited without permission.

different than in August, with the SAH (Fig. 7.3a) displaced equatorward and eastward, becoming a SIOH during LN (Fig. 7.5a), and the SAH is notably stronger during EN (Fig. 7.5e). This results in LN – EN differences at 150 hPa (Fig. 7.5i) which reflect a stronger SIOH during LN and a stronger SAH during EN. The strengthened SAH during EN is consistent with known enhanced convection over South Africa during EN [see Fig. 7.3 of *Hastenrath*, 1990].

The vertical structure of the high latitude height anomalies is also different during September, with the deep anticyclonic structure being located closer to Australia in September during both LN and EN (Figs. 7.5a-h). The high latitude LN – EN ozone minimum over the South Pacific during September (Fig. 7.2f) coincides with negative LN - EN heights in the middle stratosphere (Figs. 7.5j-l), consistent with a stronger SPV during LN. The pronounced maximum in LN – EN column ozone south of South Africa (Fig. 7.2f) is related to the presence of a strong anticyclone in the vicinity during EN (Fig. 7.5e). Note the equatorward and eastward displacement of this anticyclone toward the SIO during LN as seen in the difference plot (Fig. 7.5i).

As with August, during September, geographical variations in temperature are much more clearly related to features in the distribution of column ozone, with the wave one in midlatitude column ozone (Figs. 7.2d,e) coinciding with a wave one in temperature which is barotropic in nature (Figs. 7.6a-h). LN – EN differences in midlatitude column ozone during September (Fig. 7.2f) are clearly related (Figs. 7.6i-l), with the deep cold LN anomaly over the high latitude South Pacific coinciding with lower column ozone and the deep warm LN anomaly south of South Africa coinciding with high column ozone.

Reproduced with permission of the copyright owner. Further reproduction prohibited without permission.

In October the primary LN – EN feature in column ozone is the maximum south of Australia (Fig. 7.2i), with the pattern rotated ~90°E eastward relative to September. At 150 and 100 hPa LN favors a stronger AH and SIOH (Figs. 7.7a, b), while EN favors a stronger SAH (Figs. 7.7e, f). The difference plots (Figs. 7.7i, j) show a pronounced geopotential height maximum during LN stretching from Australia to Madagascar, which lies immediately eastward and equatorward of the maximum in LN – EN differences in column ozone (Fig. 7.2i). At 70 and 50 hPa high latitude LN – EN height differences show an amplified anticyclone over the SIO and a stronger SPV over the Southern Pacific (Figs. 7.7k-l).

Again, during October, the link between temperature and column ozone anomalies is quite clear. The barotropic LN temperature maximum (Figs. 7.8a-d) is located farther west relative to the EN temperature maximum (Figs. 7.8e-h). LN – EN temperature differences (Figs. 7.8i-l) show a strong temperature maximum south of Australia, which coincides with the LN – EN maximum in column ozone (Fig. 7.2i). Two significant aspects of the geopotential height structure during October which relate to this barotropic warm anomaly during LN include the amplified SIOH near 150 hPa during LN (Figs. 7.7i, j) and the amplified anticyclone over the high latitude SIO (Figs. 7.7k, l).

7.6. Longitude – altitude geopotential height and temperature anomaly structure

For the purpose of establishing a better picture of the dynamical structures associated with the evolution of meteorological fields throughout the ASO period as modulated by ENSO, we have analyzed monthly mean longitude-height sections of ECMWF geopotential height and temperature anomalies at 20°S, 35°S and 58°S (Figs. 7.9-7.12). EN averages are shown on the left, while LN averages are on the right.

Reproduced with permission of the copyright owner. Further reproduction prohibited without permission.

The subtropical SH UTLS region is dominated by a wave 1 structure with a positive anomaly located between 500 hPa and 70 hPa over Australia for both ENSO phases (Figs. 7.9a, b). August height anomalies at 20°S display an increased amplitude during EN (Fig. 7.9a) in comparison to those during LN (Fig 7.9b). A distinct westward shift is visible during LN relative to EN, consistent with the westward shift in convection. This wave-one pattern is also apparent in the UTLS at 35°S, but shifted westward to South Africa (Figs. 7.9c, d).

During EN geopotential height anomalies in the UTLS over South America are enhanced relative to LN and are diminished over the Eastern Pacific. The antiphased relationship between the upper and middle panels is consistent with ENSO modulation of local Hadley cells.

At 58°S during August there are significant differences in the structure of the SPV between EN and LN (Figs. 7.9e, f). During EN a larger amplitude baroclinic wave-one structure dominates, with the mid-stratospheric trough located near 0°E, while during LN the height anomalies are more barotropic and a wave-three component is more evident. During cold ENSO, there are three anticyclonic structures: near 100°W, 50°E, and 150°E, confirming the wave-three LN-EN difference pattern in Fig. 7.3l.

Temperature anomalies at 20°S (Figs. 7.10a, b) in August display a quadrupole pattern, consisting of colder mid-to-upper tropospheric air over the Atlantic Ocean (120°W-60°E), with a warm anomaly residing in the lower stratosphere overhead, and a corresponding reversal over the Indian and Western Pacific Oceans. This pattern is consistent with a reversed Walker Circulation in the lower stratosphere [*Wyrtki*, 1985a, b; *Rosenlof et al.*, 1986; *Sumathipala*, 1989; *Newell et al.*, 1996; *Kayano*, 1997]. During LN this pattern

Reproduced with permission of the copyright owner. Further reproduction prohibited without permission.

shifts westward, contracts in longitude, and becomes weaker. At 35°S (Figs. 7.10c, d) this quadrupole pattern is reversed, consistent with longitudinally-local Hadley circulations. Again, a zonal contraction and diminution of this structure is seen in LN relative to EN during August.

The fundamental wave-one nature of the SH lower stratospheric thermal anomaly has been noted in previous work [*Newman and Randel*, 1988; *Wirth*, 1991, 1993; *Quintanar and Mechoso*, 1995a, b; *Hio and Hirota*, 2002]. The wave-one structure above ~250 hPa apparent at 20°S and 35°S extends to 58°S in the same longitude bands (Figs. 7.10e, f), and the difference between EN and LN is preserved. The magnitude of the positive anomaly in August is 10 K larger during EN than during LN. Similarly, the negative anomaly region is 14 K colder during EN conditions.

In September, height anomalies at 20°S are smaller than in August for both EN and LN conditions (Figs. 7.11a, b). The EN height anomaly is 20 gpm smaller; LN conditions, on the other hand, bring smaller changes. As the sun begins to heat the SH, one may view the formation of an anticyclonic anomaly over South America (60°W) during EN but not during LN. At 35°S (Figs. 7.11c, d) there is a notable development of an anticyclone over South Africa, which is much more pronounced during EN, related to more intense convection during EN [*Hastenrath*, 1990]. This UTLS positive anomaly is coupled with a wave 1 ridge in the lower stratosphere. This coupling for LN during September is much more effective than during August (Figs. 7.11d and 7.9d).

At 58°S during September a wave-one structure dominates for both LN and EN (Figs. 7.11e, f). The structure for EN is less organized than it was during August (Figs. 7.11e, 7.9e), but the LN structure is radically different in September, with a large amplitude,

Reproduced with permission of the copyright owner. Further reproduction prohibited without permission.

westward-tilting structure (Figs. 7.11f, 7.9f). The apparent connection between the anticyclonic structure in the stratosphere over the South Pacific at 35°S and 58°S in Figs. 7.11c-f is confirmed by inspection of Fig. 7.5. Other pronounced features at 58°S in September include the mid-to-upper tropospheric anticyclones over the tip of South America and near the date line which are directly connected with the wave-one ridge in the stratosphere. South of South Africa the wave-one trough is very weak during EN, and there is a more continuous westward-tilting trough during LN. This difference in the strength of the trough is related to the warm, high-ozone anomaly seen in Figs. 7.2f and 7.6i-l.

Temperature anomalies at 20°S during September (Figs. 7.12 a,b) show a significant reduction in the amplitude of the quadrupole pattern from August for EN, but less so for LN.

At 35°S (Figs. 7.12c, d) the temperature structure remains rather similar to August, but stratospheric temperatures over South Africa are notably colder during EN, consistent with the more eastward location of the midlatitude deep warm anomaly during EN (compare Figs. 7.6e-h and 7.6a-d). This eastward shift of the barotropic warm anomaly during EN is more apparent at 58°S (Figs. 7.12 e, f). This feature is strongly correlated with the positive column ozone anomaly south of South Africa during LN (Fig. 7.2f). Opposite trends in the intensity of the SPV are apparent from August to September, diminishing for EN and strengthening for LN (Figs. 7.10e, f and 7.12e, f). This trend in the SPV continues through October.

As the sun heats the SH during October, the South American anticyclone seen at 20°S in the UTLS intensifies for both EN and LN (Figs. 7.13a, b). Strong differences between EN and LN are seen elsewhere at 20°S, with strong amplification of the broad SIO anticyclone during LN (Fig. 7.13b). At 35°S the SAH is fairly similar for both EN and LN (Figs. 7.13c,

Reproduced with permission of the copyright owner. Further reproduction prohibited without permission.

d), quite different from the very strong SAH during EN in September (Fig. 7.11c). The stratospheric ridge in the eastern hemisphere in both EN and LN at 35°S is continuous with the stratospheric ridge in that quadrant at 58°S (Figs. 7.13e, f). The LN height anomalies at 58°S in the lower stratosphere are greater than those of the previous month by 200 gpm, and greater than those of EN by 200 gpm. The overall structure of the October SPV during LN is quite robust.

From September to October the thermal anomalies at 20°S are reduced during EN (Figs. 7.14a, 7.12a) but enhanced during LN (Figs. 7.14b and 7.12b). There is a visible westward shift of the LN temperature anomalies in the UTLS at 20°S relative to EN conditions. The temperature structure at 35°S (Figs. 7.14 c, d) is rather unaffected by the progress of spring, with a broad pool of negative anomaly over the Atlantic Ocean and Africa being colder by roughly 1 K. The warm anomaly in the UTLS over the SIO and Indonesia is significantly stronger during LN relative to EN and is stronger than during September. This is consistent with the westward shift in the deep thermal anomaly south of Australia during LN (Fig. 7.8). This westward shift in the warm anomaly during LN is more readily apparent at 58°S (Figs. 7.14e, f). The magnitude of the thermal anomalies at 58°S decreases for EN (Figs. 7.12e, 7.14e) but increases for LN (Figs. 7.12f, 7.14f) from September to October. The intensification of the SPV and westward shift during LN in October is associated with the warm column ozone anomaly south of South Africa (Figs. 7.2i, 7.8i-l).

Reproduced with permission of the copyright owner. Further reproduction prohibited without permission.

7.7. Conclusions

The analysis presented in this study shows clear differences in general circulation features between EN and LN and the associated modulation of the distribution of column ozone in the SH transition from winter to spring. We have demonstrated that ENSO-induced changes in subtropical anticyclones in the UTLS are distinct during August, September, and October, and that there are corresponding unique changes in the extratropical planetary wave structures which are related to changes in column ozone. Notable examples include the westward shift of the midlatitude column ozone maximum during September and October during LN, which is related to northeastward shifts in anticyclones in the SIO basin and amplification of the long-wave ridge south of Australia. The connection between planetary wave patterns was illustrated in monthly mean plots, with interesting variability among August, September, and October. The effect of changes in tropical convection and subtropical UTLS anticyclones on planetary wave structures exhibits both static and nonlinear aspects. A more complete understanding of these processes requires further modeling and observational analysis.

Reproduced with permission of the copyright owner. Further reproduction prohibited without permission.

Table 7.1. QBO 30-50 hPa wind shear (m/s per 20 hPa, easterly in gray) for the indicated month

La Nina	1983	1984	1988	1998	1999	2000	
August	-7	-11	-3	-8	8	-13	
September	-9	-9	-5	-5	6	-14	
October	-10	-5	-4	-1	4	-12	
El Nino	**1982**	**1986**	**1987**	**1991**	**1997**	**2002**	**2004**
August	13	-7	15	-9	6	6	3
September	14	-9	15	-10	5	2	3
October	14	-10	13	-9	5	2	2

Table 7.2. Zonal mean column ozone (DU) for specified latitude bands and months

	0-60°S	0-20°S	20-40°S	40-60°S
August	298	261	297	333
September	309	269	308	347
October	311	270	308	353

Table 7.3. Zonally averaged column ozone (DU) by latitude band, month and phase of ENSO

	0-60°S		0-20°S		20-40°S		40-60°S	
	EN	LN	EN	LN	EN	LN	EN	LN
August	295	300	259	264	292	301	332	335
September	306	311	267	270	303	312	344	350
October	310	312	269	270	306	310	352	354

Reproduced with permission of the copyright owner. Further reproduction prohibited without permission.

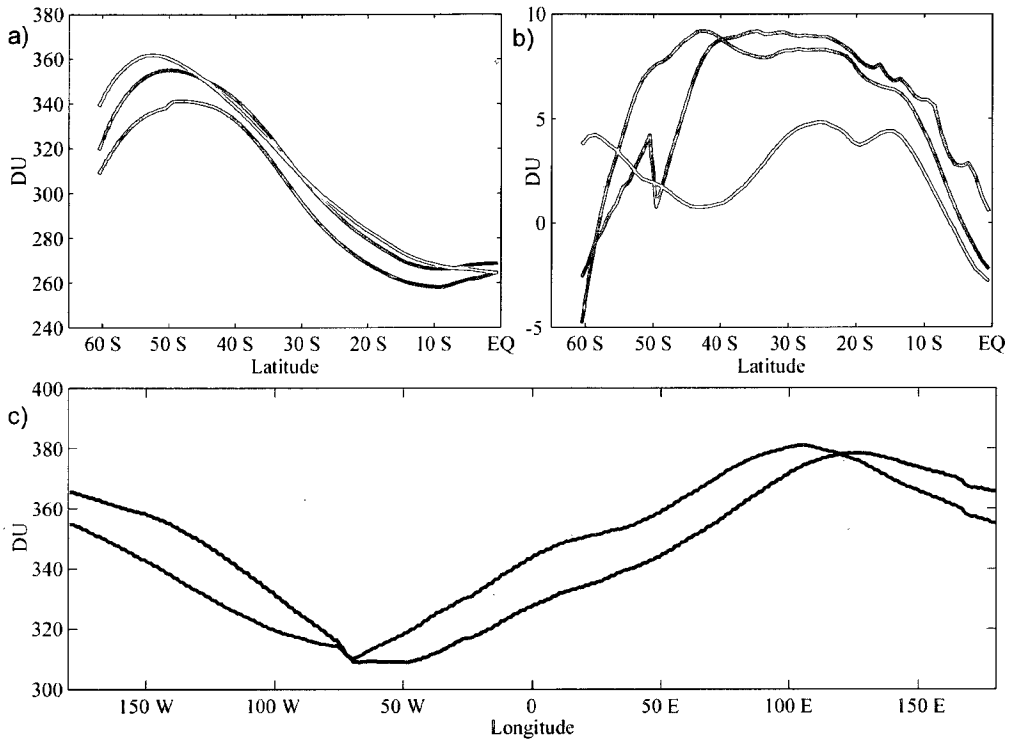

Figure 7.1. a) zonally averaged TOMS column ozone in the Southern Hemisphere for August (blue), September (green) and October (red), b) differences between La Nina and El Nino conditions and c) the longitudinal variation of column ozone averaged in the 45°-60°S band during August-October for La Nina (green) and El Nino (blue) events.

Reproduced with permission of the copyright owner. Further reproduction prohibited without permission.

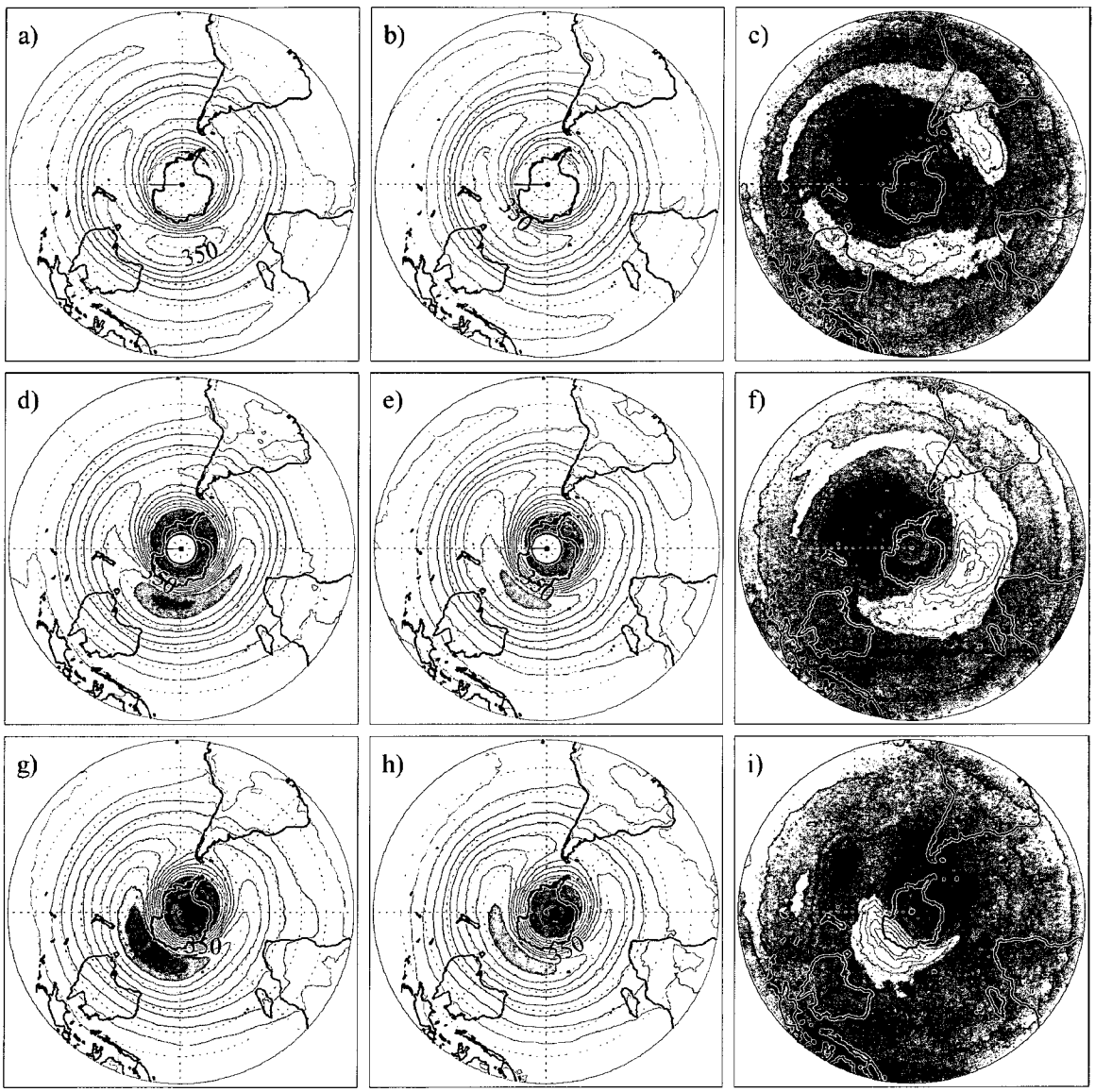

Figure 7.2. Polar stereographic projections of TOMS column ozone for a) August LN, b) August EN, c) August LN - EN, d) September LN, e) September EN, f) September LN - EN, g) October LN, h) October EN, and i) October LN - EN. The contour interval is 15 DU for LN and EN means and 5 DU for LN – EN differences.

Reproduced with permission of the copyright owner. Further reproduction prohibited without permission.

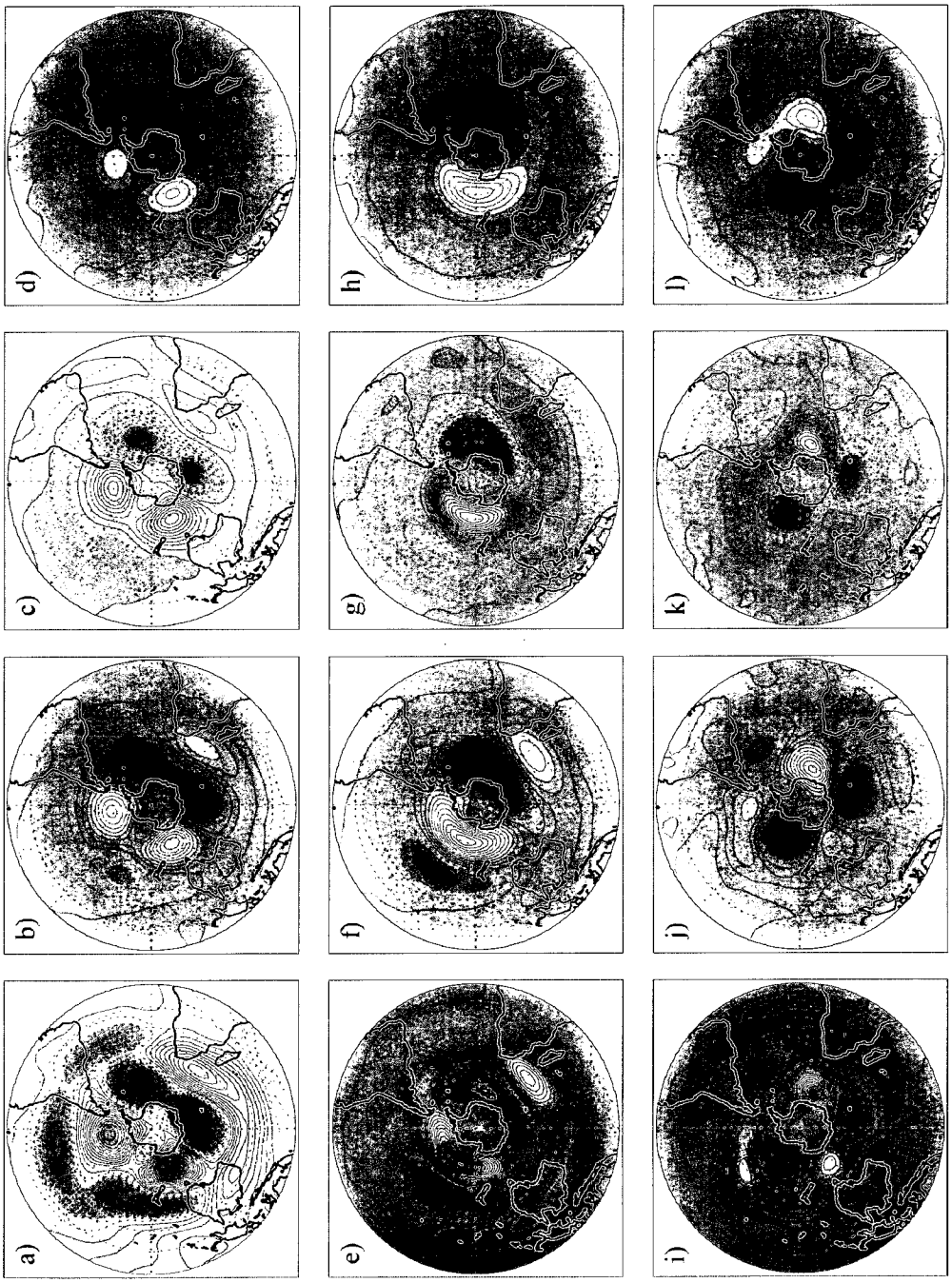

Figure 7.3. Geopotential height anomalies for August a) 150 hPa LN, b) 100 hPa LN, c) 70 hPa LN, d) 50 hPa LN, e) 150 hPa EN, f) 100 hPa EN, g) 70 hPa EN, h) 50 hPa EN, i) 150 hPa LN -EN, j) 100 hPa LN – EN, j) 70 hPa LN – EN, j) 50 hPa LN – EN. The contour interval is 10 m in a), e) and i), 20 m in b), c), f), g), j) and k) and 50 m in d), h) and l).

Reproduced with permission of the copyright owner. Further reproduction prohibited without permission.

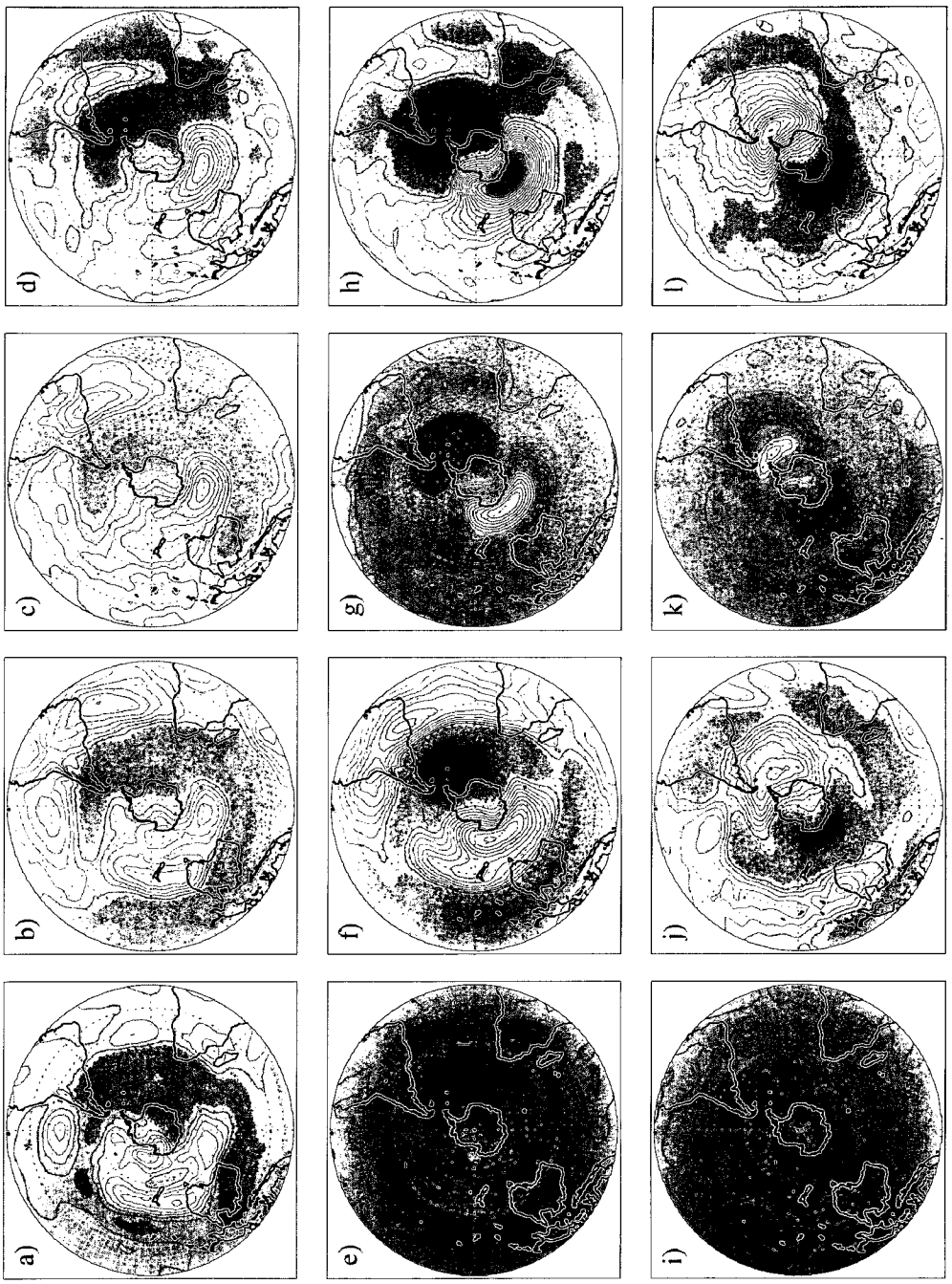

Figure 7.4. Temperature anomalies for August a) 150 hPa LN, b) 100 hPa LN, c) 70 hPa LN, d) 50 hPa LN, e) 150 hPa EN, f) 100 hPa EN, g) 70 hPa EN, h) 50 hPa EN, i) 150 hPa LN - EN, j) 100 hPa LN – EN, j) 70 hPa LN – EN, j) 50 hPa LN – EN. The contour interval is 1 K.

Reproduced with permission of the copyright owner. Further reproduction prohibited without permission.

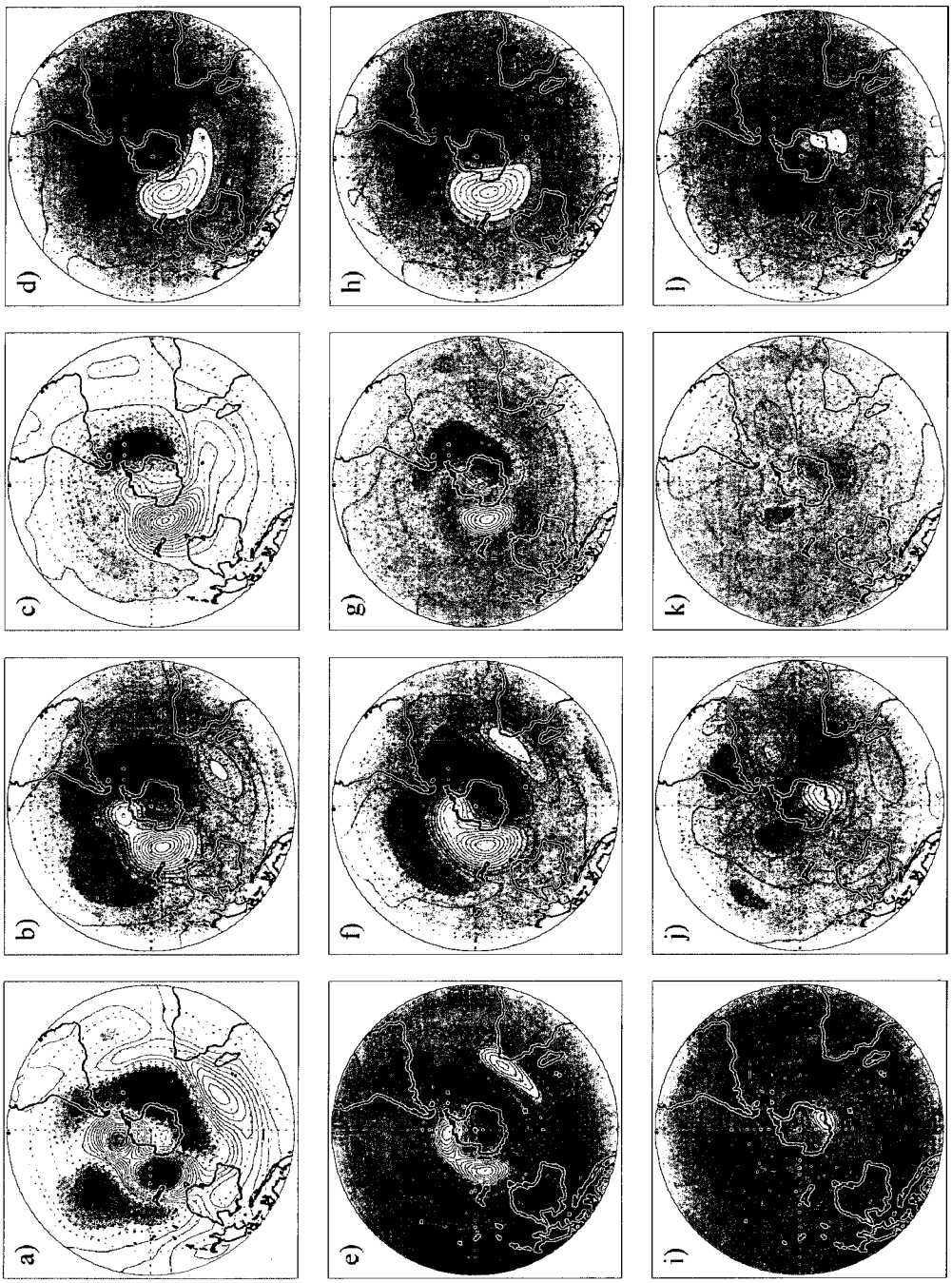

Figure 7.5. As in Fig. 7.3, except for September.

Reproduced with permission of the copyright owner. Further reproduction prohibited without permission.

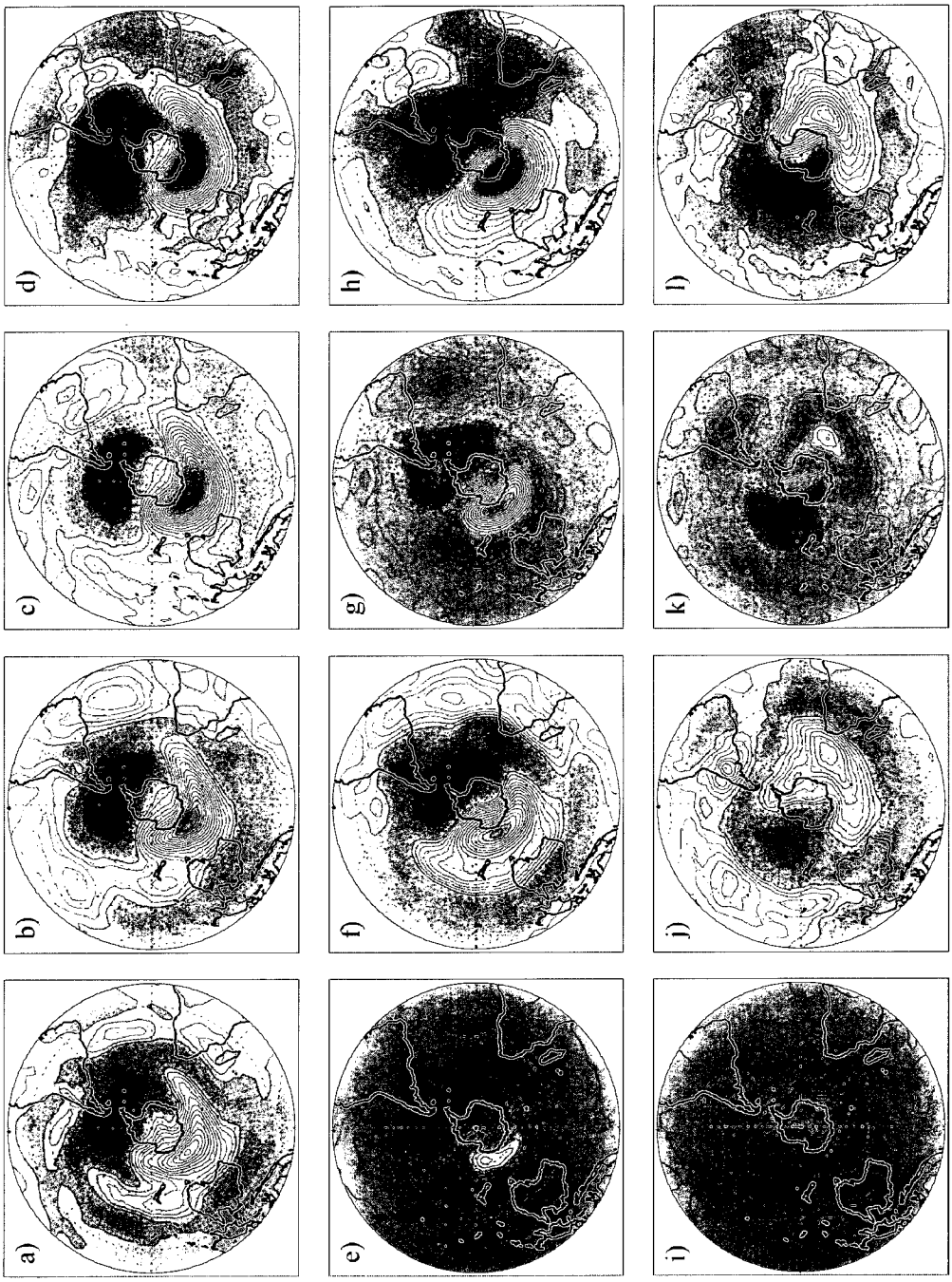

Figure 7.6. As in Fig. 7.4, except for September.

Reproduced with permission of the copyright owner. Further reproduction prohibited without permission.

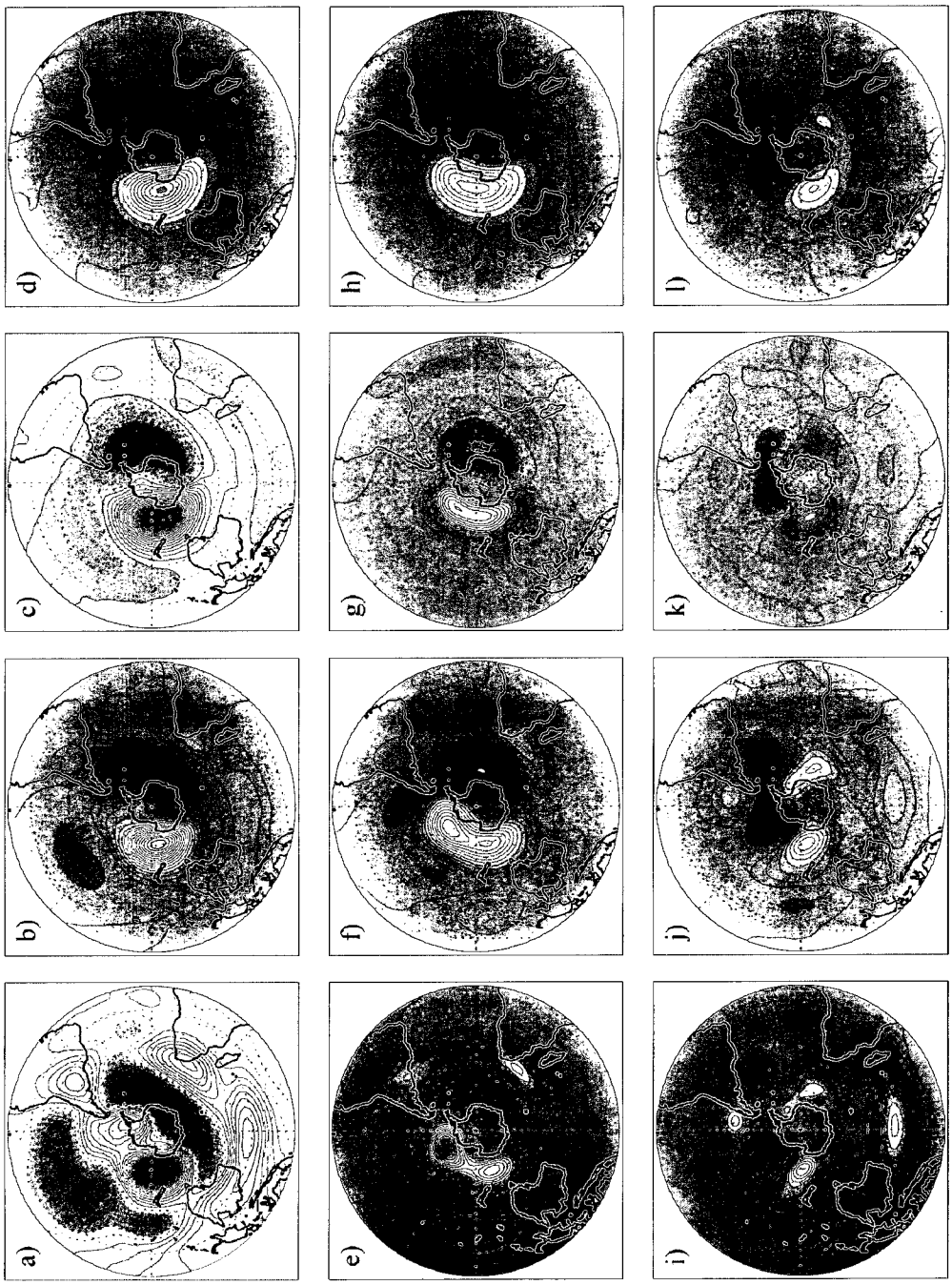

Figure 7.7. As in Fig. 7.3, except for October.

Reproduced with permission of the copyright owner. Further reproduction prohibited without permission.

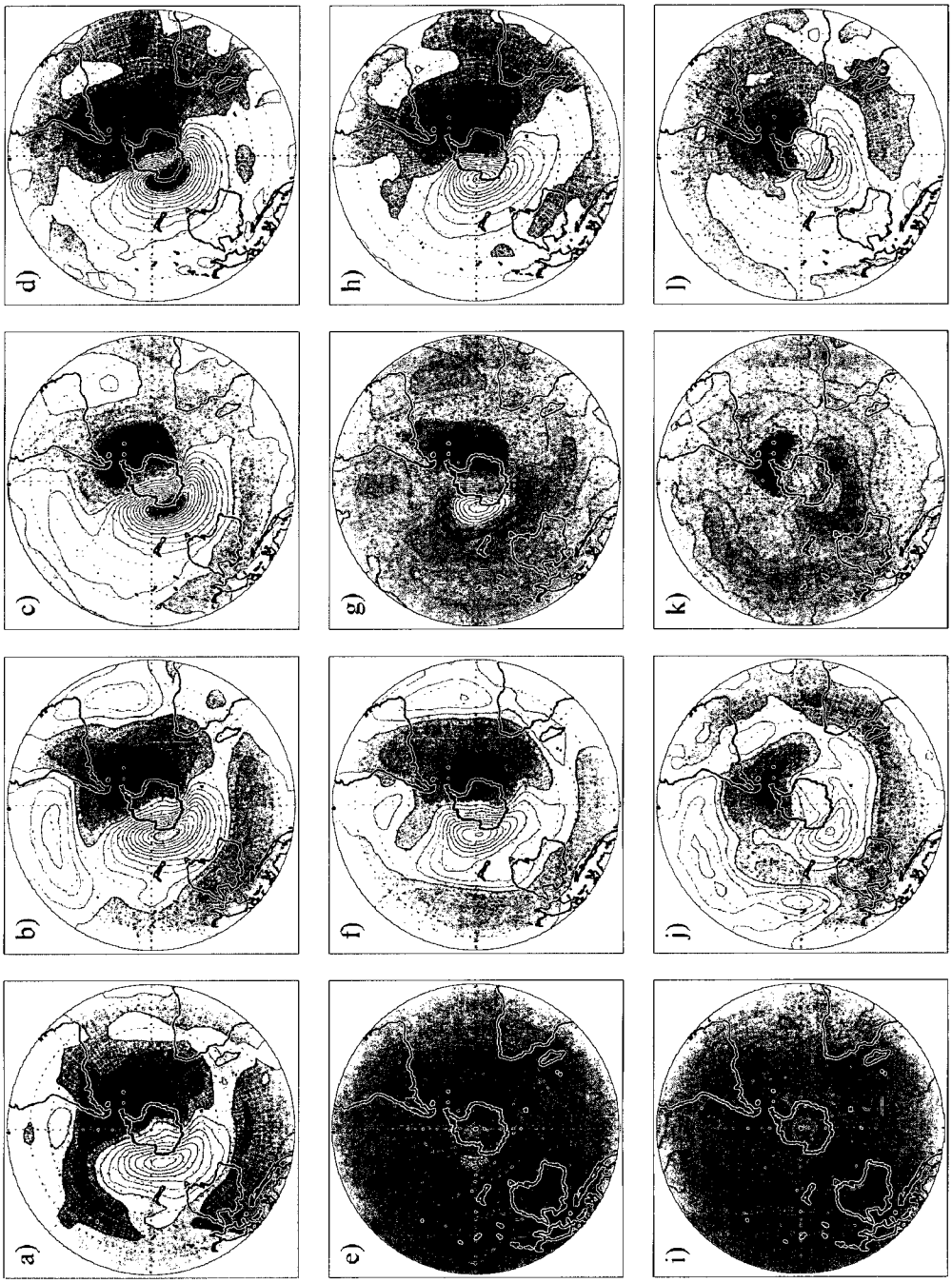

Figure 7.8. As in Fig. 7.4, except for October.

Reproduced with permission of the copyright owner. Further reproduction prohibited without permission.

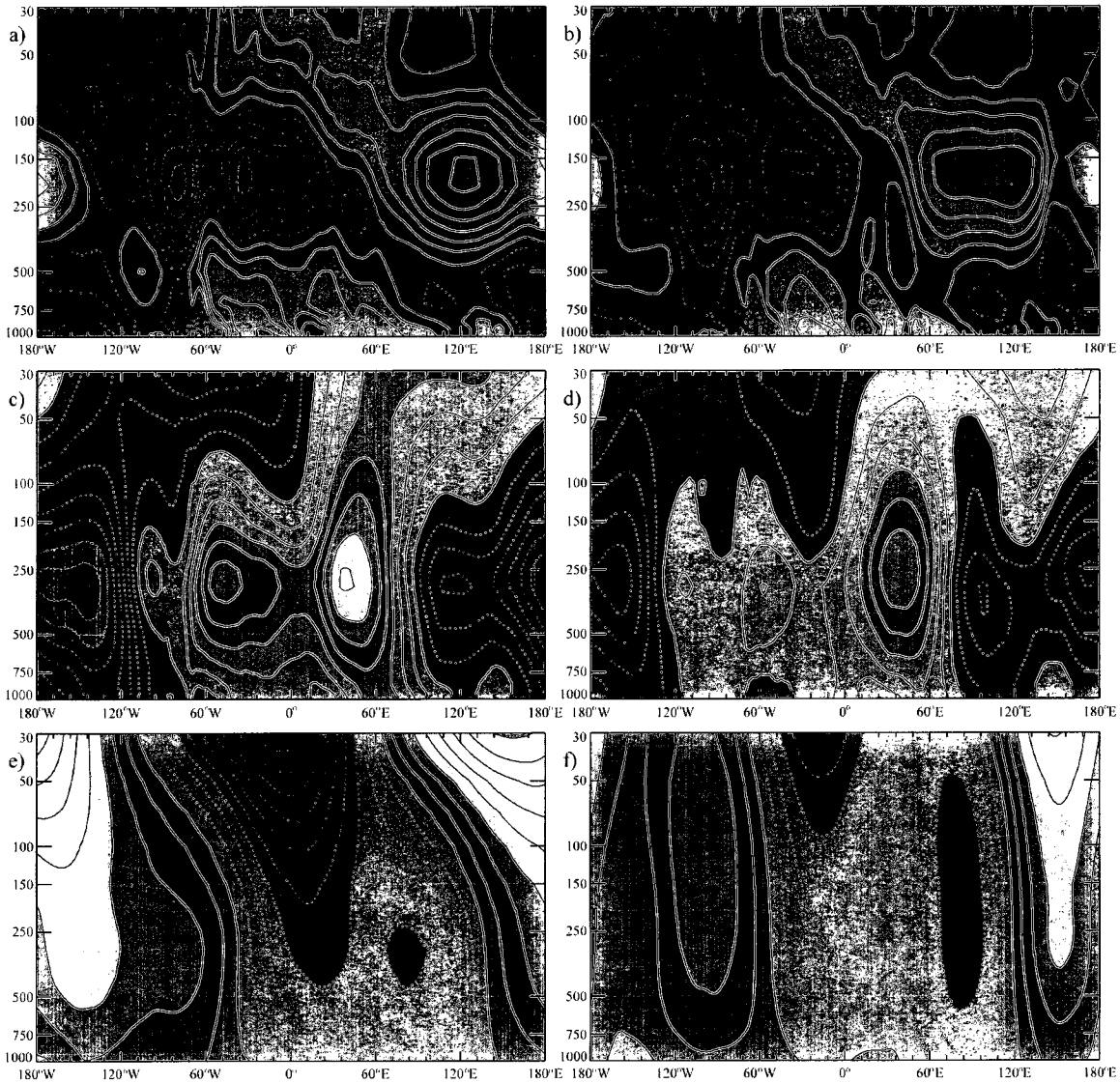

Figure 7.9. Longitude-altitude sections of August geopotential height anomalies during a) EN at 20˚S, b) LN at 20˚S, c) EN at 35˚S, d) LN at 35˚S, e) EN at 58˚S, and f) LN events at 58˚S. The contour interval is 10 gpm in a) and b), 20 gpm in c) and d) and 50 gpm in e) and f).

Reproduced with permission of the copyright owner. Further reproduction prohibited without permission.

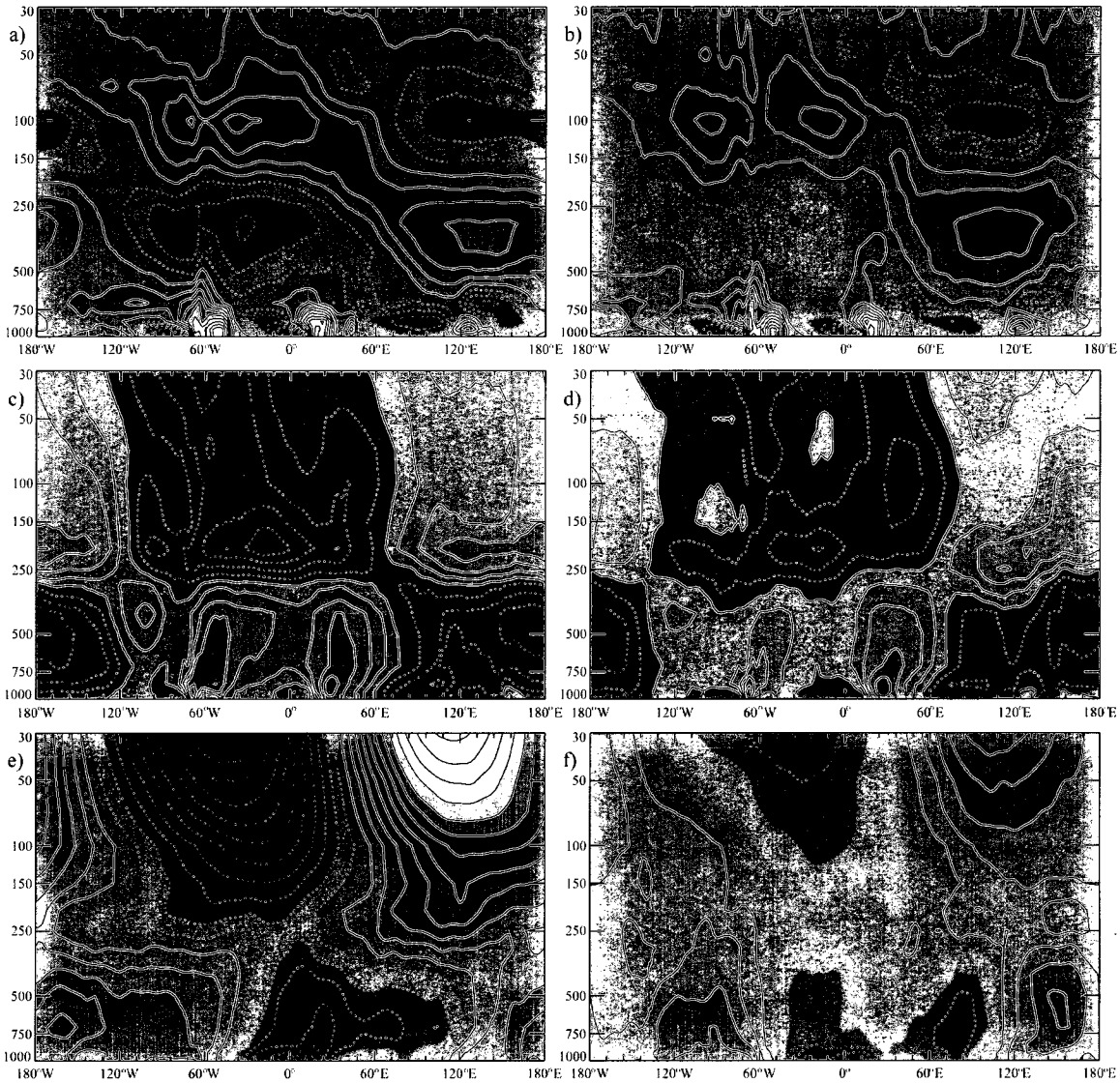

Figure 7.10. As in Fig. 7.9, except of temperature anomalies, with contour interval 1 K.

Reproduced with permission of the copyright owner. Further reproduction prohibited without permission.

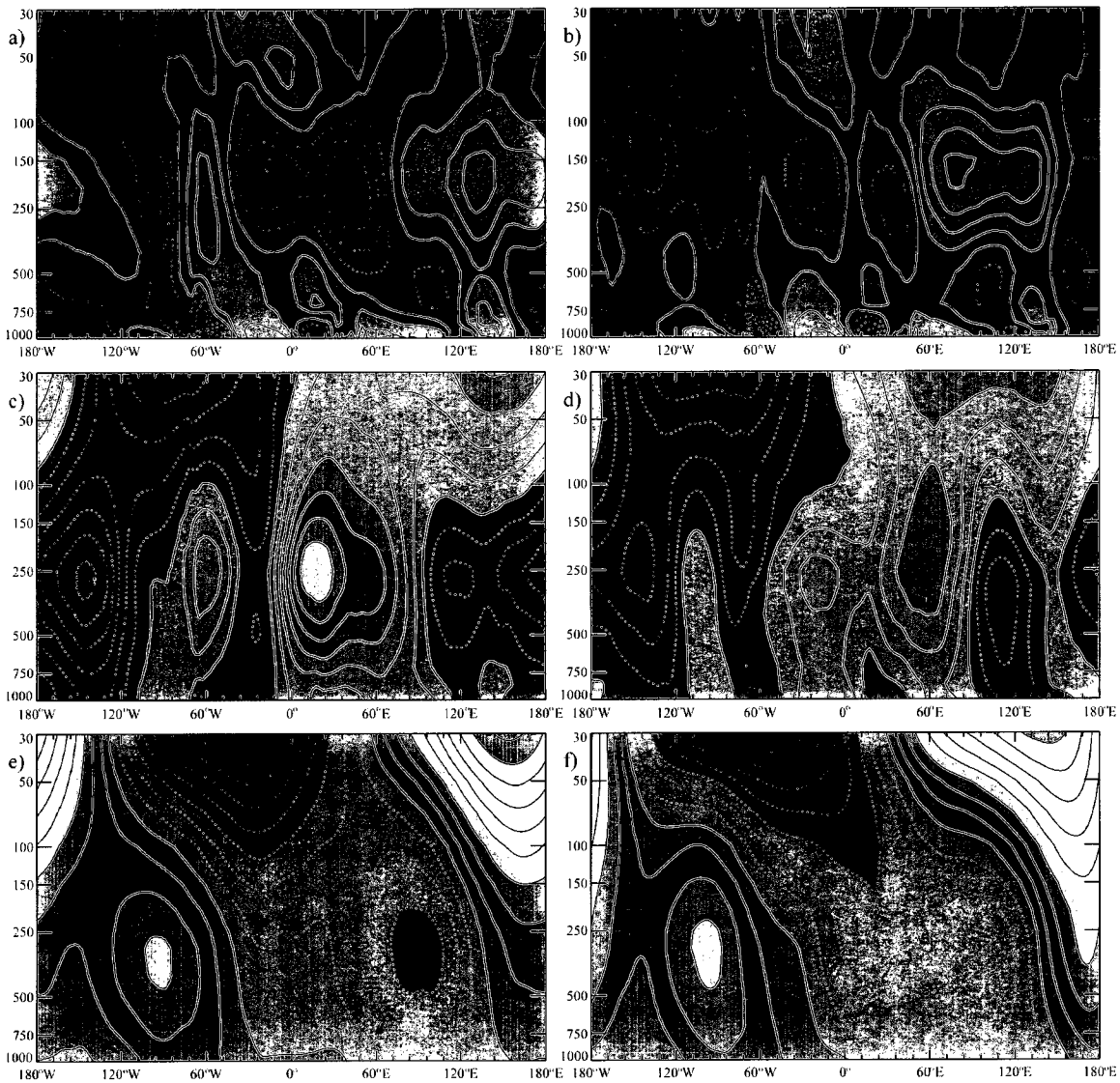

Figure 7.11. As in Fig. 7.9, except for September.

Reproduced with permission of the copyright owner. Further reproduction prohibited without permission.

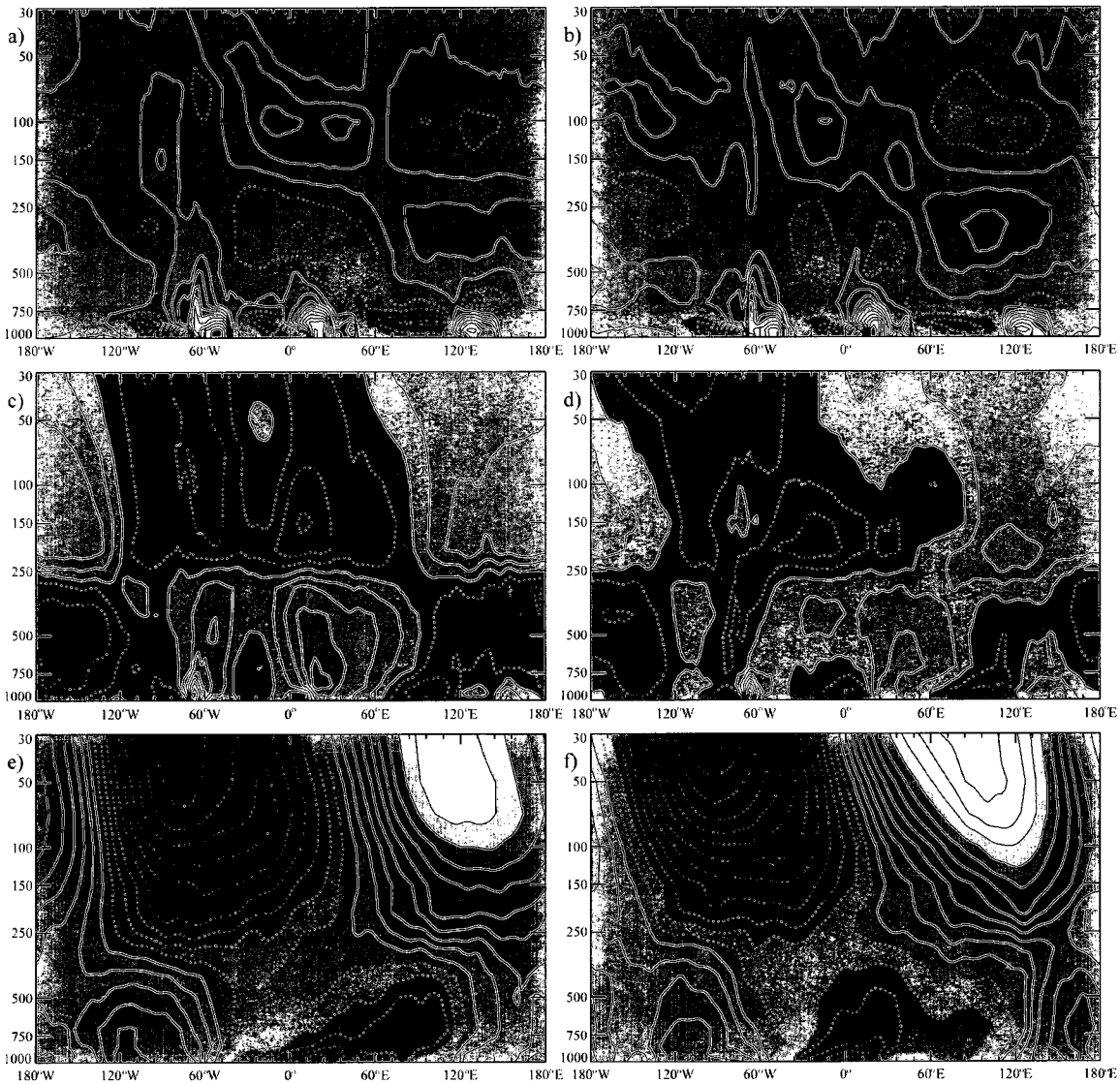

Figure 7.12. As in Fig. 7.10, except for September.

Reproduced with permission of the copyright owner. Further reproduction prohibited without permission.

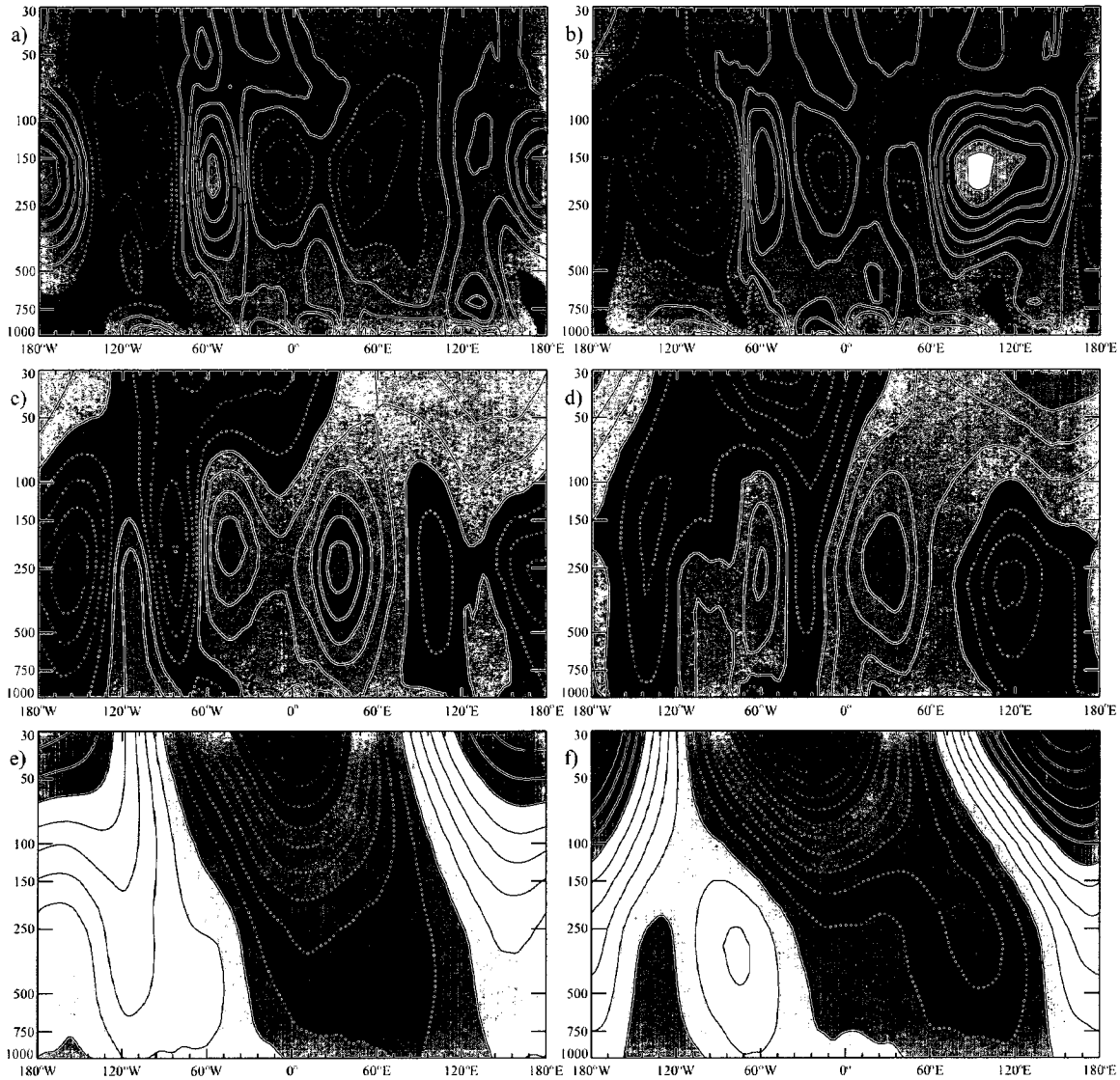

Figure 7.13. As in Fig. 7.9, except for October.

Reproduced with permission of the copyright owner. Further reproduction prohibited without permission.

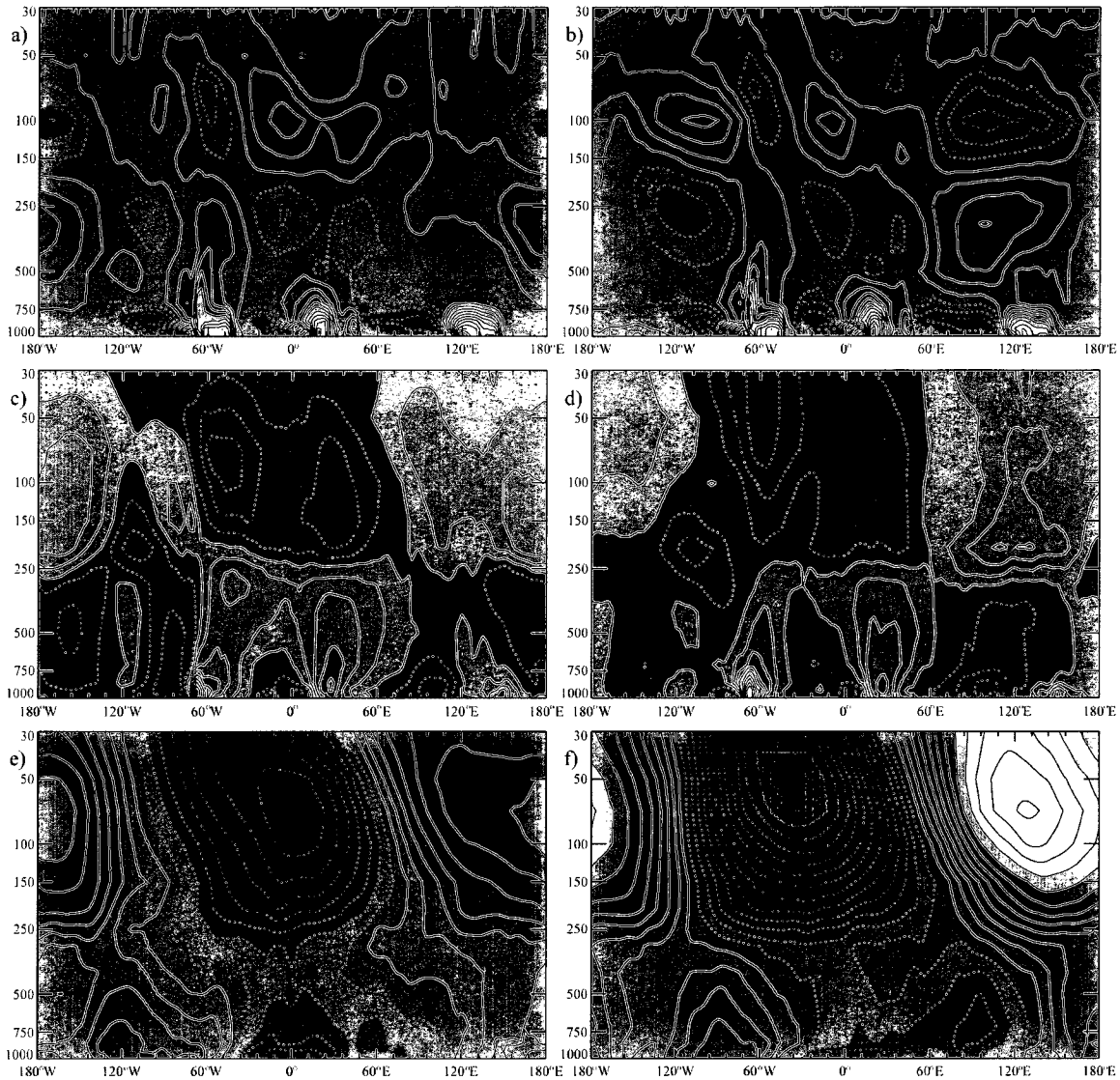

Figure 7.14. As in Fig. 7.10, except for October.

Reproduced with permission of the copyright owner. Further reproduction prohibited without permission.

Chapter 8

Conclusions

The first part of the thesis consisted of more detailed studies of processes that are responsible for the creation of dynamical regimes leading to the climatological zonal asymmetry in SH column ozone. These studies focused on two periods encompassing one month in 1998 and three months in 2000. The first observational study, consisting of 5 selected periods in August 1998 and presented in the third chapter gave an interesting insight into the differences in the life cycle of SH anticyclones in the Indian Ocean. Analysis of meteorological data as well as the calculated ozone budget showed the importance of the AH, IOH and SAH in redistributing ozone in the Indian Ocean region, leading to the peculiarly-shaped maximum in column ozone, namely the Ozone Croissant. A strong AH (southern part of the "*Gill* [1980] solution" to off-equatorial transient heating due to convection) leads to a zonally-limited column ozone maximum, while the enhanced activity of the SAH and IOH produces the zonally-elongated column ozone structure reminiscent of the Ozone Collar. The isentropic trajectory study showed the relative importance of the crossequatorial flow from the TH in shaping the wave structure of the SH. This grand anticyclone, resulting from heating of the Tibetan Plateau and responsible for a large part of the zonal mean meridional mass circulation during the boreal summer and fall, was further inspected in the introduction, together with the isentropic view on the global circulation resulting from the distribution of heat sources and sinks on Earth. This

Reproduced with permission of the copyright owner. Further reproduction prohibited without permission.

global circulation redistributes the energy and entropy from equatorial regions to higher latitudes, which is accomplished by poleward flow of high energy and entropy air parcels in the "Overworld" and an equatorward return flow of parcels with lower energy and entropy content in the "Underworld", near the surface. Even though our turbulent atmosphere introduces great variations in individual parcel trajectories and such global circulation may be presented only as the time averaged mode, the notoriety of the locations of heat sources over the Southeast Asia and the Tibetan Plateau as well as heat sinks over the extratropical Indian Ocean and Southeast Asia region leads to the preconditioning of this region needed to accomplish a large percentage of meridional mass transport. Of course, not all air particles originating in the TH circulatory system end up being entangled in the SH circulation. There is a great deal of dilution in the convective equatorial regions during the air parcels travel from the TH to the Indian Ocean region. The influence of this inflow into the SH, which constituted a major hypothesis, was found to be the decisive factor in reshaping the SH column ozone structure when it was modeled with the use of the UW-NMS. Even though the study was limited to a direct wind forcing resembling the lateral inflow, the conducted experiments showed the resulting strengthening of the AH and creation of a pool of higher ozone content air masses immediately to the south and southeast of the enhanced anticyclone over Australia by determining the pathways for the ozone-rich airmasses to descend at the edges of the AH system.

Chapter 4 focused on establishing the mechanism underlying the control of the longitudinal extent and strength of the ASWJ by outflow from the TH. The region stretching through the vast areas of Southeast Asia and the Maritime Continent was identified as a pathway the air parcels travel from the TH circulatory system crossing the

Reproduced with permission of the copyright owner. Further reproduction prohibited without permission.

equator, while being diluted in the deep convection region and ending in the SIO and AH circulatory systems. Once again the position of the column ozone maximum was shown to be located south of the ASWJ during the period of winter to spring transition in 2000, which results from the fact that most vigorous poleward and downward transport of ozone by synoptic Rossby waves occurs precisely in longitudes of this westerly jet. The ridges of traveling planetary scale waves dominant in the SH stratosphere were shown to have a preferential longitude band for the occurrence of stalling episodes. During these stalling episodes the enhancement of the IOH and/or AH together with simultaneous stalled wave 2 and 1 ridge, an ozone-rich feature, provide more ozone available for the descent into the Ozone Croissant area. This mechanism also may be seen as a direct link between tropical convective regions and lower stratosphere in the higher latitudes.

Chapter 5 contains the first part of a 10-year climatology, which provides valuable insight into the behavior of the UTLS region in the SH. As the winter to spring transition progresses, the relative strength of the AH generally diminishes, while the SAH and its western Indian Ocean manifestation grows. This is shown not only by the mean of type III but also by the changing partition between types in the 3 months analyzed. The ten Augusts include 80, 186 and 44 days of type I, II and III events, respectively, while September shows a similar partition of 91, 183 and 26 days, reflecting a very active period for the IOH. The partition is grossly remodeled into 89, 112 and 109 days in the October showing unchanged number of days when the AH was the major active anticyclone at 22°S but triple the number of days with clear enhancement of the SAH and relative calm over the central Indian Ocean. The analysis of the ASWJ is further reinforced by the momentum budget calculated for chosen types as well as for the monthly mean. This highlighted the

Reproduced with permission of the copyright owner. Further reproduction prohibited without permission.

enhanced core of the ASWJ during type I and III events. A gradual overall decay as time proceeds is worth noting and agrees with previous studies of the SH flow structure. The apparent two-core structure of the ASWJ is also attributable to the type I and III geopotential height structure. Type III events show a larger activity of the SAmH which also undergoes enhancement during the late transition period in October.

The TOMS data analysis showed a general tendency for the column ozone to increase from August to October for each year. This is due to increased availability of ozone in its production regions as time marches toward October as well as the cumulative transport processes in the wave active SH midlatitudes. The dependence of the column ozone on the type of events as well as the geometry of the TH outflow was also established, with the type I preference of a sharp ozone maximum south of the ASWJ, the elongated and weakened ozone maximum shifted toward the central Indian Ocean inherent with type II, and finally type III events which are similar to type II but with higher ozone maximum, characterized by the 300 DU contour closely following the SAH and SAmH contours.

The spectral analysis in Chapter 6 showed interesting differences between the types of events, namely: a) k=1 and 2 are stronger during type III events around 60°S in August while both type I and III are shown to be stronger than average and type II during October. The type I k=1 and 2 peaks more poleward at higher latitudes than all other types. The strong signal coming from around 20°S latitude for both wavenumbers reflects the duo of the AH and SAH projected into wave-space. One of the most important hallmarks of the winter to spring transition is the descent of the PNJ together with its poleward shift that was observed when comparing three months of the analyzed period. This is also reflected in the downward and equatorward shift of the E-P flux divergence region in the

Reproduced with permission of the copyright owner. Further reproduction prohibited without permission.

stratosphere around 60°S, with corresponding diminution of the upward wave energy propagation.

The k=3 and 4 of type I shows double the amplitude at 50°S in August, while similar feature is exhibited by k=3 of type III at 65°S in September. This is well represented in the E-P flux convergence showing a relative enhancement of the tropospheric divergence maximum in the 500-250 hPa region and similar enhancement during the September for type III, shifted poleward with respect to the monthly mean and other event types of events. The strong activity and poleward extension of the midlatitude anticyclones (AH, SAH) and the interaction between higher latitude anticyclones (SAmH and the Southeastern Pacific High) with the PV is reflected in the double maximum (35°S and 65°S) in k=4 amplitude during the September in type III. The type III events show a remarkable preference for wavenumber 5 with much higher amplitudes in the 30-60°S latitudinal band, which narrows and shifts equatorward from August to October. A similar feature is shared by type III cumulative wavenumbers 6-8. This was also further confirmed by E-P flux divergence analysis, which showed the contraction of the tropospheric and UTLS divergence regions and their equatorward shift for higher wavenumbers. The fact of projection of the AH into k=1 and 2 near 20°S line during type I events as well as the SAH further south (35°S) was examined with the help of phase plot showing the dependence of a mean position of the ridge on the event type.

The proposed mechanism for the interplay between anticyclones and the column ozone, as well as for establishing different wave regimes in the SH, is depicted in Figure 8.1 and involves the following steps:

Reproduced with permission of the copyright owner. Further reproduction prohibited without permission.

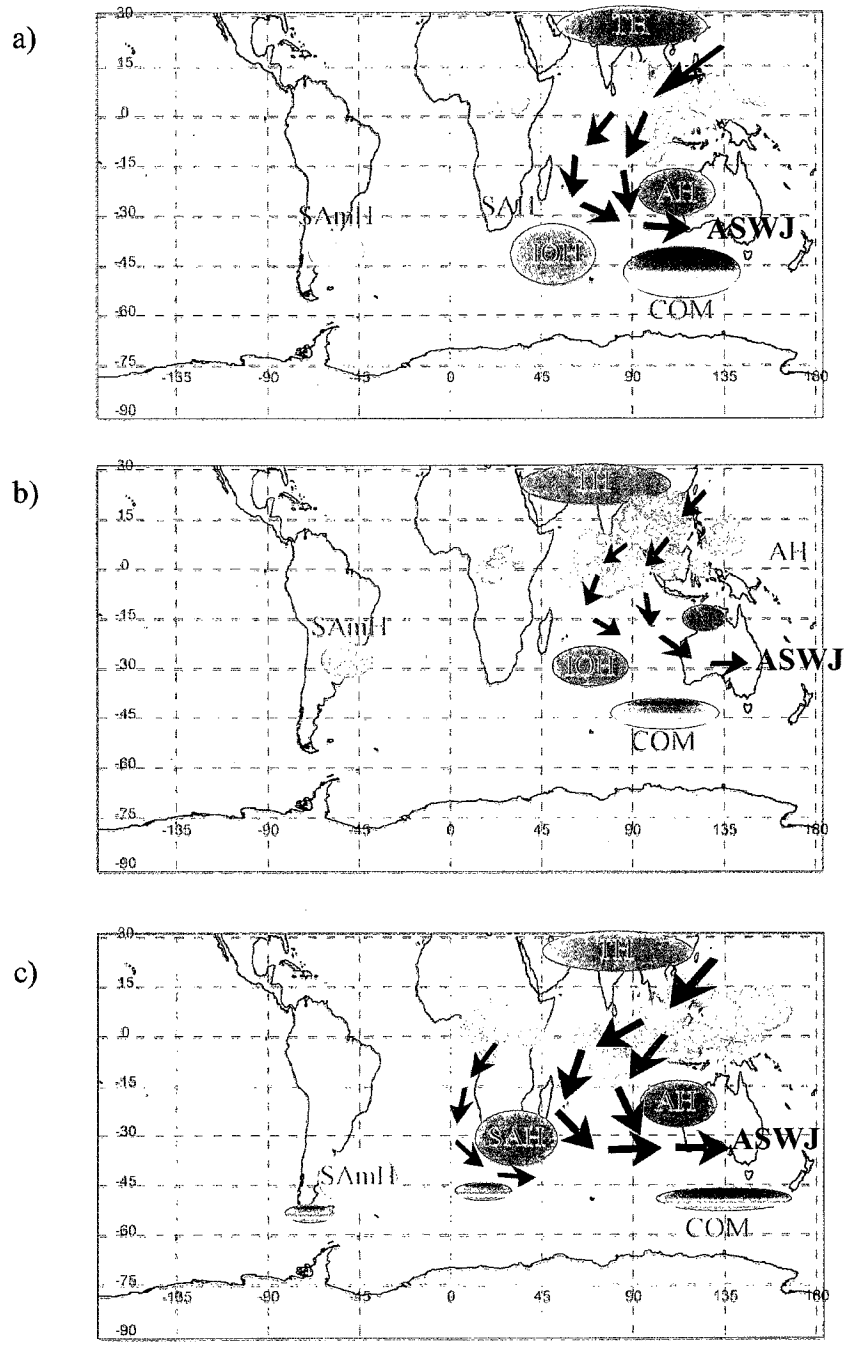

Fig. 8.1. Idealized sketch of the relationship between outflow from the TH and Asian tropical convection in the UTLS, the SIOH anticyclone system, SAmH, the Australian Subtropical Westerly Jet, and the column ozone in the SH for a) type I events, b) type II events, c) type III events. The size of feature is indicative of its strength.

Reproduced with permission of the copyright owner. Further reproduction prohibited without permission.

a) Establishment of the convective region in the Southeast Asia – Maritime Continent region. The convective region is limited to 90-110°E and eastward from that point (Fig. 8.1a) during type I events, with subdued African convection. The type II events (Fig. 8.1b) are characterized by active convection in 50-110°E region. Finally, the type III is characterized by convectively active African and 50-110°E regions (Fig. 8.1c).

b) Establishment of AH system as a direct response to the off-equatorial transient heating ('Gill solution'), with the TH being established over the heated Tibetan Plateau and modulated by the MC convection.

c) Outflow from the TH system creating a double streamer into the SH, around the AH system. Strong southward flow reaches well into 30°S during type I events (Fig. 8.1a). Smaller magnitude of southward flow over broader with correspondingly lesser magnitude maximum over the northeastern Indian Ocean during type II (Fig. 8.1b). Southward v-component limited to 30°S. Finally, type III over the broad region between 60-120°E, acting in unison with strong southward flow from the African convective region (Fig. 8.1c).

d) Southward flow effectively succumbing to the effects of rotation and anomalous momentum transported from the NH establishes the ASWJ core. A strong jet core centered over the western Australia exists during the type I events (Fig. 8.1a). The jet core is reduced and shifted eastward during type II events (Fig. 8.1b). It is strong and shifted toward the central Indian Ocean during the type III events (Fig. 8.1c). Type III events also witness a strengthening of the PNJ southward from the SAH and SAmH systems.

Reproduced with permission of the copyright owner. Further reproduction prohibited without permission.

e) Ozone transport by synoptic scale waves across the jet and brought down with air masses descending into troughs concentrate ozone into the Column Ozone Maximum (COM) area. There is a high ozone content and a sharp maximum southward of the ASWJ during the type I events (Fig. 8.1a). A smaller maximum positioned similarly occurs during the type II events (Fig. 8.1b). The strong maximum south of the Australia with the addition of secondary maximum south of the SAH system in October during type III events (Fig. 8.1c). There is a hint of an additional maximum center south of the SAmH. Proceeding toward October, increased activity of traveling planetary waves enhances the poleward and downward ozone transport into the lower stratosphere. A significant enhancement of ozone in the Australian sector occurs through frequent stalling of travelling planetary wave ridges, with co-amplification and merging with the AH and IOH highs.

The influences of the ENSO on the structure of the global circulation in the SH's UTLS and middle stratosphere region were analyzed in Chapter 7. Changes in the strength and location of anticyclonic features from the LN to EN regimes lead to reciprocal changes in location of ozone maxima. One example of this is the westward shift of the August LN maximum relative to EN, as a direct consequence of suppressed wave activity, resulting in a more localized IOH and AH. Main findings include:

a) From August through November column ozone increased throughout the SH (by 20 DU near 55°S).

b) During **La Niña** column ozone is 5-10 DU larger in 10-55°S.

Reproduced with permission of the copyright owner. Further reproduction prohibited without permission.

c) There is a 50° westward shift in the column ozone pattern during **La Niña**, with ~20 DU enhancement in the 50°W-100°E band.

d) Significant column ozone increase occurs poleward of South Africa during September and lies in a deep barotropic warm anomaly, associated with a northeastward displacement of the South Indian Ocean High (SIOH) from South Africa.

e) The October (**La Niña**) ozone maximum southward from Australia lies in a barotropic warm anomaly and is associated with northeastward displacement of the SIOH toward Australia.

f) **El Niño** conditions display an enhanced SAH (35°S) while the Australian High (20°S) displays enhancement during **La Niña** conditions.

g) The October polar vortex is stronger and more baroclinic during **La Niña** conditions. It is also shifted off the pole during those times.

The main objective of this study was to present ENSO modulation of column ozone observable from TOMS data along with the meteorological variables which govern its distribution. A more in-depth study, including full QBO analysis, disentanglement from the effects of ENSO, and mechanistic modeling reinforced by a Rossby wave breaking and Eliassen-Palm fluxes study will be the core of future manuscripts to come.

Reproduced with permission of the copyright owner. Further reproduction prohibited without permission.

Bibliography

Andrews D. G., and M. E. McIntyre (1976), Planetary waves in horizontal and vertical shear: The generalized Eliassen–Palm relation and the mean zonal acceleration. *J. Atmos. Sci*, 33, 2031–2048.

Andrews, D. G., Holton, J. R., Leovy, C. B. (1987), Middle Atmosphere Dynamics, *Academic Press*, New York, USA.

Angell, J.K. (1988), Variations and trends in tropospheric and stratospheric global temperatures, 1958-87, *J. Clim.*, *1*, 1296-1313.

Angell, J.K. (1989), On the relation between atmospheric ozone and sunspot number, *J. Clim., 2*, 1404-1416.

Angell, J.K. (1990), Variation in global tropospheric temperature after adjustment for the El Niño influence, 1958-89, *Geophys. Res. Lett.*, *17*, 1093-1096

Angell, J.K. (1992), Evidence of a relation between El Niño and QBO, and for an El Niño in 1991-2, *Geophys. Res. Lett.*, *19*, 285-288.

Annamalai, H., J. M. Slingo, K. R. Sperber, K. Hodges (1999), The mean evolution and variability of the Asian summer monsoon: Comparison of ECMWF and NCEP-NCAR reanalyses, *Mon. Wea. Rev., 127*, 1157-1186.

Aoki, H., M. Shiotani, and I. Hirota (1996), Interannual variability of the tropospheric circulation and its relation to the stratosphere in the southern hemisphere, *J. Meteor. Soc. Jpn., 74*, 509-523.

Baldwin, M. P., and T. J. Dunkerton (1998), Quasi-biennial modulation of the Southern Hemisphere stratospheric polar vortex, *Geophys. Res. Lett.*, *25*, 3343–3346.

Reproduced with permission of the copyright owner. Further reproduction prohibited without permission.

Barros A. P., Kim G., Williams E., Nesbitt S. W. (2004), Probing orographic controls in the Himalayas during the monsoon using satellite imagery. *Natural Hazards and Earth System Sciences* 4, 29-51, SRef-ID:1684-9981/NHESS/2004-4-29.

Berberry, E. H., J. Nogues-Paegle, and J. D. Horel (1992),Wavelike southern hemisphere extra tropical teleconnections *J. Atmos. Sci., 49*, 155-177.

Berbery, H. and C. Vera (1996), Characteristics of the southern hemisphere winter storm track with filtered and unfiltered data, *J. Atmos. Sci., 53*, 468-481.

Berson, F. A. (1961), Circulation and energy balance in a tropical monsoon. *Tellus* , 13, 472-485.

Bjerknes, V., J. Bjerknes, T. Bergeron, and H. Solberg (1933), *Physikalische Hydrodynamik*, 797 pp., Springer-Verlag, New York.

Bojkov, R., D. (1987), The 1983 and 1985 anomalies in ozone distribution in perspective, *Mon. Weather Rev., 115*, 2187-2201.

Bowman, K.P. (1989), Global patterns of the quasi-biennial oscillation in total ozone, *J. Atmos. Sci.*, 46, 3328–3343.

Braak C. (1929), The Climate of The Netherland Indies, *Vols. I and II. Verhandelingen No. 8, Koninklijk Magnetisch en Meteorologisch Observatiorium te Batavia*, 1602 pp.

Butcher, J. C. (1987), *The Numerical Analysis of Ordinary Differential Equations: Runge--Kutta and General Linear Methods* (Wiley).

Butchart, N. and Coauthors (2006), Simulations of anthropogenic change in the strength of the Brewer-Dobson circulation, *Climate Dyn., 27*, 727-741.

Canziani, P. O., J. R. Holton, E. Fishbein, and L. Froidevaux (1995), Equatorial Kelvin wave variability during 1992 and 1993, *J. Geophys. Res., 100(D3)*, 5193–5202.

Charlton, A. J., A. O'Neill, W. A. LaHoz, and P. Berrisford (2005), The splitting of the stratospheric polar vortex in the Southern Hemisphere, September 2002: Dynamical evolution, *J.Atmos. Sci., 62*, 590-602.

Reproduced with permission of the copyright owner. Further reproduction prohibited without permission.

Collimore, C. C., M. H. Hitchman, and D. W. Martin (1998), Is there a quasi-biennial oscillation in tropical deep convection?, *Geophys. Res. Lett., 25*, 333-336.

Collimore, C. C., D. W. Martin, M. H. Hitchman, A. H. Huesmann, and D. E. Waliser (2003), On the relationship between the QBO and tropical deep convection, *J. Clim., 16*, 2552–2568.

Crook, J. A., N. P. Gillet, and S. Keeley (2008), Sensitivity of Southern Hemisphere climate to zonal asymmetry in ozone, *Geophys. Res. Lett., 35*, L07806.

Defant A. (1921), Die Zirkulation der Atmosphäre in den gemässigten Breiten der Erde: Grundzüge einer Theorie der Klimaschwankungen. *Geograf. Ann.* 3:209–66.

Dickinson, R. E. (1971), Cross-equatorial eddy momentum fluxes as evidence of tropical planetary wave sources, *Quart. J. Roy. Meteorol. Soc., 97*, 554-558.

Drosdowsky, W. (1996), Variability of the Australian summer monsoon at Darwin: 1957-1992. *J. Climate, 9*, 85-96.

Duan AM, Wu G. (2005), Role of the Tibetan Plateau thermal forcing in the summer climate patterns over subtropical Asia. *Climate Dynamics* 24: 793-807, DOI: 10.1007/S00382-004-0488-8.

Duan AM, Liu YM, Wu GX. (2005), Heating status of the Tibetan Plateau from April to June and rainfall and atmospheric circulation anomaly over East Asia in midsummer. *Science in China. Series D, Earth Sciences* 48(2): 250-257.

Dunkerton T. J. (1978), On the mean meridional mass motions of the stratosphere and mesosphere. *J. Atmos. Sci*, 35, 2325–2333.

Dutton, J. A. and D. R. Johnson (1967), The theory of available potential energy and a variational approach to atmospheric energetics. *Advances in Geophysics,* Vol. 12, Academic Press, 333–436.

Edmon, H. J., Jr., Hoskins, B. J. and McIntyre, M. E. (1980), Eliassen-Palm cross sections for the troposphere. *J. Atmos. Sci.* , 37, 2600-2616.

Elliassen A. and E. Palm (1961), On the transfer of energy in stationary mountain waves, *Geofysiske Publikasjoner, Vol. 22(3)*, pp. 1-23.

Reproduced with permission of the copyright owner. Further reproduction prohibited without permission.

Eyring, V., et al. (2006), Assessment of temperature, trace species, and ozone in chemistry climate model simulations of the recent past, *J. Geophys. Res., 111*, D22308.

Farrara, J. D. and C. R. Mechoso (1986), An observation study of the final warming in the Southern Hemisphere stratosphere, *Geophys. Res. Lett.*, 13, 1232-1235.

Ferrel W. (1859), The motion of fluids and solids relative to the Earth's surface. *Math. Mon.* 1:140–48, 210–16, 300–7, 366–73, 397–406.

Flohn H. (1950), Neue Anschauungen über die allgemeine Zirkulation der Atmosphare und ihre klimatische Bedeutung. *Erdkunde* 4, 141-162.

Flohn H. (1957), Large-scale aspects of the "summer monsoon" in south and East Asia. *Journal of the Meteorological Society of Japan,* 35, 180-186.

Flohn H. (1960), Recent investigations on the mechanism of the "Summer Monsoon" of Southern and Eastern Asia. *Proc. Symp. Monsoons of the World,* New Delhi, Hind Union Press, 75-88.

Flohn H. (1968), Contributions to a meteorology of the Tibetan Highlands. Atmos. Sci. Paper No. 130, Colorado State University, 120 pp.

Gallimore, R. G. and Johnson, D. R. (1981), A numerical diagnostic model of the zonally averaged circulation in isentropic coordinates. *J. Atmos. Sci.* , 38, 1870-1890.

Garcia, R. R., and W. J. Randel (2008), Acceleration of the Brewer-Dobson circulation due to increases in greenhouse gases, *J. Atmos. Sci., 65*, 2731-2739.

Garcia-Herrera, R., N. Calvo, R. R. Garcia, and M. A. Giorgetta (2006), Propagation of ENSO temperature signals into the middle atmosphere: A comparison of two general circulation models and ERA-40 reanalysis data, *J. Geophys. Res., 111*, D06101.

Garfinkel, C.I., and D.L. Hartmann (2007), Effects of the El-Nino Southern Oscillation and the Quasi-Biennial Oscillation on polar temperatures in the stratosphere, *J. Geophys. Res. Atmos.*, *112*, D19112.

Reproduced with permission of the copyright owner. Further reproduction prohibited without permission.

Geerts, B. and Wheeler, M.: The Madden Julian Oscillation, *Bureau of Meteorology*, May 1998, Accessed May 08, 2009

Geller M. A., and M. F. Wu (1987), Troposphere–stratosphere general circulation statistics. *Transport Processes in the Middle Atmosphere,* G. Visconti and R. Garcia, Eds., Reidel, 3–17.

Geller M. (1988), Solar cycles and the atmosphere. *Nature*, 332, 584–585.

Gill, A. E., (1980), Some simple solutions for heat-induced tropical circulation, *Quart. J. R. Meteor. Soc., 106*, 447-462.

Gillet, N. P., and D. Thompson (2003), Simulation of recent Southern Hemisphere climate change, *Science, 302*, 273-275.

Godrey, J. S., and S. R. Rintoul (1998), The role of the oceans in southern hemisphere climate, in *Meteorology of the Southern Hemisphere, American Meteorological Society.*

Godson,W. L. (1963), in *Meteorological Abhandlungen, Volume 35*, pp. 161-206, Free University of Berlin Press.

Gray, W. M., J. D. Scheaffer, and J. A. Knaff (1992), Influence of the stratospheric QBO on ENSO variability. *J. Meteor. Soc. Jpn., 70,* 975–995.

Gray, W.M., C.W. Landsea, P. Mielke and K. Berry (1993), Predicting Atlantic basin seasonal tropical cyclone activity by 1 August, *Wea. Forecasting, 8*, 73-86.

Gruber, A., and J. S. Winston, (1978), Earth–atmosphere radiative heating based on NOAA scanning radiometer measurements. *Bull. Amer. Meteor. Soc.,* **59,** 1570–1573.

Gruber, A., and A. F. Krueger, (1984), The status of the NOAA outgoing longwave radiation data set. *Bull. Amer. Meteor. Soc.,* **65,** 958–962.

Grytsai, A. V., and Coauthors (2007), Structure and long-term change in the zonal asymmetry in Antarctic total ozone during spring, *Ann. Geophys., 25*, 361-374.

Hadley G. (1735), Concerning the cause of the general trade-winds. *Phil. Trans.* 39, 58–62.

Reproduced with permission of the copyright owner. Further reproduction prohibited without permission.

Hahn, D.G. and Manabe, S. (1975), The role of mountains in the south Asian monsoon circulation, *J. Atmos. Sci.,* 32:1515-1541.

Hamilton, K. (1993), An examination of observed Southern Oscillation effects in the Northern Hemisphere stratosphere, *J. Atmos. Sci.*, *50*, 3468-3473

Hampson, J., and P. Haynes (2006), Influence of the equatorial QBO on the extratropical stratosphere, *J. Atmos. Sci.*, *63*, 936-951.

Harnik, N., R. K. Scott, and J. Perlwitz (2005), Wave reflection and focusing prior to the major stratospheric warming of September 2002. *J. Atmos. Sci., 62*, 640-650.

Harwood R. S. (1975), The temperature structure of the Southern Hemisphere stratosphere August–October 1971, *Quart. J. Roy. Meteor. Soc*, 101, 75–91.

Hartmann D. L. (1976), The structure of the stratosphere in the Southern Hemisphere during late winter 1973 as observed by satellite. *J. Atmos. Sci*, 33, 1141–1154.

Hartmann, D.L. (1976) ,The dynamic climatology of the stratosphere in the Southern Hemisphere during late winter 1973, *J. Atmos. Sci,* 33, 1789-1802.

Hartmann D. L. (1977), Stationary planetary waves in the Southern Hemisphere. *J. Geophys. Res*, 82, 4930–4934.

Hartmann, D.L. (1979), Baroclinic instability of realistic zonal mean states to planetary waves, *J. Atmos. Sci,* 36, 1226-2349.

Hartmann, D.L., C.R. Mechoso and K. Yamazaki (1984), Observations of wave-mean flow interaction in the Southern Hemisphere, *J. Atmos. Sci,* 41, 351-362.

Hartmann, D. L., and F. Lo (1998), Wave-driven zonal flow vacillation in the Southern Hemisphere. J. Atmos. Sci., 55:1303-15.

Harvey, V. L., and M. H. Hitchman (1996), A climatology of the Aleutian High, *J. Atmos. Sci.,53*, 2088-2101.

Reproduced with permission of the copyright owner. Further reproduction prohibited without permission.

Harvey, V. L., M. H. Hitchman, R. B. Pierce, T. D. Fairlie (1999), Tropical high aerosol in the Aleutian anticyclone, *J. Geophys. Res., 104*, 6281-6290.

Harvey, V. L., R. B. Pierce, M. H. Hitchman, C. E. Randall, and T. D. Fairlie (2004), On the distribution of ozone in stratospheric anticyclones, *J. Geophys. Res., 109*, D24308.

Hasebe, F. (1980), A global analysis of the fluctuations in total ozone, II, Non-stationary annual oscillation, quasi-biennial oscillation, and long-term variations in total ozone, *J. Meteorol. Soc. Jpn., 58*, 104-117.

Hastenrath, S. (1990), The relationship of highly reflective clouds to tropical climate anomalies, *J. Clim., 3*, 353-365.

Hayashi, Y. and D.G. Golder (1993), Tropical 40-50 and 25-30 day oscillations, *J. Atmos. Sci.,* 50, 464-494.

Haynes, P. H., Marks, C. J., McIntyre, M. E., Shepherd, T. G., Shine, K. P. (1991), On the "downward control" of extratropical diabatic circulations by eddy-induced mean zonal forces, *J. Atmos. Sci., 48,* 651-678.

Held, I. M. and Schneider, T. (1999), The surface branch of the zonally averaged mass transport circulation in the troposphere. *J. Atmos. Sci.* , 56, 1688-1697.

Hendon, H. H., and D. L. Hartmann (1982), Stationary waves on a sphere: sensitivity to thermal feedback, *J. Atmos. Sci., 39*, 1906-1920.

Hendon, H. H. and B. Liebmann (1990), A composite study of the onset of the Australian summer monsoon, *J. Atmos. Sci., 47*, 2227-2240.

Hendon, H. H. and B. Liebmann (1990), The intraseasonal (30-50 day) oscillation of the Australian summer monsoon, *J. Atmos. Sci., 47*, 2909-2923.

Hines, K. M., and D. H. Bromwich (2002), A pole to pole to pole west Pacific atmospheric teleconnection during August, *J. Geophys. Res., 107(D18),* 4359.

Reproduced with permission of the copyright owner. Further reproduction prohibited without permission.

Hio, Y., and I. Hirota (2002), Interannual variations of planetary waves in the Southern Hemisphere stratosphere, *J. Meteorol. Soc. Jpn., 80*, 1013-1027.

Hio, Y., and S. Yoden (2005), Interannual variations of the seasonal march in the Southern Hemisphere stratosphere for 1979-2002 and characterization of the unprecedented year 2002, *J. Atmos. Sci., 62*, 567-580.

Hio, Y., and S. Yoden (2007), A parameter sweep experiment on quasi-periodic variations of a polar vortex due to wave-wave interaction in a spherical barotropic model, *J. Atmos. Sci., 64*, 4069-4083.

Hitchman, M. H., C. B. Leovy, J.C. Gille, and P.L. Bailey (1987), Quasi-stationary zonally asymmetric circulations in the equatorial middle atmosphere, *J. Atmos. Sci.*, *44*, 2219-2236.

Hitchman M.H. and C.B. Leovy (1988), Estimation of the Kelvin wave contribution to the semiannual oscillation. *J. Atmos. Sci., 45*, pp. 1462–1475.

Hitchman, M. H., M. McKay, and C. R. Trepte (1994), A climatology of stratospheric aerosol, *J. Geophys. Res., 99*, 20,689-20,700.

Hitchman, M. H., M. L. Buker, and G. J. Tripoli (1999), Influence of synoptic waves on column ozone during arctic summer 1997, *J. Geophys. Res., 104,* 26,547-26,563.

Hitchman, M. H., and A. S. Huesmann (2007),Aclimatology of Rossbywave breaking: Seasonal distributions and dynamical regimes, *J. Atmos. Sci., 64*, 1922–1940.

Hitchman, M. H., and A. S. Huesmann (2009), Effect of the Quasibiennial Oscillation on stratospheric jets and Rossby wave breaking, *J. Atmos. Sci., 66*, 935-946.

Hitchman, M. H., and M. J. Rogal (2009), ENSO influences on monthly mean column ozone and stratospheric geopotential height and temperature anomalies during the Southern Hemisphere winter to spring transition, *submitted to J. Geophys. Res.*

Reproduced with permission of the copyright owner. Further reproduction prohibited without permission.

Hitchman, M. H., M. J. Rogal, and I. Stajner (2009), Seasonal evolution of the Ozone Croissant: zonal contraction of monsoon outflow, and stalled planetary wave ridges, *submitted to J. Geophys. Res.*

Hoerling, M. P., and D. R. Johnson (1986), On the maintenance of the semi-permanent centers of action during January 1979, *Natl. Conf. Sci. Results First GARP Global Exp., Miami, Fla. Am. Meteorol. Soc.,* Boston, Massachusetts, 91-94.

Hollingsworth A., D.B. Shaw, P. Lönnberg, L. Illari, K. Arpe, and A.J. Simmons (1986), Monitoring of observation and analysis quality by a data assimilation system, *Mon. Wea. Rev., 114*, 861-879.

Holton, J. R. (1980), Wave propagation and transport in the middle atmosphere, *Phil Trans. Roy. Soc. Lond., A296,* 73-85.

Holton, J. R., Haynes, P. H., McIntyre, M. E., Douglass, A. R., Rood, R. B., and Pfister, L (1995), Stratosphere-troposphere exchange, Rev. Geophys., 33, 403–439.

Holton, J. R., M. J. Alexander, and M. T. Boehm (2001), Evidence for short vertical wavelength Kelvin waves in the Department of Energy-Atmospheric Radiation Measurement Nauru99 radiosonde data, *J. Geophys. Res., 106(D17)*, 20,125–20,129.

Hood, L., S. Rossi and M. Beuten (1999), Trends in lower stratospheric zonal winds, Rossby wave breaking behavior, and column ozone at northern midlatitudes. *J. Geophys. Res., 104*, 24,321-24,339.

Horel, J. D., A. N. Hahmann, and J. E. Geisler, 1989: An investigation of the annual cycle of convective activity over the tropical Americas. *J. Climate, 2*, 1388–1403.

Hoskins B. J. and D. J. Karoly (1981), The steady linear response of a spherical atmosphere to thermal and orographic forcing, *J. Atmos. Sci.* 38, pp. 1179–1196.

Hoskins B. J., I. N. James and G. H. White (1983), The shape, propagation and mean-flow interaction of large scale weather systems, *J. Atmos. Sci.* 40, pp. 1595–1612.

Hoskins BJ. (1991), Towards a PV-θ view of the general circulation. *Tellus*, 43AB: 27-35.

Reproduced with permission of the copyright owner. Further reproduction prohibited without permission.

Hudson, R. D., A. D. Frolov, M. F. Andrade, and M. B. Follette (2003), The total ozone field separated into meteorological regimes, Part 1: Defining the regimes, *J. Atmos. Sci., 60,* 1669-1677.

Hudson, R. D., M. F. Andrade, M. B. Follette, and A. D. Frolov (2006), The total ozone field separated into meteorological regimes – Part II: Northern Hemisphere mid-latitude total ozone trends, *Atmos. Chem. Phys., 6,* 5183-5191.

Hurrell J.W. (1995), Decadal trends in the North Atlantic Oscillation: regional temperatures and precipitation, *Science* 269, pp. 676–679.

Hurrell, J. W. (1996), Influence of variations in extratropical wintertime teleconnections on Northern Hemisphere temperatures. *Geophys. Res. Lett.,* 23, 665-668.

Hurrell, J.W., H. van Loon, H., D. J. Shea, D. J. (1998), "The mean state of the troposphere", in *Meteorology of the Southern Hemisphere*, American Meteorological Society.

James, I. N. (1994), *Introduction to Circulating Atmospheres.* Cambridge University Press, 422 pp.

Jeffreys H. (1926), On the dynamics of geostrophic winds. *Q. J. R. Meteorol. Soc.* 52, 85–104.

Johnson, D. R. (1980), A generalized transport equation for use with meteorological coordinate systems. *Mon. Wea. Rev., 108,* 733-745.

Johnson, D. R., M. Y. Wei, and T. Schaack (1982), Planetary-scale mass, momentum and energy exchange. International Conference on the Scientific Results of the Monsoon Experiment, Denparar, Bali, Indonesia, 26-30 October 1981, *World Meteorological Organization (WMO), Geneva, Switzerland,* 240-243.

Johnson, D. R., R. D. Townsend and M.-Y. Wei (1985), The thermally coupled response of the planetary scale circulation to the global distribution of heat sources and sinks. *Tellus*, 37A, 106-125.

Reproduced with permission of the copyright owner. Further reproduction prohibited without permission.

Johnson, D. R., M. Yanai, and T. K. Schaack (1987), Global and regional distributions of atmospheric heat sources and sinks during the GWE. *Monsoon Meteorology,* C. P. Chang and T. N. Krishnamurti, Eds., Oxford University Press, 271–297.

Johnson, D. R. (1989), The forcing and maintenance of global monsoonal circulations: An isentropic analysis. *Advances in Geophysics, 31, Academic Press*, 43–316.

Kallberg, P, et al. (2005), ECMWF Re-Analysis Project Report Series, *19*, 191 pp.

Kalnay, E., et al. (1996), The NCEP/NCAR 40-Year Reanalysis Project, *Bull. Am. Meteorol. Soc.*, 77, 437-471.

Karoly D. J., R. A. Plumb, M. Ting (1989), Examples of the horizotal propagation of quasi-stationary waves, *J. Atmos. Sci.*, *46*, 2802-2811.

Kayano, M.T. (1997), Principal modes of the total ozone on the Southern Oscillation timescale and related temperature variations, *J. Geophys.Res.*, *102*, 25,797-25,806.

Keyser, D. and M. A. Shapiro (1986), A review of the structure and dynamics of upper-level frontal zones, *Mon. Wea. Rev., 114*, 452–499.

Kida, H. (1977), A numerical investigation of the atmospheric general circulation and stratospheric-tropospheric mass exchange: II. Lagrangian motion of the atmosphere, *J. Meteorol. Soc. Jpn., 55*, 71-88.

Kiladis, G. N., and K. C. Mo (1998), "Interannual and intraseasonal variability in the Southern Hemisphere", in *Meteorology of the Southern Hemisphere*, American Meteorological Society.

Kim D, Sperber K, Stern W, Waliser D, Kang IS, et al. (2009), Application of MJO Simulation Diagnostics to Climate Models. Journal of Climate: In Press

Kinnersley, J. S., and K. K. Tung (1998), Modeling the global inter-annual variability of the ozone column due to the equatorial quasi-biennial oscillation and extra-tropical planetary wave variability, *J. Atmos. Sci.*, *55*, 1417-1428.

Reproduced with permission of the copyright owner. Further reproduction prohibited without permission.

Kinnersley, J. S., and K. K. Tung (1999), Mechanisms for the extra-tropical QBO in circulation and ozone column, *J. Atmos. Sci.*, *56*, 1942-1962.

Knox, J. A., and V. L. Harvey (2005), Global climatology of inertial instability and Rossby wave breaking in the stratosphere, *J. Geophys. Res., 110*, D06108.

Kousky, V. E., 1988: Pentad outgoing longwave radiation climatology for the South American sector. *Rev. Bras. Meteor.*, *3*, 217–231.

Koteswaram P. (1958), Easterly jet streams in the tropics. Tellus 10: 43–57.

Krishnamurti, T. N., S. M. Daggiupaty, J. Fein, M. Kanamitsu, and J. D. Lee (1973), Tibetan High and upper tropospheric tropical circulations during northern summer, *Bull. Amer. Meterol. Soc., 54*, 1234-1249.

Labitzke, K. and H. van Loon (1992), Association between the 11-year solar cycle and the atmosphere. Part V: Summer, *J. Clim., 5*, 240-251.

Lahoz, W. A., et al. (1994), Three dimensional evolution of water vapour distributions in the northern hemisphere stratosphere as observed by the Microwave Limb Sounder, *J. Atmos. Sci., 51*, 2914-2930.

Lahoz, W. A., A. J. Geer, and A. O'Neill (2006), Dynamical evolution of the 2003 Southern Hemisphere stratospheric winter using Envisat trace-gas observations, *Quart. J. Roy. Meteor. Soc., 132*, 1985-2008.

Lang T.J., Barros A. P. (2002), An investigation of the onsets of the 1999 and 2000 monsoons in Central Nepal, *Monthly Weather Review* 130, 1299-1316.

Lau, N.-C., and J. M. Wallace (1979), On the distribution of horizontal transports by transient eddies in the Northern Hemisphere wintertime circulation, *J. Atmos. Sci., 36*, 1844-1861.

Leovy C. B. and P.J. Webster (1976), Stratospheric long waves: comparison of thermal structure in the northern and southern hemisphere, *J. Atmos. Sci,* 33, pp. 1624–1638.

Reproduced with permission of the copyright owner. Further reproduction prohibited without permission.

Leovy, C. B, C.-R. Sun, M. H. Hitchman, E. E. Remsberg, J. M. Russell III, L. L. Gordley, J. C. Gille, and L. V. Lyjak (1985), Transport of Ozone in the Middle Stratosphere: Evidence for Planetary Wave Breaking, *J. Atmos. Sci, 42, 230-244.*

Li CF, Yanai M. (1996), The onset and interannual variability of the Asian summer monsoon in relation to land-sea thermal contrast. *Journal of Climate* 9(2): 358-375.

Liebmann B., and D.L. Hartmann (1982), Interannual variations of outgoing IR associated with tropical circulation changes, *J. Atmos. Sci., 39*, 1153-1162.

Liebmann B. and C.A. Smith (1996), Description of a Complete (Interpolated) Outgoing Longwave Radiation Dataset, *Bulletin of the American Meteorological Society, 77*, 1275-1277.

London, J., R. D. Bojkov, S. Oltmans, and J. I. Kelley (1976), *Atlas of the Global Distribution of Total Ozone, July 1957-June 1967*, NCAR technical note 113, 276 pp., NTIS # PB258882/AS.

Lorenz E. N. (1967), The Nature and Theory of the General Circulation of the Atmosphere. *Geneva: World Meteorol. Org.* 161 pp.

Lorenz, E. N. (1970), The nature of the global circulation of the atmosphere: a present view, In *The Global Circulation of the Atmosphere, R. M. Soc., London*, pp. 3-23.

Luo H., and M. Yanai (1983), The large-scale circulation and heat sources over the Tibetan Plateau and surrounding areas during the early summer of 1979. Part I: Precipitation and kinematic analyses. *Mon. Wea. Rev.*, 111, 922–944.

Luo H., and M. Yanai (1984), The large-scale circulation and heat sources over the Tibetan Plateau and surrounding areas during the early summer of 1979. Part II: Heat and moisture budgets. *Mon. Wea. Rev.*, 112, 966–989.

MacDowall, J. (1960), Some observations at Halley Bay in seismology, glaciology, and meteorology, *Proc. Roy. Soc., A 256*, 149-196.

Madden, R. A., and P. R. Julian (1971), Detection of a 40-50 day oscillation in the zonal wind in the tropical Pacific.*J. Atmos. Sci.*, 28, 702-708.

Reproduced with permission of the copyright owner. Further reproduction prohibited without permission.

Madden, R. A., and P. R. Julian (1994), Observations of the 40-50 day tropical oscillation: a review. *Mon. Wea. Rev.*, 122, 814-837.

Magagi R., Barros A. P. (2004), Estimation of latent hating of rainfall during the onset of the Indian monsoon using TRMM PR and radiosonde data. *Journal of Applied Meteorology*, 43, 328-349.

Manabe S., Terpstra T. B. (1974), The effects of mountains on the general circulation of the atmosphere as identified by numerical experiments. *Journal of the Atmospheric Sciences,* 31.

Manney, G. L., J. D. Farrara, and C. R. Mechoso (1991), The behavior of wave 2 in the Southern Hemisphere stratosphere during late winter and early spring. *J. Atmos. Sci.,* 48, 976–998.

Manney, G.L., L. Froidevaux, J.W. Waters, R.W. Zurek, W.G. Read, L.S. Elson, J.B Kumer, J.L. Mergenthaler, A.E. Roche, A. Oneill, R.S. Harwood, I Mackenzie, and R. Swinbank (1994), Chemical depletion of ozone in the Arctic lower stratosphere during winter 1992-93. *Nature.* 370:429-434.

Manney, G.L., R.W. Zurek, L. Froidevaux, and J.W. Waters (1995), Evidence for Arctic ozone depletion in late February and early March 1994. *Geophys. Res. Lett.* 22:2941-2944.

Manton, M. J. and McBride, J. L. (1992), Recent research on the Australian monsoon, *J. Meteorol. Soc. Jpn.* , 70, 275-285

Matsuno, T. (1966), Quasi-geostrophic motions in the equatorial area. *J. Met. Soc. Japan, 44 (1)*, 25-42.

Matsuno, T. (1970), Vertical Propagation of Stationary Planetary Waves in the Winter Northern Hemisphere. *J. Atmos. Sci.*, 27, 871–883.

McBride, J. L. (1983), Satellite observations of the Southern Hemisphere monsoon during winter MONEX. *Tellus,* 35A, 189–197.

McBride, J.L. (1987), The Australian summer monsoon. In: Chang, C-.P. and Krishnamurti, T.N., Editors, 1987. *Monsoon Meteorology*, Oxford University Press, Oxford, pp. 203–231.

Reproduced with permission of the copyright owner. Further reproduction prohibited without permission.

McBride, J.L., and Nicholls, N. (1983), Seasonal relationships between Australian rainfall and the Southern Oscillation, *Monthly Weather Review*, 111, 1998-2004.

McBride, J. L., and N. Nicholls (1983), Seasonal relationships between Australian rainfall and the Southern Oscillation, *Mon. Wea. Rev.*, 111, 1998–2004.

McCormack, J. P., and L. L. Hood (1994), Relationship between ozone and temperature trends in the lower stratosphere: Latitude and seasonal dependences, *Geophys. Res. Lett., 21(15),* 1615–1618.

McIntyre M. E. (1992), Atmospheric dynamics: Some fundamentals, with observational implications. *Proceeding of the International School of Physics "Enrico Fermi" CXV Course,* J. C. Gille and G. Visconti, Eds., North-Holland, 313–386.

Mechoso, C R. and D. L. Hartmann (1982), An observational study of traveling planetary waves in the Southern Hemisphere, *J. Atmos. Sci.* 39, 1921-1935.

Mechoso, C. R., A. O'Neill, V. D. Pope, and J. D. Farrara (1988), A study of the stratospheric final warming of 1982 in the Southern Hemisphere, *Quart. J. R. Meteor. Soc., 114*, 1365-1384.

Mote, P. W., T. J. Dunkerton, and D. Wu (2002), Kelvin waves in stratospheric temperature observed by the Microwave Limb Sounder, *J. Geophys. Res., 107(D14)*, 4218, doi:10.1029/2001JD001056.

Murakami, T. (1958), The sudden change of upper westerlies near the Tibetan Plateau at the beginning of summer season. *J. Meteor. Soc. Japan*, 36, 239-247.

Murakami, T., (1980), Empirical orthogonal function analysis of satellite-observed outgoing longwave radiation during summer. *Mon. Wea. Rev.,* 108, 205–222.

Murakami, T., (1980), Temporal variations of satellite-observed outgoing longwave radiation over the winter monsoon region. Part I: Long- period (15–30 day) oscillations. *Mon. Wea. Rev.,* 108, 408–426.

Murakami, T., (1980), Temporal variations of satellite-observed outgoing longwave radiation over the winter monsoon region. Part II: Short- period (4–6 day) oscillations. *Mon. Wea. Rev.,* 108, 427–444.

Reproduced with permission of the copyright owner. Further reproduction prohibited without permission.

Murakami, T., and A. Sumi (1982), Southern Hemisphere monsoon circulation during the 1978–79 WMONEX. Part I: Monthly mean wind fields. *J. Meteor. Soc. Japan,* 60, 638–648.

Nathan, T. R., and E. C. Cordero (2007), An ozone-modified refractive index for vertically propagating planetary waves, *J. Geophys. Res., 112*, D02105.

Newell, R. E., J. W. Kidson, D.G. Vincent and G. J. Boer (1974), The General Circulation of the Tropical Atmosphere and Interactions with Extratropical Latitudes, *Vol 2. MIT Press.* 371 pp.

Newell, R. E., et al. (1996), Vertical fine-scale atmospheric structure measured from NASA DC-8 during PEM-West A. *J. Geophys. Res., 101*, 1943-1960.

Newman, P. A., and W. J. Randel (1988), Coherent ozone-dynamical changes during the Southern Hemisphere spring, 1979-1986, *J. Geophys.Res., 93*, 12,585-12,606.

Newman, P. A., and E. R. Nash (2005), The unusual Southern Hemisphere stratosphere winter of 2002, *J. Atmos. Sci., 62*, 614-628.

Nicholls, N. (1981), Air–sea interaction and the possibility of long-range weather prediction in the Indonesian archipelago, *Mon. Wea. Rev.,* 109, 2435–2443.

Nogues-Paegle, J. E., and Z. Zhen (1987), The Australian Subtropical Jet during the Second Observing Period of the Global Weather Experiment, *J. Atmos. Sci., 44*, 2277-2289.

Nogues-Paegle, J. E., and K. C. Mo (1988), Transient response of the Southern Hemisphere subtropical jet to tropical forcing, *J. Atmos. Sci., 45*, 1493-1530.

Olsen, M. A., M. R. Schoeberl, and A. R. Douglass (2004), Stratosphere-troposphere exchange of mass and ozone, *J. Geophys. Res., 109*, D24114.

O'Neill, A., and Pope V. D. (1988), Simulations of linear and nonlinear disturbances in the stratosphere, *Quart. J. Roy. Meteor. Soc., 114,* 1063–1110.

Orsolini, Y., D. Cariolle, and M. Deque (1995), Ridge formation in the lower stratosphere and its influence on ozone transport: A general circulation model study during late January 1992, *J.Geophys. Res., 100,* 11113–11135.

Reproduced with permission of the copyright owner. Further reproduction prohibited without permission.

Orsolini, Y. J., D. B. Stephenson, and F. J. Doblas-Reyes (1998), Storm track signature in the total ozone during northern hemisphere winter, *Geophys. Res. Lett. , 25,* 2413–2416.

O'Sullivan, D.J. and T.J. Dunkerton (1995), Generation of inertia-gravity waves in a simulated lifecycle of baroclinic instability, *J. Atmos. Sci., 52*, 3695-3716.

Parish, T. R., D. H. Bromwich, and R.-Y. Tzeng (1994), On the role of the Antarctic continent in forcing large-scale circulations in the high southern latitudes, *J. Atmos. Sci., 51*, 3566-3579.

Pascoe, C.L., L.J. Gray. S.A. Crooks, M. N. Juckes, and M.P. Baldwin (2005), The quasi-biennial oscillation: Analysis using ERA-40 data, *J. Geophys. Res., 110*, D08105.

Pauluis O., Czaja A., Korty R. (2008), The Global Atmospheric Circulation on Moist Isentropes, *Science*, Vol. 321. no. 5892, pp. 1075 – 1078. doi: 10.1126/science.1159649

Peixoto, J. P., A. H. Oort, M. D. Almeida, and A. Tome (1991), Entropy budget of the atmosphere. *J. Geophys. Res.,* 96 (D6), 10981–10988.

Peixoto, J. P., and A. H. Oort, (1992), Physics of Climate. *Amer. Inst. of Phys., New York, NY.* 520 pp.

Perliski, L. M., S. Solomon, and J. London (1989), On the interpretation of seasonal variations of stratospheric ozone, *Planet. Space Sci., 37*, 1527-1538.

Pierce, R.B, and T. D. Fairlie (1993), Chaotic advection in the stratosphere: Implications for the dispersal of chemically perturbed air from the polar vortex, *J. Geophys. Res., 98*, 18589-18595.

Plumb, R.A. (1989), On the seasonal cycle of stratospheric planetary waves. *Pure Appl. Geophys., 130*, 233-42.

Pokrandt, P. J., G. J. Tripoli, and D. D. Houghton (1996), Processes leading to the formation of mesoscale waves in the midwest cyclone of 15 December 1987, *Mon. Weather Rev., 124,* 2726–2752.

Polvani, L. M., and P. J. Kushner (2002), Tropospheric response to stratospheric perturbations in a relatively simple general circulation model, *Geophys Res. Lett., 29(7)*, 1114.

Reproduced with permission of the copyright owner. Further reproduction prohibited without permission.

Postel, G. A., and M. H. Hitchman (1999), Climatology of Rossby wave breaking along the subtropical tropopause, *J. Atmos. Sci., 56*, 359-373.

Quintanar, A. I. and C. R. Mechoso (1995a), Quasi-stationary waves in the Southern Hemisphere, Part I: Observational Data. *J. Clim.*, *8*, 2659-2672.

Quintanar, A. I. and C. R. Mechoso (1995b), Quasi-stationary waves in the Southern Hemisphere, Part II: Generation Mechanisms. *J. Clim.*, *8*, 2673-2690.

Ramage C. S. (1968), Role of a tropical "Maritime Continent" in the atmospheric circulation, *Mon. Wea. Rev.*, 96, 365–369.

Randel, W. J. (1987), A study of planetary waves in the southern winter troposphere and stratosphere. Part I: Wave structure and vertical propagation, *J. Atmos. Sci., 44*, 917-935.

Randel,W. J., D. E. Stevens, and J. L. Stanford (1987), Astudy of planetarywaves in the southern winter troposphere and stratosphere. Part II: Life cycles, *J. Atmos. Sci., 44*, 936-949.

Randel W. J. (1987), The evaluation of winds from geopotential height data in the stratosphere. *J. Atmos. Sci*, 44, 3097–3120.

Randel, W.J. (1988), Anomalous circulation in the southern hemisphere stratosphere during spring 1987, *Geophys. Res. Lett., 15,* 911-14.

Randel W. J. (1988), The seasonal evolution of planetary waves in the Southern Hemisphere stratosphere and troposphere. *Quart. J. Roy. Meteor. Soc*, 114, 1385–1409.

Randel, W.J. (1990), Coherent wave-zonal mean flow interactions in the troposphere, *J. Atmos. Sci.,* 47, 439-456.

Randel, W.J., B.A. Boville and J.C. Gille (1990), Observations of planetary mixed Rossby-gravity waves in the upper stratosphere, *J. Atmos. Sci.,* 47, 3078-3091.

Randel, W. J., and I.M. Held (1991), Phase speed spectra of transient eddy fluxes and critical layer absorption. *J. Atmos. Sci.,* 48, 688-697.

Reproduced with permission of the copyright owner. Further reproduction prohibited without permission.

Randel, W. J., et al. (1993), Stratospheric transport from the tropics to middle latitudes by planetary wave mixing, *Nature, 365*, 533-535.

Randel, W.J., and J. B. Cobb (1994), Coherent variations of monthly mean total ozone and lower stratospheric temperature, *J. Geophys. Res., 99*, 5433–5477.

Randel, W. J., and F. Wu (1999), Cooling of the Arctic and Antarctic polar stratospheres due to ozone depletion, *J. Clim., 12*, 1467-1479.

Randel, W.J., F. Wu, and R. Stolarski (2002), Changes in column ozone correlated with the stratospheric EP flux. *J. Meteorol. Soc. Jpn., 80*, 849-862.

Randel, W. J., and M. Park (2006), Deep convective influence on the Asian summer monsoon anticyclone and associated tracer variability observed with Atmospheric Infrared Sounder (AIRS), *J. Geophys. Atmos., 111(D12)*, D12314.

Reiter, E. R. and Gao, D.-Y. (1982), Heating of the Tibetian plateau and movements of the south Asian high during spring. *Mon. Weather Rev.*, 110, 1694-1711.

Renwick, J. A., and M. J. Revell (1999), Blocking over the South Pacific and Rossby wave Propagation, *Mon. Wea. Rev., 127*, 2233-2247.

Rodwell, M. J., and B. J. Hoskins, Subtropical anticyclones and summer monsoons. *J. Clim*, 14, 3192-3211, 2001.

Rogal, M. J., M. H. Hitchman, M. L. Buker, G. J. Tripoli, I. Stajner, and H. Hayashi (2009), Modeling the effects of Southeast Asian monsoon outflow on subtropical anticyclones and midlatitude ozone over the Southern Indian Ocean, *submitted to J. Geophys. Res.*

Rosenlof, K.H., D.E. Stevens, J.R. Anderson, and P.E. Ciesielski (1986), The Walker Circulation with observed zonal winds, a mean Hadley cell, and cumulus friction, *J. Atmos. Sci., 43*, 449-467.

Rui, H., and B. Wang (1990), Development characteristics and dynamic structure of tropical intraseasonal convection anomalies, *J. Atmos. Sci.*, 47, 357-379.

Reproduced with permission of the copyright owner. Further reproduction prohibited without permission.

Salby M.L, D.L. Hartmann, P.L. Baily and J.C. Gille (1984), Evidence of equatorial Kelvin modes in Nimbus-7 LIMS. *J. Atmos. Sci. 41*, pp. 220–235.

Sardeshmukh, P. D., and B. J. Hoskins (1988), The generation of global rotational flow by steady idealized tropical divergence, *J. Atmos. Sci., 45*, 1228-1251.

Sassi, F., D. Kinnison, B.A. Bouville, R. R. Garcia, and R. Roble (2004), Effect of El Niño-Southern Oscillation on the dynamical, thermal, and chemical structure of the middle atmosphere, *J. Geophys. Res., 109*, D17108.

Sato, K., Y. Tomikawa, G. Hashida, T. Yamanouchi, H. Nakajima, and T. Sugita (2009), Longitudinally Dependent Ozone Increase in the Antarctic Polar Vortex Revealed by Balloon and Satellite Observations, *J. Atmos. Sci., 66*, 1807–1820.

Schaack, T. K. (1982), The global angular momentum balance for January 1979, *University of Wisconsin-Madison, Department of Meteorology, Madison, WI,* Call Number: UW MET Publication No.82.09.S1.

Schaack, T. K., D. R. Johnson, and M. Wei (1990), The three-dimensional distribution of atmospheric heating during the GWE. *Tellus*, 42A, 305-327.

Schaack, T. K. and D. R. Johnson (1994), January/July global distributions of atmospheric heating for 1986, 1987 and 1988. *J. Climate,* 7, 1270-1285.

Schneider, E. K., and R. S. Lindzen (1980), Comments on cumulus friction: Estimated influence on the tropical mean meridional circulation, *J. Atmos. Sci., 37*, 2803-2806

Schubert, S.D., and M.J. Munteanu (1988), An analysis of tropopause pressure and total ozone correlations, *Mon. Wea. Rev., 116*, 569-582.

Shapiro, M. A. (1980), Turbulent mixing within tropopause folds as a mechanism for the exchange of chemical constituents between the stratosphere and troposphere, *J. Atmos. Sci., 37,* 994-1004.

Shaw, Sir Napier (1930), Manual of Meteorology. Vol. III: The Physical Processes of Weather, *Cambridge University Press*, Cambridge.

Reproduced with permission of the copyright owner. Further reproduction prohibited without permission.

Shimizu, A., and T. Tsuda (1997), Characteristics of Kelvin waves and gravity waves observed with radiosondes over Indonesia, *J. Geophys. Res.*, 102(D22), 26,159–26,171.

Shiotani, M. and I. Hirota (1985), Planetary wave-mean flow interaction in the stratosphere: a comparison between northern and southern hemisphere, *Quart. J. Roy. Meteor. Soc., 111,* 309-334.

Shiotani, M. (1990), Low-frequency variations of the zonal mean state of the Southern Hemisphere troposphere. *J. Meteor. Soc. Japan,* 68, 461–470.

Shiotani, M., K. Kuroi, and I. Hirota (1990), Eastward travelling waves in the Southern Hemisphere stratosphere during the spring of 1983. *Quart. J. Roy. Meteor. Soc.,* 116, 913–927..

Shiotani, M. (1992), Annual, quasi-biennial, and El Nino – Southern Oscillation (ENSO) time-scale variations in equatorial total ozone, *J. Geophys. Res., 97,* 7625-7633.

Shiotani, M., and I. Hirota (1992), Planetary wave-mean flow interaction in the stratosphere: a comparison between northern and southern hemispheres, *Quart. J. R. Met. Soc., 111,* 309-334.

Shiotani, M., N. Shimoda, and I. Hirota (1993), Inter-annual variability of the stratospheric circulation in the southern hemisphere, *Q. J. R. Meteorol. Soc., 119,* 531–546.

Shiotani, M., J. G. Gille, and A. E. Roche (1997), Kelvin waves in the equatorial lower stratosphere as revealed by cryogenic limb array etalon spectrometer temperature data, *J. Geophys. Res., 102(D22),* 26,131–26,140.

Simmons, A. J., and B. J. Hoskins (1978), The life cycles of some nonlinear baroclinic waves, *J. Atmos. Sci., 35,* 414-432.

Solomon, S., et al. (2005), Four decades of ozonesonde measurements over Antarctica, *J. Geophys. Res., 110,* D21311.

Steinbrecht, W., H. Claude, U. Köhler, K. P. Hoinka (1998), Correlations between tropopause height and total ozone: Implications for long-term changes. *J. Geophys. Res., 103(D15),* 19,183-19,192.

Reproduced with permission of the copyright owner. Further reproduction prohibited without permission.

Stajner, I, L. P. Riishojgaard and R. B. Rood (2001), The GEOS ozone data assimilation system: Specification of error statistics, *Quart. J. Roy. Meteor. Soc., 127*, 1069-1094.

Stajner, I., K. Wargan (2004), Antarctic stratospheric ozone from the assimilation of occultation data, *Geophys. Res. Lett., 31*, L18108.

Stajner, I., K. Wargan, L.-P. Chang, H. Hayashi, S. Pawson, and H. Nakajima (2006), Assimilation of ozone profiles from the Improved Limb Atmospheric Spectrometer-II: Study of Antarctic ozone, *J. Geophys. Res., 111*, D11S14.

Stolarski, R. S., M. R. Schoeberl, P. A. Newman, R. D. McPeters, A. J. Krueger (1990), The 1989 Antarctic ozone hole as observed by TOMS, *Geophys. Res. Lett., 17*, 1267-1270.

Stolarski, R.S., P. Bloomfield, R.D. McPeters, and J.R. Herman (1991), Total ozone trends deduced from Nimbus 7 TOMS data, *Geophys. Res. Lett., 18*, 1015-1018.

Stolarski, R.S., R. Bojkov, L. Bishop, C. Zerefos, J. Staehelin, and J. Zawodny (1992), Measured trends in stratospheric ozone, *Science, 256*, 342 – 349.

Stolarski, R. S., R. D. McPeters, and P. A. Newman (2005), The ozone hole of 2002 as measured by TOMS, *J. Atmos. Sci., 62*, 716-720.

Straub, K.H. and G.N. Kiladis (2002), Observations of a convectively coupled Kelvin wave in the eastern Pacific ITCZ. *J. Atmos. Sci., 59*, 30-53.

Straub, K.H. and G.N. Kiladis (2003), Extratropical forcing of convectively coupled Kelvin waves during Austral winter. *J. Atmos. Sci., 60*, 526-543.

Straub, K.H. and G.N. Kiladis (2003), The observed structure of convectively coupled Kelvin waves: Comparison with simple models of coupled wave instability. *J. Atmos. Sci., 60*, 1655-1668.

Straus, D. M. (1981), Long-wave baroclinic instability in the troposphere and stratosphere with spherical geometry. *J. Atmos. Sci.,* 38, 409–426.

Stokes G. G. (1847), On the theory of oscillatory waves, *Trans. Cambridge Philos. Soc.* 8, pp. 441–455.

Reproduced with permission of the copyright owner. Further reproduction prohibited without permission.

Sumathipala W.L. (1989), Characteristics of transition seasons in the eastern hemisphere tropics, *Aust. Met. Mag., 37*, 37-45.

Swanson, G. S., and K. E. Trenberth (1981), Interannual variability in the Southern Hemisphere tropospheric circulation. *Mon. Wea. Rev.,* 109, 1879–1889.

Swinbank, R., and A. O'Neill (1994), Astratosphere-troposphere data assimilation system, *Mon. Wea. Rev., 122*, 686-702.

Thompson, D.W. J., M. P. Baldwin, and S. Solomon (2005), Stratosphere-troposphere coupling in the Southern Hemisphere, *J. Atmos. Sci., 62*, 708-715.

Thomson J. (1892), Bakerian Lecture. On the grand currents of atmospheric circulation. *Phil. Trans. R. Soc. A* 183, 653–84.

Townsend R. D. and D. R. Johnson (1981), The mass and angular momentum balance of the zonally-averaged global circulation, *ICSU/WMO GARP Conf. Proc. Int. Conf. Prelim. FGGE Data Anal. Results, Bergen, Norway, World Meteorol. Organ.*, Geneva, 542-552.

Townsend, R. D. and Johnson, D. R. (1985), A diagnostic study of the isentropic zonally averaged mass circulation during the First GARP Global Experiment. *J. Atmos. Sci.* , 42, 1565-1579.

Trenberth, K. E. (1982), Seasonality in southern hemisphere eddy statistics at 500 mb. *J. Atmos. Sci.* , 39, 2507-2520.

Trenberth, K. E., and J. G. Olson (1988), An evaluation and intercomparison of global analyses from NMC and ECMWF. *Bull. Amer. Meteor. Soc.*, 69, 1047-1057.

Trenberth K.E. (1992), Global Analyses from ECMWF and Atlas of 1000 to 10 mb Circulation Statistics, *NCAR/TN-373+STR*, 205 pp.

Trepte, C. R., R. E. Veiga, and M. P. McCormick (1993), Poleward dispersal of Mt. Pinabuto aerosols, *J. Geophys. Res., 98*, 18,563-18,573.

Tripoli, Gregory J. (1992), A nonhydrostatic mesoscale model designed to simulate scale interaction, *Mon. Weather Rev., 120*, 1342–1359.

Reproduced with permission of the copyright owner. Further reproduction prohibited without permission.

Troup, A. J. (1961), Variations in upper tropospheric flow associated with the onset of the Australian summer monsoon. *Indian J. Meteorol. Geophys.* , 12, 217-230.

Troup. A. J. (1965), The Southern Oscillation, *Q. Jl R. met. Soc.*, 91, 490–506.

Tsuda T., Y. Murayama, H. Wiryosumarto, S.W.B. Harijono and S. Kato (1994), Radiosonde observations of equatorial atmosphere dynamics over indonesia Part1: Equatorial waves and diurnal tides. *J. Geophs. Res. 99*, pp. 10491–10505.

Tsuda T., Y. Murayama, H. Wiryosumarto, S.W.B. Harijono and S. Kato (1994), Radiosonde observations of equatorial atmosphere dynamics over indonesia Part2: Characteristics of gravity waves. *J. Geophs. Res. 99*, p. 10,507-10,516.

van Loon, H. V., and R. Jenne (1972), The zonal harmonic standing waves in the Southern Hemisphere, *J. Geophys. Res., 77*, 992–1003.

van Loon, H., and K. Labitzke (1987), The Southern Oscillation, Part V: The anomalies in the lower stratosphere of the Northern Hemisphere in winter and a comparison with the Quasi-Biennial Oscillation, *Mon. Weather Rev., 115*, 357-369.

van Loon, H., C. S. Zerefos, and C. C. Repapis (1982), The Southern Oscillation in the stratosphere, *Mon. Weather Rev., 110*, 225-229.

Venne D. E. and J.L. Stanford (1982), An observational study of high-latitude stratospheric planetary waves in winter, *J. Atmos. Sci.,* 39, pp. 1026–1034.

Vincent, D. G., and P. L. Silva Dias (1998), Meteorology of the tropics: Pacific Ocean, in *Meteorology of the Southern Hemisphere, American Meteorological Society.*

Wallace J.M. and V.E. Kousky (1968), Observational evidence of Kelvin waves in the tropical stratosphere. *J. Atmos. Sci., 25,* 900–907.

Wallace, J. M. (1978), Trajectory slopes, countergradient heat fluxes and mixing by lower stratospheric waves, *J. Atmos. Sci., 35,* 554-558.

Reproduced with permission of the copyright owner. Further reproduction prohibited without permission.

Wallace J. M., Gutzler D. S. (1981), Teleconnections in the geopotential height field during the Northern Hemisphere winter, *Mon. Weather Rev.*, *109*, 812.

Wang, B. (1988), Dynamics of Tropical Low-Frequency Waves: An Analysis of the Moist Kelvin Wave, *J. Atmos. Sci.*, 45, 2051-2065.

Webster, P. J. (1972), Response of the tropical atmosphere to local, steady forcing, *Mon. Wea. Rev.*, *100*, 518-541.

Webster, P. J. and S. Yang (1992), Monsoon and ENSO: Selectively Interactive Systems. *Quart. J. Roy. Meteor. Soc.*, 118, 877-926.

Wei, M.-Y., D. R. Johnson, and R. D. Townsend (1983), Seasonal distributions of diabatic heating during the First GARP Global Experiment. *Tellus,* 35A, 241–255.

Wheeler, M., G.N. Kiladis and P.J. Webster (2000), Large-scale dynamical fields associated with convectively-coupled equatorial waves. *J. Atmos. Sci., 57*, 613-640.

Wheeler, M.C. and H.H. Hendon (2004), An all-season real-time multivariate MJO index: Development of an index for monitoring and prediction. *Mon. Wea. Rev., 132*, 1917-1932.

Wheeler, M.C. and J.L. McBride (2005), Australian-Indonesian monsoon, in: W.K.M. Lau and D.E. Waliser (eds), *Intraseasonal Variability in the Atmosphere-Ocean Climate System*. Praxis, Springer Berlin Heidelberg, pages 125-173.

White, G. H. (1982), An observational study of the Northern Hemisphere extratropical summertime general circulation, *J. Atmos. Sci., 39*, 24–40.

Wirth, V. (1991), What causes the seasonal cycle of stationary planetary waves in the southern stratosphere? *J. Atmos. Sci., 48*, 1194-1200.

Wirth, V. (1993), Quasi-stationary planetary waves in total ozone and their correlation with lower stratospheric temperature. *J. Geophys. Res., 98*, 8873-8882.

Reproduced with permission of the copyright owner. Further reproduction prohibited without permission.

Wu, G., Y. Liu, T. Wang, R. Wan, X. Liu, W. Li, Z. Wang, Q. Zhang, A. Duan, and X. Liang (2007), The Influence of Mechanical and Thermal Forcing by the Tibetan Plateau on Asian Climate. *J. Hydrometeor.*, 8, 770–789.

Wyrtki, K. (1985), Sea level fluctuations in the Pacific during the 1982-83 El Niño, *Geophys. Res. Lett.*, *12*, 125-128.

Wyrtki, K. (1985), Water displacements in the Pacific and the genesis of El Niño cycles, *J. Geophys. Res.-Oceans*, *90*, 7129-7132.

Yanai, M. S., Esbensen, S., and Chu, J. H. (1973), Determination of bulk properties of tropical cloud clusters from large-scale heat and moisture budgets. *J. Atmos. Sci.*, 30, 611-627.

Yanai M, Li C, Song Z. (1992), Seasonal heating of the Tibetan plateau and its effects on the evolution of the Asian summer monsoon. *Journal of the Meteorological Society of Japan* 70: 319-351.

Yanai, M., and R. H. Johnson (1993), Impacts of cumulus convection on thermodynamic fields. *Representation of Cumulus Convection in Numerical Models of the Atmosphere, Meteor. Monogr.,* No. 46, Amer. Meteor. Soc., 39–62.

Yanai, M., and C. Li (1994), Mechanism of Heating and the Boundary Layer over the Tibetan Plateau. , 122, 305–323.

Yanai, M., and T. Tomita (1998), Seasonal and Interannual Variability of Atmospheric Heat Sources and Moisture Sinks as Determined from NCEP–NCAR Reanalysis. *J. Climate*, 11, 463–482.

Yao, C.-Y. (1994), Geographical variation in the annual and quasi-biennial cycles in the tropical lower stratosphere, M. S. thesis, University of Wisconsin – Madison, 130 pp.

Ye D. (1981), Some characteristics of the summer circulation over the Qinghai-Xizang (Tibet) Plateau and its neighborhood. *Bulletin of the American Meteorological Society* 62, 14-19.

Reproduced with permission of the copyright owner. Further reproduction prohibited without permission.

Yeh T.-C., S.-W. Lo, and P.-C. Chu (1957),The wind structure and heat balance in the lower troposphere over Tibetan Plateau and its surroundings. *Acta Meteor. Sin.*, 28, 108–121.

Yeh T.-C., and Y.-X. Gao (1979), *The Meteorology of Qinghai-Zizang (Tibet) Plateau.* Science Press, 278 pp.

Young, R.E., and H. Houben (1989), Dynamics of Planetary-Scale Baroclinic Waves during Southern Hemisphere Winter. *J. Atmos. Sci.*, 46, 1365–1383.

Zhang, C. (2005), The Madden Julian Oscillation, *Reviews of Geophysics*, 43, RG2003, doi:10.1029/2004RG000158.

Zhang J. J., Zhu Baozheng, Zhu Fukang, et al. (1988), Advances in Qinghai-Xizang Meteorology, Science Press, Beijing, 14-89.

Reproduced with permission of the copyright owner. Further reproduction prohibited without permission.

Appendix A: List of variables

Symbol	Variable
N	Brunt-Vaissala Frequency
T	Temperature
t	Time
θ	Potential temperature
β	Meridional gradient of Coriolis parameter
f	Coriolis parameter
l	Meridional wavenumber
k	Zonal wavenumber
m	Vertical wavenumber
ε	$(f_o/N)^2$
$\bar{u}$	Zonal mean flow
c	Zonal trace speed
λ	Wavelength
φ	Latitude
r	Earth's radius
R	Gas constant adjusted by $(p_o/p)^{1/(cp/cv)}p_o^{-1}$
p	Pressure
Φ	Geoptential
Q	Eulerian heating
X, Y	Friction
F	Eliassen-Palm vector
$\nabla \cdot F$	Eliassen-Palm vector divergence
ψ_0	Base streamfunction waveamplitude
q	Quasi-geostrophic potential vorticity
$[q]_y$	Meridional gradient of qgpv

Reproduced with permission of the copyright owner. Further reproduction prohibited without permission.

θ_R	Reference potential temperature
K	Total wavenumber

Reproduced with permission of the copyright owner. Further reproduction prohibited without permission.